# Clocked Atom Delivery to a Photonic Crystal Waveguide: Simulations and Experiments

Thesis by

Lucas Sky Peng

In Partial Fulfillment of the Requirements for the
Degree of
Doctor of Philosophy

Caltech

CALIFORNIA INSTITUTE OF TECHNOLOGY
Pasadena, California

2019
Defended May 13, 2019

# ACKNOWLEDGEMENTS

First, my thanks go to Jeff Kimble for providing me the opportunity to be a part of his outstanding research group and work in the exciting fields of Quantum Optics and Atomic Physics. During the past six years, Jeff has consistently challenged me with various ambitious projects. It is Jeff's effort and vision that enabled the progress that we have made in Lab 2 and the group. I always feel motivated and have a better understanding of the problem at hand after a long conversation with Jeff. I have learned a lot not only about physics but also about how to approach research in general from Jeff, and I am sure it will be a great asset for the rest of my career.

I would also like to thank my colleagues from Lab 2, where all the work in this thesis was done. Jae Hoon Lee, Mike Martin, Juan Muniz, and Andrew McClung built the Lab 2 photonic crystal waveguide experiment from scratch, which continues to function to this day. When I first started in the group, it was Jae who taught me the essential vacuum system techniques. Mike helped me improving my early electronics design, and I am impressed by his extensive knowledge and hands-on experience. Andrew always comes up with exciting and new ways to do things, and I learned a great deal from him.

In my last three years at the Kimble group, I worked closely with Juan Muniz and Alex Burgers. Juan is one of the most determined people I have met. Under his guidance, I learned how to operate the complex machine that is the Lab 2 apparatus, and more importantly, to expand on the experimental setup. I could not have asked for a better mentor. Alex is an excellent labmate and also a good friend. He never hesitated to get his hand dirty doing various jobs in the lab. I am grateful to have both of you to share both the disappointing and the triumphant moments in this journey.

Su-Peng Yu and Jon Hood laid the foundation of the device design and fabrication process, and this research would be impossible without them. I would like to thank the "original" Lab 11 team, including Chen-Lung Hung, Akihisa Goban, and Mingwu Lu for enlightening discussions. To the current Lab 11 crew, Jean Baptiste

Beguin, Xingsheng Luan, and Zhongzhong Qin, I would like to thank you for your support, and I am sure the new experimental setup will be a success and produce great results! I would also like to offer my thanks to our theoretical collaborators, Prof. Darrick Chang, and Ana Asenjo-Garcia for fruitful discussions, Charles Ross for our endeavor on calculating Casimir-Polder potential, and Scott Curtis for always keeping track of our accounts and purchases and making the bureaucracy invisible to us.

To my friends, Ken Wong, Chia-Chuan Liu, Yu-Hung Lai, Chun-lin Liu, Kevin Burdge, Xin-Wei Wang, Yun Mou, Chan U Lei, Gene Kao and Linhan Sheng, thank you for your support and accompany, my Ph.D. journey would be colorless without you guys. I would like to thank my family – my grandparents and parents – for their persistent support throughout my life. And finally, I express my appreciation to I-Hui Huang for her love and support.

# ABSTRACT

Integrating atomic physics with nanophotonics devices provides a new research platform for quantum optics and many-body physics. The robustness and scalability of advanced lithographic fabrication technology provide powerful tools to enhance and control atom-photon interaction. Dispersion engineered photonic crystal waveguides (PCWs), such as the alligator photonic crystal waveguides (APCWs) described in this thesis, allow stable trapping and probing of atoms via guided modes (GMs). By tuning the photonic band-edges of the PCWs, the photon-mediated interactions between atoms can be modified. This thesis describes simulations and experiments that develop a quantitative understanding of atomic motion near the surfaces of APCWs. The atoms are delivered to APCWs using optical lattice. Synchronous with the moving lattice, transmission spectra for a guided-mode probe field are recorded as functions of lattice transport time and frequency detuning of the probe beam. With these 2D "clocked" spectra, we have been able to validate quantitatively our numerical simulations, which are based upon a detailed understanding of atomic trajectories that pass around and through nanoscopic regions of the APCW under the influence of optical and surface forces. By introducing auxiliary GMs of various polarizations and intensities, we have begun to control the atomic trajectories to some degree. For example, atoms can be guided to the central vacuum gap of the APCW at predetermined times and with known AC-Stark shifts. The applications of combining clocked atom delivery and numerical simulation include enabling high fractional filling of optical trap sites within PCWs, calibration of optical fields within PCWs, and utilization of the time-dependent, optically dense atomic medium for novel nonlinear optical experiments.

# PUBLISHED CONTENT AND CONTRIBUTIONS

A. P. Burgers, L. S. Peng, J. A. Muniz, A. C. McClung, M. J. Martin, and H. J. Kimble. (2019). “Clocked atom delivery to a photonic crystal waveguide”. In: *Proceedings of the National Academy of Sciences* 116(2):456–465. DOI: `10.1073/pnas.1817249115`.

LSP participated in the construction of the experiment apparatus, performed the experiments, analyzed the experimental data, performed numerical simulations and participated in the writing of the manuscript.

# TABLE OF CONTENTS

# LIST OF ILLUSTRATIONS

## *Chapter 1*

# INTRODUCTION

Achieving strong and controllable interactions between atoms and photons at the quantum level has been a central goal in the fields of atomic physics and quantum optics [19]. Historically, the simplicity and the ready availability make atomic systems a platform for observing fundamental quantum phenomena, such as in nonclassical statistics of light emitted by single atoms [60] and reversible vacuum Rabi oscillations between a single atom and a photon [15, 86, 99]. In many fields of research, including quantum information science, quantum optics, and quantum metrology, interacting systems of atoms and photons are an important resource.

With the increasing level of experimental control and the complex interaction that can occur between light and atoms, atomic systems are becoming a platform for investigating new types of many-body phenomena. These phenomena open up new links from quantum optics and atomic physics to quantum information theory and condensed matter. Some of these new areas of research include the self-organization of atoms due to the strong two-way interaction between atom and optical forces [8, 17, 32], and strongly interacting photon gases [12, 80, 111]. The appeal of atomic systems arises from the fact that ultracold atoms are close to an ideal isolated quantum system, ultra-high vacuum keeps atoms isolated from the environment, and the ability to cool atoms to ultracold temperature eliminates inhomogeneity. These properties make neutral atoms a possibility for realizing scalable quantum computers [27].

Conventionally, atom-light interaction is implemented with a macroscopic, free-space setup. In free-space, even for tightly-focused laser beams, the strength of atom-photon interaction is limited [102]. A common way to enhance the interaction strength is to place an atom in a resonant cavity, wich Purcell first suggested [84]. Intuitively, it can be understood as the light bouncing multiple times in the cavity, which therefore greatly increases the probability of interaction between an atom and photon. Another way of understanding this is that the cavity modifies the local density of optical states (LDOS) at the resonant frequency [70]. The Purcell factor can capture this enhancement, which is defined as the ratio of decay rate into the resonator mode to the decay rate into all other modes. For a cavity QED system, the

Purcell factor $P_c$ is given by

$$P_c \equiv \frac{\Gamma_c}{\Gamma'} = \frac{3Q}{4\pi^2}\left(\frac{\lambda_0^3}{V_m}\right) \tag{1.1}$$

where $\Gamma_c$ is the decay rate into the cavity mode, $\Gamma'$ is the decay rate into all other modes, $Q$ is the quality factor of the cavity, $\lambda_0$ is the wavelength of the atomic transition and $V_m$ is the mode volume of the cavity. It is obvious from this formula that higher-Q cavities and those with tighter confined modes can obtain a greater Purcell factor.

Cavities are not the only structure that can enhance atom-light interaction. Over the past decade, there has been an effort to migrate to microphotonic and nanophotonic platforms [2, 38, 39, 70, 98]. The robustness and scalability provided by advanced lithographic fabrication technology may eventually lead to atomic physics and quantum optics on a chip. The integration of ultra-cold atoms with nanophotonic devices leads to strong atom-photon interactions that not only quantitatively advance Quantum Optics but which also create qualitatively new paradigms for atom-photon interactions [20, 33, 42, 71, 83]. Owing to small optical loss and tight confinement of the electromagnetic field, nanoscale devices are capable of mediating long-range atom-atom interactions by way of optical photons in the guided modes (GMs) of the structures. In a complementary fashion, underlying lattices of atoms in one and two-dimensional dielectric structures can mediate long-range interactions between photons [41, 42, 51]. With advanced fabrication capabilities brought by nanophotonics, such physical processes provide novel possibilities for quantum communication, computation, networks, and metrology, as well as for quantum phases of light and matter [20, 41, 42, 51, 71, 83].

In the 1980s, it was suggested that dielectric structures with periodic dielectric constant can be used to modify the LDOS [55, 108]. These media are called photonic crystals, as the photons in photonic crystals behave similarly to electrons in a solid-state crystal [54]. For a one-dimensional photonic crystal, also called a photonic crystal waveguide (PCW), the Purcell factor $P_{wg}$ is given by

$$P_{wg} \equiv \frac{\Gamma_{1\mathrm{D}}}{\Gamma'} = \frac{3n_g}{4\pi}\left(\frac{\lambda_0^2}{A_m}\right) \tag{1.2}$$

where $\Gamma_{\mathrm{1D}}$ is the decay rate into the waveguide, $n_g \equiv c\left(\frac{\partial\omega}{\partial k}\right)^{-1}$ is the group index, $k$ is the wave vector, $A_m \equiv \frac{V_m}{a}$ is the mode area, and $a$ is the lattice constant of the PCW. From this expression, it is apparent that to increase the Purcell factor, we need to reduce the mode area $A_m$ and increace $n_g$.

Besides increasing the strength of atom-light interaction between atoms and the PCW guided mode (GM), PCWs have another interesting property, light with certain frequencies may not be able to be guided along the PCW, regardless of its wave vector $k$. The frequency range for which no GM is supported is called the photonic bandgap. If the atomic transition frequency is in the bandgap, as shown in Fig. 1.1b, the atom can not decay into the PCW guided mode. In this regime, the photon forms a bound state around the atom. The incoherent interaction between the field and the atoms is greatly suppressed while the coherent exchange between atoms along the device can still present. In this regime, the strength and range of the interactions between atoms mediated by photons confined in the bound states can be tuned by controlling the frequency difference between the atom transition frequency $\omega_{\mathrm{atom}}$ and the band-edge frequency $\omega_{BE}$. This flexibility makes PCW a unique platform to explore many-body systems of photons and atoms. Hood et al reported observations in this regime with cesium atoms trapped near the PCW. [50].

If the atomic transition frequency is outside of the bandgap, the emitted photon is then guided in the PCW, as shown in Fig. 1.1a. A large $n_g$ can enhance the rate of spontaneous emission into the guided mode [22]. Goban et al reported the collective interaction of an array of atoms can exhibit superradiance emission into the guided mode. [40].

The complex structures of fields in nanophotonic system and the polarization dispersion relationships can be very different from free space. This makes it difficult to apply conventional laser cooling and trapping techniquew to nanophotonic systems. One goal of this thesis is to explore the possibility of trapping atoms as close as $\sim$100 nm to the dielectric surfaces.

## 1.1 The Scientific Goals of Clocked Atom Delivery Experiment

In comparison to the rapidly expanding theoretical literature, to date experimental progress has been modest in integrating atoms and nanophotonics. Important laboratory systems include optical nanofibers, where $\simeq 10^3$ atoms have been trapped

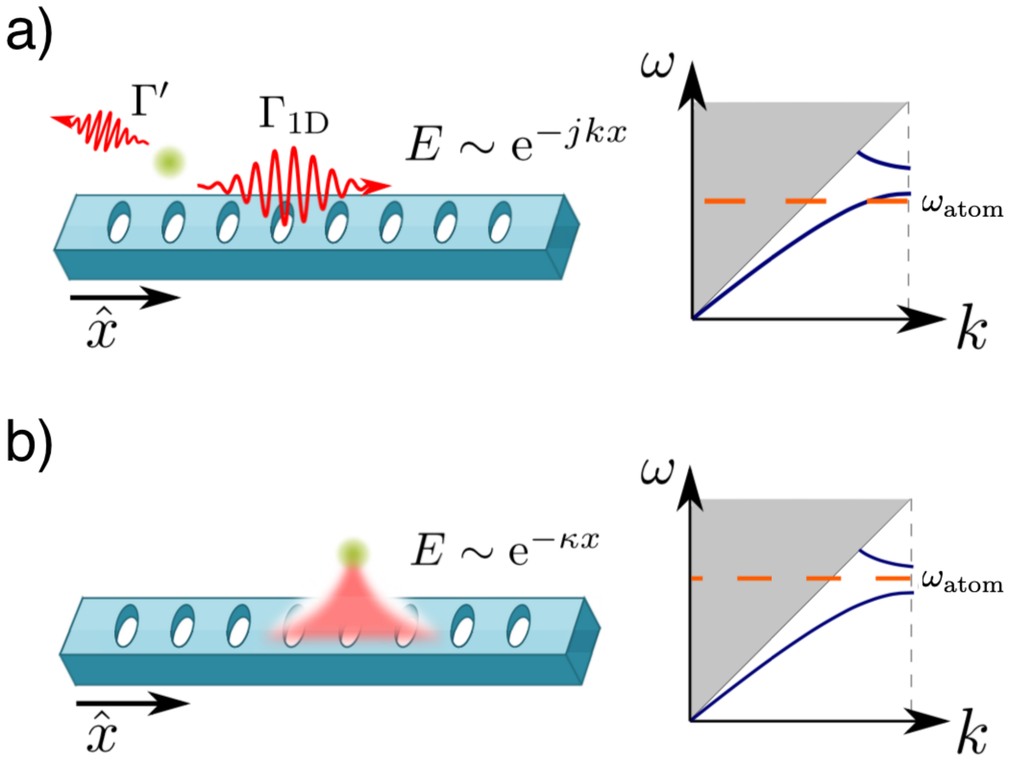

Figure 1.1: a) When the atomic transition frequency is guided, outside of the bandgap. An atom near the PCW can emit into a both the PCW guided mode with rate $\Gamma_{1D}$ and into any other mode with rate $\Gamma'$. b) When the atomic transition frequency is in the bandgap, the atom can no longer decay into the PCW guided mode, and the photon forms a bound state around the atom.

$\simeq$ 220 nm from fiber surfaces [9, 38, 43, 92, 103]. Dispersion engineered photonic crystal cavities [98, 100] and waveguides [40, 50] have achieved strong atom-photon coupling, albeit with only a few atoms trapped $\simeq$ 150 nm from dielectric surfaces. A grand challenge for this emerging field remains the laboratory attainment of one and two-dimensional atomic lattices with high filling fraction and strong coupling of single atoms and photons within the GMs of the nanophotonic structures.

For the PCWs considered here, strong atom-field coupling requires devices designed for atomic physics that provide both stable atom trapping and large atom-photon coupling at the atom trapping sites [20, 52]. In the optical domain, suitable PCWs have lattice constant $a \simeq 350$ nm for dielectric constant $\epsilon \simeq 4$. Single-atom localization with optical traps inside vacuum voids of unit cells then constrains far-off resonance traps (FORTs [46]) to volume $(\Delta x, \Delta y, \Delta z) = (30, 100, 140)$ nm for energy of 100 $\mu$K, where $x$ is along the waveguide, $y$ is along the 250 nm vacuum gap direction, and $z$ is perpendicular to the waveguide plane. It is necessary to transport and cool Free-space atoms within these tiny FORTs. Such transport, cooling, and trapping of atoms near and within nanoscopic dielectric structures requires adaptations of existing techniques from atomic physics [6, 29, 82, 106], as well as the invention of new protocols, such as hybrid vacuum-light traps [20, 52].

Thereby motivated, in this thesis we describe various investigations aimed at developing better quantitative understanding and new tools for the control of atomic motion under the influence of optical and surface forces near nanophotonic PCWs, as illustrated in Fig. 1.2. An important goal of this research is to formulate and validate *in situ* diagnostics that enable atoms to be conveyed from free space into GM optical traps within a PCW, ultimately with high fractional filling of each lattice site.

More specifically, our system shown in Fig. 1.2 consists of a quasi-one-dimensional PCW whose band structure arises from periodic modulation of the outer edges of two parallel dielectric beams with a central vacuum gap, resulting in the so-called 'Alligator Photonic Crystal Waveguide' (or 'APCW') [40, 50, 109]. A moving optical lattice transports trapped atoms into and through the APCW with velocity $v_{\text{lattice}} = 0.51$ m/s and temperature $T_{\text{lattice}} \simeq 20\mu$K in the frame of the moving lattice. Synchronous with the moving lattice, we record the transmission spectra as functions of lattice transport time and detuning of weak GM probes. Due to the periodicity of the lattice delivery, we can offset the recorded spectra in time by integer multiples of the lattice period and coherently combined to create time-dependent 'clocked spectra' with temporal (spatial) resolution of $\simeq 100$ ns ($\simeq 50$ nm).

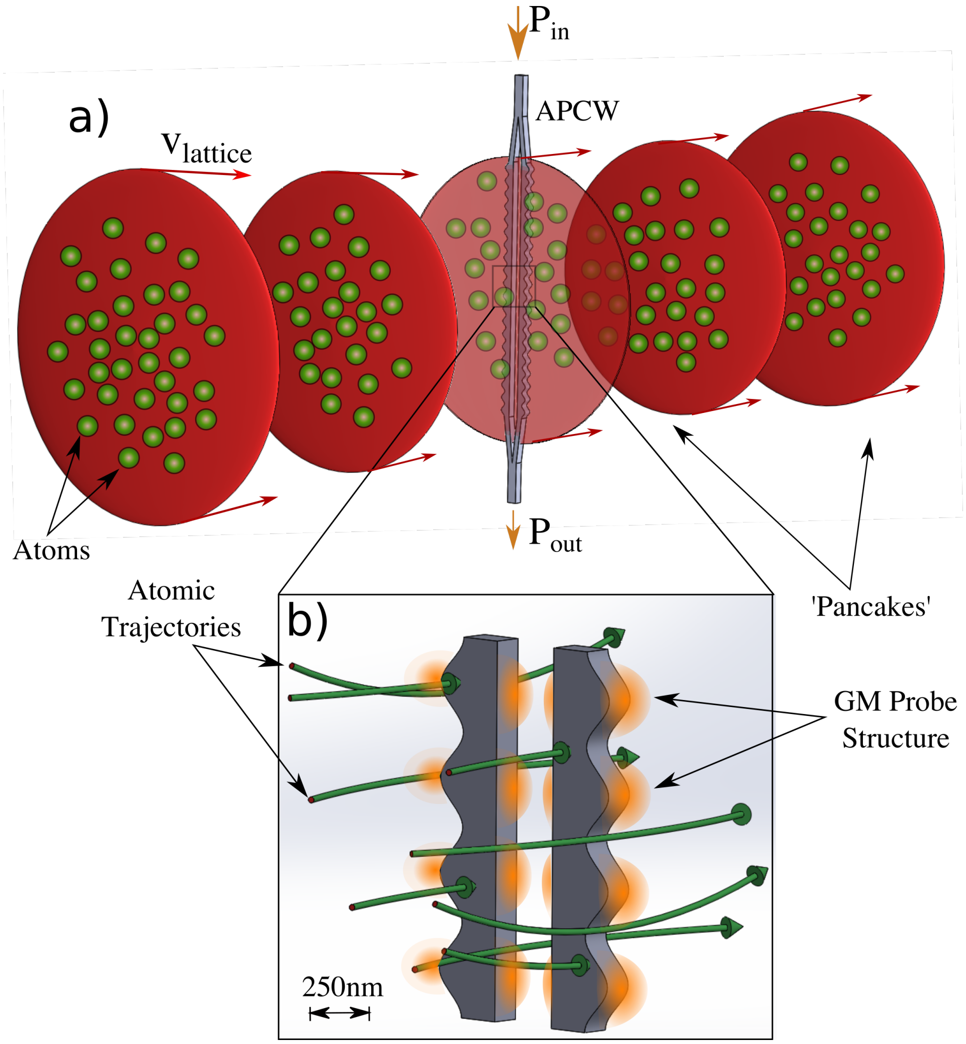

Figure 1.2: (a) Atomic delivery to the ‘alligator’ photonic crystal waveguide (APCW) in our experiment is achieved by creating an optical conveyor belt from a 1D free-space lattice. The atoms, trapped in ‘pancakes’ of high laser intensity, are transported to the device at a speed $v_{\text{lattice}}$ and interact transiently with the APCW. The atomic signature is read out through changes in the transmission of a weak, near resonant probe ($P_{\text{in}} \rightarrow P_{\text{out}}$) that is an electromagnetic mode of the waveguide. (b) Depiction of atom trajectories showing the transient nature of the atoms as they pass through, around and ‘crash’ into the APCW. The bright probe modes on the ‘teeth’ and center of APCW illustrate the TE-like guided mode (GM) intensity near a TE bandedge (here the dielectric bandedge at ≃ 894 nm (D1 line of Cesium)). While these trajectories are merely an illustration, calculated atomic trajectories are presented along with comparisons to experimental data in Fig. 6.3.

These measurements allow us to quantitatively validate our numerical simulations and there by provide understanding of atomic trajectories passing around and through nanoscopic regions of the APCW. For example, we infer that the number of atoms transported into the 250 nm wide vacuum gap of the APCW during each lattice period is of order unity (*i.e.*, $\sim 10^6$ atoms/sec into the central vacuum gap). Introducing auxiliary GM fields provides a spatially varying AC-Stark shift, which can control atomic trajectories arriving to the central vacuum gap at predetermined times and with known AC-Stark shifts.

This quantitative understanding of atomic transport through the nanoscopic APCW provides new tools for the integration of ultracold atoms and nanophotonics, some of which we describe here. For example, following Ref. [6], we consider the transfer of atoms from the moving optical lattice into GM trap sites along the APCW by way of single-photon scattering events triggered by the temporal phase of the moving lattice.

The research reported in this thesis has many important antecedents in AMO physics. Historic measurements of transmission for atomic beams passing through nanofabricated arrays of slits led to among the first observations of interferometry with atomic deBroglie waves, that were followed over the next decades by precision measurements of many fundamental atomic properties (Ref. [26] for a review), including atom-surface interactions important to our work. Pioneering experiments to measure atomic line shifts and decay rate modifications for atoms near surfaces were also made in other microscopic geometries with atomic transmission recorded through various structures [47, 53, 96], which are likewise quite relevant for our system. Early work in atomic vapors led to measurements of the spectral line distortion for Cs atoms, which surface forces on the atoms induced [13, 21, 79]. More recent experiments investigate the role of Casimir-Polder (CP) forces on simulated trajectories of thermal ($\sim 300$ K) atoms interacting with nanoscopic slot waveguides and accompanying experiments verifying the importance of CP when explaining the experimental result [87].

Among many experiments with laser cooled atoms, landmark measurements of CP forces were made by ‘bouncing’ atoms from evanescent fields [64], as well by utilizing interactions with BECs at controlled distances from a dielectric boundary, again with atom loss being the relevant variable [68, 78]. Perhaps closest in spirit and implementation to the present work are pioneering experiments and numerical simulations for cold atoms moving near nanoscopic optical fibers [89], micro-toroid resonators [1, 95], and PCWs [39], which employed light transmission and reflection from the respective optical structures to link experiment and numerical simulation of atomic motion, rather than by direct atomic detection.

## 1.2 Thesis outline

In Chapter 2, I discuss in detail the structure and guided modes of the APCW. The guided modes that we use in this research include a TE-like polarized GM at cesium D1 and D2 transitions, and a TM-like polarized GM for which the APCW acts like a uniform waveguide at the cesium D1 and D2 transitions. These GMs are the building blocks for our trapping scheme, and their spatial variation of Stark shift can help us identify different classes of atomic trajectories using clocked spectra. I also discuss how we can make a 3D stable trap in the center vacuum gap of the APCW by balancing the GM power within a specific range. We also investigate the possibility of trapping atoms in the center vacuum gap using trapping scheme similar to the one described in Ref. [6]. Also, special care is necessary to when deciding the guided mode trap frequency to eliminate the "phase slipping" between the trap and the dielectric structure.

In Chapter 3, I introduce relavant atomic physics concepts and experimental apparatus involved in this experiment. Various laser cooling and trapping methods are required to transport the atom from the source MOT to the science MOT and finally to the chip. The vacuum system, laser system, and the relevant electronic control system are also documented. During the course of my Ph.D. study, we developed multiple experimental procedures and routines to minimize the probability of error. I document the process of gluing fibers to the chip and transferring the chip to the science chamber. Finally, I discuss the method of tuning the APCW band structure so that the band-edge frequency or one of "cavity" resonances are at the desired frequency. Since cesium atoms coat the device and shift the device band-edge, I discuss means for recovering APCW from cesium coating.

In Chapter 4, I specifically focus on the optical lattice conveyor belt system that transports the atom from the science MOT to the chip. I discussed the loading and cooling atoms into the optical lattice, the transport from the science MOT to the APCW. Moreover, I introduce an essential tool for our research, the clocked spectrum. A clock spectrum is a 2D spectrum as a function of detuning and time, in which is embedded information of atomic motion and the interaction between atoms and the GM at resolution of 50 nm in space and 100 ns in time.

In Chapter 5, I present a numerical simulation program that simulates the 2D and 3D atomic trajectories around the APCW. The functionality of the simulation program includes simulating atomic trajectories, outputting the result of the simulation as movies, and calculating the APCW transmission spectrum as a function of detuning and time. I designed the simulation program to work with potential feature size across multiple order of magnitudes effectively, and although we only use it to simulate atomic trajectories around one particular APCW, the simulation program works with any 2D and 3D nanostructures.

In Chapter 6, I discuss our investigations on the interaction between cesium atoms and APCW. By fitting the APCW transmission spectrum to a transmission model, we can extract various parameters that characterize the interaction between atoms and the APCW. Also by utilizing the clocked spectrum technique, we can observe how the fields of strong (~100 μW) Stark GMs affect the atomic trajectories. We find rich phenomenology related to temporal and spatial variations of AC Stark shifts and vacuum surface forces, all of which strongly affect the atomic motion. By comparing the experimental results to numerical simulations, we can calibrate the guided mode intensity and more importantly, distinguish signals that arise from atoms interacting with different parts of the region around the APCW. This valuable data provides "actionable" timing and detuning information to trigger single photon trapping. I also discuss the attempts to cool and trap atoms into the center vacuum gap of the APCW.

In Chapter 7, I discuss a different kind of experiment. Instead of sending a CW weak (~100 pW) probe, we used strong (~100 nW peak power) nanosecond pulses to probe the atoms passing through the APCW. The pulse durations are much smaller than the atomic lifetime $\tau \simeq 30\text{ns}$ , which is in turn much shorter than the atom transit time through the APCW, so we can trigger the pulses to interact with an optical system with selected interaction parameters. Probing the optically dense atomic medium as it moves through the APCW allows us to explore new nonlinear optical experiments, such as soliton propagation, as investigated in Ref. [61].

## *Chapter 2*

# ALLIGATOR PHOTONIC CRYSTAL WAVEGUIDE

In this chapter, I will first provide a simple description of the theory for 1D photonic crystal waveguide. I then explain the structure of alligator photonic crystal waveguide (APCW), the band diagram and guided mode (GM) profiles in detail. Finally, I present a scheme of trapping atoms in the gap of the APCW.

## 2.1 A Short Introduction to Photonic Crystal Waveguides

In this section, we focus on 1D photonic crystal waveguides. A photonic crystal is a periodic arrangement of material with spatially varying dielectric constant. In a 1D photonic crystal, the dielectric constant $\epsilon(x)$ varies periodically along direction $x$.

Here I outline the process of solving the modes for any given photonic crystal structure [54]. For a linear dielectric we can write a harmonic mode as a certain field pattern times a complex exponential:

$$\vec{H}(\vec{r},t) = \vec{H}(\vec{r})\exp(i\omega t) \tag{2.1}$$

$$\vec{E}(\vec{r},t) = \vec{E}(\vec{r})\exp(i\omega t) \tag{2.2}$$

where $\vec{E}(\vec{r},t)$ and $\vec{H}(\vec{r},t)$ are the macroscopic electric and magnetic fields. By solving the Maxwell equations, we can get the master equation for solving photonic crystal modes

$$\nabla \times \left(\frac{1}{\epsilon(\vec{r})}\nabla \times \vec{H}(\vec{r})\right) = \left(\frac{\omega}{c}\right)^2 \vec{H}(\vec{r}), \tag{2.3}$$

where $\epsilon(\vec{r})$ is the dielectric profile of the photonic crystal. From the master equation, we can see this is an eigenvalue problem, with the field patterns $\vec{H}(\vec{r})$ of the harmonic modes as the eigenvectors, and $(\omega/c)^2$ as the eigenvalues. We can solve the master eq. 2.3 to find the modes $\vec{H}(\vec{r})$ for a given frequency. We can then recover the electric field by

$$\vec{E}(\vec{r}) = \left(\frac{-ic}{\omega\epsilon(\vec{r})}\right)\nabla \times \vec{H}(\vec{r}) \tag{2.4}$$

Now, we can consider a 1D photonic crystal with dielectric constant profile $\epsilon(x)$. The 1D photonic crystal has unit cell length of $a$, so $\epsilon(x+a) = \epsilon(x)$. The discrete translational symmetry along a 1D photonic crystal leads to an $x$-dependence for $\vec{H}(x)$, that is

$$\vec{H}(x) \propto \exp(ik_x x)\vec{u}(x) \tag{2.5}$$

where $\vec{u}(x)$ is a periodic function, $\vec{u}(x+a) = \vec{u}(x)$. This is Bloch's theorem. The Bloch state with wave vector $k_x$ and the Bloch state with wave vector $k_x + mb$ are identical, with $b = 2\pi/a$ and $m$ being integer. The $k_x$'s that differ by integral multiples of $b$ are identical physically. We only need to consider $k_x$ in the range of $-\pi/a < k_x < \pi/a$, which is called the Brillouin zone. Moreover, by solving $k_x$ for all frequency $\omega$, it is possible to trace out the band diagram of the photonic crystal. As the magnitude of modulation of the dielectric constant increases, a gap in frequency appears. In this frequency range, no mode, regardless of $k_x$, is guided in the crystal. Creating a photonic band gap. As modes approach the light line ($\omega(\beta) = c\beta$), they are increasingly weakly guided.

## 2.2 Alligator Photonic Crystal Waveguide

This section provides an overview of the alligator photonic crystal waveguide (APCW) utilized in our experiments, including the relevant GMs of the waveguide, the coupling of light into and out of these GMs, and the structural support of the waveguide. More details about device fabrication and characterization can be found in Refs. [74, 109, 110].

Fig. 2.1 shows the projected band diagram of the APCW. The diagram only shows the region near the edge of the first Brillouin zone. We can catagorize the guided modes by the symmetries of the electric field. If in the $yz$-plane the electric field is unchanged after reflection about $z = 0$ line, the GM is said to have even $y$ symmetry; otherwise if the electric field $y$ component gain a minus sign after reflection about $z = 0$ line, the GM is said to have odd $y$ symmetry. The categorization is the same for $z$. The y-odd-z-even mode has the electric field parallel to the $y$ direction in the gap of the APCW, which can be coupled to by sending light with linear polarization in $y$ direction to the input coupler. We call this mode the TE mode. The y-even-z-odd mode has the electric field parallel to the $z$ direction in the gap. This mode can be coupled to by sending light with linear polarization in $z$ direction to the coupler. We call this mode the TM mode. For both TE and TM band, the lower branch is called the dielectric band, because at $\beta_x \approx \pi/a$ the field concentrates in the thick part of the dielectric; the upper branch is called the air band and the field concentrates in the thin part.

We made the APCWs used in our experiments by patterning the desired geometry using electron beam lithography on a 200 nm-thick layer of Silicon Nitride (SiN) grown on a 200 μm-thick Silicon substrate, which we follow with various stages of chemical processing [74, 110]. The APCW forms by external sinusoidal modulation of two parallel nano-beams to create a photonic bandgap for TE modes with band edges at the strong dipole-allowed transition lines of Cesium (Cs), the D1 line near 894 nm and the D2 line near 852 nm. The overview of the APCW device is shown in Fig. 2.2. The APCW is suspended by single-beam waveguides across an open window. The size of the window is large enough for beams necessary for laser trapping and cooling to pass through. On both sides of the APCW, the single-beam waveguides are supported by a series of tethers. The tether that is closest to the coupler is angled to maintain tensions in the waveguide. It is possible to place many APCW devices on a single chip; usually, a chip has 16 devices.

Fig. 2.3(a) displays a scanning-electron microscope (SEM) image of the central section of an APCW. The 'X' and 'O' points indicate regions of high GM intensity for TE-polarized light with frequencies near the dielectric (D1) and air (D2) band-edges, respectively. The coordinate system adopted for our subsequent analyses is shown together with the dimensions of the device and the principal polarizations of relevant GMs supported by the dielectric structure. Calculated and measured dispersion relations for such devices are presented in Ref [50] where good quantitative agreement is found.

The top row of Fig. 2.3(b) provides a cross-section of the two dielectric beams that form the APCW overlaid with intensity profiles for the D1 TE, D2 TE and TM polarizations for the $x$ coordinate corresponding to the widest sections of the APCW. Note that the TM mode's regions of highest intensity are on the top and bottom surfaces of the dielectric, while the TE mode is primarily bright in the center (vacuum gap between the beams) and on the sides. The bottom row of Fig. 2.3(b) provides a cross-section of a unit cell of the APCW at $z = 0$ overlaid with intensity profiles for the D1 TE, D2 TE, and TM polarizations. The D1 TE mode is at the dielectric band of the TE mode, so the intensity concentrates at the thick part of the unit cell; while

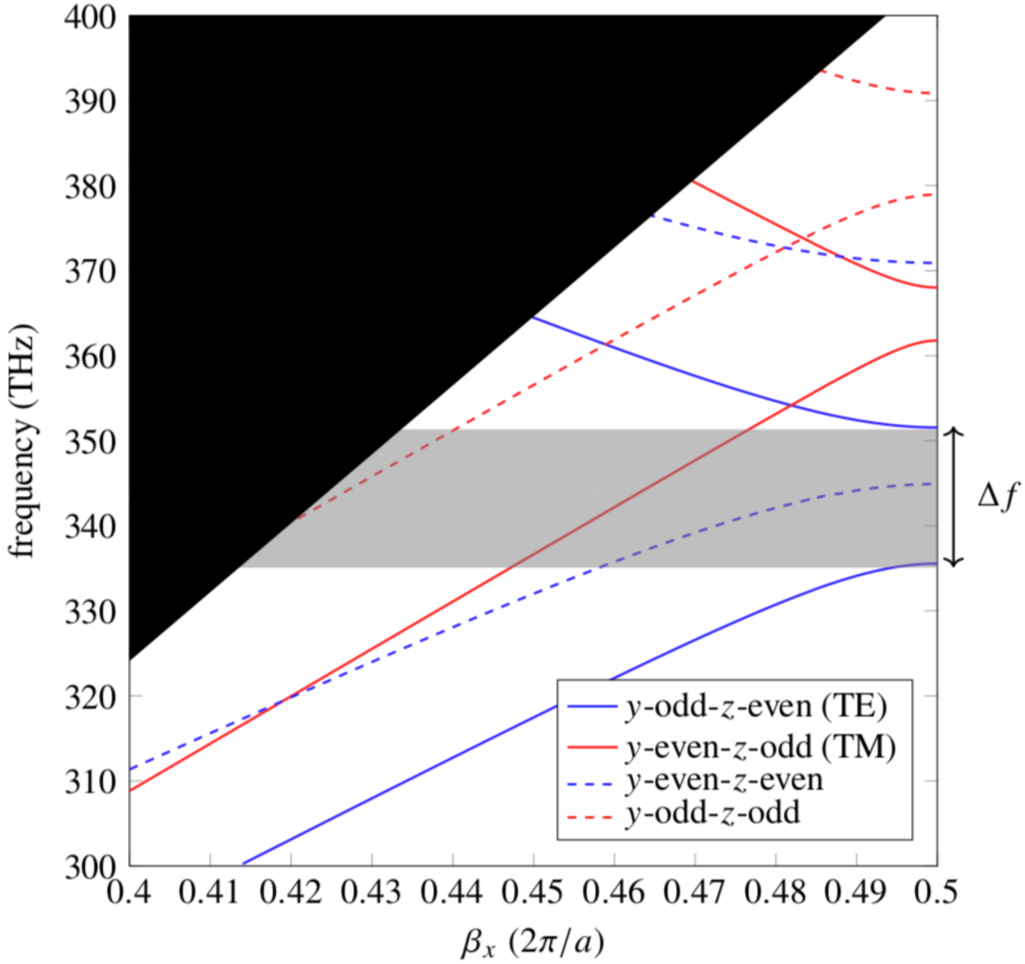

Figure 2.1: APCW band diagram. The red bands have odd $z$ symmetry and the blue bands have even $z$ symmetry. The band represented with solid lines are the modes which can be excited by the input coupler of our devices in the experiment. Shaded gray region represents the gap for the y-odd-z-even (TE) mode. The two bandedges are designed to be aligned to the cesium D1 and D2 transition. The black region is the region above the light line ($\omega = c\beta$).

the D2 TE mode is at the air band of the TE mode, so the intensity concentrates at the thin part of the unit cell. As for the TM mode, since the D1 and D2 transition are far from the TM band gap so the APCW acts approximately as a waveguide. This causes the TM GM intensity profile to be uniform along the $x$ direction. For operation near the band edges of the TE mode, spontaneous emission rates, $\Gamma_{1D}$, into the waveguide are strongest for atoms coupled to TE GMs ($\Gamma_{1D}/\Gamma' \leqslant 10$), and significantly weaker for emission into TM GMs [50, 109]. Additionally, near the TE bandedges for D1 and D2, the Bloch functions develop high-contrast standing

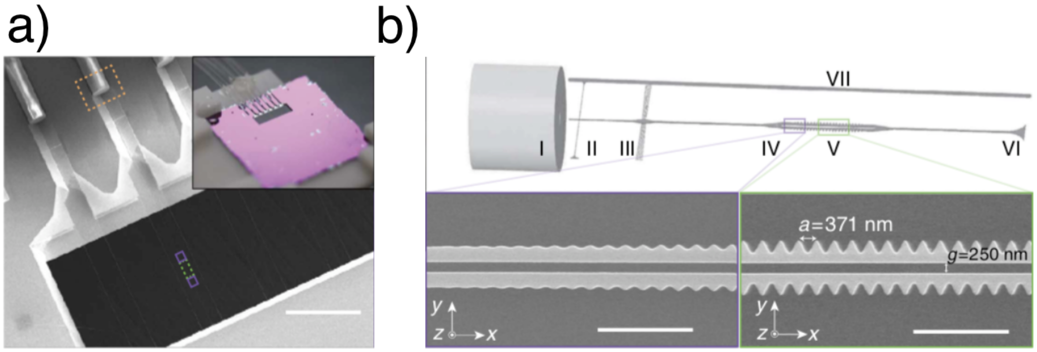

Figure 2.2: Overview of the integrated alligator photonic crystal waveguide (APCW) device. (a) SEM image of the silicon chip showing an integrated optical fiber (orange box) coupled, via a SiN nanobeam waveguide, to the APCW region (purple and green boxes). The APCW is located within a 10 × 2mm through window (black region without dielectrics) where free-space atoms and cooling lasers are introduced. Inset shows a picture of the chip and the optical fibers glued to a vacuum-compatible holder. Scale bar, 0.5 mm. (b) Detailed schematic of the suspended SiN waveguide. Light enters the system via the optical fiber (I) butt-coupled to the free end of the waveguide (II) which is supported by a tether array (III). Near the center of the through window, the waveguide transitions into a double nanobeam, followed by tapering (IV) and APCW (V) sections, and again tapers out to terminate into the substrate (VI). Two parallel rails are added symmetrically to support the structure (one rail is illustrated in VII). The insets, corresponding to the purple and green boxes in (a), show SEM images of segments of the tapering (IV) and APCW (V) sections, respectively. Scale bars in IV and V, 2 µm. [74, 109, 110].

waves along $x$, which are useful for creating dipole trapping potentials (FORTs) for atoms within the waveguide [52, 109]. The TM GMs, near D1 and D2 have low contrast in the $x$ direction and resemble simple GMs of an unstructured waveguide. A figure of these modes and the resulting trapping potentials is provided in section 2.3.

The structure depicted in Fig. 2.3(c) illustrates the APCW connected to single-beam waveguides on either end and thereby suspended in the center of a 2 mm wide window in the Silicon chip to allow optical access for delivering and manipulating cold atoms near the APCW. Well beyond the ends of the APCW, a series of tethers are attached transversely to the single-beam waveguides along $\pm y$ to anchor the waveguides to two side rails that run parallel to the $x$ axis of the device to provide thermal anchoring and mechanical support.

Light is coupled into and out of the GMs of the APCW by conventional optical fibers that are mode-matched to the fields to/from the terminating ends of the waveguide [109]. The overall throughput efficiency from input fiber through the device with the APCW to output fiber is approximately 20 % for the experiments I describe here.

The silicon chip containing a set of APCWs is affixed to a ceramic holder using heat-cured, low out-gassing glue. Each of eight devices is connected using separate input and output fibers aligned to the respective waveguide by V-grooves etched into the substrate [109]. The same heat-cured glue is utilized to fix the fiber position within the V-groove. This entire assembly with 16 coupling fibers for 8 devices is mounted in a vacuum chamber approximately 20 mm from a magneto-optical trap (MOT) from which cold cesium atoms are transported to an individual APCW by way of an optical conveyor belt described in the next section.

### 2.3 Trapping Scheme

It is possible to ultilize the GMs of the alligator photonic crystal waveguide (APCW) to create stable trapping potentials in the vacuum gap between the dielectric beams [52, 109]. GMs at each band edge exhibits a periodic structure within the APCW as seen in Fig. 2.4.

A two-color trap utilizes the periodic structure of the APCW by tuning one GM to a higher frequency (58 GHz) than the free-space atomic resonance so that the dipole force repels the atoms from this band edge. The second GM is tunned to a frequency lower than the atomic resonance (600 GHz) creating an attractive potential. Though these dipole force GMs are at different wavelengths, the Bloch modes of the structure set the scale for the trap locations. The result of this two-color trap scheme leads to the trapping potentials shown in Fig. 2.4.

For the data presented in this thesis, atoms are traveling at 0.51 m/s through these trapping potentials, transiting the roughly 100 nm trap size in only 200 ns. To achieve trapping, it is necessary to cool and trap the atoms in times shorter than traditional mechanisms for laser cooling and trapping of atoms. Hence we must incorporate a faster trapping scheme, here based upon that utilized in Ref. [6]. The atoms arrive in one of the ground state manifolds, say $F = 4$, and enter the trap region. The configuration of the trap is such that the surface for $F = 4$ is shallow compared to $F = 3$, so that the atoms pick up little additional kinetic energy as they move down into the trap. When the atoms are near the trap center, an optical pumping pulse promotes population to an electronic excited state where it decays with roughly equal probability to $F = 3$ or $F = 4$. Atoms decaying to $F = 4$ will simply continue their motion and ‘roll’ out of the conservative potential; however, atoms decaying to $F = 3$ will retain approximately the same kinetic energy only now on the different trap surface for $F = 3$. The kinetic energy of the atoms is now insufficient to overcome the trap potential for $F = 3$ and the atoms are now trapped. A schematic of this process is provided in Fig. 2.5. In the trapping scheme described above, triggering the optical pumping pulse to initiate the state transfer must be done at a specific time to ensure the atoms transfer to near the minimum of the $F = 3$ surface. Clocked delivery provides important information about when the atoms are arriving into the center of the APCW, but perhaps more importantly, the clocked signal provides us with a trigger for the optical pumping pulse. This is another useful advantage in utilizing the clocked delivery method we describe in this thesis.

## 2.4 Phase Slipping

For the trapping scheme to work, it is important that all the GMs intensity profile are aligned with the dielectric profile $\epsilon(x)$. With full device simulations, we showed that the intensity profile and the dielectric profile do not necessarily align. For example, Fig. 2.6a, shows a full device simulation of a TE mode. It is obvious to see that the GM intensity is not uniform across the APCW; this is caused by the finite reflection from the taper region of the APCW. The two taper regions form a weak cavity around the photonic crystal [50], and this results in amplitude and phase modulation of the GM intensity along the device. The phase slipping phenomenon can be clearly seen in the two insets in Fig. 2.6a. In Fig. 2.6ai the GM intensity maxima are at the thin part of the APCW and in Fig. 2.6aii the GM intensity maxima are at the thick part of the APCW. Fig. 2.6b shows the TE GM intensity pattern as functions of position $x$ along the APCW and probe detuning $\delta_{BE} = \nu_p - \nu_{BE}$ relative to the dielectric band edge. In this figure, we can identify three resonances at $\nu_1$, $\nu_2$ and $\nu_3$. The phase slipping is also observed in 1D toy model simulations, which are done with Stanford Stratified Structure Solver ($S^4$) [69]. Fig. 2.6c shows the 1D simulated GM intensity profile along the APCW at $\nu_2$, as indicated by the blue dashed line in

Fig. 2.6b. Fig. 2.6d shows $\Delta_{\text{phase slip}}$, the distance between an intensity maximum to the nearest thick part of the dielectric along the device. $\Delta_{\text{phase slip}}$ varies from $-0.25$ to 0.25 along the device, where $\Delta_{\text{phase slip}} = 0$ means the intensity maxima is at the thickest part of device and $\Delta_{\text{phase slip}} = \pm 0.5$ means the intensity maxima is at the thinnest part of the device. This slipping means that if the D1 and D2 components of the trap are not aligned to the same resonance order on their respective side, the D1 and D2 components will not be aligned. Even when they are aligned to the same resonance order, the trap is only aligned at the center of the "supermode" anti-node.

One way to eliminate the phase slip is to utilize the symmetry of the supermodes. Instead of aligning the trap frequency to one of the APCW cavity resonances, we can tune it between the resonances, at the anti-resonance. For example, the blue dashed line in Fig. 2.7a indicates the anti-resonance between the second and the third resonances. The intensity profiles and $\Delta_{\text{phase slip}}$ along $x$ direction are shown in Fig. 2.7b and 2.7c for single trapping beam being input from one end of the APCW. At the anti-resonance, the intensity profile is no longer symmetric about the center of the APCW. By contrast, the intensity profile is always symmetric about the center of the APCW in Fig. 2.7d. Here the trap beams are counter-propagating in the APCW, the intensity profile from the two beams are complementing each other, making the intensity profile of the two beams combined much smoother, as shown in Fig. 2.7d. As for $\Delta_{\text{phase slip}}$, the combination of two counter-propagating beams completely cancel, making the intensity maxima coincide with the thick part of the PACW. The intuition to understand this is that for each supermode packet, at the anti-node $\Delta_{\text{phase slip}} = 0$ and at the node the $\Delta_{\text{phase slip}} = \pm 0.5$. The supernodes from the two counter-propagating beams interleave, so that the points on the APCW where the intensity is purely from one of the beams have $\Delta_{\text{phase slip}} = 0$. Anywhere between these points $|\Delta_{\text{phase slip}}|$ is approximately reverse proportional to the intensity so that the two $\Delta_{\text{phase slip}}$ cancel out. We can see this effect in Fig. 2.7e. This phase slipping canceling technique allows us to focus on tunning the device to place the probe frequency at the desired location, such as at the first resonance or slightly inside the band-gap. Then, we can place the far-detuned GM trap frequencies at any anti-resonance.

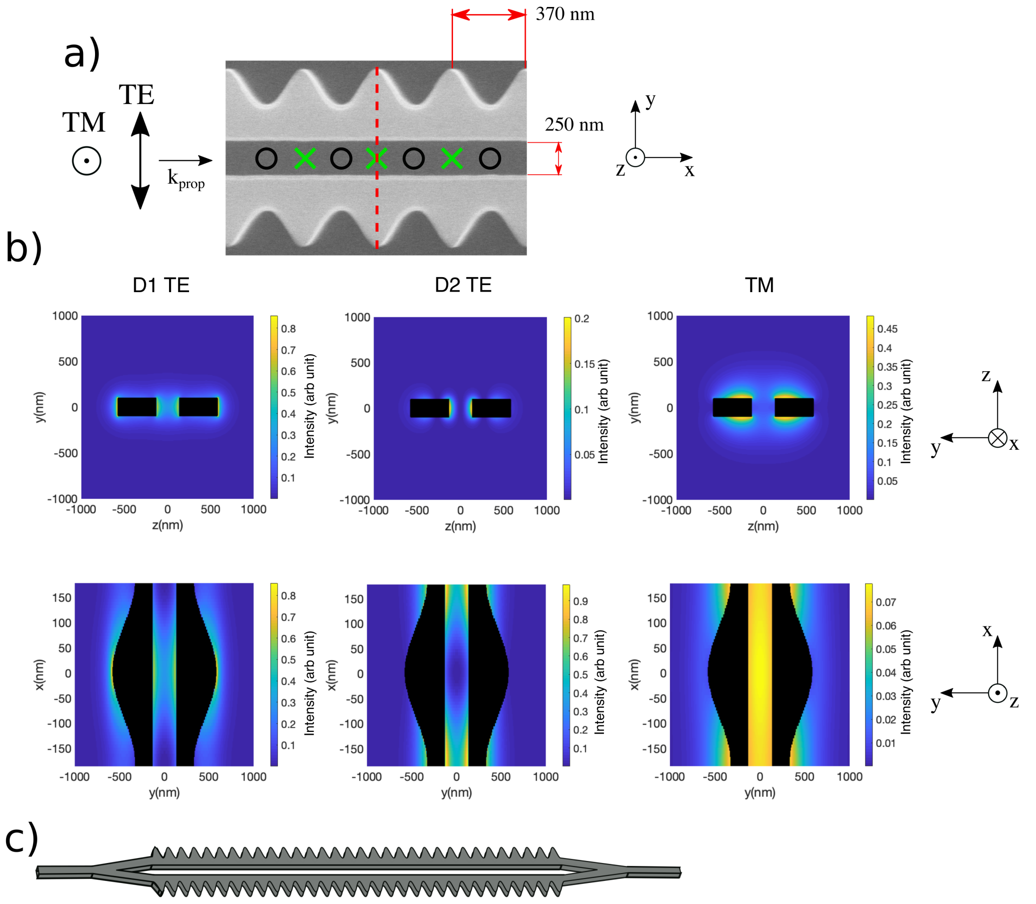

Figure 2.3: Details of the alligator photonic crystal waveguide (APCW) used in our experiments. a) An SEM image of 4 unit cells of the APCW taken in the center region of the waveguide. The unit cell spacing is 370 nm, the vacuum gap between the beams is 250 nm, and the Silicon Nitride is 200 nm thick. ‘X’s (‘O’s) indicate the regions of the APCW where TE guided light at the dielectric or D1 (air or D2) bandegde is brighteste. b) The intensity distribution of the D1 TE, D2 TE and TM polarizations. The top row shows the $y - z$ cross-section of GMs supported by the structure at a single slice in the $y$ direction, indicated by the red dashed line in (a). The bottom row shows the $xy$ cross-secton of the GMs within a unit cell at $z = 0$. The D1 transition is at the dielectric band of the TE mode, so the intensity concentrates at the thick part of the APCW. The D2 transition is at the air band of the TE mode, so the intensity concentrates at the thin part of the APCW. The D1 and D2 transition is far from the TM band gap, so the intensity is qpproximately uniform along $x$. c) The 150 unit cells of the APCW are formed from single rectangular waveguides on either end that split at Y-junctions into parallel, modulated beams. The entire structure is suspended in vacuum by transverse tethers connected to supporting side rails (not shown) [74, 109, 110].

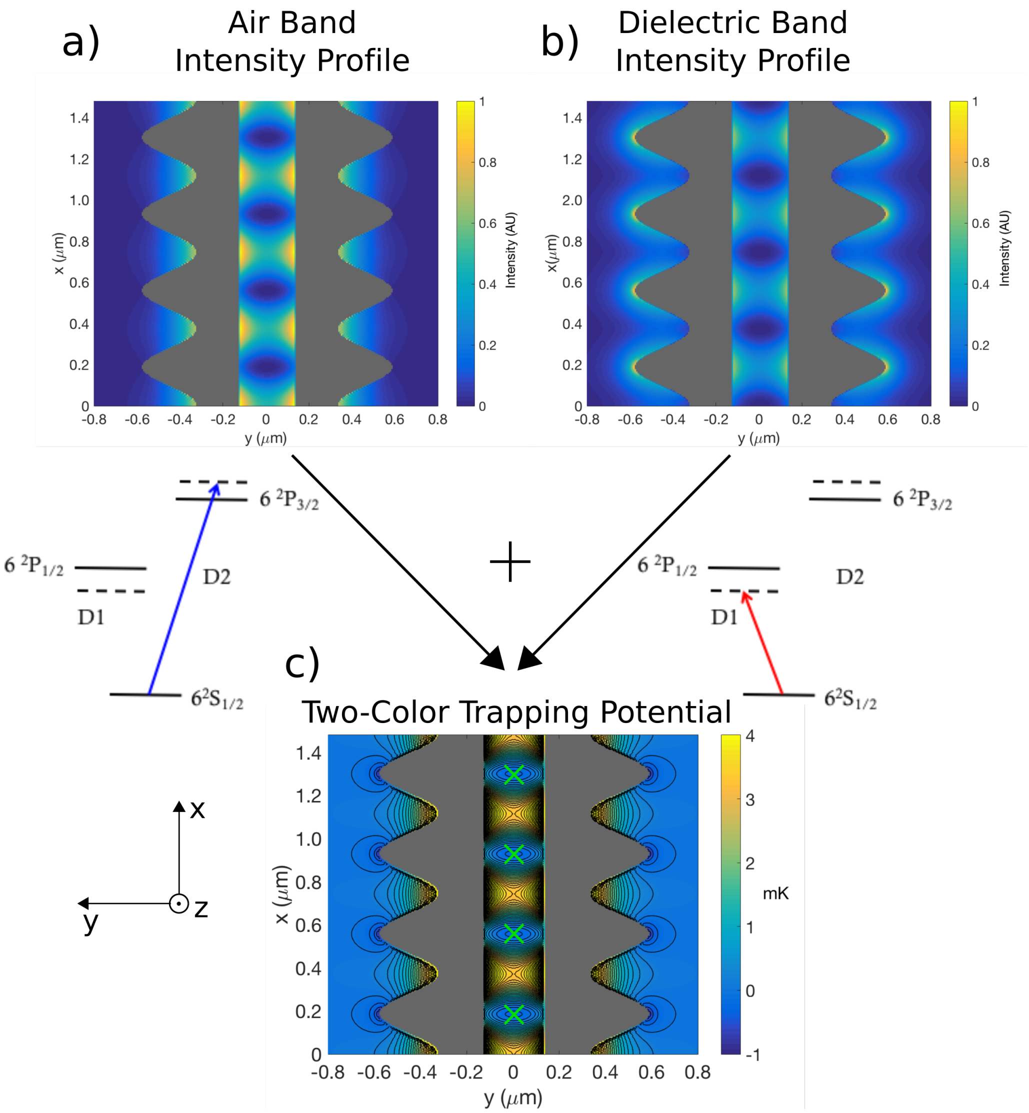

Figure 2.4: Stable trap sites within the alligator photonic crystal waveguide (APCW) created using blue and red detuned beams at the air bandedge and dielectric bandedge [52, 109]. a) By way of a repulsive optical dipole force, atoms are kept off the walls of the structure. b) An attractive optical dipole force creates a periodic trapping potential along the length (*x* direction) of the waveguide. This red detuned trap light also creates an attractive potential primarily utilized to create confinement out of the page (*z* direction). c) Total optical trap with the green 'X's' indicating stable trapping points.

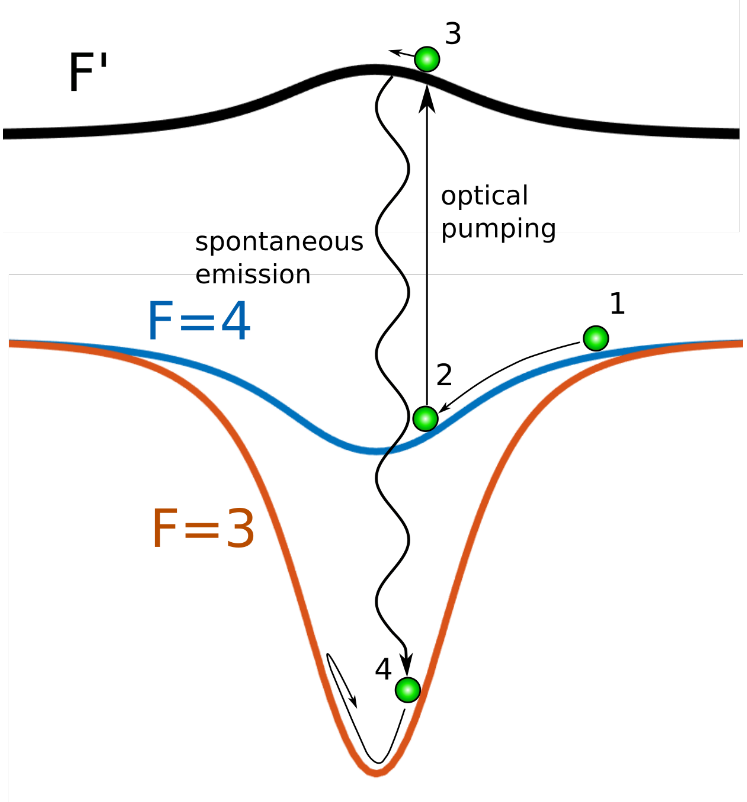

Figure 2.5: A schematic of the implementation of an adaptation of the scheme in Ref. [6] here illustrated for a cross-section of the GM trap. Atoms arrive into the trap within the APCW structure in $F = 4$ and accelerate down the $F = 4$ potential (point 1) . When the atom is near the center of a unit cell of the APCW, an optical pumping pulse is triggered exciting the atom to a higher electronic F' state (point 2). The atom is in the excited state for a short time before decaying through spontaneous emission (point 3). If the atom decays to $F = 3$ it retains approximately the same kinetic energy but now the potential barrier around it is larger than the atom's kinetic energy (point 4). The atom is thus trapped on the $F = 3$ trap surface.

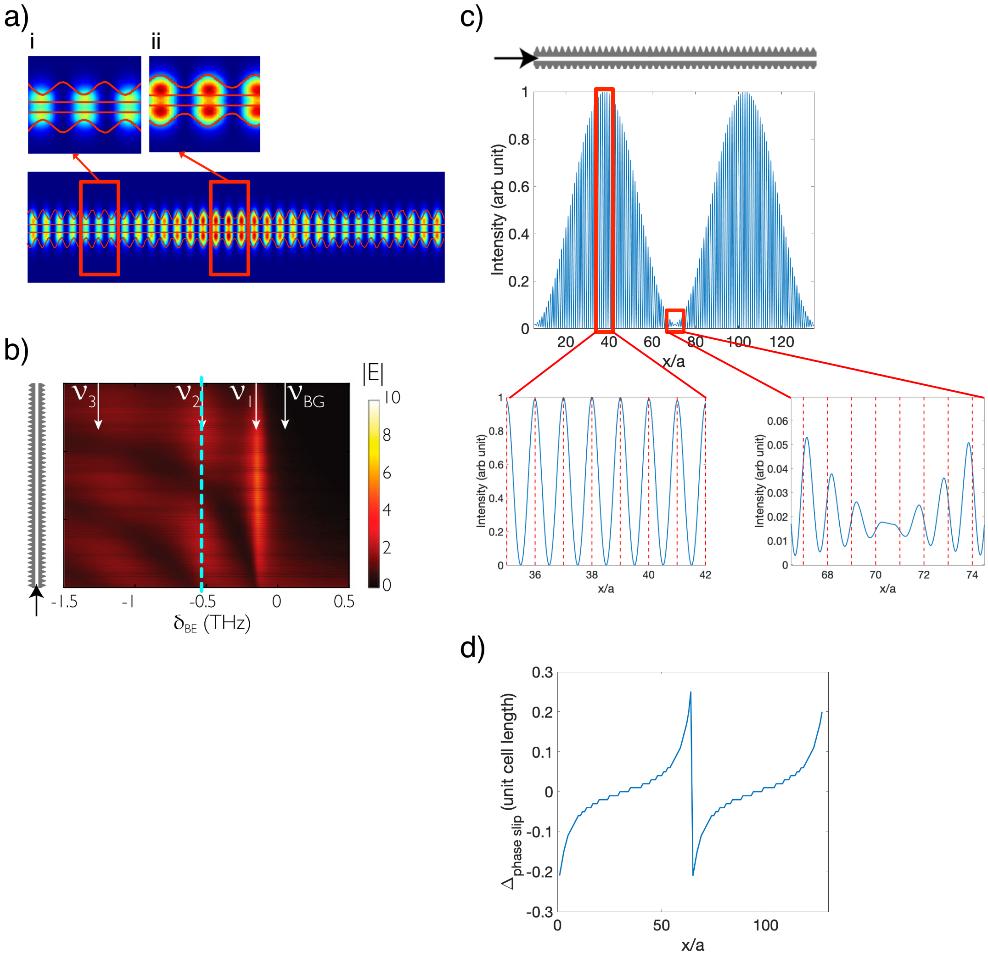

Figure 2.6: Illustration of the phase slipping between GM and APCW dielectric. a) A full device simulation of a TE GM, the GM intensity profile is no aligned with the APCW dielectric structure, which is indicated by the red lines. Simulation done by Xingsheng Luan. i) The intensity maxima aligns to the thinnest part of the device. ii) The intensity maxima aligns to the thickest part of the device. b) calculated electric field magnitudes along the APCW as functions of position $x$ along the PCW and probe detuning $\delta_{BE} = \nu_p - \nu_{BE}$ relative to $\nu_{BE}$ for the dielectric band edge [50]. c) Simulation result of 1D toy model done in $S^4$ [69]. The intensity profile along $x$ at the second resonance $\nu_p = \nu_2$.Insets show the alignment of intensity and the dielectric structure. The red dashed lines indicate locations with highest dielectric constant. d) $\Delta_{\text{phase slip}}$ along $x$ at the second resonance $\nu_p = \nu_2$. Within one "supermode" packet the intensity maxima slip from the thickest part of the APCW ($\Delta_{\text{phase slip}} = 0$) to the thinnest part of the APCW ($\Delta_{\text{phase slip}} = \pm 0.5$).

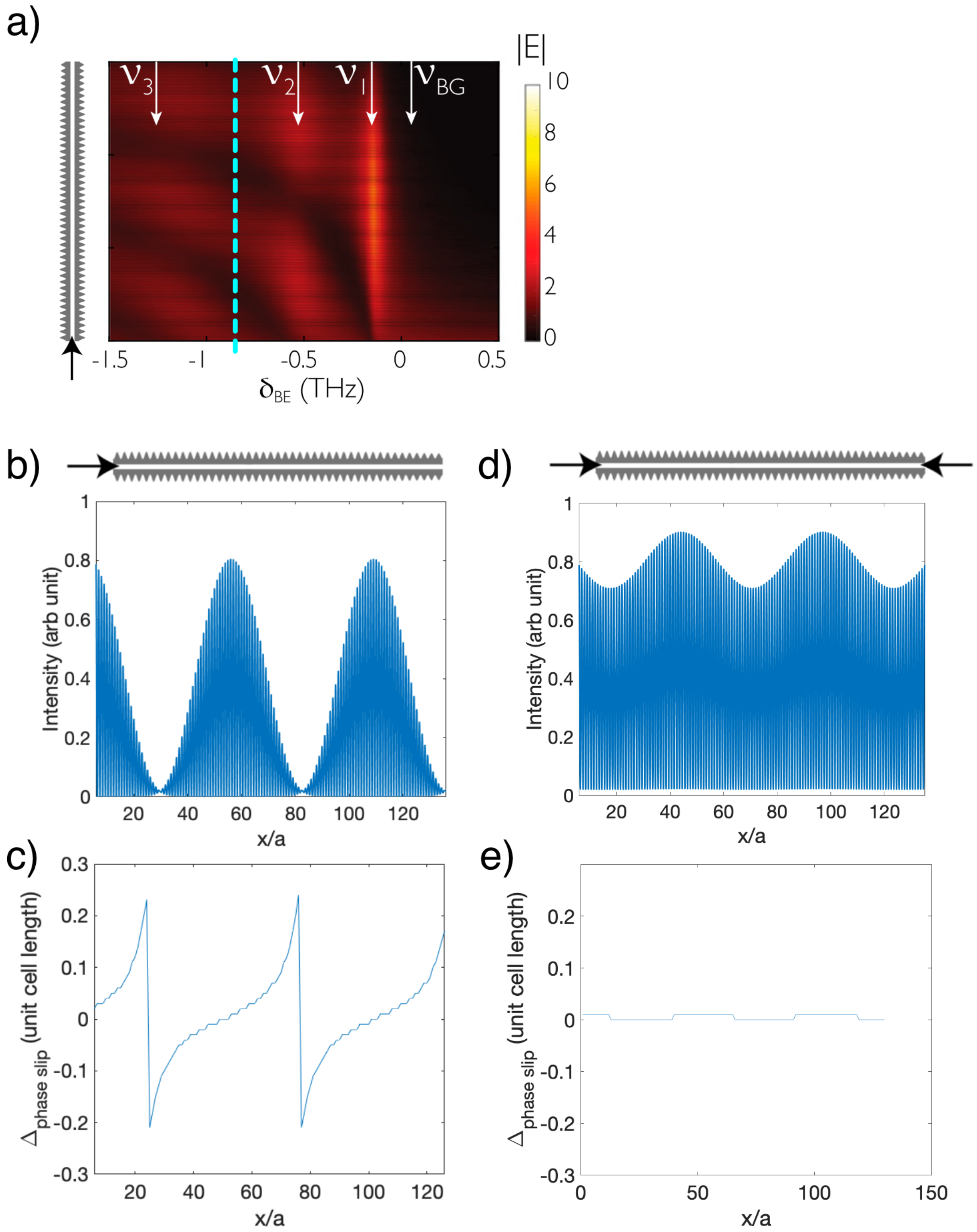

Figure 2.7: Eliminating APCW phase slipping. a) calculated electric field magnitudes along the APCW as functions of position $x$ along the PCW and probe detuning $\delta_{BE} = \nu_p - \nu_{BE}$ relative to $\nu_{BE}$ for the dielectric band edge [50]. b) The TE intensity profile along $x$ between the second and the third resonances $\nu_p = \nu_{2.5}$, as indicated by the blue dashed line in (a). c) $\Delta_{\text{phase slip}}$ along $x$ when $\nu_p = \nu_{2.5}$. Within one "supermode" packet the intensity maxima slip from the thickest part of the APCW ($\Delta_{\text{phase slip}} = 0$) to the thinnest part of the APCW ($\Delta_{\text{phase slip}} = \pm 0.5$). d) Two GMs at $\nu_p = \nu_{2.5}$ counter-propagate in the APCW. The supermode intensity profile is now more uniform. e) With two GMs at $\nu_p = \nu_{2.5}$ counter-propagate in the APCW, $\Delta_{\text{phase slip}} \approx 0$ along the APCW.

## *Chapter 3*

# EXPERIMENT SETUP AND ATOMIC PHYSICS

This chapter describes the atomic physics concepts and techniques that we utilized in our experiment. Laser cooling and optical trapping are the basic building blocks of the experiment, and it is necessary to overcome fundamental and technical challenges to apply traditional AMO techniques to a nanophotonics experiment. Furthermore, I have included extensive documentation of the experimental apparatus and the processes that we developed.

### 3.1 Atomic Physics Toolbox

Laser cooling and optical dipole trapping are well-established techniques in atomic physics [76]. Alkali atoms are widely used in cold atom experiments due to the existence of closed cycling transitions and availability of lasers at the relevant transition, which enable atomic cooling and trapping with relatively simple setups. The low recoil limit $T_r = \frac{\hbar^2 k^2}{k_B M}$ and small recoil velocity $v_r = \frac{\hbar k}{M}$ associate with a heavy alkali metal atoms like cesium make it suitable for experiments that combine atomic physics and nanophotonic platforms. The following sections will describe the atomic physics and experimental techniques that we use in our experiment.

The electron configuration of $^{133}$Cs is $[Xe]6s^1$, which has only one valence electron. So the total obrit angular momentum (**L**) and spin angular momentum (**S**) only depend on this single valence electron. The fine structure is a result of the coupling between the **L** and **S**. The equation $\mathbf{J} = \mathbf{L} + \mathbf{S}$ gives the total electron angular momentum operator, which limits the total electron angular quantum number between the range $|L - S| < J < L + S$. For the ground state of cesium, $L = 0$ and $S = \frac{1}{2}$ so the one fine structure ground state has $J = \frac{1}{2}$. For the first excited state $L = 1$ and $S = \frac{1}{2}$, so the two excited states correspond to $J = \frac{1}{2}$ and $J = \frac{3}{2}$. The transition from the ground state to $J = 1/2$ excited state is the $D_1$ $(6^2S_{\frac{1}{2}} \longrightarrow 6^2P_{\frac{1}{2}})$ transition and transition to $J = 3/2$ is called $D_2$ $(6^2S_{\frac{1}{2}} \longrightarrow 6^2P_{\frac{3}{2}})$ transition. The left side of the Fig. 3.1 shows the fine structure of cesium.

The origin of the hyperfine structure is from coupling between **J** and the total nuclear angular momentum **I**. The total atomic angular momentum **F** is given by $\mathbf{F} = \mathbf{J} + \mathbf{I}$. And similar to **J**, total atomic angular momentum quantum number is limited between the range $|J - I| < J < J + I$. The nuclear spin of $^{133}$Cs cesium is $\frac{7}{2}$, so for the ground state which $J = \frac{1}{2}$, $F = 3$ or $F = 4$. In absence of magnetic field, the hyperfine splitting of the ground state is exactly $\Delta_{\mathrm{HFS}} = 9.192631770$GHz. For the $D_1$ excited state, which $J = \frac{1}{2}$ also, $F = 3$ or $F = 4$. And for the $D_2$ excited state, for which $J = \frac{3}{2}$, which make $F$ takes the value 2,3,4 or 5. As shown in Fig. 3.1.

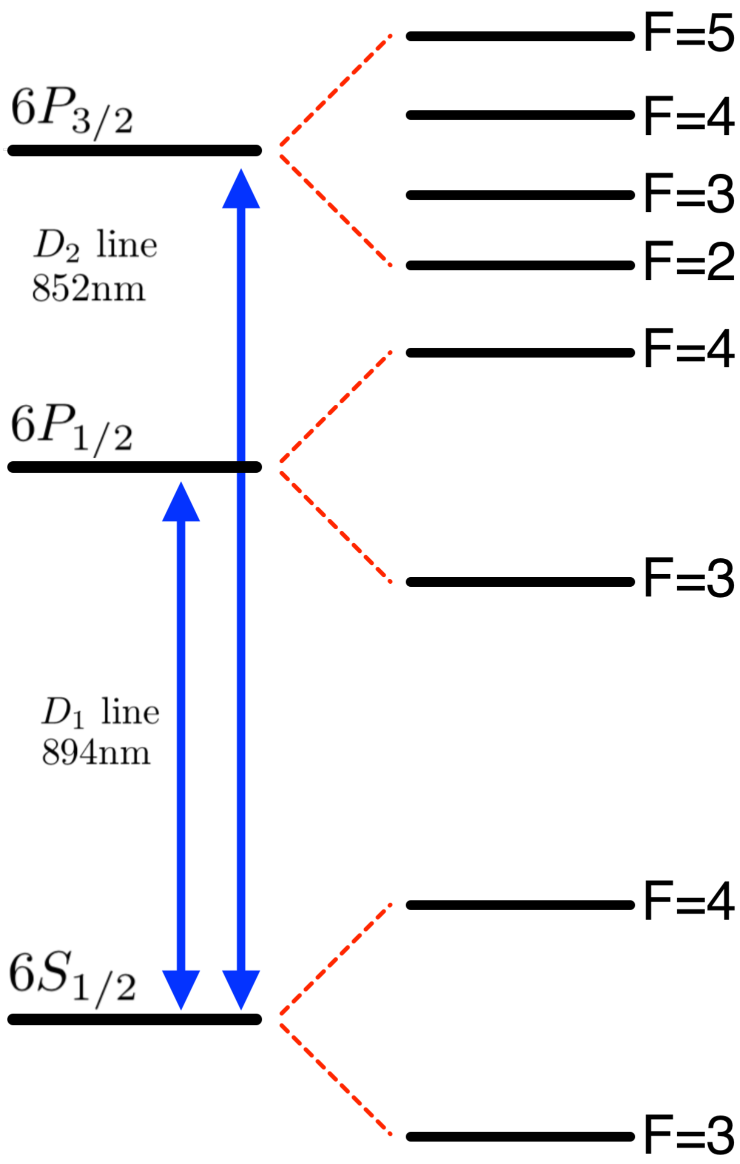

Figure 3.1: The fine and hyperfine structure for $^{133}$Cs.

## Laser Cooling

### Doppler Cooling

When an atom in the laser beam with frequency $\omega_L$ close to transition frequency $\omega_0$, the atom can absorb a photon with frequency $\omega_0$ and transition to the excited state. When the atom is excited, it gains a momentum of $\hbar\vec{k}$ in the direction of the laser beam. After some time the atom decays and emits a photon also with frequency $\omega_0$. While the gain of momentum from the photon absorption is directional, the emitted photon from decay is random in direction, so the mean momentum transfer is zero. The rate of photon absorption by an atom is $R_{sc}$, and every photon transfers $\hbar\vec{k}$ to the atom, so the average force on the atom is $\langle\vec{F}\rangle = R_{sc}\hbar\vec{k}$. The scattering rate $R_{sc}$ depends on the detuning between the laser and the atom transition frequency $\delta = \omega_L - \omega_0$ and the saturation parameter $s_0 = I/I_s = 2\frac{\Omega^2}{\Gamma^2}$, where $\Gamma$ is the decay rate and $\Omega$ is the Rabi frequency [76], namely

$$R_{sc} = \frac{\frac{s_0\Gamma}{2}}{1 + s_0 + (\frac{2\delta}{\Gamma})^2}. \tag{3.1}$$

The atom scatters the most when the laser is on resonance. For a laser beam that is red detuned $\delta < 0$, the atom will scatter the most when it is moving with velocity $v = \frac{\delta}{k}$ against the direction of the laser. If two red detuned counter-propagating beams with the same intensity overlap with an atom, the atom will eventually be cooled down. When the atom moves to the right it will receive more momentum kicks to the left and vice versa. Due to the finite linewidth of the atom transition, the maximum atom velocity that one is able to cool with Doppler cooling is $v_c = \frac{\Gamma}{k} \approx 1\,\mathrm{m\,s^{-1}}$. When cooling from the dragging force balances with the heating from the spontaneous emission momentum kick it reaches the minimum temperature. This minimum temperature, the Doppler temperature follows $T_D = \hbar\frac{\Gamma}{2k_B}$ [23, 76]. The Doppler temperature is $T_D = 125\,\mu\mathrm{K}$ for cesium. The cycling transition is extremely useful for laser cooling, since usually many photons ($\sim 10^5$) have to be scattered to slow down the atom from 300 K. The cesium $6S_{1/2}F = 4, m_F = 4 \longrightarrow 6P_{3/2}F = 5, m_F = 5$ transition is closed for $\sigma^+$ laser light. However, there is still a small probability for cesium atoms to fall into the $F = 3$ ground state, so the additional repumping beam is required to pump these atoms back into the $F = 4$ ground state.

### Sub-Doppler Cooling

In early experiments of laser cooling, researchers were surprised to discover that atoms can be cooled to well below $T_D$ [67, 81]. Due to the more complex electron configuration than the two-level model used to explain Doppler cooling. Also, in these experiments, the trap lifetime significantly increased when the relative polarization alignment of two counter-propagating beams is off. Two groups developed a model for laser cooling that can explain this lower temperature [28, 101]. The critical feature of the theory is that it takes the sublevels such as Zeeman and hyperfine structure into account. As an atom moves through the light field, the optical pumping among these sublevels provide the mechanism for cooling below $T_D$.

When atoms move through a light field with polarization gradients, the ground state population of the atoms is redistribution by optical pumping from the light field. Transitions among these magnetic sublevels require angular momentum exchanges between the light field and the atoms, and different light polarizations at different locations in a polarization gradient favors different angular momentum transfers. This optical pumping mechanism, coupled with the variation of ground state light shifts, makes the atoms move through a series of hills and valleys while the ground state being redistributed. For example, considering an atom with $J_g = \frac{1}{2} \longrightarrow J_e = \frac{3}{2}$ in a lin $\perp$ lin optical molasses. In a lin $\perp$ lin polarization gradient, two counter-propagating lasers with linear polarization that are perpendicular to each other create a polarization gradient that varies from $\sigma^+$ to $\sigma^-$ within $\lambda/4$. At $\sigma^+$ polarization the atom is pumped to the magnetic ground state $M_g = \frac{1}{2}$ and at $\sigma^-$ the atom is pumped to $M_g = -\frac{1}{2}$. The ground state light shift depends on the $M_g$ value, when the light is $\sigma^+$ polarized, the $M_g = \frac{1}{2}$ has larger light shift, and when the light is $\sigma^-$, the $M_g = -\frac{1}{2}$ has larger light shift. Generally, for any transition $J_g \longrightarrow J_e = J_g + 1$, optical pumping pumps atoms into the state with the larger light shift. So, as atoms move through the polarization gradient, they move up a potential hill and then pump into the state with a larger shift. Each optical pumping event the absorbed photon has a lower frequency than the emitted photon, so the kinetic energy is dissipated. This process is called Sisyphus cooling or polarization gradient cooling (PGC) [76].

The recoil temperature limits that which the PGC can reach. When a photon is emitted, the atoms obtain a recoil velocity of $v_r = \hbar k/M$. The corresponding temperature is the recoil limit temperature $T_r = \frac{\hbar^2 k^2}{k_B M}$, which was generally regarded as the low limit for optical cooling processes. For cesium the recoil limit is $T_r = 180\,\mathrm{nK}$.

Besides cooling atoms, trapping is also crucial for experiments. A standard technique for trapping atom is the magneto-optical trap (MOT) [76, 85]. The MOT cools atoms by using an inhomogeneous magnetic field and radiative selection rules. The MOT is a robust setup since it is very tolerable on the power and polarization imbalance. The magnetic field can easily be obtained by air-cooled coils, making it a standard tool in a cold atom lab. In a MOT, the magnetic field gradient is generated using a pair of coils in anti-Helmholtz configuration. Three pairs of counter-propagating beams in $\sigma^+ - \sigma^-$ configuration are overlapped at the center of the trap where $B = 0$. The magnetic field gradient creates spatial dependent Zeeman shifts, which causes an imbalance in the scattering force from the lasers, therefore, drives the atoms toward the center of the trap. The $\sigma^+ - \sigma^-$ optical molasses also provide velocity damping for cooling.

**Optical Dipole Trap**

The optical dipole trap or far-off-resonance trap (FORT) traps atoms using an intense, far-detuned light field. A FORT relies on interactions between an atom's electric dipole and the far-detuned light [45]. Due to the far-detuned nature of the trap, the optical excitation can be kept extremly low, which prolong the atom trap life-time. Usually the trap is insensitive to the groundstate sub-level because the trap beam is far-detuned, this make it suitable for experiments involving internal ground-state dynamics. The usual complex notation for electric field is $\vec{E}(\vec{r},t) = \hat{e}\tilde{E}(\vec{r})\exp(-i\omega t) + c.c.$ and the atomic dipole moment is $\vec{p}(\vec{r},t) = \hat{e}\tilde{p}(\vec{r})\exp(-i\omega t) + c.c.$, where $\hat{e}$ is the unit polarization vector. The amplitude of the dipole moment $\tilde{p}$ correlates with the field amplitude $\tilde{E}$ by the complex polarizability $\alpha(\omega)$

$$\tilde{p} = \alpha(\omega)\tilde{E} \tag{3.2}$$

The dipole potential $U_{\text{dip}}$ of the induced dipole in the electric field is given by

$$U_{\text{dip}} = -\frac{1}{2}\langle \vec{p} \cdot \vec{E} \rangle = -\frac{1}{2\epsilon_0 c}\Re(\alpha) I \tag{3.3}$$

Where $I = 2\epsilon_0 c \left|\tilde{E}\right|^2$, and the bracket indicate time average over an optical cycle. For a red-detuned ($\delta < 0$) FORT beam, $U_{\text{dip}}$ is negative, which attracts atoms to the intensity maxima. For a blue-detuned ($\delta > 0$) FORT beam the potential is positive, which repels atoms from the intensity maxima. The optical dipole trap is a very flexible trap since the light pattern can be shaped using a different technique. For example, using digital mirror array and holographic methods atoms can be arranged in arbitrary patterns in 2d and 3d [7, 112]. Also, the interference pattern of various coherent fields can be used to create complex periodic optical lattices in any spatial dimension. These optical lattice are commonly used in quantum simulation experiments [14, 24] and optical atomic clocks [72]. Optical tweezers [5], tightly focus laser beams, can be used to trap single atom and perform precise quantum control [35, 56, 57].

For a two-level atom the scattering rate $\Gamma_{sc}$ from the red-detuned FORT is [45]

$$\hbar\Gamma_{sc} = \frac{\Gamma_0}{\delta} U_{\text{dip}} \tag{3.4}$$

Where $\Gamma_0$ is the decay rate. To decrease $\Gamma_{sc}$ to prolong lifetime, it is preferable to use a trap beam with large detuning.

### Scalar, Vector, and Tensor Light Shifts

The complex polarizability $\alpha(\omega)$ mentioned in the previous section is a simplification. Here I present a more realistic description of the light shift and dipole potential. The realistic complex polarizability is tensorial, we can write [94]

$$U(\vec{r}) = -E_\mu^{(-)}(\vec{r}) E_\nu^{(+)}(\vec{r}) \alpha_{\nu\mu} \tag{3.5}$$

where Kramers–Heisenberg polarizability tensor is

$$\alpha_{\mu\nu} = 2 \sum_k \frac{\omega_{ik} \langle \phi_i | \hat{d}_\mu | \phi_k \rangle \langle \phi_k | \hat{d}_\nu | \phi_i \rangle}{\hbar(\omega_{ik}^2 - \omega^2)} \tag{3.6}$$

The tensorial $\alpha_{\mu\nu}$ can be divided into scalar, vector, and tensor light shifts [94]

$$\bar{\alpha}(\omega, \mathbf{e}) = \alpha_s(\omega)\bar{\mathbf{I}} + \alpha_v(\omega)(\mathbf{e} \times \mathbf{e}^*) \cdot \frac{\mathbf{F}_z}{F} + \alpha_t(\omega)\frac{3|\mathbf{e} \cdot \mathbf{e}_z|^2 - 1}{2}\left(\frac{3\mathbf{F}_z^2 - \mathbf{F}^2}{F(2F-1)}\right) \tag{3.7}$$

Where $\alpha_s(\omega)$, $\alpha_v(\omega)$ and $\alpha_t(\omega)$ are scalar, vector and tensor polarizabilities respectively. $\bar{\mathbf{I}}$ is the identity operator, $\mathbf{F}$ is the angular momentum operator, and $\mathbf{F}_z$ is the angular momentum operator for the $z$ direction. In a linear polarized light field, only the scalar and tensor polarizabilities are relevant. The vectorial component which depends on $m_F$ is relevant when the polarization has elliptical components. The tensor polarizability $\alpha_t(\omega)$ vanishes for the cesium D1 transition ground state and excited state, since for these states $J = \frac{1}{2}$. The ground state and excited state light shift can be calculated using this expression and the data for the transitions can be found in Ref. [65, 88].

### Degenerate Raman sideband cooling (DRSC)

In our experiment, atoms trapped in the optical lattice are transported over ~2 cm of distance. In order to maximize transport efficiency and increase the lifetime, it is desirable to cool atoms into the vibrational ground state. One way to achieve this is degenerate Ramen sideband cooling (DRSC), which is first demonstrated for atom trapped in a 1D optical lattice [105]. In this method, the atom sample is initially prepared in the $|3, 3, n\rangle$ state, where $n$ is the vibrational quantum number in the tightly confined direction, in our case, the z-direction that is along the optical lattice has much tighter confinement comparing to the radial direction $\nu_z \gg \nu_r$. An external magnetic field $\mathbf{B}$ is applied to create the Zeeman splitting, such that the states $|3, 3, n\rangle$ and $|3, 2, n-1\rangle$ are degenerate, as seen in Fig. 3.2. During the cooling cycle, a degenerate Raman transition moves the atom from $|3, 3, n\rangle$ to $|3, 2, n-1\rangle$, and then an optical pumping transition moves the atom to $|3, 3, n-1\rangle$; thus the whole cycle removes one vibrational quantum. Since the atom is in the Lamb-Dicke regime, for which the wave-packet size of the atom $\Delta x_0$ is much smaller than the wavelength of the cooling transition $\eta \equiv k\Delta x_0 << 1$, the photon recoil can only change the vibration momentum with probability $\eta$. In the DRSC scheme, the trapped light also acts as the Ramen transition beam. To create the Raman coupling between the states that differ by one angular momentum quantum number $m_F$, we introduce an angle $\alpha$ between the two counter-propagating beams that create the optical lattice creating a vector shift in the lattice potential. The coupling strength is [30]

$$\langle 3, 2, n-1|U(\vec{r})|3, 3, n\rangle = \epsilon U_0 \eta \frac{(6n)^{1/2}}{2} \sin(\alpha)\sin(\beta) \tag{3.8}$$

Where $\beta$ is the angle between the external magnetic field $\mathbf{B}$ and the lattice wavevector $\vec{k}$, $U_0$ is the trap depth, $\epsilon$ is a coupling strength factor for the Raman transition at the lattice detuning, $\eta$ is the Lamb-Dicke parameter.

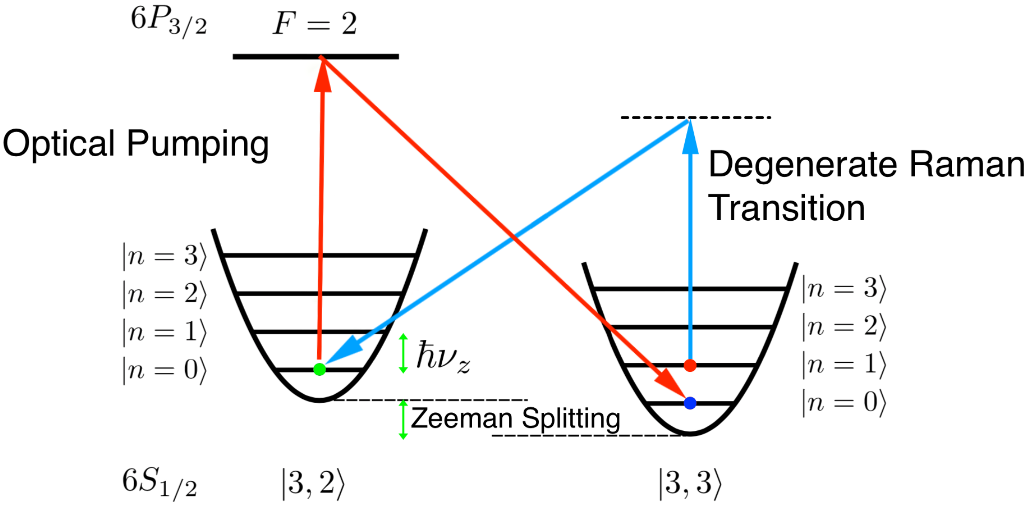

Figure 3.2: Degenerate Raman sideband cooling (DRSC) for an atom trapped in a tight trap with $\eta \ll 1$ [105]. An external magnetic field is applied to create the Zeeman splitting, such that the state $|3, 3, n\rangle$ and $|3, 2, n-1\rangle$ are degenerate. A degenerate Raman transition (blue arrows) reduces the vibrational quanta by one, then an optical pumping transition (red arrows) accumulates the atom in the ground and dark state (the blue dot).

## 3.2 Experiment Apparatus

### Experimental process: overview

In this section I describe a summary of our experimental process; more detail of the experimental process and data analysis will be present in Chapter 4, while this chapter will focus more on the experimental apparatus. The experimental process starts by pushing, with a near-resonant pulsed beam, a continuously loaded MOT in the source chamber down a differential pumping tube to the science chamber

[77]. The pushed atoms are recaptured in the science chamber MOT where we load them into a 1D optical lattice. The 1D lattice loads from atoms in the science MOT by way of an interval of polarization gradient cooling (PGC), which is followed by a degenerate Raman sideband cooling (DRSC) interval to achieve a final axial temperature of 12 µK[77]. Once the atomic sample has been loaded and cooled, one beam of the optical lattice is frequency chirped to move the optical lattice along with the atoms in it. The atoms are conveyed over a distance of 20 mm to the center region of a particular APCW device via the moving $1D$ optical lattice with temperature in the moving lattice frame (typically 10 to 30µK) much less than the lattice depth (typically ∼ 300microK to ∼ 500µK). As the confined atomic cloud passes a chosen APCW, atoms near the waveguide are interrogated by a guided-mode (GM) probe injected into the APCW. The transmitted and reflected probe light is detected by single-photon counting modules (SPCMs) with a time stamp recorded for each detected photon. Scattered lattice light that emerges in a GM is likewise detected and is used to generate a real-time zero crossing signal. The lattice time tags and the probe time tags are registered to each other and a ‘clocked’ histogram created for a single lattice period as described in Chapter 4.

### Experimental apparatus: overview

The full experimental apparatus, which consists of two optical tables, is present in the block diagrams Fig. 3.22 for optical table 1 and Fig. 3.23 for optical table 2. Fig. 3.4 to Fig. 3.21 show the implementations of each component, these figures are modified from Jean Baptiste Beguin’s diagrams.

Optical table 1 consists of setups for the cooling and repumping laser, D2 phase lock laser and the break out boards. The cooling master laser is a homemade ECDL laser locked to the crossover peak between the cesium D2 $F = 4 \longrightarrow F = 3$ transition and the D2 $F = 4 \longrightarrow F = 4$ transition with Pound-Drever-Hall technique [34], as shown in Fig. 3.5. The cooling master laser beam is guided to a break-out board where it is amplified by a Topica BoosTA tapered laser amplifier (TA) to ∼25 mW, which is ample for various parts of the experiment. Using a series of polarization elements and double-pass AOM setups, the output of the TA is split into seven beams each can be frequency and amplitude modulated. These beams are used for science MOT cooling, source MOT cooling, pushing beam, absorption imaging, guided mode Doppler cooling, and DRSC depumping beam. The DRSC depumping beam is frequency-shifted to the cesium D2 $F = 4 \to F = 4'$ transition, the other beams are frequency-shifted close to the cesium D2 $F = 4 \to F = 5'$. Fig. 3.4 shows this setup. If the D2 phase lock laser is set to address the transitions from the D2 $F = 4$ ground state, about 100 µW of the laser power can be split and mixed with the output of the D2 phase lock laser to provide a beat note for locking. The repumping laser is a homemade ECDL locked to the crossover peak between the cesium D1 $F = 3 \to F = 3'$ transition and the cesium D1 $F = 3 \to F = 4'$ transition with PDH scheme. The repumping master laser's power is amplified with injection locking a second diode, which is referred to as repumping laser slave. This set up is shown in Fig. 3.7. The output laser of the repumping laser slave is split into two paths; one path is frequency shifted to the cesium D1 $F = 3 \to F = 4'$ to provide repumping laser for both source and science MOT. The other path is then frequency shifted to the cesium D1 $F = 3 \to F = 3'$ and can be mixed with the output of the D2 phase lock laser to provide the beat note for locking if the D2 phase lock laser has to address transitions from the D2 $F = 3$ ground state. Section 3.2 explains the details of the D2 phase lock laser, and the setup is presetned in Fig. 3.8.

Optical table 2 including the vacuum chambers, guided mode trap setup, characterization setup, D1 phase lock laser system and the filtering setup for optical lattice, guided modes, and probe. Section 3.2 describes the details of the vacuum system and the MOT configuration. The D1 and D2 guided mode trap beams are generated by two commercial ECDL lasers. One near the cesium D1 transition and the other near the cesium D2 transition, these lasers can be tuned over 20 nm wavelength range. Each guided mode laser is split in two and pass through a pair of double-pass AOMs The two paths are frequency-shifted such that there is a 100 MHz difference in frequency, so that the guided mode trap beam from the two inputs of an APCW add incoherently to minimize vector light shift. The setups relevant to the GM are presented in Fig. 3.11, Fig. 3.12, Fig. 3.13 and Fig. 3.14.

The D1 phase lock laser system is mostly used for providing the D1 probe. Two Vescent DBR lasers are phase locked with respect to each other in this system, one laser is locked to the D1 $F = 3 \to F = 3'$ transition and the other laser phase locked to the first laser using a Vescent D2-135 Offset Phase Lock Servo. The phase lock can be either done at around 1 GHz to address the D1 $F = 3 \to F = 4$ transition, or at around ~9 GHz for addressing the D1 $F = 4$ ground state. This wide frequency tuning range makes the phase lock laser system versatile and easy to tune to any frequency in the D1 manifold. For example the flattening beam in the trapping scheme described in Chapter 2 is realized using the D1 phase lock laser.

The transmitted output from the APCW consists of the probe, guided modes, and scattered lattice. The ability to separate light of different frequencies with high extinction ratio is crucial for obtaining clock spectra, which provide useful information of atomic dynamic close to the device within one optical lattice period ($<1$ μs; more details in Chapter 4). Especially when guided modes are being toggled or amplitude modulated, a high extinction ratio is necessary to prevent leaked guided mode trap beams from contaminating the clocked spectra. We use lithographically patterned volume Bragg gratings (VBGs) for frequency filtering. VBGs can be aligned to reflect with high efficiency ($> 95\,\%$) light within a 40 GHz bandwidth for any polarization. The central wavelength can be easily adjusted by changing the VBG incidence angle. For light outside of the 40 GHz bandwidth, transmission across the VBG is almost lossless ($<0.1\,\%$). We usually use a pair of VBGs to combine and separate light with different frequencies. For example, the probe and the guided mode trap beams need to be combined before they are sent to the device, this is done with setup shown in Fig. 3.19. The VBG setup can also separate the probe from the guided mode trap beams at the transmission side, in some cases the frequency difference between the probe and one of the trap beams is only ~300 GHz (~1 nm). A pair of VBGs can reduce the guided mode trap beams by 60 dB, for example, this is done with in Fig. 3.15

We use absorption imaging to characterize the science MOT and atoms trapped in the optical lattice. For imaging atoms in the $F = 4$ ground state, absorption imaging is done by illuminating the atoms with the imaging beam from the break-out board in Fig. 3.22 and imaging the shadow cast by the atoms onto a CCD camera. For atoms in the $F = 3$ ground state, we use the probe beam from the D1 phase lock laser. Absorption imaging is sensitive to energy shifts, so the tomography of the trap can be resolved by taking multiple images with different detunings. The temperature of the MOT or the atoms in the optical lattice can be measured with time-of-flight imaging. The cooling and trap beams are turned off, and multiple images are taken sequentially with fixed time-steps. The temperature can be extracted by fitting the change of size in time.

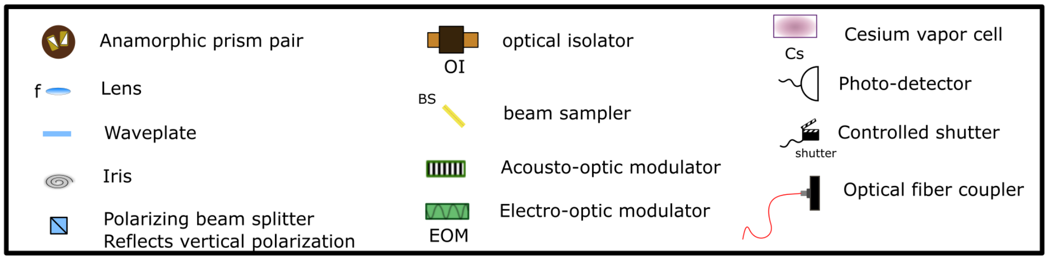

Figure 3.3: The legend for the experimental apparatus diagrams.

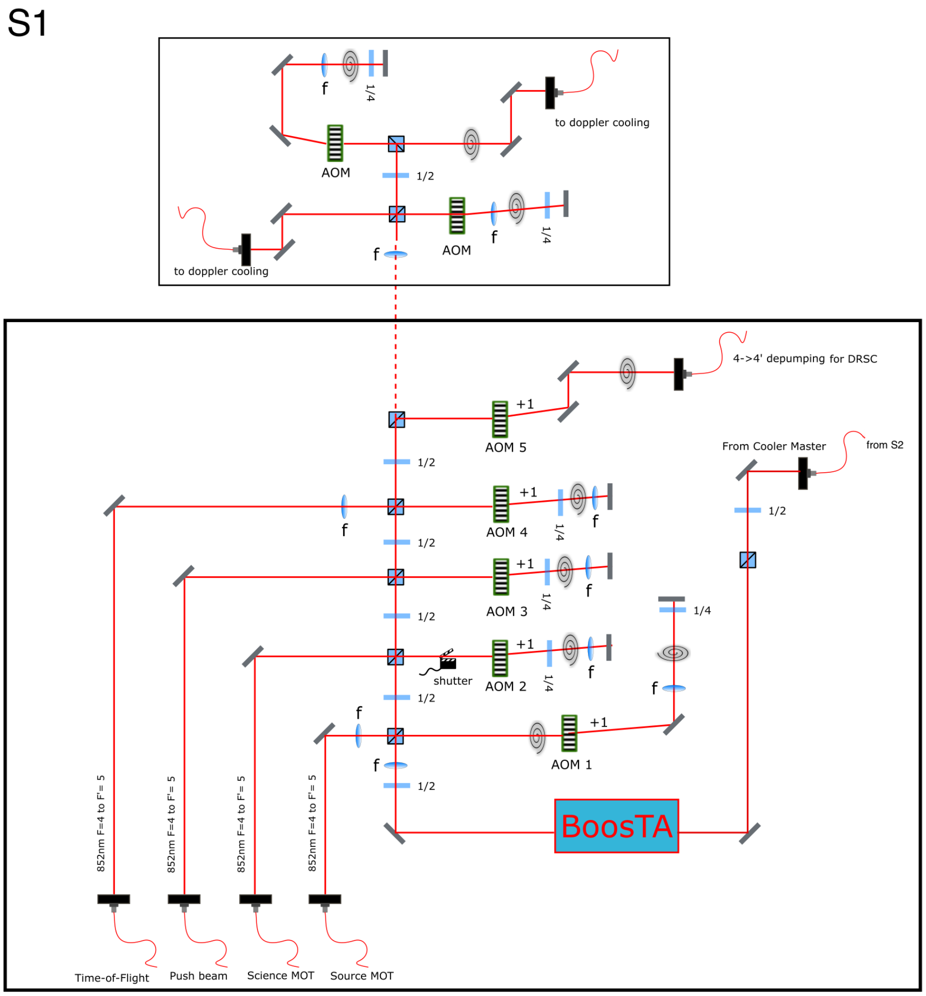

Figure 3.4: Setup 1: The Toptica BoosTA tapered amplifier amplified the laser from the cooling master laser to ∼25 mW. Using a series of polarization elements and double-pass AOM setups, the output of the TA is split into seven beams each can be frequency and amplitude modulated. These beams are used for science MOT cooling, source MOT cooling, pushing beam, absorption imaging, guided mode Doppler cooling, and DRSC depumping beam.

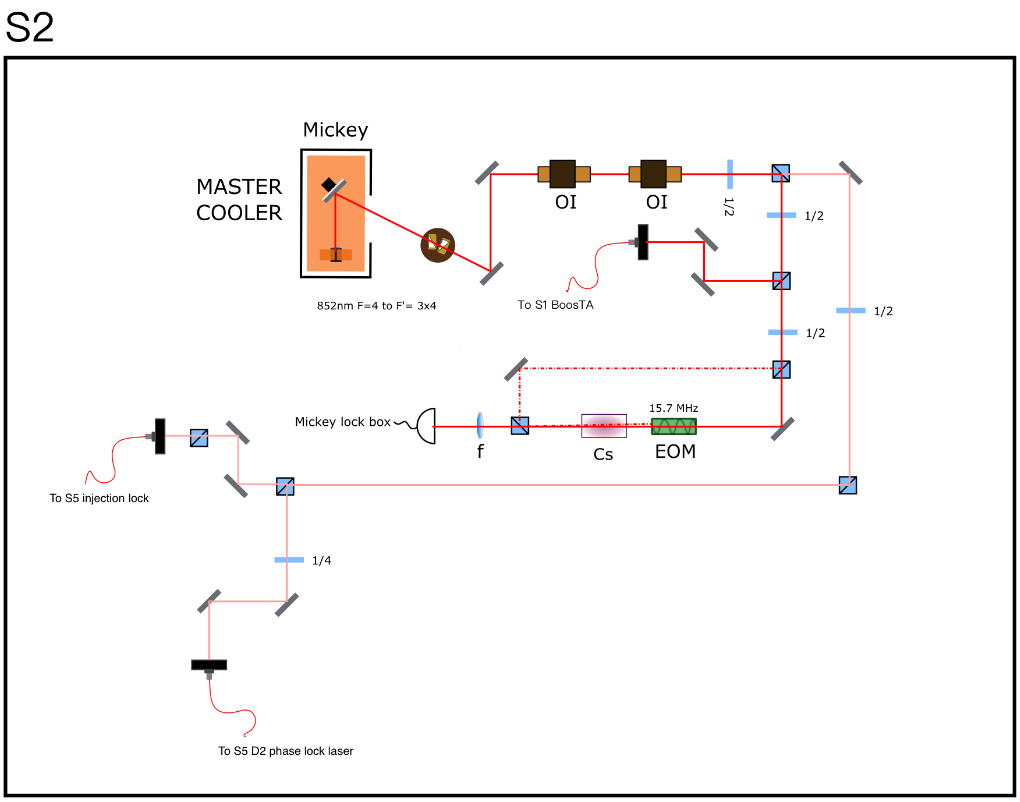

Figure 3.5: Setup 2: The cooling master setup. The cooling master laser is a homemade ECDL laser locked to the crossover peak between the cesium D2 $F = 4 \longrightarrow F = 3$ transition and the D2 $F = 4 \longrightarrow F = 4$ transition with Pound-Drever-Hall technique [34].

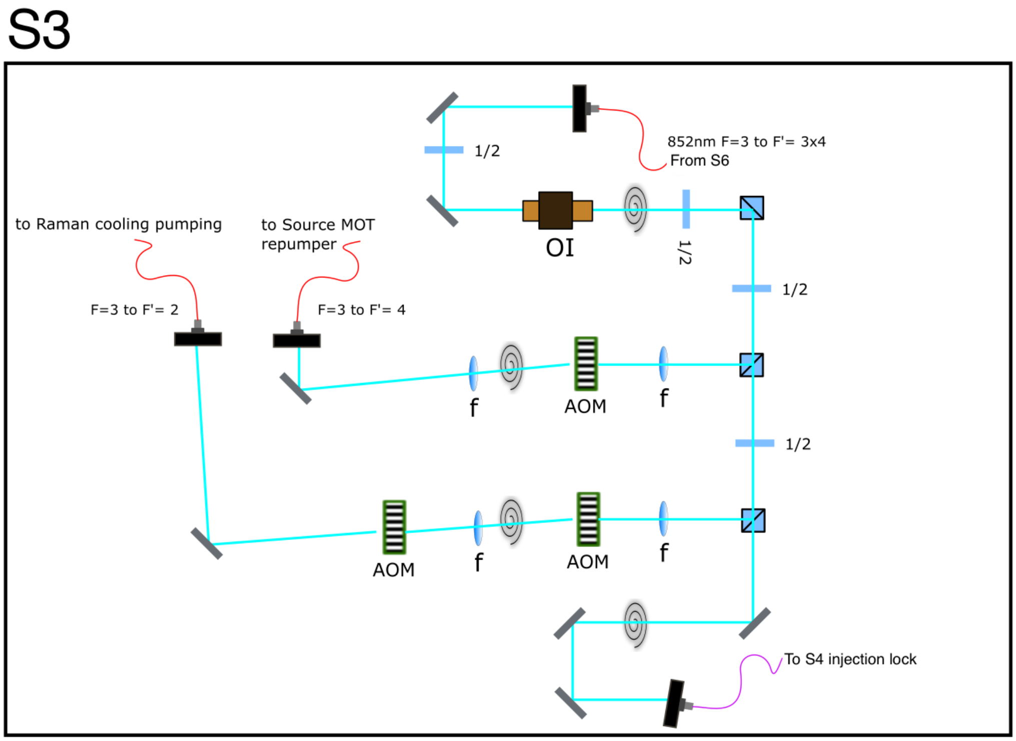

Figure 3.6: Setup 3: This setup split the laser from the repumper master laser to provide the DRSC cooling beam, the srouce MOT repumper and injection lock the repumper slave laser in setup 4.

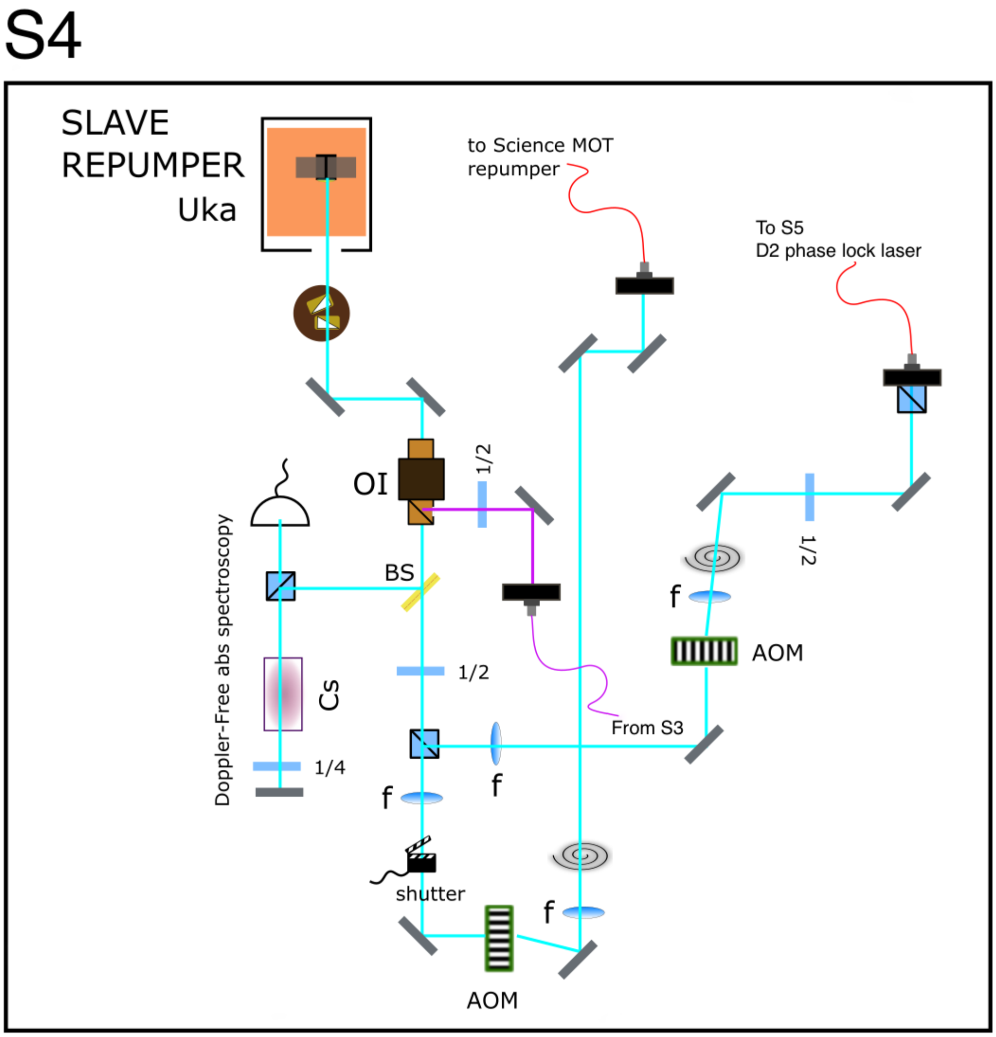

Figure 3.7: Setup 4: The repumping master laser's power is amplified with injection locking a second diode, which is referred to as repumping laser slave.

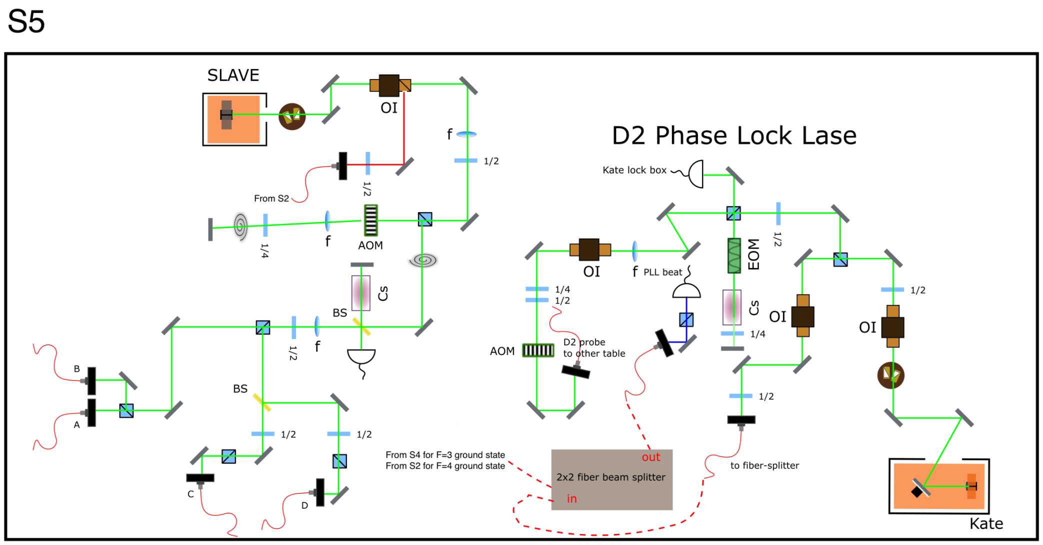

Figure 3.8: Setup 5: The cooling slave laser setup and the D2 phase lock laser. The detail description of the D2 phase lock laser is presented in Section 3.2

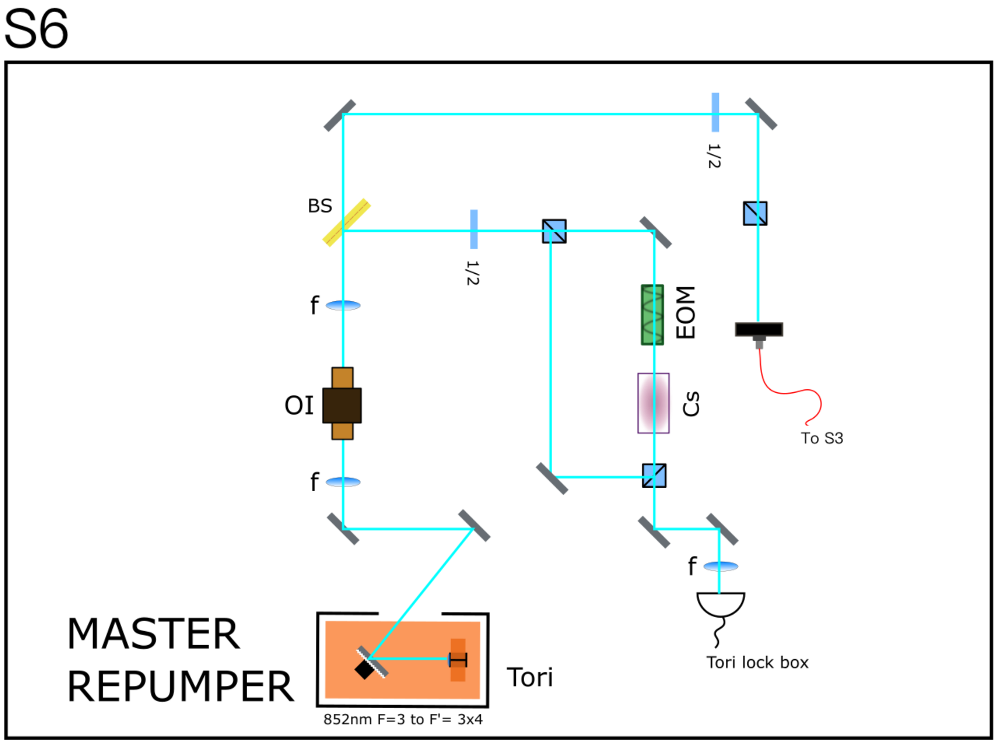

Figure 3.9: Setup 6: The repumper master setup. The repumper master laser is a homemade ECDL laser locked to the crossover peak between the cesium D2 $F = 3 \longrightarrow F = 3$ transition and the D2 $F = 3 \longrightarrow F = 4$ transition with Pound-Drever-Hall technique.

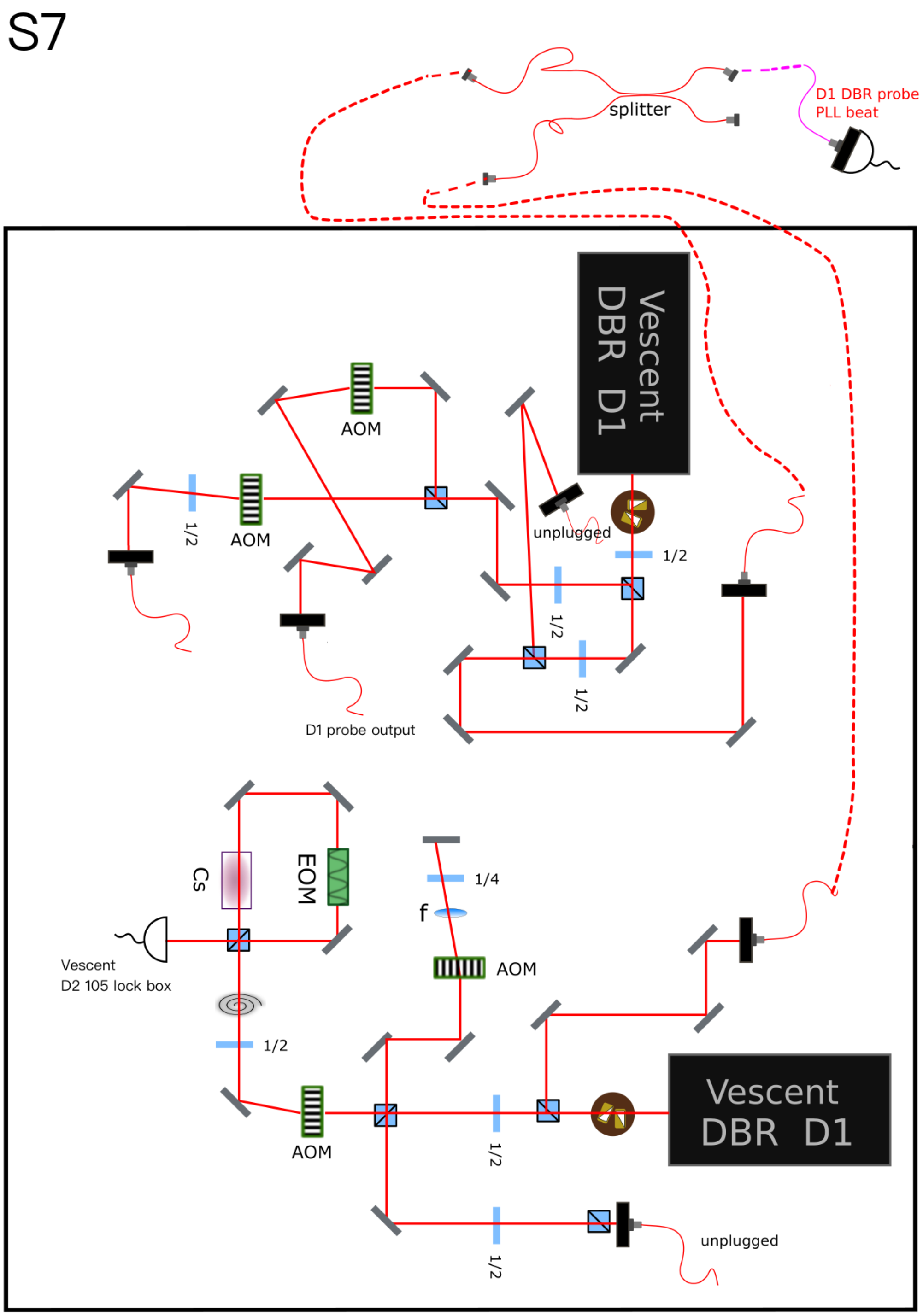

Figure 3.10: Setup 7: The D1 phase lock laser setup. The D1 phase lock laser system is mostly used for providing the D1 probe. Two Vescent DBR lasers are phase locked with respect to each other in this system, one laser is locked to the D1 $F = 3 \rightarrow F = 3'$ transition and the other laser phase locked to the first laser using a Vescent D2-135 Offset Phase Lock Servo. The phase lock can be either done at around 1 GHz to address the D1 $F = 3 \rightarrow F = 4$ transition, or at around ~9 GHz for addressing the D1 $F = 4$ ground state. This wide frequency tuning range makes the phase lock laser system versatile and easy to tune to any frequency in the D1 manifold.

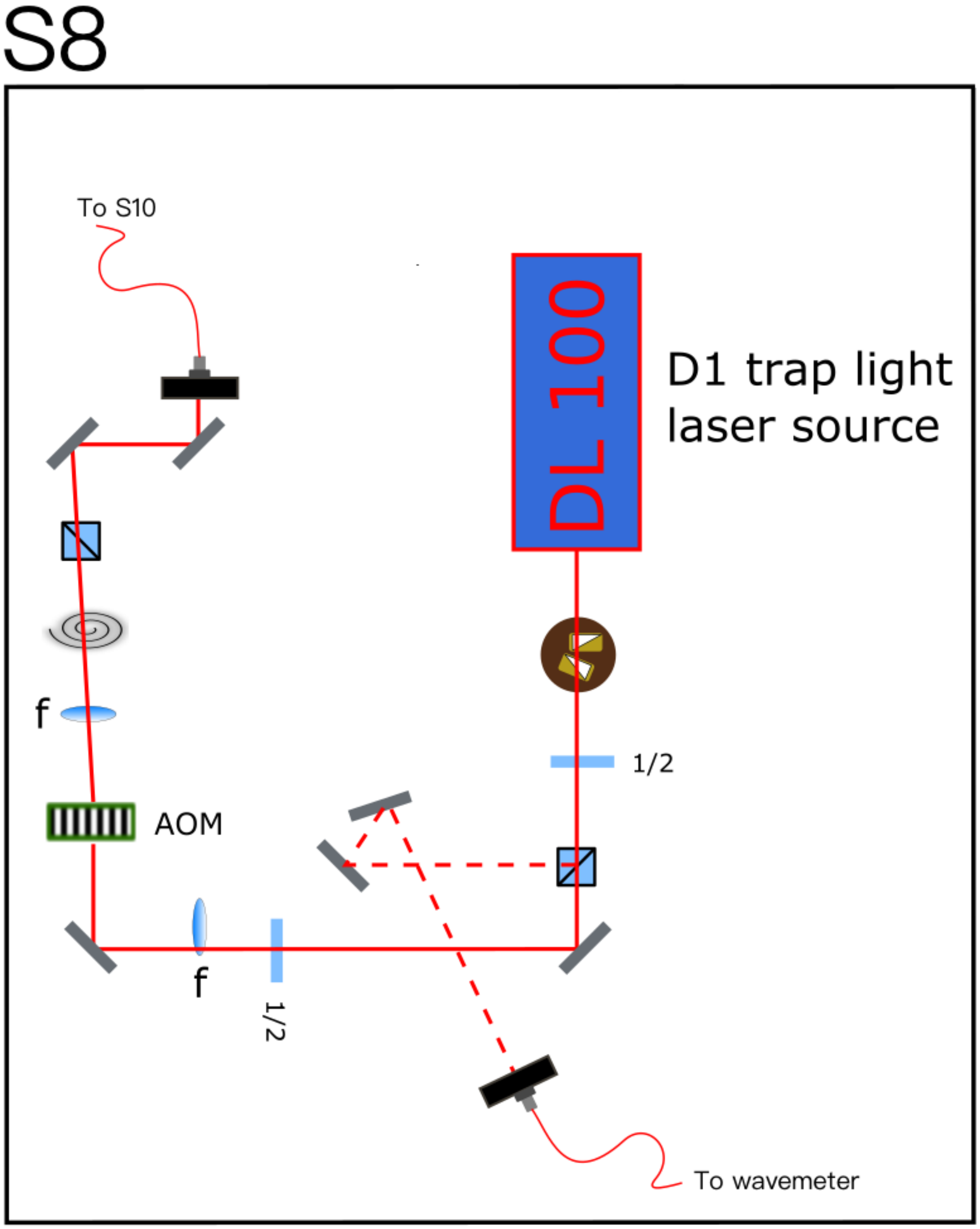

Figure 3.11: Setup 8: The setup with a Toptica DL 100 laser for D1 GM.

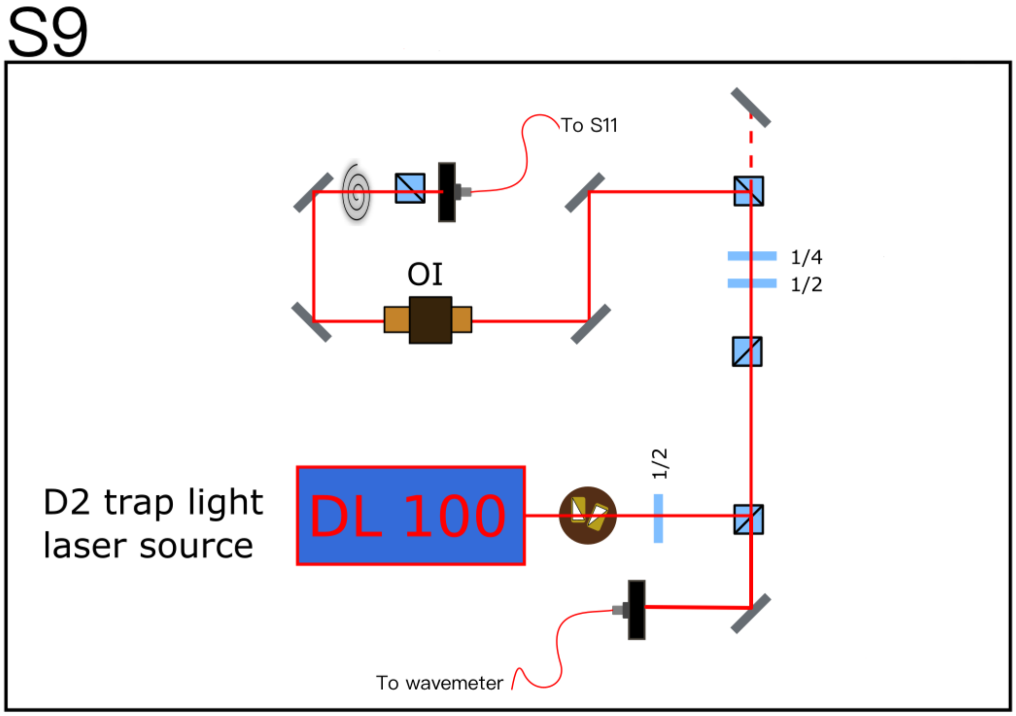

Figure 3.12: Setup 9: The setup with a Toptica DL 100 laser for D2 GM.

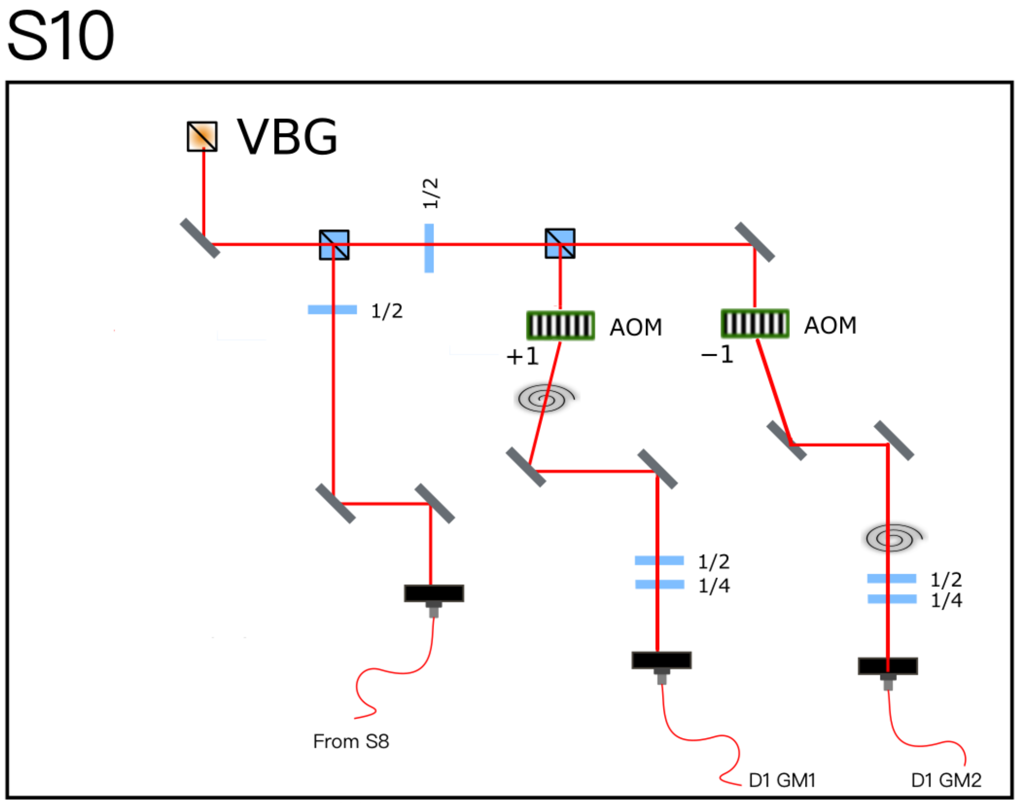

Figure 3.13: Setup 10: The D1 GM laser from S8 is split in two and pass through a pair of double-pass AOMs The two paths are frequency-shifted such that there is a 100 MHz difference in frequency, so that the guided mode trap beam from the two inputs of an APCW add incoherently to minimize vector light shift.

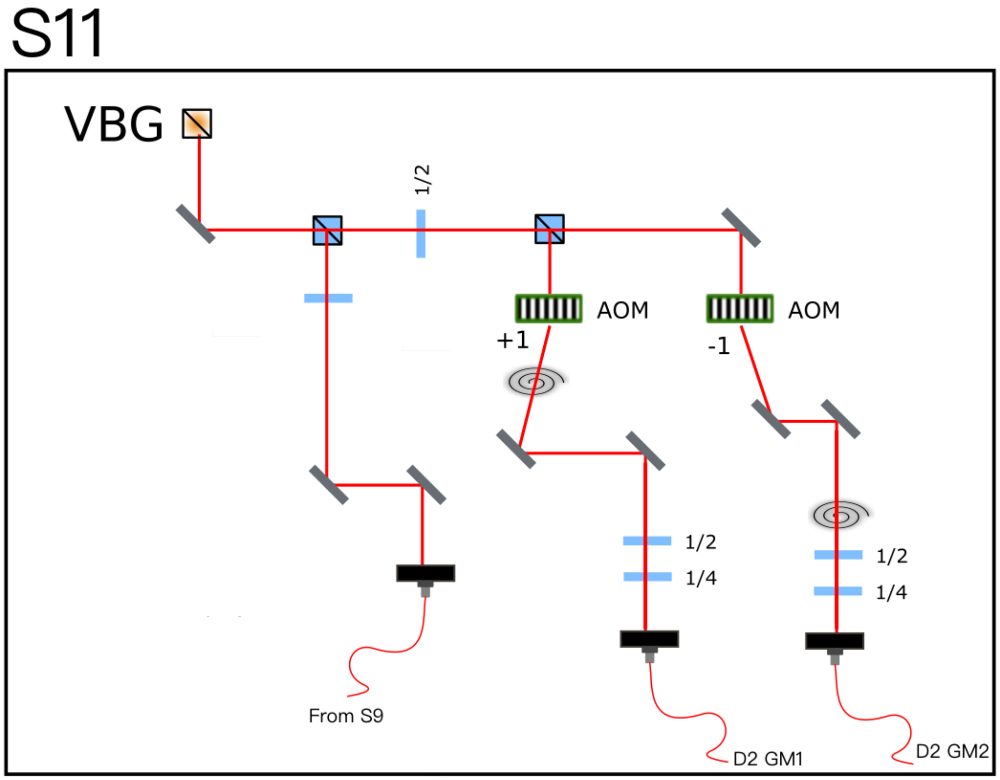

Figure 3.14: Setup 11: The D2 GM laser from S9 is split in two and pass through a pair of double-pass AOMs The two paths are frequency-shifted such that there is a 100 MHz difference in frequency, so that the guided mode trap beam from the two inputs of an APCW add incoherently to minimize vector light shift.

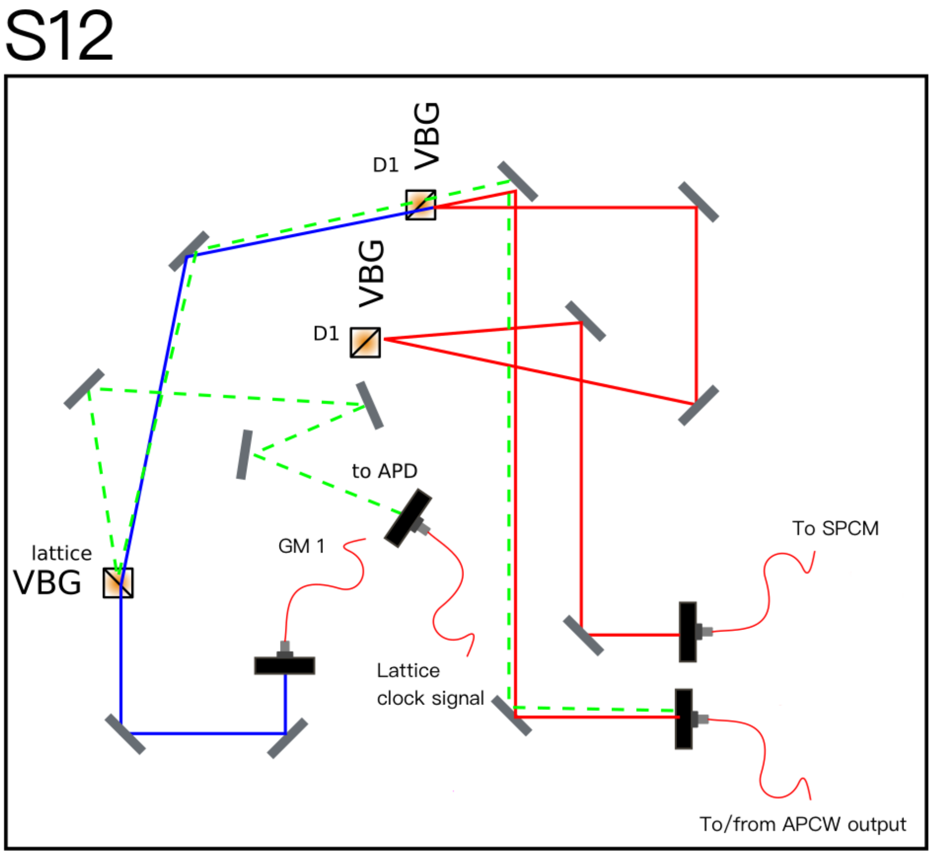

Figure 3.15: Setup 12: The transmitted probe from the APCW is reflected by the APCW and guided to the SPCM. The leaked lattice light transmits through the VBG and is guided to a APD to generate the clocked signal. GM is also sent to the APCW with this setup.

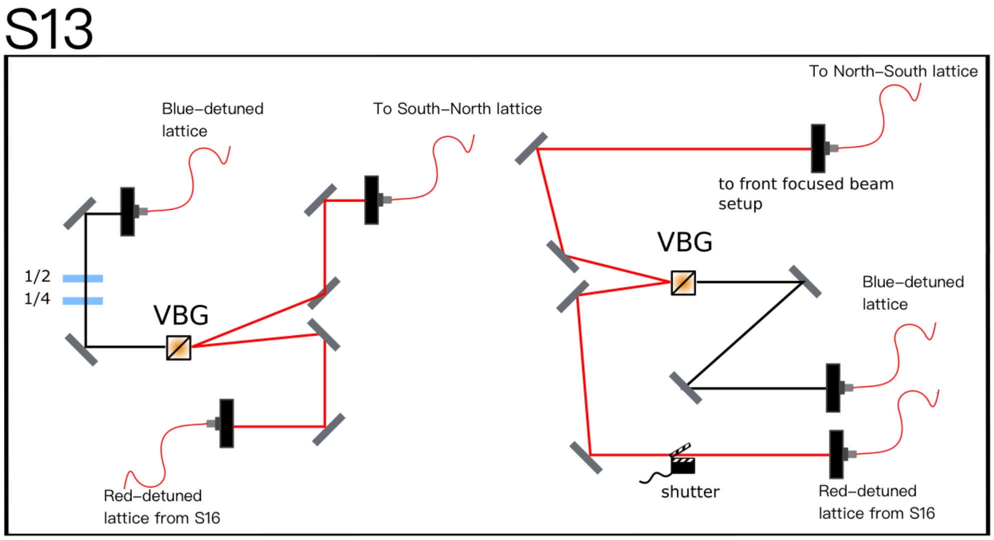

Figure 3.16: Setup 13: When using both blue-detuned and red-detuned optical lattice, this setup can combine the two optical lattice beams.

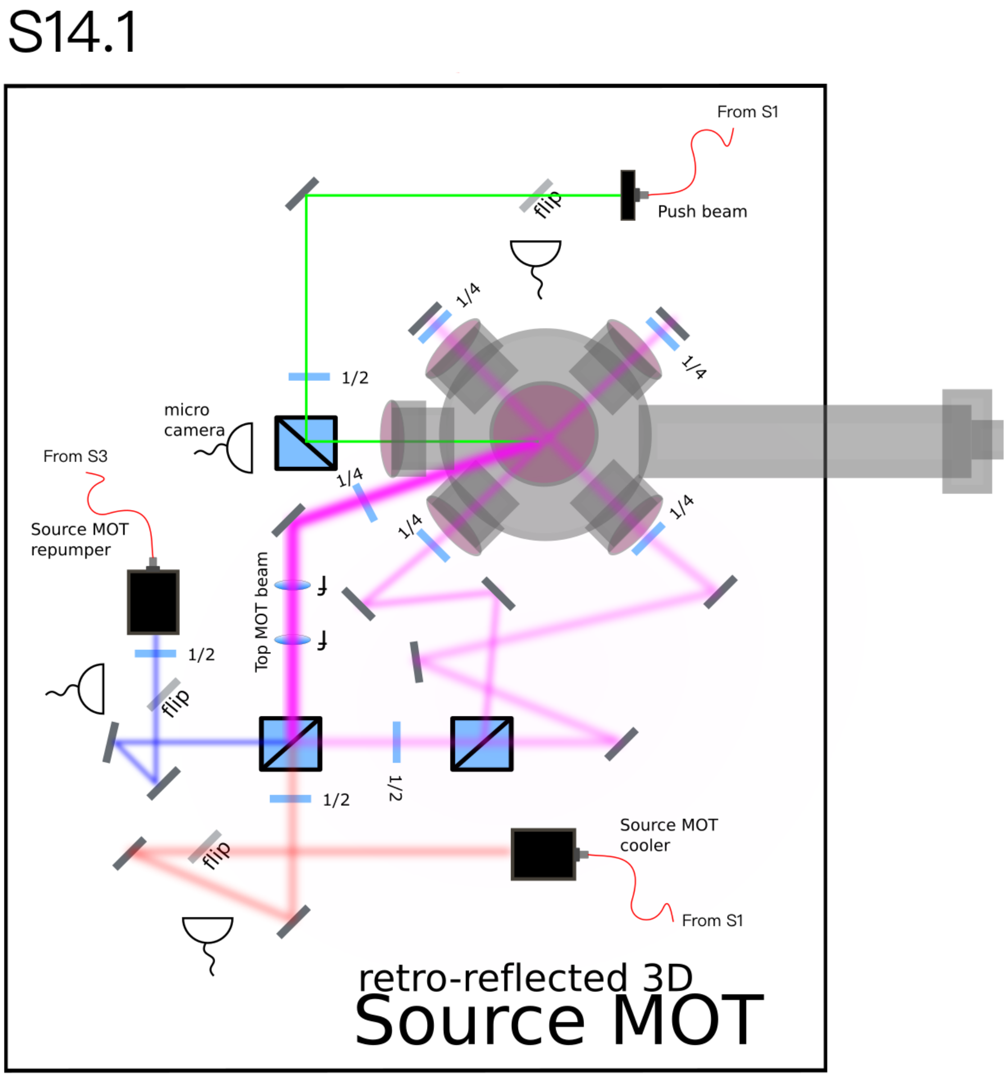

Figure 3.17: Setup 14.1: The source chamber and the source MOT setup. The srouce MOT is a conventional 6 beams setup, and a near resonance push beam is used to push the atoms to the science chamber.

S14.2

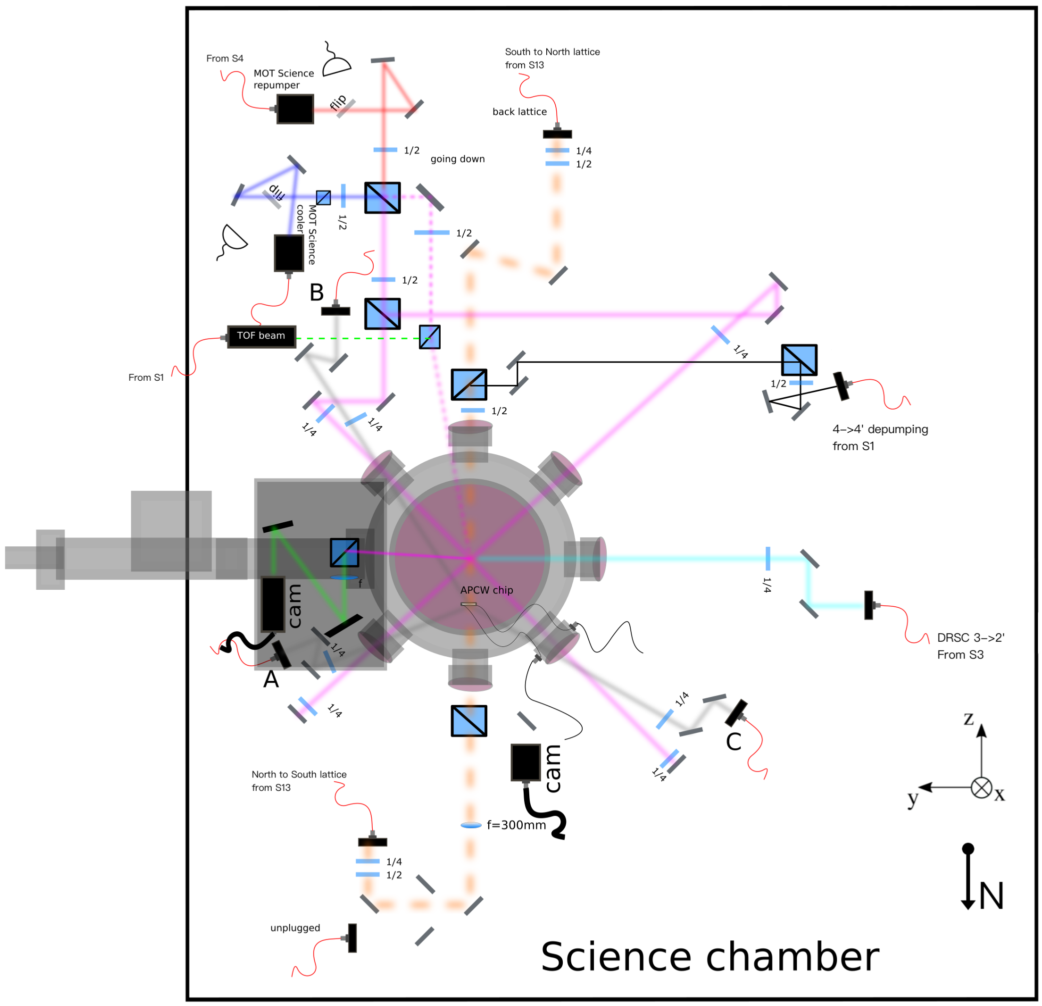

Figure 3.18: Setup 14.2: The science chamber setup.

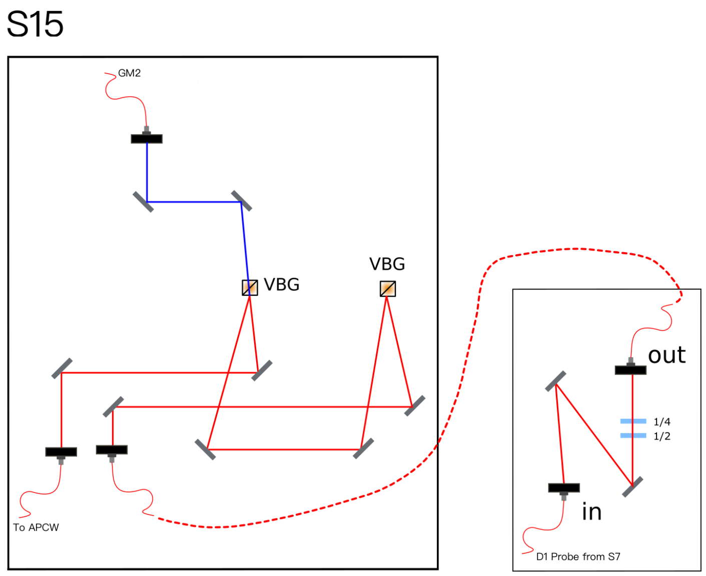

Figure 3.19: Setup 15: The two VBGs are used to combine the GM and the probe.

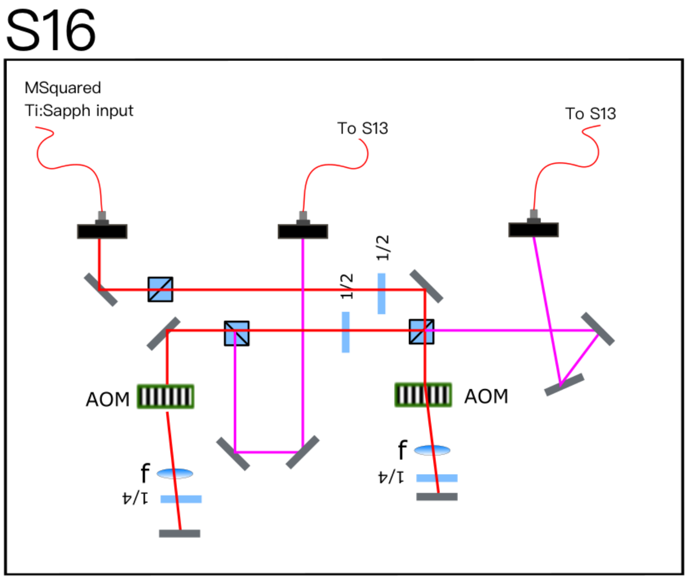

Figure 3.20: Setup 16: This setup split the ~300 mW laser from a MSquared Ti:sapph laser into two beams for the counter-propogating optical lattice beams.

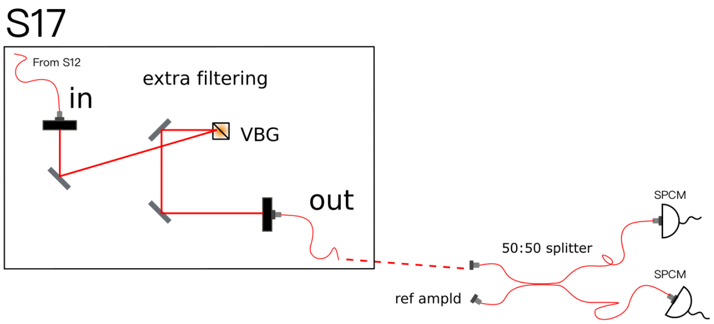

Figure 3.21: Setup 17: The extra filtering setup for filtering out GM before SPCM.

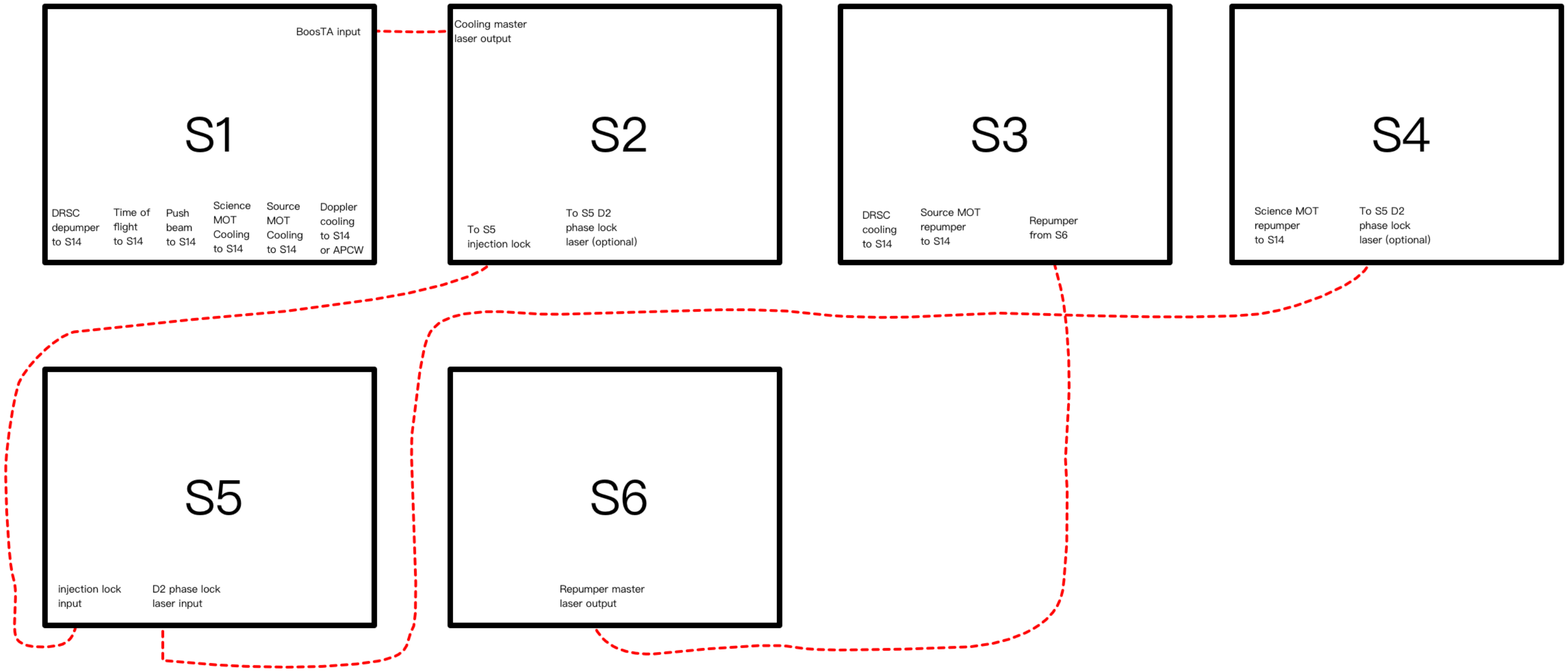

Figure 3.22: Optical Table 1: Including a $F = 4 \rightarrow F = 5$ cooling master/slave laser setup, a $F = 3 \rightarrow F = 4$ repumping master/slave laser setup, D2 phase lock laser and break out boards to supply the laser to various parts of the setup.

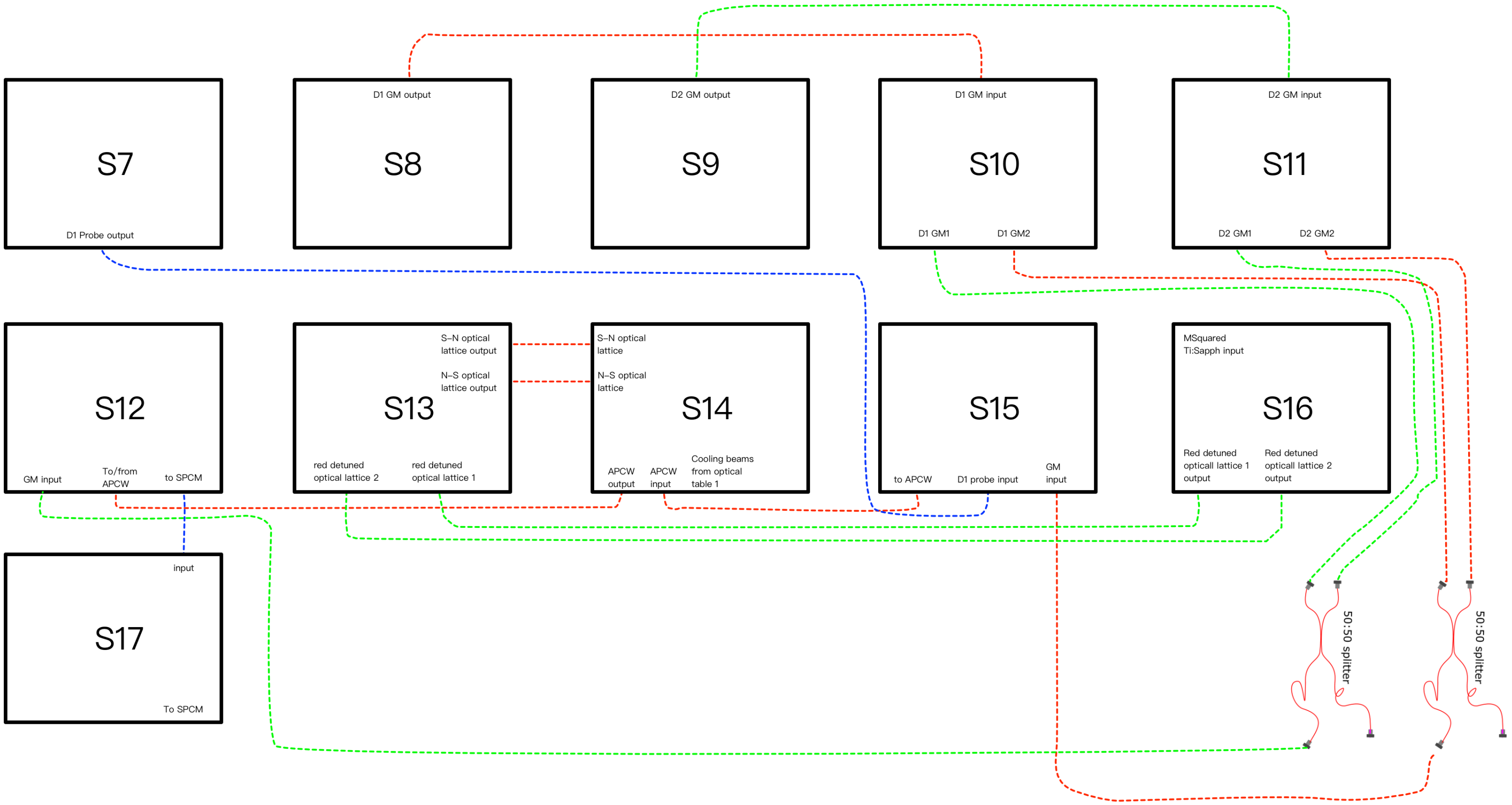

Figure 3.23: Optical Table 2: Including the vacuum chambers, guided mode trap setup, characterization setup, D1 phase lock laser and the filtering setup for optical lattice, guided modes and probe.

### Vacuum System and Magneto-Optical Traps

The vacuum system consists of two Kimball Physics multi-CF chambers separated by 70 cm. The smaller chamber is a 2.75 inch diameter spherical hexagon, referred to as the "source chamber", and the larger chamber is a 6 inch diameter spherical octagon, referred to as the "science chamber". The two chambers are connected by several components, including an inline valve at the center, which allows us to open the science chamber while maintaining vacuum at the source chamber. On each side of this inline valve, there is an ion pump for achieving ultra-high vacuum and an angle valve to which a turbo pump can be attached when pumping the chamber. In the tube connected to the source chamber, there is a differential pumping tube which is 8 inches long and 0.16 inches in diameter. This tube is necessary for reducing the conductance between the source and science chamber, which keeps the cesium partial pressure in the science chamber low. The low cesium partial pressure help increases trap lifetimes and also prevent cesium corrosion of the APCW. The pressure of the science chamber is around $1 \times 10^{-9}$ torr. The connection tube runs east-west. The chip is installed in the science chamber connected with an aluminum arm to a groove grabber on the northern viewport of the science chamber. The chip is installed in a way that the APCWs run vertically which is offset from the center to the north by 2 cm. More detail on chip installation will be described in this chapter.

The MOT in the source chamber (referred to as the source MOT) is loaded from room temperature cesium background, using the standard six-beam configuration and anti-Helmholtz coils, which create a gradient of $\sim 10\,\mathrm{G\,cm^{-1}}$. Cesium atoms are cooled with 10 MHz red-detuned D2 $F = 4 \rightarrow F = 5$ cycling transition and re-pumped with D2 $F = 3 \rightarrow F = 4'$ beams. Once the source chamber is loaded, atoms are transferred to the science chamber with a pushing beam, as described in Refs. [31, 77, 107]. When atoms arrive at the science chamber, they are re-captured by the science MOT. Six 1 inch circularly polarized beam that comes from the science mot beam from the break-out board in Fig. 3.22 which are split into three parts that are 40 mW and are retroreflected. The repumper co-propagates with the vertical beam and usually carries about 10mW of power. An anti-Helmholtz coils pair with a radius of 14 cm generates $15\,\mathrm{G\,cm^{-1}}$ at the center of the science chamber. There are also three pairs of Helmholtz coils pair aligned in three directions to provide uniform magnetic field at the center of the science chamber, which can adjust the position of the MOT.

While we usually use the red-detuned optical lattice beams, the optical lattice setup has the ability to deliver both red detuned and blue-detuned lattice beams. The output from two Ti:Sapph lasers one for red detuned lattice and one for blue detuned lattice are both split into roughly equal power and then feed to the optical filtering board (shown in Fig. 3.16), where the blue and the red optical lattice beams are combined by a pair of VBGs. And send to the optical lattice fiber launcher. More detail on the atomic dynamic and optical lattice is explained in Chapter. 4.

### D2 Phase Lock Laser

The setup of the D2 phase lock laser is similar to that of the D1 phase lock laser. A homemade ECDL laser is phase locked to another laser via locking the beat note between the two lasers to a reference RF signal. The beat note and the RF signal are sent to a Hittite HBT digital phase-frequency detector (HMC439QS16G), which can detect phase and frequency differences from 10 to 1300 MHz. If the frequency difference is positive, the detector maps the phase difference $\phi_+$ of $0 < \phi_+ < 2\pi$ to the output voltage between 0 and 2V, and if the frequency difference is negative, the detector map the phase difference $\phi_-$ of $0 < \phi_- < 2\pi$ to the output voltage between 0 and $-2$V. A home-made locking box then locks this voltage to zero with two PI loops. The faster loop with $\sim$2 MHz bandwidth takes the voltage from the detector and feedback to the ECDL diode current control voltage $V_{\text{current}}$, which modulate the ECDL current. The fast feedback loop is fast enough to phase lock the ECDL. However, the long term drift accumulates and ECDL mode hops in around 10 min. So, the other slower PI loop with $\sim$2 kHz bandwidth takes $V_{\text{current}}$ as input and locks it to zero, to minimize the DC and frequency component of $V_{\text{current}}$ below $\sim$2 kHz. This eliminates the long term drift and prevents the diode from mode hops. The output of the slow PI loop is the ECDL grating piezo voltage $V_{\text{piezo}}$. The piezo has a much lower responding frequency bandwidth compared to current, and with a larger continuous laser frequency tuning range, thus it is ideal for absorbing the long-term drift. The D2 phase lock laser can be tuned to cover more than 1 GHz from any transition in the D2 manifold; this makes it very versatile. We used the D2 phase lock laser for the D2 guided mode probe, and we can also use it for gray molasses cooling technique.

## 3.3 Experimental diagnostics

### APCW Fiber Coupling and Transfer

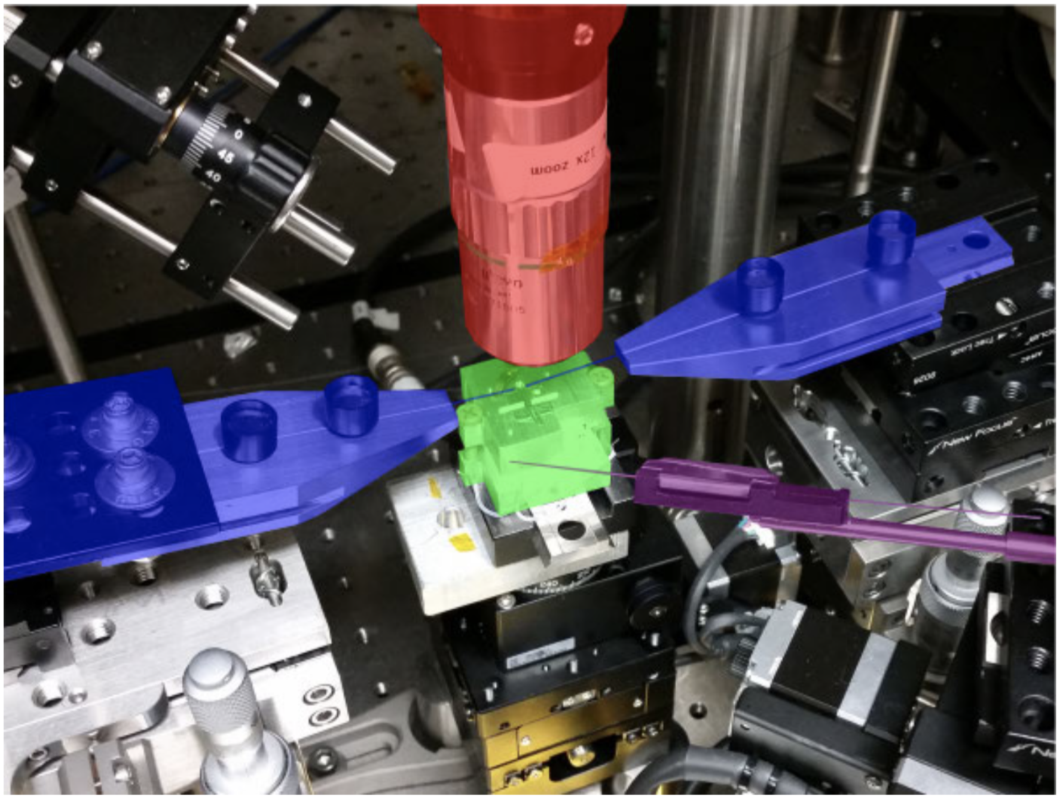

Figure 3.24: Glue bot. False color image of the fiber gluing apparatus. Green highlights the aluminum mounting block, blue the glue bot fiber holder, red the microscope objective, and purple the glue applicator. The mounting block, fiber holder and glue applicator are mounted on stacks of computer-controlled motorized stages. Figure courtesy of Andrew McClung.

In our experiment various guided-modes are coupled into and out of the device through optical fibers. These optical fibers are secured with heat-curing epoxy, and butt-coupled to the fiber couplers on the chip, similar to the process describes in Ref. [25]. Then the chip is installed into the science chamber. This section describes the fiber gluing and chip transfer process.

During the course of the experiment, we have tried two types of glue, UV-curing, and heat-curing. UV-curing Epoxy Dymax OP-29 for fixing the chip to the chip holder and strain relief, Dymax OP-4-20632 for gluing fibers to the chip. For heat-curing Epoxy, we use EPO-TEK 353NDPK for all the gluing. In our experience, the heat-curing epoxy is much more reliable compared to the UV-curing glue. The viscosity of the 353NDPK glue is low out of the box for gluing, in order to prevent

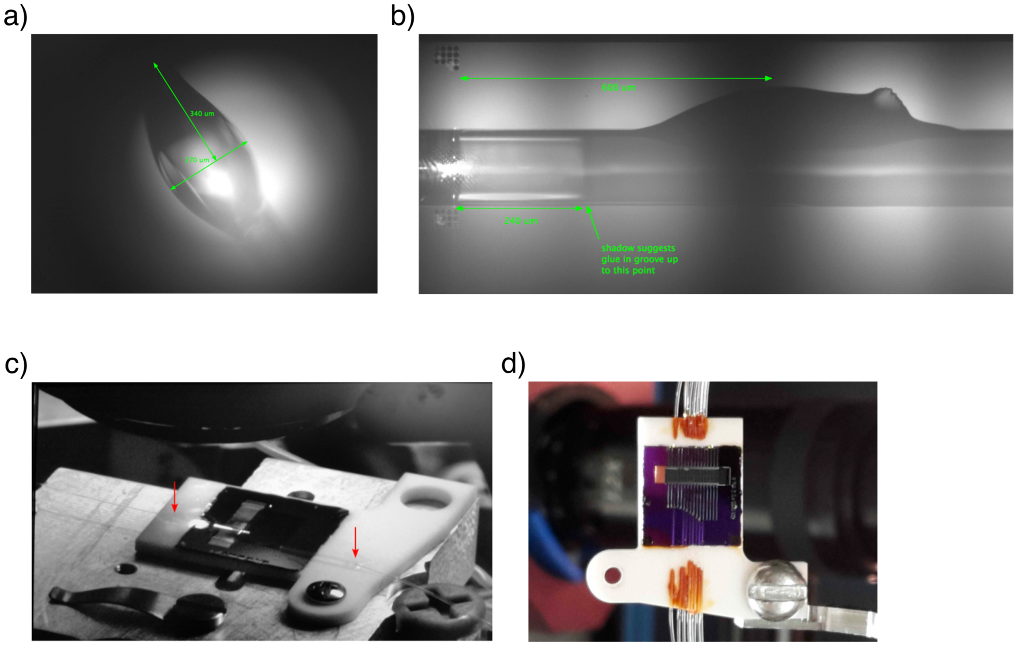

Figure 3.25: a) The optimal amount 5 nL of glue for fiber gluing as viewed from the glue-bot microscope. In practice, the appropriate size of the glue droplet is determined by the relative size between the glue droplet and the fiber radius. b) An example of butt-coupled and glued fiber. The distance between the fiber tip and the fiber coupler tether should be ~10 µm, and with properly pre-cured glue with amound depict in (a) the glue should seep into the space between the fiber and the vee-groove, which manifest as a dark shadow. Ideally the glue should stop before the fiber tip, if too much glue is used or if the glue is not pre-cured for long enough, the glue can go over the fiber tip and risk contaminating the fiber tip or even gluing the fiber tip to the fiber coupler. c) Photo of chip glued to a Mecor chip holder, red arrows indicate locations of strain relief glue. d) Chip and chip holder assembly mounted to the arm. The dark red regions on the chip holder are cured glue. In this photo 16 fibers are glued to the chip, connecting to 8 APCW devices.

the glue from overflow the vee-groove, the glue has to be thickened by pre-curing. The glue is pre-cured on a Scholar hotplate on the third tick for three minutes. During the course of a full day gluing process, the glue get thicken and needs to be prepared again.

During the gluing procedure, the chip holder is held in place by an SEM clip on top of an aluminum mounting block, with a 35 Ω resistive heater integrated into the mounting block. It is important to insert a piece of clean vacuum foil between the mounting block and chip holder to protect the devices from condensates, which is pointed out by Szilard Szoke from Oskar Painter group. Then the chip is placed on top of the chip holder. To avoid thermal shock, we heat and cool the assembly slowly with a ramp of $2\,\mathrm{V\,min^{-1}}$ for the voltage applied across the resistive heater. At 20 V (11 W) the assembly is at 110 and is hot enough for gluing. We use a clean (stripped and wiped with IPA), cleaved fiber taped to an ESD screwdriver (referred to as manual fiber tool) to manually apply small drops on three corners of the chip to tack it down to the chip holder.

Fibers are aligned in the vee-grooves and glued in place after the chip has been tacked to the mounting block. A few millimeters of acrylate coating has been removed from the fiber allowing the stripped fiber to fit into the vee-groove. The length of the stripped fiber must be longer than the vee-groove for the fiber to properly aligned. Sufficient length of acrylate coating must remain for the fiber on the mounting block to be glued for “strain relief”. The fiber is spliced to a characterization setup so that proper alignment can be achieved by monitoring the reflection spectrum while placing fiber in the vee-groove, due to the delicate nature of the operation the fiber is manipulated with fiber holder mounted on a stack of computer-controlled motorized stages (blue in Fig. 3.24). Each fiber is glued into the vee-groove by applying glue with the glue applicator (purple in Fig. 3.24) at a displacement of ~500 μm from the coupler, as shown in Fig. 3.25b. The glue is applied with the computer-controlled “glue bot” whose sets of motor control 5 degrees of freedom of the movement and rotation (all degrees of freedom, except rotation along the axis of the fiber) of clean, cleaved fiber. Johnathan Hood designed and assembled the glue bot. We applied a small drop at the tip of the fiber, and clean the tip with the manual fiber tool until the droplet size (5 nL) is close to the one shown in Fig. 3.25a. This size is optimal such that the glue will not flood the vee-groove, yet enough to seep into the vee-groove to properly secure the fiber. After the fiber is glued into the vee-groove, a larger drop of glue is applied with the manual fiber tool over the mounting block as the red arrows indicate in Fig. 3.25c, to “strain relieve” the fiber so that pulling does not stress the fiber at the coupler. After the strain relieve glue has cured, the robustness of the glued fiber is tested by tugging the fiber lightly. If the bond is adequate, the fiber is cut and removed from the glue bot. The next fiber is spliced into the characterization setup. We glue all the fibers on the “front” side of the chip in order before proceeding to the “back” side of the chip to keep the vee-groove parallel to the glue bot’s fiber holder groove. With these “best practices” we were able to reliably glue a total of sixteen fibers, coupled to eight devices. The number of fibers is only limited by the number of the through holes available on the feedthrough.

After all the fibers are glued and secured, the chip assembly is then attached to an aluminum arm mounted on a CF multiplexer using a groove grabber (Kimball Physics MCF275-GrvGrb-CB03). Fibers are threaded through the multiplexer and the fiber feedthroughs. Teflon feedthroughs have one to four holes with a diameter of 250 µm drilled in them. These Teflon feedthroughs are placed in CF-Swagelok adapter with 1/8 tube diameter. After the threading, the fibers are adjusting to the appropriate length to provide enough slack and to avoid the laser beams in the chamber. The Swagelok are then tightened to one full rotation beyond finger-tight to provide enough compression to hold vacuum. Since the gluing process happens in a different lab from the vacuum chamber. We have built a vessel to transfer the chip assembly from lab to lab, consisting of an acrylic box with a CF flange to which the assembly can be mounted. And the box is purged with nitrogen. After installation, the science chamber is ready for pumping.

### APCW charecterization and tuning

Exposing ACPWs to cesium results in shifting of device spectrum and degradation. Fig. 3.26 shows a processed SEM image of two APCWs after the chip removed from the science chamber. Two SEM images are taken, one of an unused device and one of an APCW that was heavily used in the experiment. The two SEM images are compared and the difference is colored in green. The nature of this cesium corrosion is discussed extensively in Andrew McClung's thesis, and the result is summarized here. The optical properties of metallic cesium can be calculated with the Drude model for metals. Near the D1 line transitions the refractive index of cesium is $n \approx 0.3 < 1$. Any additional layer of material on an APCW will result in a frequency shift. A thin layer of material of $n < 1$ will cause a blueshift; whereas material of $n > 1$ will result in a redshift. The experimentally observed shift is consistently red; we believe the shift is not due to metallic cesium coating. Instead, the redshift is believed to be origin from a dielectric ($n > 1$) coating generated through an unknown surface chemistry process. This cesium corrosion process can be reliably reversed by heating the APCW with strong GM modes. The cesium desorption process involves sending TE guided mode with power ranges from 50 µW to 400 µW from both sides of the APCW. From our experience there seems to be a "threshold" power for the cesium to start desorbing. To find the threshold power,

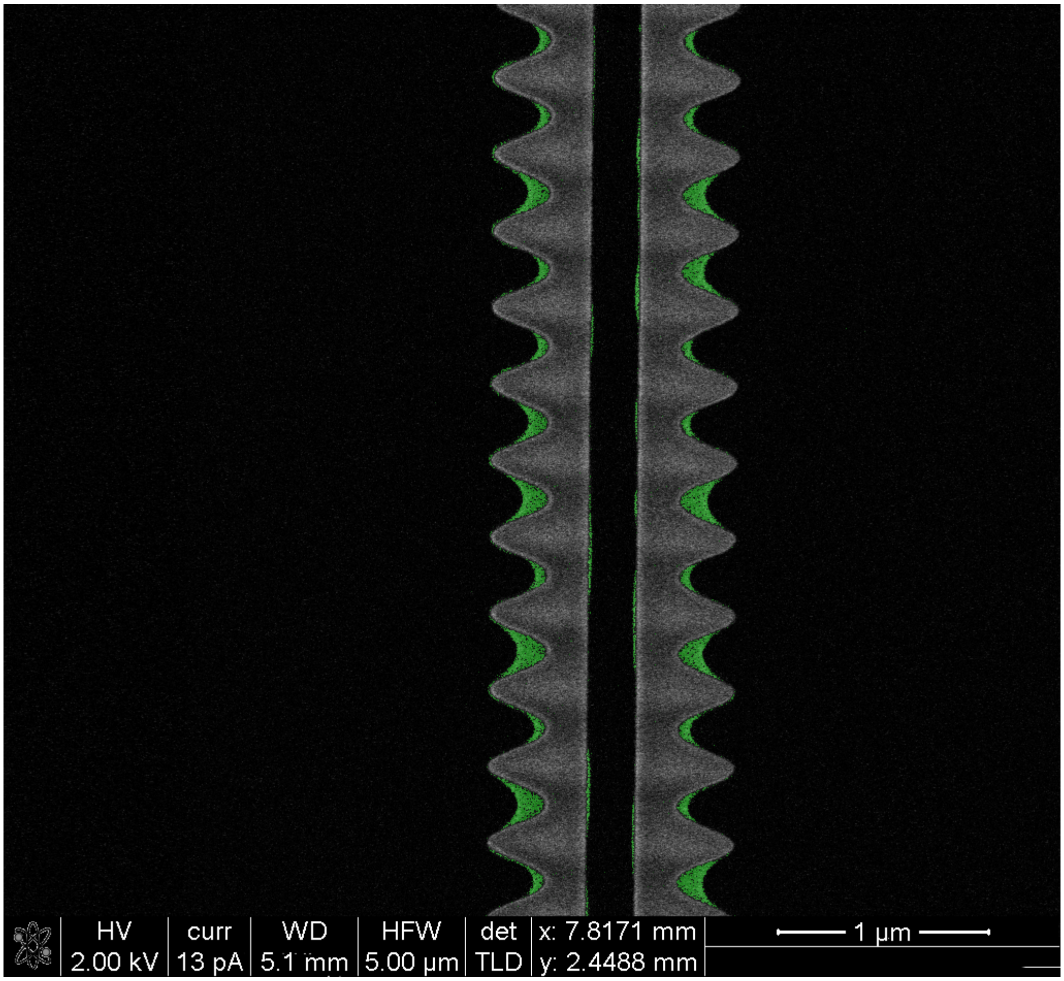

Figure 3.26: Cesium corrosion: Two SEM images, one of an unused device, and the other of a heavily coated device are compared with the difference colored with green. Due to the red-shift cause by this additional material, we do not believe it to be metallic cesium.

we usually start with lower power and heat the device for 5 min and compare the device spectrum, and repeat the process until the threshold power is reached and the device spectrum starts to shift. The desorption process can take up to an hour. We found that the threshold power increases as an APCW went through more desorption processes, and the power handeling of the device decreases. Eventually, the device cannot be shifted back even with GM power as high as ~400 µW from both sides, and usually break during the process. The number of desorption processes a device can withstand varies greatly from device to device, ranging from just two to upwards of 20 times.

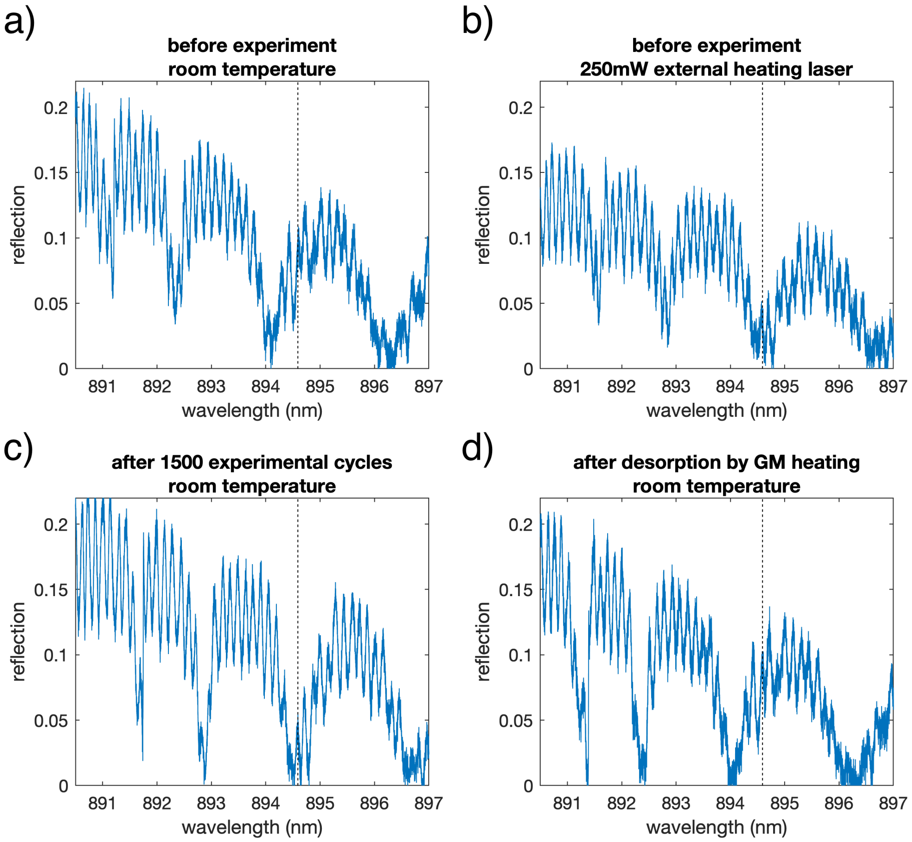

Figure 3.27: APCW tuning process: dashed veritcal line indicate cesium D1 transition. a) APCW spectrum at room temperature taken before experiment. b) Chip heated with a 250 mW external laser, red-shifted the APCW spectrum by 0.5 nm. Cesium D1 transition aligned to the third resonance on the air band. c) After 1500 atom delivery with optical lattice, the device is red-shifted so that the heating beam is not required for the cesium D1 transition to align with the third resonance. d) After the APCW is heated with two conter-propogating TE GM with power ~200 µW each, the spectrum is shifted to its original position.

During an experiment, it is important to maintain a stable device spectrum. For example, in most cases, it is preferable to place the probe in the peak of the transmission spectrum. Also, as discussed in Chapter 2, to cancel the phase slip of the TE GM trap, the TE GM trap frequency should be placed in the dip of the transmission spectrum. Due to the cesium corrosion, the device has to be tuned from time to time. Fig. 3.27 shows a typical experimental tuning process. During this experiment, the cesium D1 probe is aligned to the third resonance on the air band of the APCW. At room temperature the device is blue-shifted by 0.5 nm from alining the third resonance to the cesium D1 line, as shown in Fig. 3.27a. Before the experiment, the device is red-shifted with a 250 mW external heating laser and the cesium D1 line is aligned to the third resonance, as shown in Fig. 3.27b. During the experiment, the APCW spectrum is taken regularly and as the cesium accumulates on the device the heating laser power gradually decreases to compensate for the red-shift caused by the cesium corrosion. In Fig. 3.27c, after 1500 experimental cycle (atom delivery by optical lattice) the APCW spectrum is shifted by 0.5 nm, so that the D1 transition is aligned with the third resonance without heating. Finally, the APCW is heated with two TE GMs each with power of ~200 µW desorb the cesium, and shifted the APCW to its original position, as shown in Fig. 3.27d.

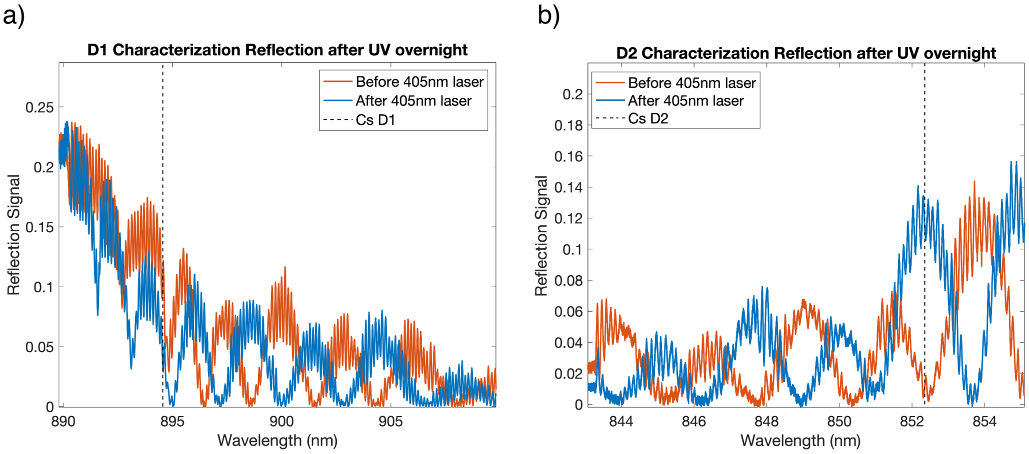

Figure 3.28: Cesium desorption with LIAD: a 404 nm laser shined externally on an APCW overnight, blue-shifted the device by ~2 nm.

Another way that we have explored to desorb cesium atoms is through light-induced atomic desorption (LIAD) [48]. LIAD is a technique to drive the alkali atoms off the walls, which has been used by some cold atom experiments to temporarily increase the partial pressure of alkali to load MOT. In our experiment, a 404 nm laser shines on the APCW overnight. A ~600 MHz blueshift is observed after the LIAD process, as shown in Fig. 3.28. However, the power handling capacity was greatly reduced; the device failed soon afterward with less than 100 µW GM power. Therefore, this technique is not recommended.

### Microwave spectroscopy

During the experiment, the bias coils are set to cancel any residual magnetic field at the lattice position. To set the current of the bias coils, microwave spectroscopy is performed to measure the Zeeman shift due to the residual magnetic field. Once the MOT beams and repumper beams are turned off, and a 1ms depumper pulse pumps all the atoms to $F = 3$. A microwave pulse with carrier wave frequency at the cesium ground state hyperfine splitting coherently transfers the atoms from the $F = 3$ ground state to the $F = 4$ ground state, a $\pi$ pulse transfers all the atoms to $F = 4$. When residual magnetic fields are present, there are several frequencies that the atoms can be transferred for different $m_F$ ground states. As the microwave polarization is not well defined, the transition can happen at all 15 frequencies. The magnitude of these shifts are determined by the $g_F$ coefficient; for $F = 3$, $g_F = -350\,\mathrm{kHz\,G^{-1}}$, and for $F = 4$, $g_F = 350\,\mathrm{kHz\,G^{-1}}$. After the $\pi$ pulse the number of atoms in $F = 4$ is measured by absorption imaging as described in Section 3.2. Fig. 3.29 shows the microwave spectra; the blue trace shows the spectrum with a residual magnetic field, which shows multiple peaks corresponding to transitions between different Zeeman sublevels. By scanning the bias coils' current to cancel the magnetic field, the peaks converge, as shown with the red trace. Once the magnetic field is zeroed to $\pm 10\,\mathrm{mG}$, it can usually remain for a few months.

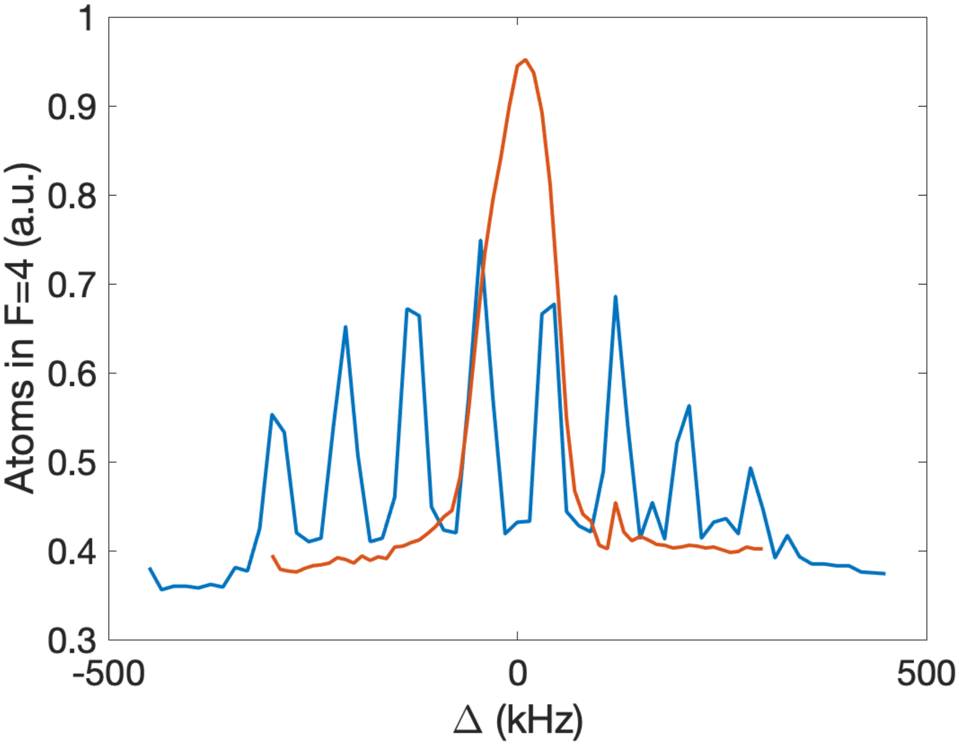

Figure 3.29: Microwave spectroscopy of untrapped atoms at the center of the science chamber. The atoms are prpared in $F = 3$ ground state and are exposed to a $\pi$ microwave pulse. After that the atom number in $F = 4$ ground state is measured. If residual magnetic fields are present, the spectrum broadens. And the Zeeman sublevels are resolved if the field is too big, as shown with the blue trace. The red trace shows the microwave spectroscopy when the residule magnetic field is canceled to ±10 mG.

## *Chapter 4*

# LOADING AND DELIVERY OF ATOMS

Previous experiments with strong coupling of atoms to nanophotonic structures have relied upon tight focusing of far-off-resonance traps (FORTs [46]) to confine a single atom [98, 100] or several atoms [40, 50] 100 to 200nm above nanophotonic cavities and waveguides. To further investigate atomic motion and atom-field interactions near nanophotonic devices, our current approach uses a moving optical lattice that repetitively delivers atoms to the surfaces and central vacuum gap of a nanoscopic APCW. Although each lattice period results in of order one atom entering the central vacuum gap of the APCW, a recursive scheme for transferring atoms from the moving lattice to stationary FORT sites within the APCW (as described in chapter 2) could create a 1D lattice of single atoms with high fractional filling in time ~1 ms (*e.g.*, a sequence of 1800 lattice periods each lasting ~1 μs).

The periodic delivery of atom to the APCW manifest as the clocked spectra, which the photon detected by the SPCM are distributed within the time for adjacent optical lattice pancake to pass the APCW $\tau_{\text{lattice}}$. The clocked spectra contain rich information of the atom motion and atom-light interaction near the APCW [16]. In order to observe the clocked spectrum, various experimental conditions have to be met. The following chapter first explains in detail the optical lattice setup, loading and cooling atoms into the optical lattice, and the experiment requirements essential for observing the clock spectra. Then, the experimental results and the method of processing them will be present.

## 4.1 Loading the Optical Lattice

The schematic of the optical lattice apparatus and the transmission/reflection measurement setup are shown in Fig. 4.1. The optical lattice beams are originated from an M-squared Ti:sapphire laser located in an adjacent room from the Science MOT chamber and is delivered by a 20 m long fiber. The light is then split into two paths with equal power, and each path passes through an acousto-optic modulator (AOM) with a double pass setup which shifts the frequency of both beams up by 80 MHz. Each beam is then launched from a fiber launcher with a 15 mm asphere lens that

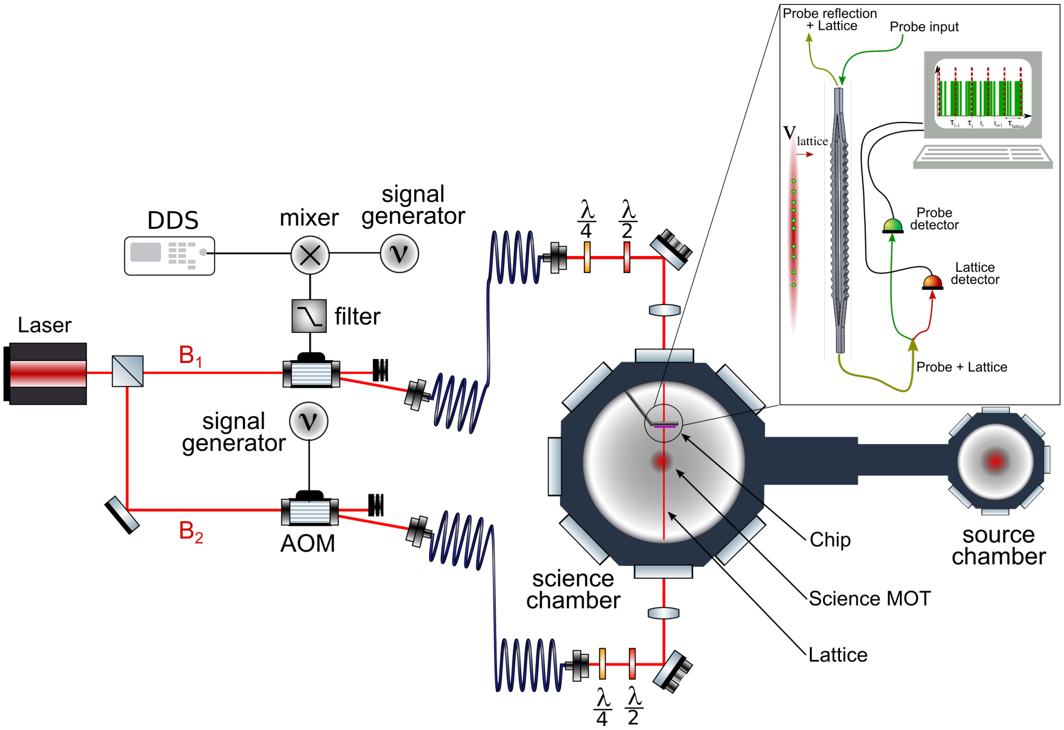

Figure 4.1: Schematic of the optical lattice apparatus. The Science chamber is loaded by pushing a source MOT from the Source chamber through a differential pumping tube to the Science chamber. The 1D optical lattice (conveyor belt) originates from a Ti:Sapph laser and is split sending each beam, $B_1$ and $B_2$, to an acousto-optic modulator (AOM). One of the AOMs receives a frequency chirp sequence from a direct digital synthesizer (DDS) creating a moving optical lattice that conveys the atoms to a particular APCW on a chip with multiple such devices. (Inset) The atoms interact with the waveguide through GMs of the structure, in particular a weak probe tunned around the atomic free-space resonance. The probe light and lattice light are separated by Volume Bragg Gratings (VBGs) and each detected and digitized to create the histograms presented in the manuscript.

collimates the beam to a waist of 1.5 mm. Both beams are then focused with a pair of achromatic doublet lenses with focal length of 30 cm that are both mounted on a pair of 3-axis translational stages position on the opposite sides of the chamber. The two beams are aligned to maximize the coupling into the fiber launcher on the opposite side; coupling efficiency of around 50 % is routinely achieved. The two beams are both focused to a plane about 7 mm away from the chip between the chip and the MOT, which is about 1.7 mm from the science MOT. At the image plane, the beam waist is measured to be 60 µm. During experiments, the power of both beams are adjusted to around 120 mW at the fiber launcher, and the polarizations of both beams, which are set by two pairs of PBS right before the viewports, are perpendicular to the direction of the APCW, i.e the polarization is in $y$ direction. For all experiments with red-detuned optical lattice presented in this thesis, the Ti:Sapph laser is tuned to 853.68 nm and free running without locking to minimize amplitude noise. This detuning is 550 GHz below the Cesium atomic D2 transition, and is selected by scanning finely to avoid the photoassociation effect [66] which can lead to atom loss.

In order to increase the number of atoms delivered to the APCW, it is important to load the optical lattice with high efficiency. The process of loading atoms from the MOT to the optical lattice is similar to the method described in ref. [62]. The first step of loading the optical lattice is to overlap the optical lattice beams with the science MOT spatially, the position of the MOT is controlled by adjusting the current in the science MOT bias (shim) coils. The MOT beams remain on after the optical lattice beams turned on for 40 ms. During this loading time, the repumper power is greatly reduced to ~20 mW, increasing the population of atoms in $F = 3$, in order to reduce the loss rate due to resonant MOT light re-scattering and hyper-fine exchange collisions. At this time the detuning of the $F = 4 \rightarrow F = 5'$ MOT light is also increased, and the bias coil current is dynamically changed to maximize the overlap between the MOT and the optical lattice beams. At the end of this process, which last 50 ms, the quadrupole magnetic field is turned off, and the bias coils are set to cancel the magnetic field generated from transient Eddy currents and any residual magnetic field at the atoms' position, the residual magnetic field is measured with microwave spectroscopy that measures the Zeeman shifts of the Cesium ground states. We are able to load the optical lattice with $\sim 2 \times 10^6$ atoms with a temperature close to the Doppler temperature (145 μK).

Further cooling for the atoms trapped in the optical lattice is performed with the DRSC method [104] as described in section 3.1. The DRSC process cools the atom to its axial vibrational ground state. In order to create the desired Raman coupling, the polarizations of the optical lattice beams are rotated by 15° respective to each other with a liquid crystal wave plate. An $F = 3 \rightarrow F = 2'$ pumping beam with 1 mm waist shines on the atoms from the $y$ direction at low power (1 μW). To create the degeneracy of the Zeeman sublevels between adjacent vibrational levels, as described in section 3.1, a bias magnetic field is also applied in the $y$ direction. This bias magnetic field is scanned while the atoms are held in the trap for ~100 ms and released for time-of-flight measurements. The bias magnetic field is optimized to minimize the atom cloud size and maximize the optical density. The DRSC process only cools the atom in the axial direction of the optical lattice. However, the radial direction is also cooled due to motion mixing between the axial and radial directions. In the experimental sequence the DRSC process last for 35 µs and the atoms are cooled to $T_{\text{axial}} = 12\,\mu\text{K}$ and $T_{\text{radial}} = 30\,\mu\text{K}$.

To summarize, the moving optical lattice loaded with cold atom is prepared by loading a 1D dipole trap from Cesium atoms confined in the science MOT. The dipole trap is formed using two counter-propagating $\text{TEM}_{00}$ laser beams ($B_1, B_2$), each with waist $w_0 \simeq 60\,\mu\text{m}$ at the device and red detuning from the Cs D2 line. The atoms are thus trapped in a series of "pancakes" around intensity maxima along $z$ with spacing at $\lambda_{\text{laser}}/2 = 452\,\text{nm}$. For each experimental trial, $\sim 2 \times 10^6$ atoms are loaded into the free-space lattice, and the spatial extent of the atomic sample spans $\sim$ 1800 pancakes. After the atoms are loaded into the 1D lattice, polarized perpendicular to the waveguide (*i.e.* linearly polarized along $y$), we utilize degenerate Raman sideband cooling (DRSC) to cool the atomic sample to $T \simeq 12\,\mu\text{K}$.

## 4.2 Delivering Atoms to the APCE

After the atoms are loaded and cooled into the optical lattice following the DRSC process, the atoms are ready to be delivered to the APCW. The current Lab 2 setup is capable of delivering atoms with final velocity ranges from $8.5\,\text{cm}\,\text{s}^{-1}$ to $85.2\,\text{cm}\,\text{s}^{-1}$ which correspond to $\nu_{\text{chirp}} = 200\,\text{kHz}$ and $\nu_{\text{chirp}} = 2\,\text{MHz}$ respectively. In all experiments the lattice accelerates from $0\,\text{m}\,\text{s}^{-1}$ to the final velocity in 100 µs, this acceleration is $4.26 \times 10^3\,\text{m}\,\text{s}^{-2}$ for $\nu_{chirp} = 1\,\text{MHz}$ is possible due to the strong axial confinement of the optical lattice and the cold temperature of the atom. The trap depth limits the maximum acceleration of the lattice, for the 120 mW optical lattice beams in the experiment, the maximum acceleration is $a_{\text{max}} = U_0 k/m = 2 \times 10^5\,\text{m}\,\text{s}^{-2}$, which is about 50 times larger than the acceleration used in the experiment. This strong confinement allows us to move the lattice with a simple linear ramp, instead of a more complex chirpping frequency profile to minimize the force acting on the atoms. The lifetime of the atoms in the optical dipole trap is ~200 ms which limits the lowest velocity of the lattice, at the lowest velocity of $\sim 10\,\text{cm}\,\text{s}^{-1}$ it takes ~250 ms for atoms to arrive at the APCW, and the transmission dip is only ~5 % due to the loss of the atom. The highest velocity is limited by the bandwidth of the AOMs and the bandpass filter that filtered the RF signal after the mixing.

The difference between the RF signals that drive two AOMs in the double pass setup determines the speed of the optical lattice conveyor belt. One of the AOM is driven by an $\nu_{\mathrm{RF1}} = 80\,\mathrm{MHz}$ RF signal, while the other AOM is driven by another RF signal with frequency $\nu_{\mathrm{RF2}} = (80 + \frac{\nu_{\mathrm{chirp}}}{2})\mathrm{MHz}$. This RF signal is generated by mixing a 70 MHz RF signal with the output from a direct digital synthesis (DDS) (AD9854) with frequency $(10 + \frac{\nu_{\mathrm{chirp}}}{2})\mathrm{MHz}$ and then filtered by a bandpass filter centered at 80 MHz with 5 MHz bandwidth to remove the additional frequency components generated in the mixing process. The DDS output is in the form of $10 + \frac{\nu_{\mathrm{chirp}}}{2}\mathrm{MHz}$, so the frequency difference between the two beams is $\nu_{\mathrm{chirp}}$, the factor of two comes from the double pass of the AOM. The arbitrary frequency ramp profile $f(t)$ are programmed on an Arduino microprocessor which then writes the profile into the memory of the DDS through an SPI port.

A number of factors limit the lifetime of the atoms in the moving optical lattice. In the following sections losses due to collisional processes, parametric heating, and adiabatic heating will be discussed.

### Collisional Processes

The heating rate from the absorption and spontaneous re-emission processes from a far-detuned dipole trap is $P_{heat} = k_B T_{\mathrm{rec}} \bar{\Gamma}_{\mathrm{sc}}$. Where $T_{\mathrm{rec}}$ is the recoil temperature, for Cesium $T_{\mathrm{rec}} = 198.34\,\mathrm{nK}$. And $\bar{\Gamma}_{\mathrm{sc}}$ is the average scattering rate. For a red far-detuned lattice, the heating rate is [45]:

$$\dot{T}_{\mathrm{red}} = \frac{2/3}{1+\kappa} T_{\mathrm{rec}} \frac{\Gamma}{\hbar|\Delta|} \hat{U} \tag{4.1}$$

where $\Gamma = 2\pi \times 5.22\,\mathrm{MHz}$ is the decay rate of the Cesium D2 line. $\kappa$ is the ratio between potential and kinetic energy, for a 3D harmonic trap $\kappa = 1$. And $\hat{U}$ is the trap depth, which is typically $260\,\mu\mathrm{K}$ for the optical lattice. The heating rate from the spontanious re-emission is then$\dot{T}_{\mathrm{red}} = 21\,\mu\mathrm{K\,s^{-1}}$, which is a small contribution to the heating rate in our experiment.

The largest contribution of the heating is due to collisional processes. The single-particle loss rate from the background gas collision at a pressure of $1 \times 10^{-9}$, the lifetime is ~1 s. When the Cesium atoms are in the $F = 4$ ground state, the lifetime suffers from two-body loss from hyperfine changing collisions, for which an atom acquires velocity of ~5 m s$^{-1}$ when it collides with another atom and changes from $F = 4$ to $F = 3$. A lifetime measurement shows $\tau = 200$ ms lifetime for $F = 3$ ensembles, and $\tau = 80$ ms lifetime for a mixed $F = 3$ and $F = 4$ ensemble. In the experimental sequence the $F = 4 \rightarrow F' = 4$ depumping beam used in the DRSC process is kept on during the lattice transport to keep most atoms in the $F = 3$ ground state.

Another two body loss process is the photoassociation process [66], which for certain dipole trap frequencies, colliding atoms are excited and form bounded molecular states, which then decay and release the kinetic energy. The optical lattice frequency is scanned finely to avoid frequencies that mediate photoassociation effect.

### parametric Heating

One of the methods of measuring the optical lattice trap frequency is utilizing parametric heating. When the trap depth is modulated at the frequency twice the trap frequency, atomic motion can be parametrically driven, thus reducing the lifetime of the trap. In Fig. 4.2, the atoms are delivered to near the chip, and the optical lattice beams are aplitude modulated with 10 %. The measurement shows two resonances, one at 1.3 kHz and the other at 420 kHz. The higher frequency resonance indicates that the axial direction trap frequency is 210 kHz, and the lower frequency resonance shows that the radial trap frequency is 650 Hz. The $\nu_{\text{axial}} = 210$ kHz and $\nu_{\text{radial}} = 650$ Hz agree very well with a 260 μK deep optical lattice, which predicts $\nu_{\text{axial}} = 210$ kHz and $\nu_{\text{radial}} = 670$ Hz.

The reflection of the optical lattice beams from the APCW creates a spatial amplitude modulation. So in the frame of a moving optical lattice pancake, the trap depth is modulated with frequency multiples of the chirp frequency $\nu_{\text{chirp}}$. Therefore, to avoid heating from parametric heating the optical lattice chirp frequency $f_{\text{chirp}}$ should be higher than $\nu_{\text{axial}}$ and $\nu_{\text{radial}}$. Fluctuations in the laser intensity have also been proven to heat atoms in optical dipole traps [90]. For an optical dipole trap with relative intensity spectral density $S_I(\nu)$, the heating rate associated with a trap frequency $\nu_t$ is

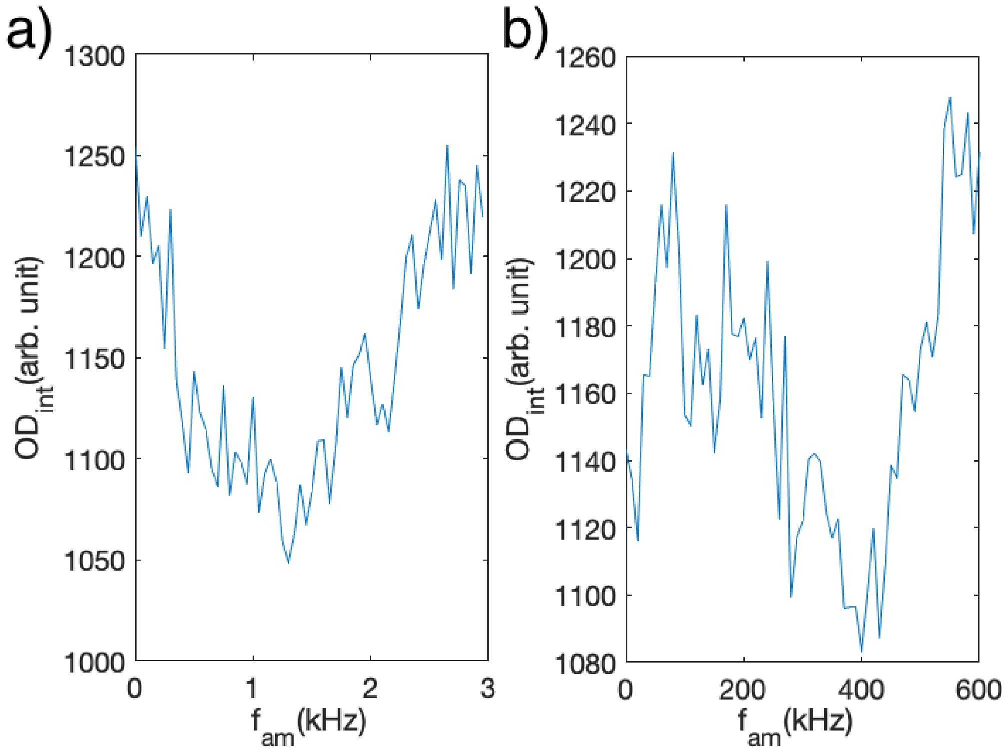

Figure 4.2: The optical lattice beams are amplitude modulated with 10 % after the atoms stop near the chip. The atoms are held for 20 ms, then the sum of the optical density of the camera pixels are calculated as $OD_{\text{int}}$, which act as a proxy for atom number in the trap. a) The resonance at 1.3 kHz indicates a trap frequency at 650 Hz. b) The resonance at 420 kHz indicates a trap frequency at 210 kHz. The 210 kHz is the trap frequency in the axial direction and 650 Hz is the trap frequency in the radial direction.

$\Gamma_I(\nu_t) = \pi^2 \nu_t^2 S_I(2\nu_t)$ [90]. The power spectrum of the Ti:Shapp laser is measured, and except for a peak near 75 kHz, the noise reaches the shot noise limit of the photocurrent. For the trap frequency of 210 kHz, the time constant contributions from the laser amplitude noise is estimated to be 10 s. More detailed analysis of the amplitude and phase noise contributions can be found in Juan Muniz's thesis.

### Adiabatic Heating

If the optical lattice beams are kept at the same power, the beam diameter and the intensity change as the atom move from the MOT to the chip. In a typical experiment with $\nu_{\text{chirp}} \sim 1$ MHz, it takes about 60 ms for the atoms to arrive at the APCW, which is much longer compared to the trap oscillation period, which means the atom transport process is an adiabatic process. For the atoms trapped in the optical lattice, the trap is deforming and deepening along the way, and the atoms temperature changes similar to the compression of gas in a box. This effect has a significant implication for the Lab 2 experiment.

The optical lattice beams are focused 7 mm from the chip, which is closer to the chip than to the MOT. So if the optical lattice beams powers are constant, the atoms will be hotter then the initial temperature when they arrive at the APCW.

From the adiabatic theorem, we can show that the ratio between the trap frequency and the temperature stays constant during an adiabatic process, namely

$$\begin{aligned} \frac{\nu_{\text{axial}}}{T_{\text{axial}}} &= \text{const} \\ \frac{\nu_{\text{radial}}}{T_{\text{radial}}} &= \text{const} \end{aligned} \tag{4.2}$$

Using the simulation method described in Chapter 5, a simulation of atoms being transport for 3.5 cm is shown in Fig. 4.3. The simulation is done using a scalar Gaussian beam potential without the device present. Few thousands atoms are initialized into a pancake 2.5 cm away from the focus and is thermalized to $T = 30\,\mu\text{K}$. The chirp frequency is set to $\nu_{\text{chirp}} = 1\,\text{MHz}$, so that the velocity is $0.43\,\text{m}\,\text{s}^{-1}$. At the focus the axial and radial temperature are $T_{\text{axial}} = 90\,\mu\text{K}$ and $T_{\text{radial}} = 210\,\mu\text{K}$ respectively, in agreement with eq. 4.2.

In order to ameliorate the adiabatic heating effect, in the experiment sequence, the optical lattice beams power are ramped down as the atoms approach the focus point. One way to measure the effectiveness of this approach is the so-called “torture test”. In a torture test sequence the chirp frequency $\nu_{\text{chirp}}$ switches between positive and negative with a ramping time of 100 µs in between, to move the atoms 2.5 cm from the science MOT through the focus point and then bring the atoms back to the MOT position repeatedly. Every time the atoms return to their initial position an absorption image is taken to measure the OD. By maximizing the OD after the torture tests, we show that by keeping the trap as flat as possible, the transport is more efficient and keeps the atoms colder.

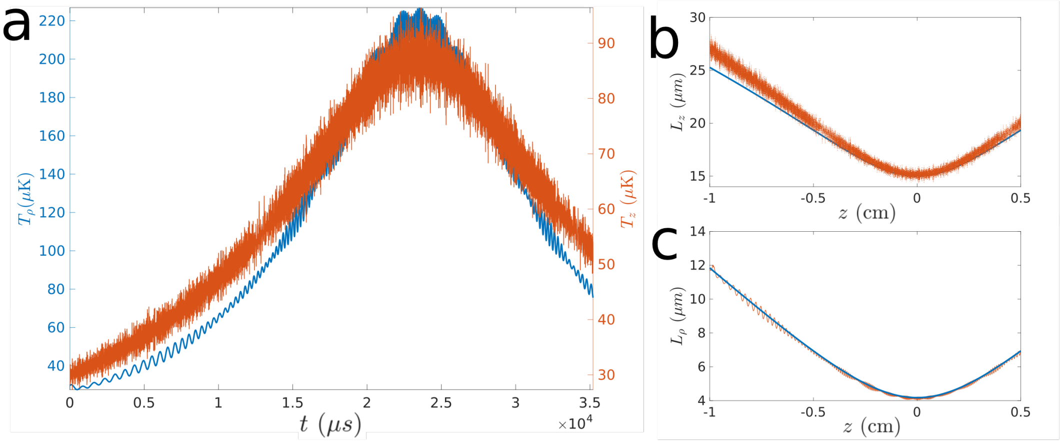

Figure 4.3: Numerical simulation of a long lattice transport. In (a) the momentum distribution is used to determine the temperature along axial and radial directions at a given time. The red trace temperature in the axial direction, while the blue trace is the temperature in the radial direction. In (b) and (c) the width of the position distribution is plotted as the cloud moves for the radial and axial directions. The blue traces show the model's prediction for the radial and axial sizes.

### Clocked Lattice Signal

By measuring the scattered lattice light from the transmission fiber using a Hamamatsu APD (C10508-01), and sending the analog signal to a zero-crossing detector circuit based on the AD790JN comparator, a digital signal with frequency $\nu_{\text{chirp}}$ can be obtained. Since the atoms are loaded and cooled in the optical lattice and transported to the APCW, with the pancakes also passing through the device also with frequency $\nu_{\text{chirp}}$, periodic dips in the transmission signal spacing $\tau_{\text{lattice}}$ in time are expected.

However, observe a probe transmission signal with frequency of $\nu_{\text{chirp}}$ was more difficult than we expected. It turned out that the precise alignment of the optical lattice beams to the APCW is extremely critical. The roughness on the device due to fabrication imperfections scatters light, and are distributed everywhere on the device as shown in ref. [39]. The granular natural and the uneven distribution of the perfection and the ability to AC coupled and amplify the leaked lattice light APD signal, allow us to measure the phase dependent signal from the leaked lattice light. However, if the wavefront of the optical lattice is not aligned perfectly with the APCW, even if it is only one wavelength difference in both ends of the device, that is a $\frac{852\,\text{nm}}{370\,\text{nm}\times 130} = 1.01°$, the atoms will arrive completely out of phase along the APCW. To align the optical lattice wavefront to the APCW, we first translate the front optical lattice beams to the margin of the chip where the surface is flat and make sure the reflected beam counter-propagates with the input optical lattice beam, and then translate the beam to the device with the 3-axis translational stage. The rear optical lattice beam is then aligned by maximizing the coupling into the front optical lattice beam launcher. After carefully aligned the optical lattice beam to the chip with this method, we were able to observe the periodic (*i.e.* “clocked”) modulation of the probe transmission signal.

## 4.3 Experiment Sequence

The time diagram of time-dependent laser beams and control signals in the experiment sequence are summarized in Fig. 4.4. A single experiment sequence last 550 ms. After the sequence, the voltages, beam intensities and frequencies are held for 1 to 2 second, for replenishing the MOT. And the sequence is repeated to deliver the next batch of atoms. The experiment sequence can be separated into five segments: loading MOT, loading lattice, DRSC, lattice delivery, and end experiment. In the “loading MOT” section in Fig. 4.4, the MOT bias field control voltages change slowly to move the atoms from MOT position to align with the optical lattice. In the “loading lattice” and "DRSC" sections the optical lattice is turned on, and the optical lattice is loaded using the method described in section 4.1, note the rapid changes in MOT bias field control voltage and science MOT cooling beam power and detuning around $t = 150\,\mathrm{ms}$, which is optimized to maximize the atom loading efficiency. In the “lattice delivery” section, the $F = 4 \to F = 4'$ depumping beam is kept on after the “DRSC” section to keep most of the atoms in the $F = 3$ ground state to increase the lifetime, as described in section 4.2. Also, as mentioned in section :adiabatic, to maintain the same trap depth during delivery, the lattice beams power decrease as the atoms approach the APCW. A “stop and go” experiment is performed in this example, as the lattice chirp frequency $\nu_{\mathrm{chirp}}$ drop to 0 MHz for 10 ms and then reaccelerates the atoms to $1.1\,\mathrm{cm\,s^{-1}}$ ($\nu_{\mathrm{chrip}} = 1.2\,\mathrm{MHz}$) again. At the end of the sequence, all the control voltages and laser beam configuration are returned to their initial states, and the MOT starts reloading for the next experimental cycle.

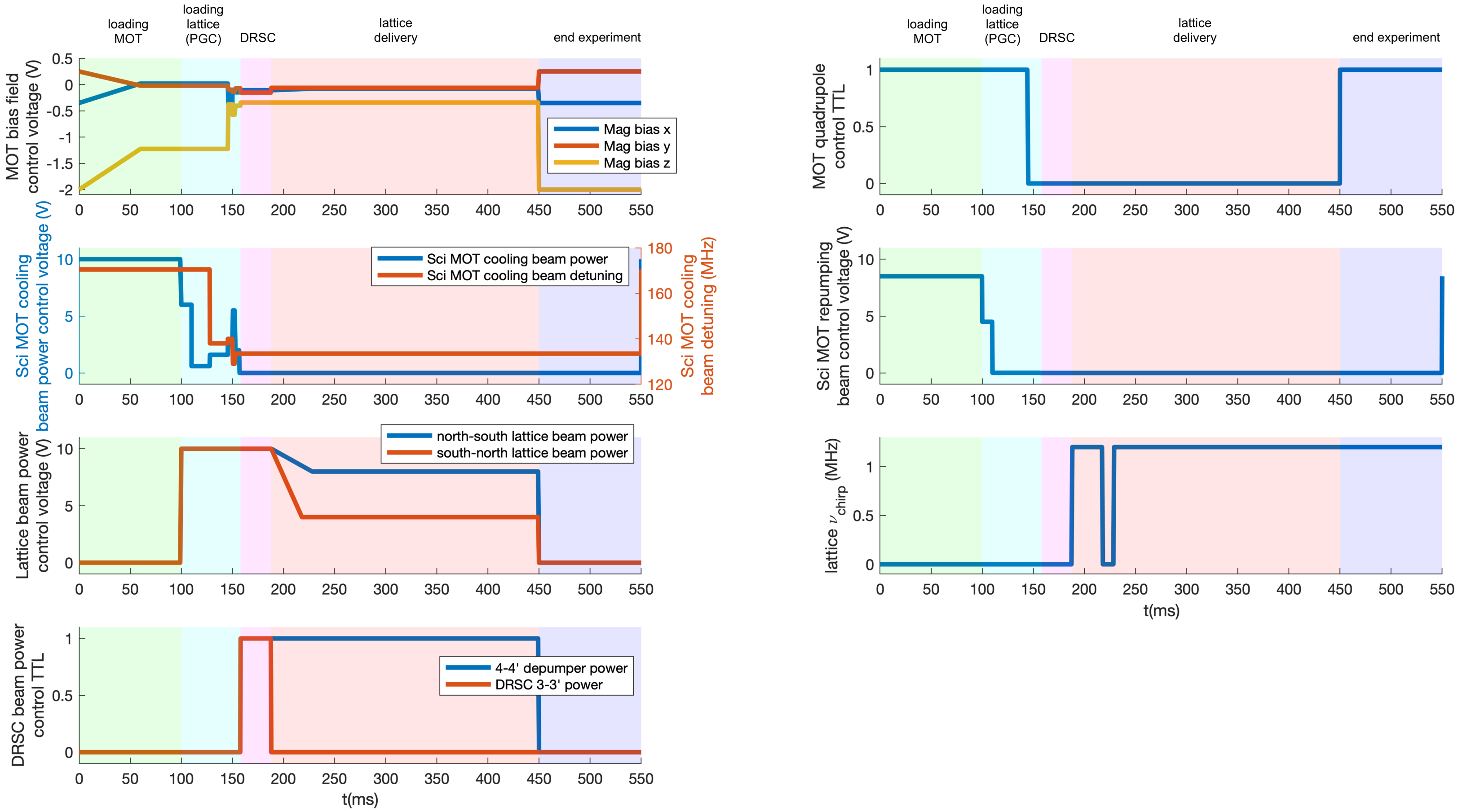

Figure 4.4: A time diagram for the time dependent signals for a "stop and go" lattice delivery experiment sequence. The sequence is separated into 5 sections, in the "MOT loading", the MOT is moved to alignt with the optical lattice. The optical lattice is loaded in the "loading lattice" and "DRSC" sections. The loaded atoms are delivered to the APCW in the "lattice delivery" section. The final section "end experiment" is reserved for resetting the experiment configuration.

## 4.4 Experiment Results

### Measurement Settings

In most experiments, the atomic interaction with the APCW is probed using a 10 to 100pW weak probe of frequency $\omega_{\text{probe}}$ input to either a TE or TM GM of the waveguide. The input probe is tuned near the Cs D1 line transition ($6S_{1/2}F = 3 \rightarrow 6P_{1/2}F = 4$), because it has the strongest relative hyperfine transition strength factors $S_{F=3,F'=4} = \frac{3}{4}$ [93]. As described in Chapter 3, the probe goes through several VBGs that separate and combine various beams. The probe and guided mode trap beams are combined and delivered to the APCW through an optical fiber. On the other (output) side of the APCW, a similar VBG setup separate the output probe and the optical lattice beam and send them to their respective detectors. A simplified diagram is shown in Fig. 4.5. In qualitative terms, atoms located within 100 – 200 nm from the surfaces of the APCW result in additional absorption and dispersion for a probe field transmitted at $\omega_{\text{probe}}$ relative to the device with no atoms. By recording transmission spectra obtained by scanning $\omega_{\text{probe}}$ around the free-space Cs D1 ($6^2S_{1/2} \rightarrow 6^2P_{1/2}$) $F = 3 \rightarrow F' = 4$ transition at frequency $\omega_{\text{a}}$, we obtain quantitative information related to light shifts of transition frequencies and modified decay rates that atoms experience in transiting near the structure [50]. A more precise understanding of atomic trajectories on scales $\lesssim$ 50 nm and $\lesssim$ 100 ns can be gained by utilizing the periodic arrival of atoms by the moving optical lattice supplemented by auxiliary, far-from resonance GM fields that strongly perturb internal atomic states and thus atomic motion. More comparison of experimental and simulation with various guided mode will be discussed in Chapter 6.

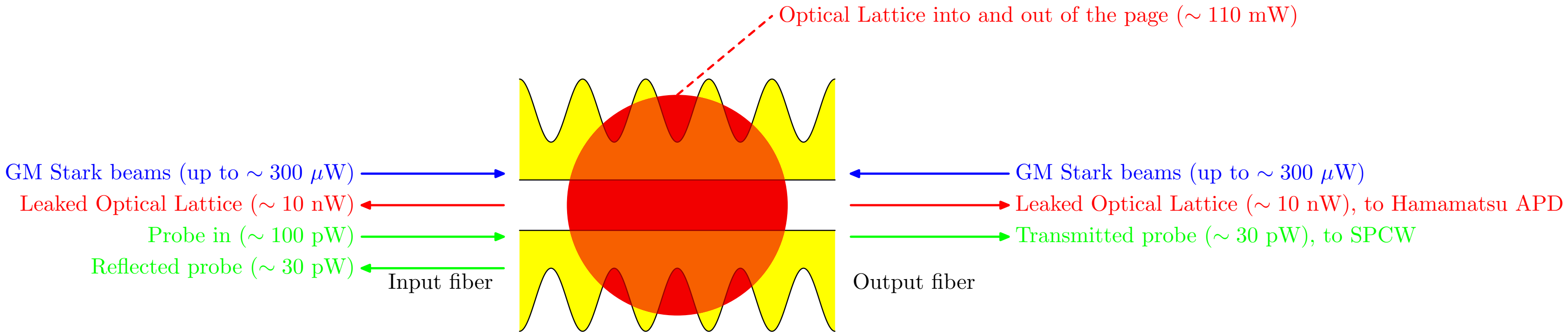

Figure 4.5: Optical beams involved in clocked atoms delivery measurement and their respective power. The probe and the GM stark beams are combined and send to the APCW trough the “input fiber”. The “output fiber” carrys the output probe and the leaked optical lattice light to a bread board with the VBG setup, which separates the probe and optical lattice light and send them to their respective detectors.

### Stop-and-go

In order to evaluate the effectiveness of the atoms loading and delivery process, and also remove atoms that are not being trapped in the optical lattice, we utilize an experiment sequence that we called "stop-and-go". In a "stop-and-go" sequence, the atoms are transported from the science MOT and stop at 1 mm away from the device. After that, the lattice stops for 10 ms before reaccelerating and delivery the atoms through the device. The untrapped atoms continue flying when the trapped atoms stop, which can be seen in fig. 4.6a. A common tool to study the signal is the time-detuning plot, such as Fig. 4.6a and Fig. 4.6b. The normalized transmission $T(\omega_p)/T_0(\omega_p)$ is plotted in a two-dimensional plot for which the horizontal axis is the time and the vertical axis is the probe detuning $\Delta_p$. $T_0(\omega_p)$ is the transmission for a probe at frequency $\omega_p$ when no atom is around the device. In earlier experiments, the untrapped atoms can contribute up to 20 % of the signal. In the latter experiments, the loading and cooling are greatly improved, using the "torture test" technique to optimized parameters. As shown in fig. 4.6b no untrapped atoms are visible when the optical lattice stopped.

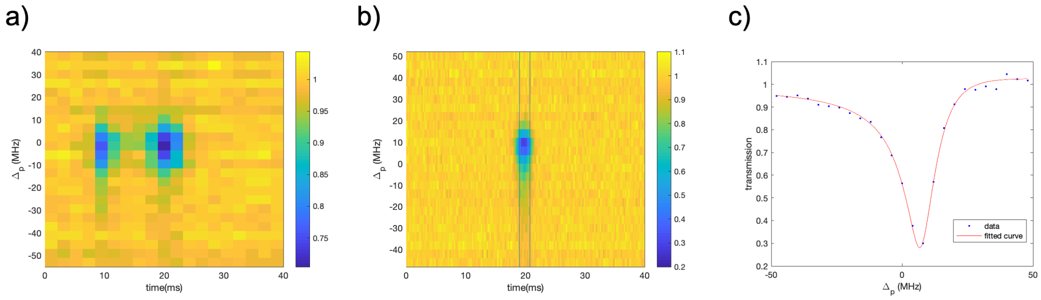

Figure 4.6: a) Transmission spectrum for stop-and-go experimental sequence, the absorption due to untrapped atoms at ~10 ms are atoms that are not trapped in the optical lattice continue moving through the APCW after the optical lattice is stopped. The absorption at ~20 ms is from atoms trapped in the optical lattice. b) After optimizing the cooling of atoms in the the optical lattice, the absorption at ~10 ms is gone. c) The fit parameters extracted for the spectra by combining 3 ms from 18 ms to 21 ms (between the black lines in (b)) and fitting to a transmission model given in Ref. ([50]). The fitting values are the AC stark shift caused by the optical lattice $\Delta_{\mathrm{AC}} = 6.9\,\mathrm{MHz}$, the effective coherent coupling term $J_{\mathrm{1D}}^{\mathrm{eff}} = -2.1\,\mathrm{MHz}$, $\Gamma_{\mathrm{1D}}^{\mathrm{eff}} = 13.9\,\mathrm{MHz}$ and $\Gamma' = 5.6\,\mathrm{MHz}$

We fit the measured spectra to a transmission model of the probe field through the PCW that was developed in [3, 50], which is expressed as follows:

$$T(\Delta_p, t) = \left| \frac{\Delta_p + i\Gamma'/2}{(\Delta_p + J_{\mathrm{1D}}^{\mathrm{eff}}(t)) + i(\Gamma' + \Gamma_{\mathrm{1D}}^{\mathrm{eff}}(t))/2} \right|^2 . \tag{4.3}$$

Here $\Delta_p = \omega_{\mathrm{probe}} - \omega_a$ is the detuning between the probe frequency and the free-space atomic resonance frequency, $\Gamma'$ is the atomic decay rate into all modes (mostly free-space) other than the GM of interest, and $\Gamma_{\mathrm{1D}}^{\mathrm{eff}}(t)$ and $J_{\mathrm{1D}}^{\mathrm{eff}}(t)$ are the emission rate into the waveguide and the atom-atom coupling rate for the GM of interest, respectively. The time dependence of $\Gamma_{\mathrm{1D}}^{\mathrm{eff}}$ and $J_{\mathrm{1D}}^{\mathrm{eff}}$ arises from the periodic arrival and transit of the atoms. For the ideal case of a single lattice ‘pancake’ with atomic and probe frequencies near the band edges of the APCW, we would find that

$$\Gamma_{\mathrm{1D}}^{\mathrm{eff}}(t) = \sum_{i=1}^{N_{\mathrm{at}}} \Gamma_{\mathrm{1D}}^{ii}\left(r_i(t)\right), \tag{4.4}$$

where $N_{\mathrm{at}}$ is the number of atoms within a single pancake and $r_i$ is the position of the $i^{\mathrm{th}}$ atom.

However, in our experiment, it is difficult to disentangle the number of atoms interacting with the waveguide and the spatial variation of $\Gamma_{\mathrm{1D}}$ for different atoms and trajectories. Hence, we introduce $\Gamma_{\mathrm{1D}}^{\mathrm{eff}}$ as an effective atomic coupling to the waveguide, and likewise for the term $J_{\mathrm{1D}}^{\mathrm{eff}}$, which was found to be quantitatively adequate for the analyses in [50]. In microscopic terms, $J_{\mathrm{1D}}^{ij}$ and $\Gamma_{\mathrm{1D}}^{ij}$ relate to the real and imaginary components of the Green’s function for radiative interactions between atoms $(i, j)$, mediated by the GM of interest of the APCW.

In Fig. 4.6c an average spectrum between 19 to 20.5 ms is fitted to Eq. 4.3, The fitting values are the AC stark shift cause by the optical lattice $\Delta_{\mathrm{AC}} = 6.9$ MHz which is consistant with the AC stark shift cause by the 80 mW lattice beams, the effective coherent coupling term $J_{\mathrm{1D}}^{\mathrm{eff}} = -2.1$ MHz, $\Gamma_{\mathrm{1D}}^{\mathrm{eff}} = 13.9$ MHz and $\Gamma' = 5.6$ MHz.

### Clocked Spectrum

By utilizing the lattice delivery method illustrated in Fig 4.7(ai-aii), atoms arrive to the APCW trapped in a sequence of pancakes, with the repetition frequency of arrivals given by $f_{\text{chirp}}$ and periodicity $\tau_{\text{lattice}} = 1/f_{\text{chirp}}$. During the passage of any one pancake, a small fraction ($\sim 10^{-8}$) of the lattice power is scattered by device imperfections into GMs of the APCW and propagates to both ends, where it is efficiently coupled into optical fibers and then separated from the probe fields using volume Bragg gratings (VBGs) [38]. The leaked lattice light (with a power of $\sim$5 nW) is detected by an avalanche photodiode (APD), with the resulting current observed with high signal-to-noise and contrast (*i.e.*, oscillating from near zero to a sequence of maxima with contrast $\simeq 0.7$ and period $\tau_{\text{lattice}}$ to provide a 'fringe signal'). The photocurrent is directly digitized and recorded with an FPGA, as well as processed in real-time using a threshold detector that converts the fringe signal to a single time marker for each pancake, which we call the lattice synchronous markers, defined as $\tau_i$ (*i.e.*, the red dashed lines in Fig. 4.7b at time $i \times \tau_{\text{lattice}}$ for the $i^{\text{th}}$ pancake). These synchronous markers provide a consistent clock to register time stamps of each (separately) detected probe photon transmitted by the APCW (*i.e.*, green bins in Fig. 4.7b) with the movement of the lattice through the structure. The random nature of the device imperfections on both the top and bottom can alter the timing of the lattice scattering into the APCW relative to the atom arrival. Fig. 4.8 shows the intensity scattered by various parts of the APCW plot against the phase of the opticall lattice, the random distribution of the imperfection on the APCW generates a random combination from these components, resulting a distinct phases phase from device to device. While this introduces a level of uncertainty, it manifests as a global phase offset which is consistent for all measurements on a single device, but can vary between different waveguides. To compare the clocked spectra measured with different GM intensity to simulation, as will be described in detail in Chapter 6, the clocked spectrum with no GM are shifted to align with the simulation and this phase offset is applied uniformly for the subsequent measurement.

The transmitted probe counts, recorded on a single photon counting module (SPCM) and digitized, from the passage of each lattice pancake can then be offset in time by lattice number (*i.e.*, for pancake $i$, $t_{\text{i,clock}} = t_i - \tau_i$, where $\tau_i = i \times \tau_{\text{lattice}}$) and summed over all pancakes $\{i\}$ to produce a 'clocked' record as illustrated schematically in Fig. 4.7c, where $t$ refers to the clocked time for a sequence of $N_p$ pancakes passing near the APCW. Histograms built from the time differences between the lattice time stamps and the probe time stamps reveal microscopic information about atom motion near the APCW. For example, Fig 4.7d displays a measured histogram that clearly evidences the phase-sensitive nature of the atom arrival for a single probe detuning matching the free-space Cs D1 transition $F = 3 \rightarrow F' = 4$. In Fig. 4.7 and throughout the thesis, the probe transmission with atoms is normalized to the transmission through the waveguide when no atoms are present. The use of the Cs D1 transition for probing instead of the D2 cycling transition is to avoid the tensor shifts of the D2 excited states that arise from the lattice detuning from the D2 line. For lattice period $\tau_{\mathrm{lattice}} = 833$ns, minimum transmission (*i.e.*, maximum loss) is observed around the clocked time $t \simeq 450$ns, corresponding to increased atom number near the APCW as in Fig. 4.7ai. By contrast, maximum transmission (and minimum loss) is evident near $t = 0, 833$ns as in Fig. 4.7aii with lattice antinodes (and hence atom number for a red detuned FORT) located away from the device.

To gain greater insight into atomic motion and internal state shifts for atoms near the APCW (*e.g.*, AC Stark shifts and resulting forces), we create two-dimensional clocked spectra by combining measurements as in Fig 4.7d for a sequence of probe detunings, $\Delta_{\mathrm{p}} = \omega_{\mathrm{probe}} - \omega_{\mathrm{a}}$. For each value of $\Delta_{\mathrm{p}}$, time bins of recorded probe counts over the lattice period with atoms present are normalized to the probe counts at the same detuning but absent atoms in the lattice. Fig. 4.7e provides an example of a measured two-dimensional clocked spectra for a weak TM probe beam. For each detuning $\Delta_{\mathrm{p}}$ of the probe beam, typically 5 to 10 trials of the experiment are combined, with each trial consisting of 1800 lattice pancakes and repeated every 2 s.

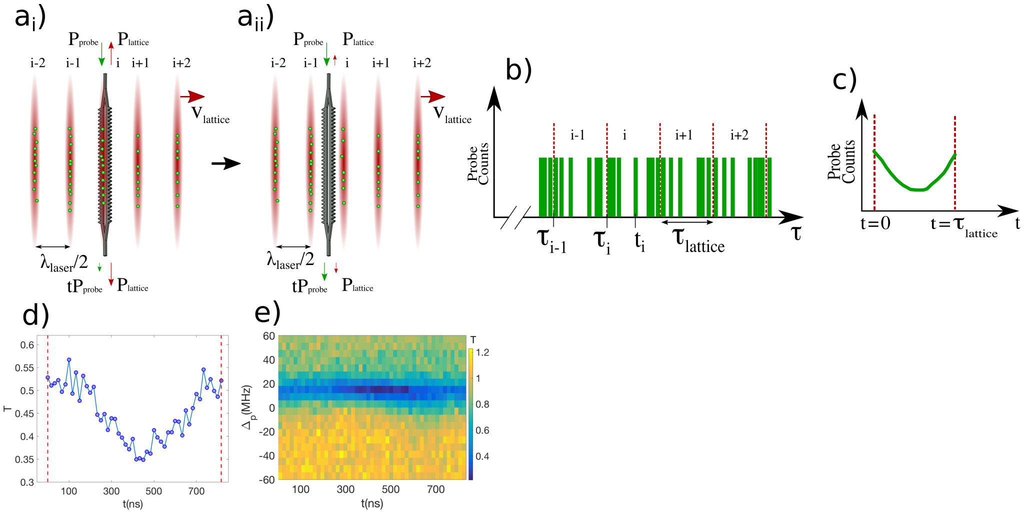

Figure 4.7: This figure details the concept of the clocked atom delivery and how the data is analyzed to recover a phase sensitive atomic signal. ai) Atoms trapped in pancakes by the 1D lattice are delivered to the structure when a chirp sequence is placed on one of the lattice beams creating a conveyor belt. aii) A half period later the ‘pancakes’ have moved $\lambda_{\text{laser}}/4$ relative to the APCW. b) Probe photon counts placed on the same time axis as the lattice sync signal. By building a histogram from probe time stamps ($t_i$) between successive lattice sync time stamps ($\tau_i$, $\tau_{i-1}\ldots$) we can recover the phase sensitive nature of the atom delivery. c) All the individual lattice time periods are folded together into a single histogram indicating that the atomic signature is phased with the lattice signature. d) For a single probe detuning we can observe this clear phase sensitive signal when the probe photon time stamps are referenced to the closest preceding time stamps of the lattice. e) By scanning the probe detuning we can create this 2D image in lattice time $t$ and probe detuning $\Delta_{\text{p}}$ to gain more insight into the arrival time of different classes of atoms and extract spectra for various arrival times. This information helps to determine the coupling of the atoms to the waveguide and can reveal time dependent AC-Stark shifts.

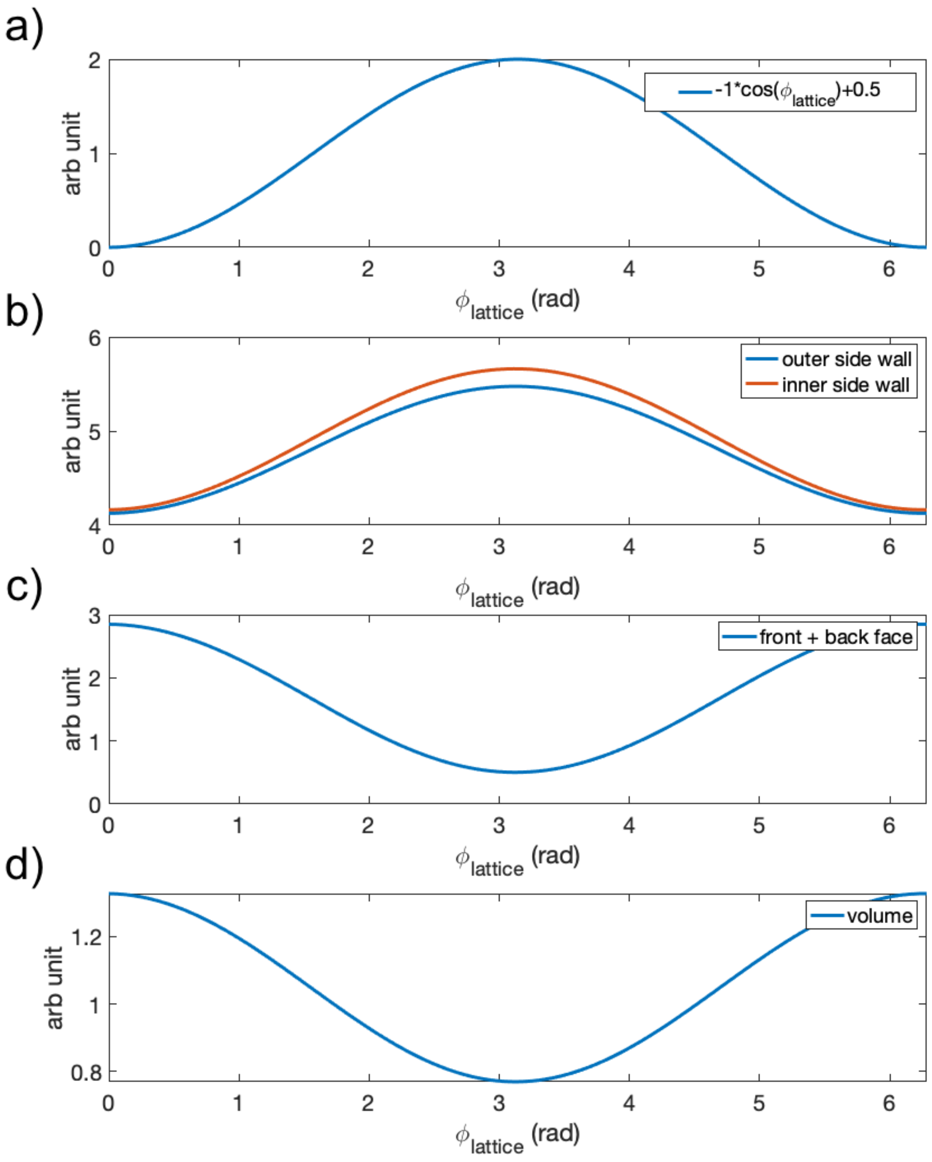

Figure 4.8: Numerical calculation of the phase of optical lattice light scattered by various parts of the APCW. a) The light intensity at the ceter gap of the APCW plot against the optical lattice phase $\phi_{\text{lattice}}$. b) The scattered light from the outer and inner wall of the APCW, calculated by integrating the intensity 10 nm within the APCW surface. c) The scattered light from the front and back sides of the APCW, calculated by integrating the intensity 10 nm within the APCW surface. d) The scattered ligh from the whole APCW, calculated by integrating the intensity over the whole APCW volume.

*Chapter 5*

# ATOMIC TRAJECTORIES SIMULATION

Numerical simulations of atom motion in a moving optical lattice and through the near fields of the APCW can be utilized to understand the nanoscopic dynamics of atoms near the APCW. Together with a model based upon optical transfer matrices for atoms located near the APCW, theoretical simulations for clocked transmission spectra can be generated for comparison to experiment. The comparison of the experimental results and the simulations will be explored in detail in chapter 6. Such comparisons can also aid the design and operational validation of GM optical traps and test techniques for loading small volume ($(\Delta x, \Delta y, \Delta z) = (30, 100, 140)$nm) GM traps in short times ($\sim$1 µs) numerically.

In the Lab 2 experiments the several fields interact with the atoms, including lattice, guided modes, cooling beams and Casimir Polder potentials are approximately separable in time and space $\vec{E}_{\text{total}}(\vec{r}, t) \approx \sum_i \vec{E}_{i,r}(\vec{r}) \times T_i(t)$. The trajectory simulation program is designed to calculate atom trajectories in potentials created by a sum of separable fields in both 2D and 3D. The internal working of the simulation is optimized to increase performance to enable faster exploration of the parameter space for various aspects of APCW experiments. For example, we explore how different GM and probe configurations effect the clocked spectrum, examine how different time-dependent lattice power profiles affect the atom temperature, experiment with time-dependent GM trap depth . . . etc. The simulation program also features a field tree data structure that is designed to minimized the memory usage, a portion of the simulation region can be at higher resolution compared with the rest of the simulation region, so it is possible to simulate atomic trajectories in mm$^2$ size regions while also calculate the atom dynamic around the APCW, which required nm$^2$ resolution.

In this chapter, I describe the simulation process and the usage of the trajectory simulation program, the consideration and the design of the simulation algorithm and then present the results of the simulations.

Certainly, the agreement between simulation and measurement can be considerably improved by extending the simulations to more faithfully capture the complexity of the APCW, including 3D full APCW device and the internal states of the atoms, and implementing more accurate calculations of CP potentials for all surfaces of the APCW as in Ref. [52], which is nontrivial. Such improvements could enable more advanced measurements to be undertaken, such as quantitative validations of CP potentials in the spirit of Refs. [10, 26].

## 5.1 Simulation Process

The functionality of the simulation program includs calculating the atomic trajectories with given initial condition and time-dependent optical potential, outputting the movies of the potential and the trajectories, calculating the APCW transmission and reflection spectra.

The overview of the simulation process is summarized in the flowchart in Fig. 5.1. First, the fields and potentials stored in HDF5 format are read in and initialized in the field tree data structure, which optimized for memory usage, as explained in section 5.3. Then, the initial condition of the atoms are distributed in the optical potential according to Boltzmann distribution for a specific radial and axial temperature or read in from previous simulation output. 2D or 3D atom trajectories are calculated by solving the equations of motion of atoms in optical dipole force and Casimir-Polder potentials. For the case of a 2D simulation with a TE probe, the best place to place the simulation domain is the brightest part of the probe, for a D1 TE probe that is the $yz$ plan that cut the thickest part of the APCW and for a D2 TE probe the thinnest part. For a 3D simulation, and the guided mode at the $X$ point, the probe intensity profile is aligned with the dielectric structure, a simulation domain contains a single unit cell the $x$ direction, and periodic boundary applies for atoms across the $x$ direction boundary. However, if the guided mode is not at the $X$ point, the guided mode intensity profile is not aligned with the dielectric structure, then a whole device simulation is required, which is very memory intensive. When simulated a 2 µm by 2 µm in the $yz$ plane simulation domain our workstation with 256GB memory can perform simulation on 30 unit cells, which is still not enough to simulate the full device.

In order to calculate the APCW transmission/reflection spectrum, the atom trajectories are sampled and if the simulation is in 2D, distributed along the $x$ direction with the probability distribution $P(x)$, depending on the probe intensity profile (*i.e.*, TE or TM mode). For a TE probe, the probe intensity varies as $\sin^2(\frac{\pi x}{a})$, where $a$ is the length of a unit cell. The intensity of the probe weights the coupling of the probe GM to the atoms. So atom trajectories are also distributed along the $x$ direction with probability $P(x) = \sin^2(\frac{\pi x}{a})$. For the TM probe, the probe power is uniform along the $x$ direction, so the atom trajectories are also distributed uniformly. After distributing the atoms' trajectories, the APCW transmission spectra can be calculated with the transfer matrix model by representing 'distributed' atom $i$ at position $(x_i(t), y_i(t), z_i(t))$ and the waveguide segment between atoms with approximate transfer matrices, the details of the transfer matrix model are presented in section 5.4.

### Usage

The code of the simulation program can be found on `https://github.com/lucasp0927/trajectory_julia`.

The trajectory simulation program can be run with the following command.

```
user@localhost:~\$ julia trajectory.jl -C [config file] -I [input files
↪  prefix] -O [output files prefix] [-TMS]
```

The three main functionalities of the trajectory simulation program are to simulate trajectories, generate trajectories movies and calculate transmission spectra for a photonic crystal waveguide. These corresponding to the T, M, and S options respectively. The I and O options for input and output files required when needed.

The coordinate convention of the trajectory simulation program is different from the APCW coordinate convention. With the APCW coordinate convention, the APCW is along the $x$ direction, the $y$ direction cuts across the gap and the $z$ direction is parallel to the optical lattice beam. With the simulation coordinate convention, the $x$ and $z$ directions are swapped, so the APCW is along the $z$ direction and optical lattice parallel to the $x$ direction.

With the `-T` or `-trajectory` option the simulation program generates trajectories either with atom initial positions and velocities read in from another trajectory file specified in the configuration file, or initialized with temperature and regions specified in the configuration files. The simulation program will store the calculated trajecotries in files with the `output files prefix`. For example with the `output files prefix` as `output_file_`, the output file names are `output_file_i.h5`, where *i* is the job number specified in the `job-config` section in the configuration file.

With the `-M` or `-movie` option the simulation program generates movies of the trajectories and the time-dependent potential in `.mp4` format with the time range, time step, spatial range and resolution specified in the configuration files. With the `-T` or `-trajectory` option enabled, the program generates the movies using trajectories calculated; otherwise the program reads trajectories from files with the `input files prefix`. For example, with `input files prefix` being `input_file_`, the program will generate movies for `input_file_i.h5` sequentially, where *i* is the job number specified in the `job-config` section in the configuration file. The program stores the movies in files with `output files prefix`. For example with `output files prefix` as `output_file_`, the output file names are `output_file_traj_i.mp4`, where *i* is the job number specified in the `job-config` sectoin in the configuration file.

With the `-S` or `-spectrum` option the simulation program generates the transmission spectra for a photonic crystal waveguide structure. For a 2D simulation, the waveguide is extended out of the simulation domain, and for a 3D simulation, the waveguide is along the third ($z$) dimension. The relevant parameter for spectrum calculation, such as the probe profile, $\Gamma_{1D}$, $\Gamma'$, waist size of the optical lattice beam, atom number for a single experiment, iteration number for averaging, frequency range and time range are specified in the configuration file. For a 2D simulation, additional parameters such as the contrast of the probe, the distribution of the atoms within a unit cell is required for extrapolating the trajectories along the photonic crystal waveguide dimension. With the `-T` or `-trajectory` option enabled, the program generats the spectrum using trajectories calculated, otherwise the program reads trajectories from files with the `input files prefix`. The program stores the spectra in files with `output files prefix`. For example with `output files prefix` as `output_file_`, the output file names are `output_file_i_spectrum_data_gm.h5`, where *i* is the job number and `gm` is the name of the probe profile specified in the `job-config` section in the configuration file. The clocked spectrum can be obtained by processing the spectrum data as discussed in chapter 4.

The configuration file is segmented into five sections. Refer to section 5.3 for the definition and explanation of the `Field` data types:

1. `simulation-type:` Indicates the dimension of the simulation, can be either `2D` or `3D`.
2. `material-config:` Contains a `ScalarFieldNode` for indicating the dielectric structure. Positions with dielectric shoud have value larger than one and positions with vacumm should have value zero.
3. `field-config:` Multiple `ScalarFieldNode`s for optical potentials that generate AC Stark shift for generating trajectories, movies and spectra can be included in this section. Each `ScalarFieldNode` are aligned individually, interpolated to the resolution of the field with the highest resolution in the node, to conserve memory usage. For example, fields requiring high resolution such as Casimir Polder potential should be separated in an individual `ScalarFieldNode`. The unit of the value sampled from the root field node should be in Kelvin.
4. `trajsolver-config:` Options for the trajectory solver. Including simulation parameters, ODE solver parameters, periodic conditions, boundary conditions, atom initialization configuration and time range for saving.
5. `job-config:` Scaning field amplitude, and options for analyzing the trajectories, for movies and spectra generation. To simulate trajectories, generate trajectories movie and calculate transmission spectrum, the scaling of the field or FieldNode specified in the `jobs` section will be replaced with the `scaling` expression in the `jobs` section, with `@i` subtitute with *i* from `range_i_start` to `range_i_end` with step `range_i_step`.

Source Code 5.1 shows an example of the configuration file with comment for a 3D simulation. All time units are in μs and lengh units are in nm.

Source Code 5.1: 3D simulation configuration YAML file.

```
#All time unit in us.
#All length unit in nm.
#
#3D simulation
#210kHz lattice trap frequency
```

```
#with blue TM stark beam guided mode
#with Casimir Polder Potential
#
#initial atom position read from previous simulation output
simulation-type: 3D
#atom removed when hitting material
material-config:
    material:
        field-type: ScalarFieldNode
        dim: 3
        fields:
            apcw:
                field-type: ScalarField
                D-type: Float
                dim: 3
                init-type: file
                filename: /home/lucaspeng/data/potential/3D/material_big.h5
                variable: mat
                pos: [8150, 23150 ,-40]
                size: [3690, 3690, 450]
                scaling: "t->1.0"
        scaling: "t->1.0"
fields-config:
    casimir-polder:
        field-type: ScalarFieldNode
        dim: 3
        fields:
            casimir-polder-ground-state:
                field-type: ScalarFieldNode
                dim: 3
                fields:
                    casimir-polder1:
                        field-type: ScalarField
                        D-type: Float
                        dim: 3
                        init-type: file
                        filename:
                        ↪  /home/lucaspeng/data/potential/3D/6s1_2cp.h5
                        variable: cp_down
                        pos: [9400.0,23940.0, -8.0]
                        size: [1200, 1430, 386]
                        scaling: "t->1.0"
                    casimir-polder2:
```

```
                    field-type: ScalarField
                    D-type: Float
                    dim: 3
                    init-type: file
                    filename:
                    ↪  /home/lucaspeng/data/potential/3D/6s1_2cp.h5
                    variable: cp_up
                    pos: [9400.0,24630.0, -8.0]
                    size: [1200, 1430, 386]
                    scaling: "t->1.0"
            scaling: "t->1.0"
        casimir-polder-excited-state:
            field-type: ScalarFieldNode
            dim: 3
            fields:
                casimir-polder1:
                    field-type: ScalarField
                    D-type: Float
                    dim: 3
                    init-type: file
                    filename:
                    ↪  /home/lucaspeng/data/potential/3D/6p1_2cp.h5
                    variable: cp_down
                    pos: [9400.0,23940.0,-8.0]
                    size: [1200, 1430, 386]
                    scaling: "t->1.0"
                casimir-polder2:
                    field-type: ScalarField
                    D-type: Float
                    dim: 3
                    init-type: file
                    filename:
                    ↪  /home/lucaspeng/data/potential/3D/6p1_2cp.h5
                    variable: cp_up
                    pos: [9400.0,24630.0,-8.0]
                    size: [1200, 1430, 386]
                    scaling: "t->1.0"
            scaling: "t->-0.0"
field:
    field-type: ScalarFieldNode
    dim: 3
    fields:
        lattice-beam:
```

```
                field-type: VectorFieldNode
                dim: 3
                fields:
                    right-beam:
                        field-type: VectorField
                        D-type: Complex
                        dim: 3
                        init-type: file
                        filename:
                        ↪   /home/lucaspeng/data/potential/3D/lumerical_field_small.h5
                        variable: field_right
                        pos: [0.0, 15000.0, -40]
                        size: [20000, 20000, 450]
                        scaling: "t->1.0+0.0im"
                    left-beam:
                        field-type: VectorField
                        D-type: Complex
                        dim: 3
                        init-type: file
                        filename:
                        ↪   /home/lucaspeng/data/potential/3D/lumerical_field_small.h5
                        variable: field_left
                        pos: [0.0, 15000.0, -40]
                        size: [20000, 20000, 450]
                        scaling: "t->exp(im*(-2*pi*1.2*t))"
                scaling: "t->-0.0001008184" #210k
            guided-mode:
                field-type: ScalarFieldNode
                dim: 3
                fields:
                    tmd2:
                        field-type: ScalarField
                        D-type: Float
                        dim: 3
                        init-type: file
                        filename:
                        ↪   /home/lucaspeng/data/potential/3D/tmd2_3d_k01.h5
                        variable: Eabs2
                        pos: [8150, 23150, -40]
                        size: [3690, 3690, 450]
                        scaling: "t->2.0"
                scaling: "t->1.0"
        scaling: "t->1.0"
```

```
trajsolver-config:
    simulation-config:
        traj_num: 100000
        tstart: 97.0
        tend: 125.0
        tdiv: 0.01
    solver-config:
        solver: ADAMS
        reltol: 1e-10
        abstol: 1e-7
    periodic-condition:
        dim: 3
        start: 0
        end: 370
    boundary-condition:
        xmin: 8500.0
        xmax: 20000.0
        ymin: 20000.0
        ymax: 30000.0
        zmin: -10.0
        zmax: 380.0
    atom-config:
        init-type: from-file
        filename: /home/lucaspeng/data/lucas/result/init_result/init.h5
        time: 97.0
        radial-temperature: 450e-6 #irrelavent when reading initial
        ↪   condition from a file
        axial-temperature: 450e-6 #irrelavent when reading initial
        ↪   condition from a file
        init-speed: -340.8 #irrelavent when reading initial condition from
        ↪   a file
        init-range: #initialize atoms in pancake [x1 x2 y1 y2], irrelavent
        ↪   when reading initial condition from a file
            pancake1: [68776.0, 69226.0, 100.0, 49900.0]
            pancake2: [68350.0, 68810.0, 100.0, 49900.0]
            pancake3: [67924.0, 68384.0, 100.0, 49900.0]
            pancake4: [67495.0, 67958.0, 100.0, 49900.0]
            pancake5: [67069.0, 67532.0, 100.0, 49900.0]
    in-boundary: #for 2D simulation only
        beam1: [9890.0, 10110.0, 10110.0, 9890.0,
                24380.0, 24380.0, 24910.0, 24910.0]
        beam2: [9890.0, 10110.0, 10110.0, 9890.0,
                25090.0, 25090.0, 25620.0, 25620.0]
```

```
    out-boundary: #for 2D simulation only
        edge: [100.0, 69900.0, 69900.0, 100.0,
               100.0, 100.0,   49900.0, 49900.0]
    save-range:
        tstart: 98.0
        tend: 124.0
job-config:
    #scan guided-mode scaling from 1 to 16 in step of 1
    type: single-scan-scaling
    range_i_start: 1
    range_i_step: 1
    range_i_end: 16
    plot-range: [25,1250]
    jobs:
        job1:
            field: guided-mode
            scaling: "t->(@i-1.0)*1.0"
    filter: #filter trajectories, options: none, gap, sides, other.
        type: none
        tstart: 101.0
        tend: 124.0
        roi: [9000.0, 11000.0, 11000.0, 9000.0, 26000.0, 26000.0, 24000.0,
        ↪   24000.0]
        gap: [9900.0, 10100.0, 10100.0, 9900.0, 24900.0, 24900.0, 25100.0,
        ↪   25100.0]
        side1: [9900.0, 10100.0, 10100.0, 9900.0, 25610.0, 25610.0,
        ↪   40000.0, 40000.0]
        side2: [9900.0, 10100.0, 10100.0, 9900.0, 10000.0, 10000.0,
        ↪   24390.0, 24390.0]
    movie-output:
        tstart: 98.0
        tend: 123.0
        tdiv: 0.02
        #tstart: 111.25
        #tend: 112.85
        #tdiv: 0.01
        range: [9000.0, 11000.0, 24000.0, 26000.0, 0.0,370.0]
        res: [10.0,10.0,10.0]
    probe:
        field:
            field-type: ScalarFieldNode
            dim: 3
            fields:
```

```
            ted1:
                field-type: ScalarFieldNode
                dim: 3
                fields:
                    ted1:
                        field-type: ScalarField
                        D-type: Float
                        dim: 3
                        init-type: file
                        filename: /home/lucaspeng/data/potential/3D/ted1_3d_k10.h5
                        variable: Eabs2
                        pos: [8150, 23150, -40]
                        size: [3690, 3690, 450]
                        scaling: "t->2000.0"
                scaling: "t->1.0"
            tmd2:
                field-type: ScalarFieldNode
                dim: 3
                fields:
                    tmd2:
                        field-type: ScalarField
                        D-type: Float
                        dim: 3
                        init-type: file
                        filename: /home/lucaspeng/data/potential/3D/tmd2_3d_k01.h5
                        variable: Eabs2
                        pos: [8150, 23150, -40]
                        size: [3690, 3690, 450]
                        scaling: "t->2500.0"
                scaling: "t->1.0"
        scaling: "t->1.0"
spectrum:
    name: ["ted1","tmd2"]
    mode: 1 #for 2D simulation only
    vector-shift: 1
    gamma-1d: 1.0
    gamma-prime: 5
    lattice-width: 32000 #in nm
    lattice-unit: 370 #for 2D simulation only
    atom-beam-waist: 30000 #in nm
    pos-variance: 0.05 #for 2D simulation only
```

```
        k-ratio: 1.0 #k = Xpoint_k * k-ratio
        use-all-atom: true #overwrite total-atom-number when true
        total-atom-number: 100000
        avg-atom-number: 2000
        iteration: 20
        frequency: #in MHz
            start: -46
            end: 50
            step: 2.0
        time: #in us
            start: 110.36
            end: 117.0275
            step: 0.020825
```

In appendix, Source Code A.1 shows a configuration file for a 2D simulation.

## 5.2 Julia Programming Language

The simulation program is written in Julia programming language. In this section I list the reasons for choosing the language instead of a more traditional programming language such as C/C++, python . . . , etc.

The Julia programming language [11] is a relatively young programming language designed for high-performance numerical analysis and computing, which has several unique designs. First, common languages that are used for high-performance numerical calculations like FORTRAN and C/C++ are usually compiled ahead of time, where the executed code is tuned to the specific task and the hardware it is running on, which achieve fast calculation. By contrast a scripting language that is easy to develop such as Python and MATLAB is interpreted, with interpreter reading and executing the code, which is usually much slower compared to compiled code. Julia code runs after compilation, like C/C++ and Fortran which make it fast, however unlike C/C++ and Fortran, which are compiled ahead of time, Julia is compiled during runtime or “just in time” (JIT). So the language looks more like an interpreted language.

Because compilers can only build machine code for specific data types, most compiled languages are statically typed so that the programmer has to declare the type of every variable, which makes the code more troublesome to develop. In contrast, in a dynamically typed language like Python, any variable can be any type at any given time, which makes developing easier but much harder to create specialized machine code ahead of time. Julia circumvents the problem by only compiling a piece of code (*e.g.*, a function) when needed, and the JIT compiler compiles a specialized version of the code for its associated types and caches it. If the same piece of code is called with different types, the JIT compiler recompiles it for the different types and caches the new machine code in another location. Subsequent runs use the appropriate specialized machine code without the need to recompile.

Another interesting design is the type hierarchy system and meta programming capability that make Julia a great language for constructing abstract data types, which allows great flexibility and code reusability. Two powerful features of Julia are hierarchical data types and multiple-dispatch. Data elements can have different underlying representations, which are called types. For example, numeric values can be represented in different ways, such as integer, floating point number, rational number . . . . Each representation can also vary by the amount of memory it uses. For example, an `Int8` integer occupies 8 bits space, and a `Float64` floating point number occupies 64 bits. In Julia, all types are organized in a tree structure hierarchy. At the tree's root, there is a special type `Any`, and all other types reside under it directly or indirectly. Fig. 5.2 shows the data type hierarchy for the `Number` data type; the arrow in Fig. 5.2 points from a type to its subtype. The leaves (types with no subtype) are called concrete types, which have underlying data implementations and are allowed to have instances. The nodes in the type tree that are not concrete types (leaves) are abstract types which cannot have corresponding instances, but programmers can write code that generalizes for any of its subtypes. In short, the data hierarchy system allows a subtype to inherit the behaviors of its supertype.

As a simple example, suppose we write a function `plus_one` that expects a variable $n$ of type `Number` and return $n + 1$:

```julia
function plus_one(n::Number)
   return n+1
end
```

The function will work correctly regardless of $n$'s concrete type. Therefore, with the datatype hierarchy, a type can inherit the behaviors of its supertypes, this functionality is called multiple-dispatch. Also, the JIT (just in time) compiler will compile a different version of `plus_one` for the respective data type of $n$ during runtime, which generates specialized machine code for each data type of $n$, which ensure high performance despite being a dynamical type language.

### 5.3 Field Tree Data Structure

A trajectory simulation of the Lab 2 experiment involves various fields and potentials of different sizes and feature sizes. To properly simulate the thermalization from the delivery of atoms from the science MOT to the APCW, atoms are distributed 70 µm away from the APCW, where the diffraction pattern from the APCW is weak. This sets the size of the simulation domain required for the optical lattice beams. For a 2D simulation, The size of the simulation domain of the optical lattice light field is on the order of $\sim$100 µm × $\sim$100 µm and the resolution is $\sim$10 µm × $\sim$10 µm. For the guided modes the size of the simulation domain is ~4 µm × ~4 µm and the resolution ~5 nm×~5 nm. And, for the Casimir-Polder potential, although the range is short ~2 µm×~2 µm; however, due to the steep change of the potential a really fine resolution is needed $\sim$1 nm×$\sim$1 nm. Therefore the simulation program has to incorporate fields calculated from different sources with various size and resolution easily.

Since the atoms are trapped in the moving optical lattice, the solution is highly oscillatory. In order to obtain a numerically accurate solution, fine time step is required. Due to the fine time step, the potential is frequently interpolated, which is a time-consuming operation. To reduce the number of interpolation calculation, several ideas are considered.

A simple method is to prepare a 3D (4D) array of the time-dependent potential for a series of times for a 2D (3D) simulation, and do a 3D (4D) interpolation when the potential is sampled. This method works well for small simulation domains with a smaller size of potential data. However, for a simulation of a large system like for optical lattice and APCW, it is impossible to fit this array into a reasonable amount of memory. So an algorithm that can quickly interpolate the potential at any given time and space is required. For this purpose, the simulation program utilizes Julia's type hierarchy system to build a field tree data structure. With the tree data structure, a small array can be sampled from the potential quickly, and the interpolation calculation is required only once to provide values for the ODE solver. Fig. 5.3 illustrates the data type hierarchy. At the root of the data type hierarchy, there is a `Field` root node. There are four concrete data type `ScalarField`, `VectorField`, `ScalarFieldNode` and `VectorFieldNode`. Where `ScalarField` and `ScalarFieldNode` are subtypes of `AbstractScalarField`, and `VectorField` and `VectorFieldNode` are subtypes of `AbstractVectorField`. And finally, `ScalarFieldNode` and `VectorFieldNode` are subtypes of abstract type `FieldNode`. These types are used to construct a tree data structure as the one illustrates in Fig. 5.5. Each node in the field tree data structure is represented by one of the concrete types in the field data type hierarchy. The leaves of the field tree have to be either of type `ScalarField` or `VectorField`, which contain the information to describe the field, including:

- The dimension of the simulation, *e.g.* 2D or 3D.
- The position and the size of the field.
- The resolution of the field.
- An array that stores the field $\vec{E}_r(\vec{r})$, for example a vector field for a 2D simulation will have the dimention $3 \times n \times m$. And a Sacalar field for a 3D simulation will have the dimension of $l * n * m$.
- A scaling function $f(t)$, which describes how the field scales with time, that $E(\vec{r}, t) = E_r(\vec{r}) \times f(t)$.

The `ScalarFieldNode` and `VectorFieldNode` are for parent nodes in the field tree data structure, a `ScalarFieldNode` can only have types that belong to the `AbstractScalarField` (`ScalarField` and ScalarFieldNode) as its child. And a `VectorFieldNode` can has types belong to both `AbstractScalarField` and `AbstractVectorField` (all four concrete type in the Field data type hierarchy). The parent nodes contain the follwoing information:

- The children of the node.
- The dimension of the simulation

- A scaling function $f(t)$

The field data structure makes it easy to incorporate output from various sources, such as Comsol, Lumerical, MPB, MEEP, and MATLAB regardless of the simulation domain and resolution. Before the atom trajectory simulation started, the field tree data structure has to be "aligned". The alignment process calculates the optimal size and resolution for all the fields in the tree data structure so that all points on the grid aligned together, as illustrated in Fig. 5.4. And the information is updated accordingly, as shown in Fig. 5.6 which is the tree in Fig. 5.5 after alignment. The default is to align with the resolution of the field with the finest resolution in the tree. Due to memory constraint, often not all the fields can be interpolated to the finest resolution, for example, a 3D simulation with optical lattice and Casimir-Polder potential. In this case, it is possible to create multiple field tree data structure, one for Casimir-Polder and the other for the rest of the fields. The two field trees are interpolated separately, and the results added together.

After the alignment process, the data structure is ready for interpolation. The field tree data structure is traversed in pre-order fashion to extract a small array ($4 \times 4$ for cubic interpolation) around the point of interest. For the `VectorField` or `VectorFieldNode` under a `ScalarFieldNode` parent node, the absolute value is calculated. After traversing field tree data structure, the small array is interpolated. The multiple dispatch design of Julia makes developing algorithms operating on the field tree data structure flexible and fast.

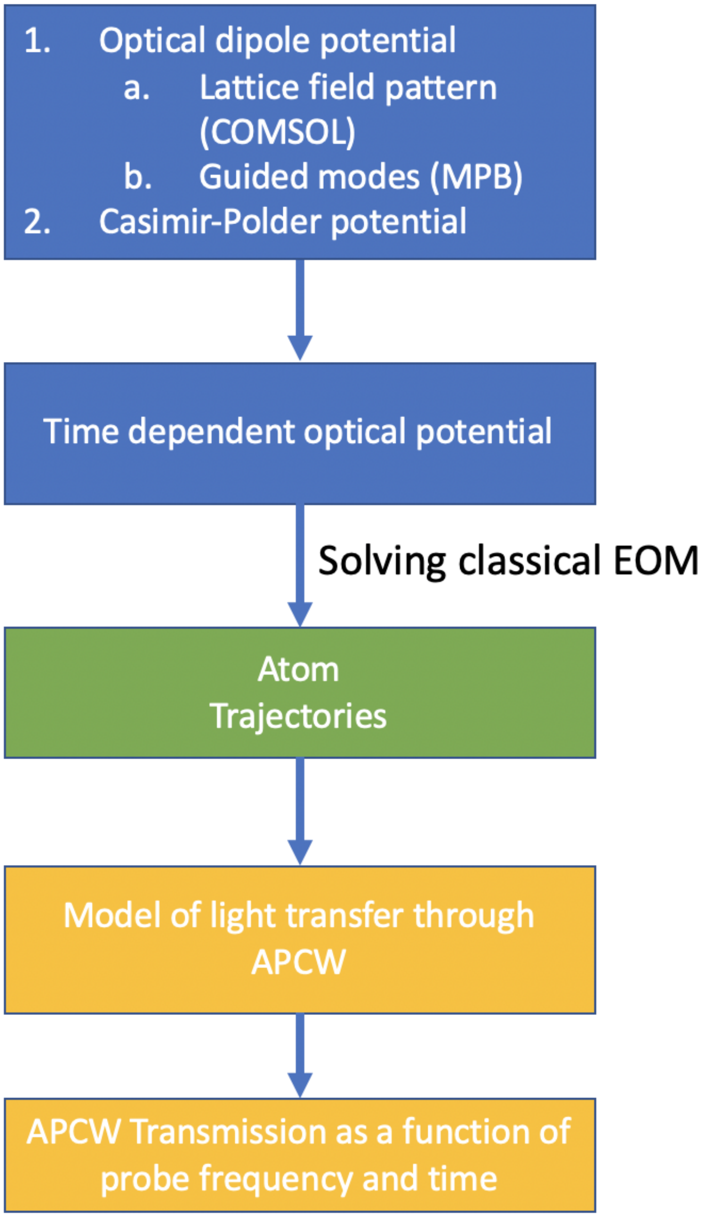

Figure 5.1: The flowchart of the numerical simulation. First, the optical dipole potentials and the Casimir-Polder potential are calculated and combined to form the total time-dependent potential. Then, atoms are initialized into the optical potential far (70 μm) from the APCW and the equations of motion solved to generate the atom trajectories. The transmission $T(\Delta_p, t)$ as a function of probe detuning and time is then calculated with the transfer matrix model.

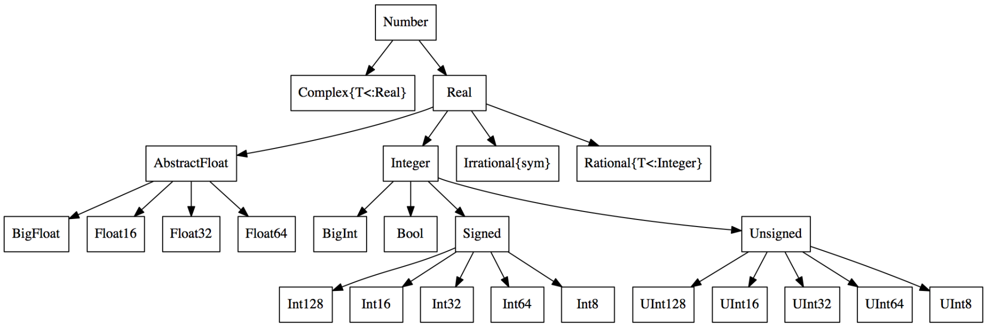

Figure 5.2: A good example of Julia's type hierarchy is the Number abstract types. Arrows point from a supertype to its subtype. The leaves are concrete type, which are allowed to have representive instances. All types that are not leaves are abstract types. A subtype inherit its supertypes' behaviors through mutiple dispatch. Image from: `https://en.wikibooks.org/wiki/Introducing\_Julia/Types`

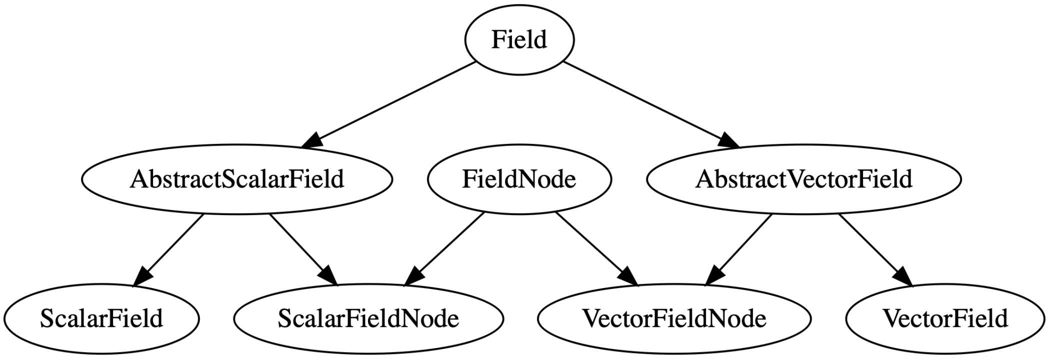

Figure 5.3: Field data type hierarchy: `ScalarField` and `ScalarFieldNode` are data type represent scalar fields which are both belong to the `AbstractScalarField` supertype. `VectorField` and `VectorFieldNode` are data type that represent vector fields and are both belong to the `AbstractVectorField` supertype. In the field tree data structure as shown in Fig. 5.5 and Fig. 5.6 `ScalarField` and `VectorField` can only be the leaves, while the `ScalarFieldNode` and `VectorFieldNode` are the parent nodes which both belong to the `FieldNode` supertype.

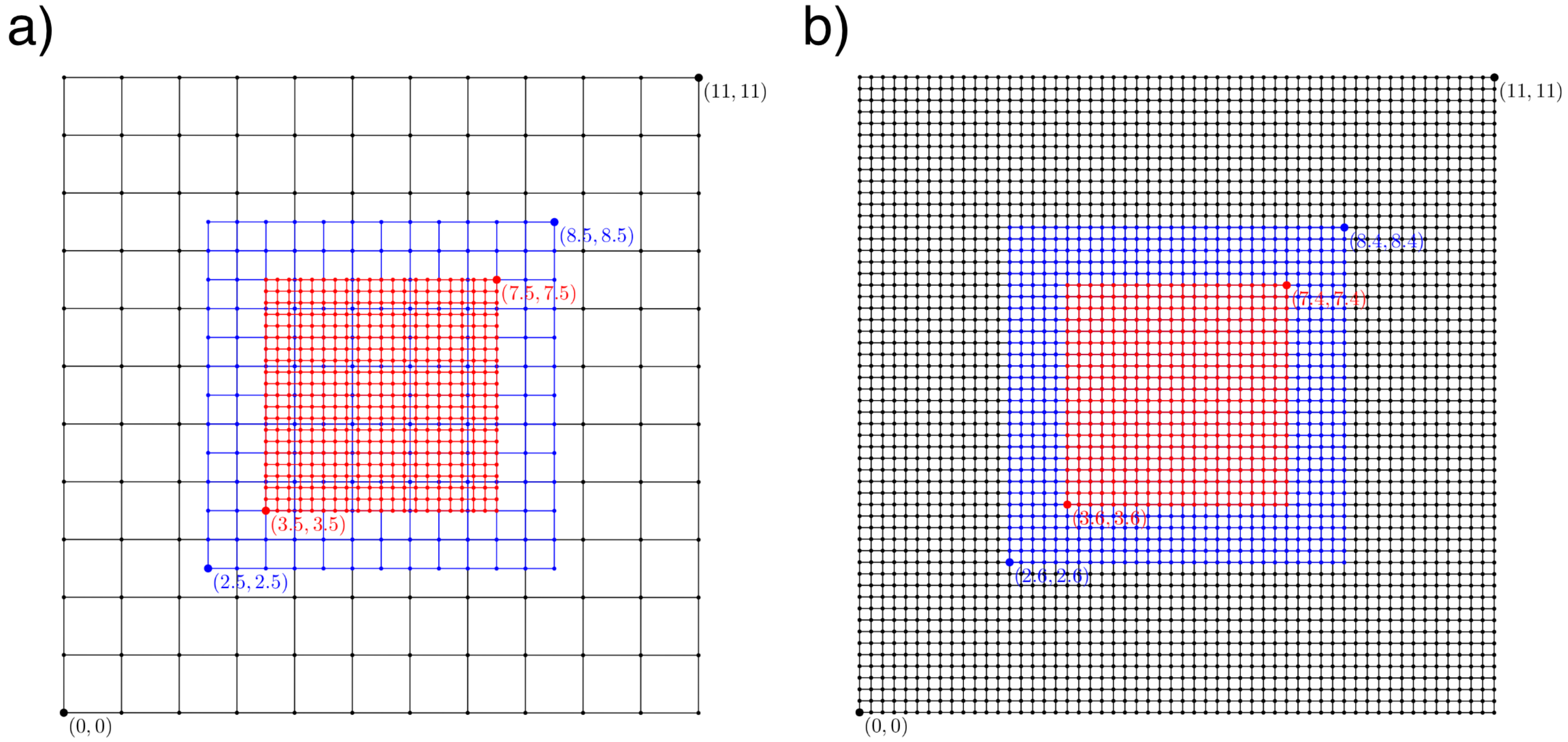

Figure 5.4: An illustration of the alignment process, in a) Three fields, black, red and blue are of different sizes and resolutions. b) After the alignment process, the three fields have the same resolution and all grid points are aligned.

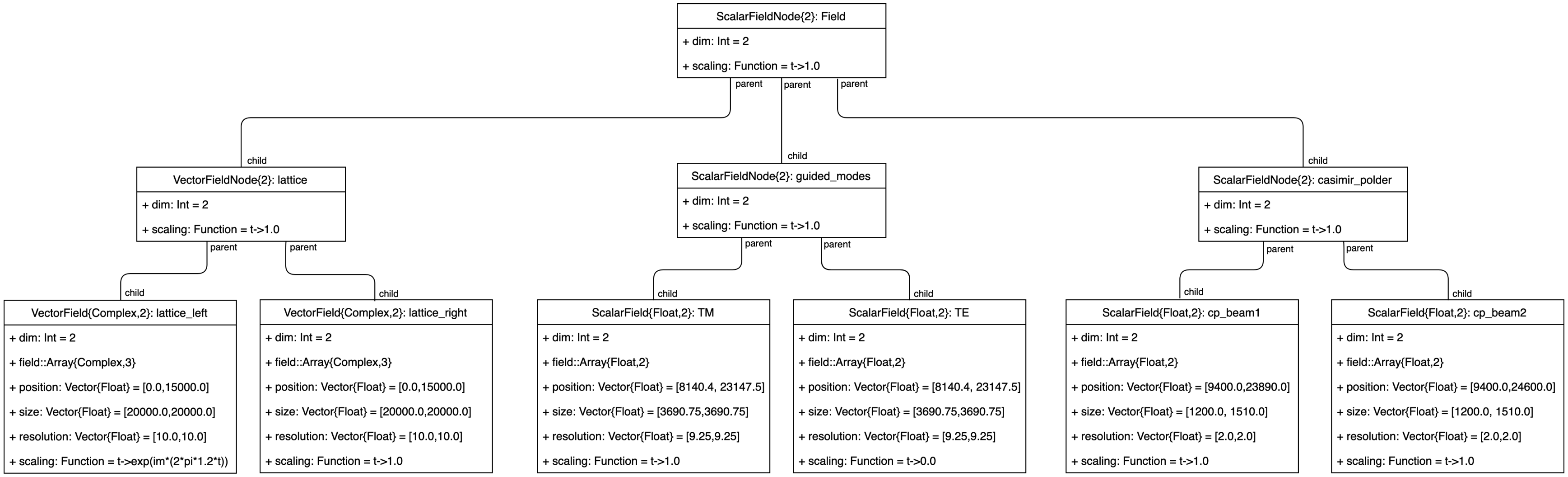

Figure 5.5: A field tree data structure for a 2D simulation before alignment, similiar to the ones used in the trajectories simulation. Under the root node "Field" there are three `FieldNode` a `VectorFieldNode` "lattice" for the optical lattice beams, two `ScalarFieldNode`s "guided_modes" and "casimir_polder" for the guided mode trap and the Casimir-Polder potential. Under each `FieldNode` are their respective components, the two optical lattice beams for "lattice", the TE and TM GM for the "guided_modes" and the Casimir-Polder potential of both beam for the "casimir_polder". The fields are incorporated from different sources, optical lattice beams from COMSOL or Lumerical, guided modes from MPB and Casimir-Polder potential from MATLAB, which all have various sizes and resolutions.

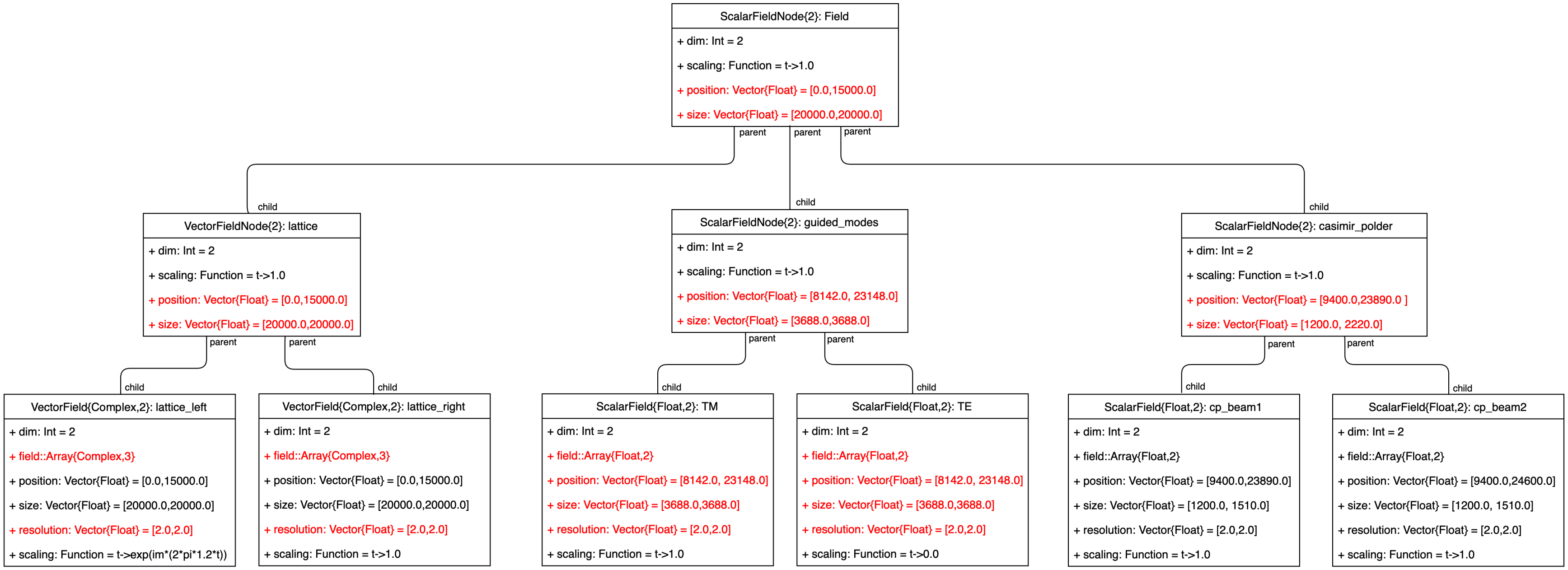

Figure 5.6: A field tree data strucure for a 2D simulation after aligning. The information changed by the alignment process is indicated with red.

### ODE Solver

After experimenting with various ODE solvers, I selected the SUNDIALS (SUite of Nonlinear and DIfferential/ALgebraic Equation Solvers)[49] library for atomic trajectories simulation. The SUNDIALS suite is built around multistep methods, which are more efficient than other methods when the cost of function calculation is high. Multistep methods gain efficiency by keeping the information from previous steps rather than discarding it. Specifically, I selected CVODE-Adams, an Adams-Moulton solver implementation in SUNDIALS[97] for the simulation and the solution converges with absolute tolerance smaller than $10^{-6}$ and relative tolerance smaller than $10^{-10}$. By profiling the simulation, I found that $\sim$50 % of the time is used in sampling and interpolating the field, and another $\sim$50 % spend on the ODE solver. So a multistep ODE solver which is efficient with high-cost function calculation is indeed an optimal choice.

## 5.4 Transfer Matrix Model

To calculate the APCW transmission spectrum as a function of time, the atom trajectories are randomly sampled according to the experimentally measured density of $\simeq 500$ atoms per pancake. The sampled atom trajectories are then distributed along the $x$ direction with probability proportional to the probe intensity in the APCW, as shown in Fig. 5.8. For example, for a TE probe with a frequency near the APCW TE band edge, the atom trajectories are distributed with a $\cos^2(\pi x/a)$ probability distribution, where $a$ is the APCW unit cell spacing (370 nm), to approximate the high contrast TE Bloch mode. For a TM probe with a frequency near the Cs D1 or D2 transitions, the TM band edges are both far from the probe frequency [50] with low contrast Bloch modes (*i.e.*, effectively traveling waves), so that the atom trajectories are distributed uniformly along $x$. Since our GM probe field is far below saturation, the transmission of the system as a function of probe frequency can be calculated with the transfer matrix model [3, 18, 50].

Light propagation along the APCW and atoms system can be modeled with the transfer matrix model. For a probe with detuning $\Delta_p$ relative to shifted ground-state and excited-state transition frequency, the transfer matrix of an atom is:

$$M^{\text{atom}}(\Delta_p, \Gamma_{1\text{D}}, \Gamma') = \begin{pmatrix} t - \frac{r^2}{t} & \frac{r}{t} \\ -\frac{r}{t} & \frac{1}{t} \end{pmatrix} \tag{5.1}$$

where $r = -\frac{\Gamma_{1\text{D}}}{\Gamma_{1\text{D}} + \Gamma' - i2\Delta_p}$ and $t = 1 + r$ [18].

And for a waveguide of length $l$ and angular wavenumber $k$,

$$M^{\text{wg}}(k, l) = \begin{pmatrix} e^{ikl} & 0 \\ 0 & e^{-ikl} \end{pmatrix} \tag{5.2}$$

The atom trajectories distributed along the $x$ direction with coordinate $(x_i(t), y_i(t), z_i(t))$. To calculate the transmission at time $t$, the $i^{\text{th}}$ atom can be modeled with the transfer matrix $M_i^{\text{atom}}(\Delta, \Gamma_{1\text{D}}, \Gamma')$ in Eq. 5.1, with the detuning $\Delta_p$ calculated from ground-state and excited-state light-shifts induced by the lattice, GM and CP potential. The emission rate into the waveguide $\Gamma_{1\text{D}}$ is proportional to the probe intensity profile, and $\Gamma'$ is the decay rate into free-space and other GMs. The waveguide segment $i$ between atom $i-1$ and atom $i$, can be modeled with eqn. 5.2. The total transfer matrix $M^{\text{tot}}$ is the product of all transfer matrices along the waveguide, $M^{\text{tot}} = \prod_{i=1}^{n}(M_i^{\text{wg}} \times M_i^{\text{atom}})$, where $n$ is the number of the sampled atoms, as shown in Fig. 5.8. The transmission of the APCW and atoms system can then be extracted from the total transfer matrix $M^{\text{tot}}$.

## 5.5 Simulation Results

### Movies

The following movies present two cases of simulated 2D trajectories for no TM Stark GM (Movie 1) and including a TM Stark GM (Movie 2). The potentials present in the simulation are determined by the free-space conveyor belt lattice, the CP potential near the dielectric surface (particularly visible in Movie 1 as the constant potential around the dielectric structure) and GMs of the waveguide (only present in Movie 2). The black dots represent individually calculated atomic trajectories initialized in 5 separate pancakes and launched 60 µm from the waveguide at time $\tau = 0$ (time counter observed in upper left corner of the movies). The black dots become red a single frame before the trajectory intersects the boundary of the dielectric structure and are removed from the simulation. The lattice speed in free-space is 0.51 m s$^{-1}$, lattice depth is 500 µK, and initial temperature $T = 150$µK for atoms trapped in the lattice. Note that the number of atoms is much larger per pancake for the movies (ie 20000 atoms per pancake) than the experiment ($\approx$ 500 atoms per pancake) to illustrate the multitude of trajectories a single atom could potentially follow. The two gray rectangles are a cross section at the thick part of the APCW, as indicated by the red dashed line in Fig. 2.3a.

### Movie 1: Red lattice delivery of atoms with no Stark GMs

This movie is of atomic trajectories using the conditions of Fig. 5.7(a) in the main text (no Stark GM). The four frames in Fig. 5.7(a) are generated using a single pancake of atoms from this simulation movie. The link to the movie can be found here: `https://dx.doi.org/10.14291/vd6s-6h38`.

### Movie 2: Red lattice delivery with blue detuned TM Stark GM

This movie portrays the conditions of Fig. 5.7(d) in the main text (in the presence of a TM Stark GM). Here, the blue detuned TM Stark GM repels atoms from the dielectric surfaces and imposes position and time dependent AC-Stark shifts. As before, the four frames in Fig. 5.7(d) indicate the evolution of a single pancake taken from this simulation movie. The link to the movie can be found here: `https://dx.doi.org/10.14291/r6xg-j678`.

### Simulation Results

The simulated atomic trajectories near the APCW for a single pancake with initial loading temperature $T_{\mathrm{initial}} = 100\,\mu\mathrm{K}$ and no GM ( $U_{\mathrm{GM}} = 0$) are shown in Fig. 5.7a. Notable features include: phase advances and retardations as each ‘pancake’ nears and departs from the central plane of the APCW, which leads to atomic acceleration and deceleration, and a significant flux of atoms entering the central 250 nm vacuum gap of the APCW.

To calculate the APCW transmission spectrum as a function of time, the atom trajectories are randomly sampled according to the experimentally measured density of $\simeq$ 500 atoms per pancake. The sampled atom trajectories are then distributed along the $x$ direction with probability proportional to the probe intensity in the APCW. For example, for a TE probe with frequency near the APCW TE band edge, the atom trajectories are distributed with a $\cos^2(2\pi x/a)$ probability distribution, where $a$ is the APCW unit cell spacing (370 nm), to approximate the high contrast Bloch mode.

For a TM probe with frequency near the Cs D1 or D2 transitions, the TM band edges are both far from the probe frequency [50] with low contrast Bloch modes (*i.e.*, effectively traveling waves), so that the atom trajectories are distributed uniformly along $x$. Since our GM probe field is far below saturation, the transmission of the system as a function of probe frequency can be calculated with the transfer matrix model [3, 18, 50].

For an initial loading of five consecutive pancakes, Fig. 5.7(b) shows the transmission spectrum of a weak TM probe $T(\Delta_p, t)$ calculated from the resulting simulated trajectories by way of a matrix transfer model. By applying the same analysis as previously described for our experiments (namely, folding the five pancakes spectra into one optical lattice period), a clocked spectrum can be generated over the time scale $\tau_{\text{lattice}}$, with the result shown in Fig. 5.7(c). The clocked spectrum is also present in Fig. 6.3(e.)

The simulation results with a calculated blue detuned TM stark GM are shown in Figs. 5.7d-f, note that the TM Stark GM alters the atom trajectories and induces AC Stark shift in the transmission spectra. The blue detuned TM stark GM allows atoms at different region around the APCW to be separated by different AC Stark shifts, as evidenced in Fig. 6.3 and Fig. 5.7(f), two classes of atoms trajectories can be identified: 1) Atoms that go around the sides of the APCW, experience little AC stark shift from the TM Stark GM and remain trapped in the optical lattice standing wave. These atoms contribute to the horizontal strip around 8 MHz in Fig. 5.7(f), as indicated by the blue dashed line. 2) Atoms that interact with the APCW GM strongly on the surface facing the incoming atoms and in the vacuum gap of the APCW. These atoms contribute to the negative AC Stark shifted feature in Fig. 5.7(f). As atoms climb up the strong repulsive potential, the negative AC Stark shift increases, creating the downward slopping feature, indicated by the red dashed line in Fig. 5.7(f). For atoms that bounce back or pass through the gap, the AC Stark shift decreases in magnitude, as indicated by the white dashed line in Fig. 5.7(f). More insight of atom motion around the APCW can be extracted from the clocked spectrum as explained in the next chapter.

## 5.6 "Ping Pong" Atom Trapping

One interesting simulation scenario is to vary both optical lattice trap frequency and the guided mode trap frequency and observe the atom dynamic in the center gap of the APCW. In Fig. 5.9 the optical lattice chirp frequency $\omega_{\text{chirp}}$ is kept at 1 MHz and both the optical lattice trap frequency and the guided mode trap frequency are scanned from 0 MHz to 2 MHz. Both trap frequencies are calculated by approximating the bottom of the traps with a quadratic function. Fig. 5.9a shows such simulation in 1D and Fig. 5.9b shows the same simulation with 2D. Both simulations show some similar features; the most obvious is the local maxima at guided mode trap frequency at $\sim$1.4 MHz and optical lattice trap frequency slightly above 1 MHz. This phenomenon is robust against the dimension and the detailed implementation of the guided mode trap, as long as the potential provides confinement perpendicular to the optical lattice direction. Closer inspection of the movies of these simulation shows that the atoms in the trap oscillate at 1 MHz in the time-dependent combination of the optical lattice and GM trap. So when atoms oscillate to the top part of the trap, they coincide with the peak of the optical lattice which pushes the atoms back into the trap, which leads to increase of the atom number in the trap. However, to implement this scheme in the lab would require precise control of both optical lattice and guided mode trap frequency, which are not within the accuracy of our experiment yet.

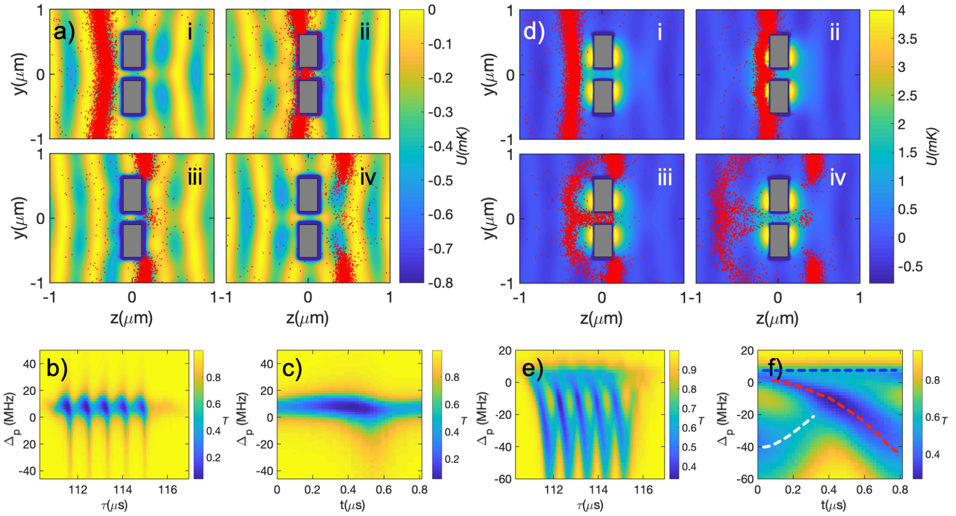

Figure 5.7: Simulated 2D atom delivery and the corresponding simulated clocked spectra. Note that the atom number in panels (a) and (d) is much larger per pancake than in the experiment in order to illustrate the multitude of trajectories a single atom could potentially follow. a) The atomic trajectories without any APCW GM at 4 different times. The two gray rectangles are a cross section at the thick part of the APCW, as indicated by the red dashed line in Fig. 2.3(a). i) shows atomic trajectories at $\tau = \tau_i$, ii) at $\tau = \tau_i + \frac{2}{3}\tau_{\text{lattice}}$, iii) at $\tau = \tau_{i+1} + \frac{1}{3}\tau_{\text{lattice}}$ (where $\tau_{i+1} = \tau_i + \tau_{\text{lattice}}$) and iv) at $\tau = \tau_{i+2}$. b) By simulating multiple pancakes and sampling from the trajectories, a spectrum of multiple pancakes can be calculated. c) A clocked spectrum generated by folding the multiple pancake spectrum. Here the lattice configuration for clocked time $t = 0$ is shown in a)i and iv (*i.e.* the timing when the highest intensity of the lattice is at $z = 0$). d) The atomic trajectories with an intense blue TM Stark beam. Timing is the same as (a). e) The transmission spectrum for 5 pancakes with a blue TM guided mode. f) Clocked spectrum with a blue TM Stark beam. Notable features of (d),(e) and (f) include: 1) Atoms that go around the sides of the APCW experience little AC stark shift from the GM and remain trapped in the optical lattice standing wave. These atoms contribute to the horizontal strip around 8 MHz, as indicated by the blue dashed line in (f). 2) Atoms that interact with the APCW GM strongly on the surface facing incoming atoms and in the vacuum gap of the APCW. These atoms contribute to the negative AC Stark shifted feature. As atoms climb up the strong repulsive potential, the negative AC stark shift increases, creating the downward sloping feature, as indicated by the red dashed line. And as the atoms bounce back or pass through the gap, the AC Stark shift decreases in magnitude, as indicated by the white dashed line.

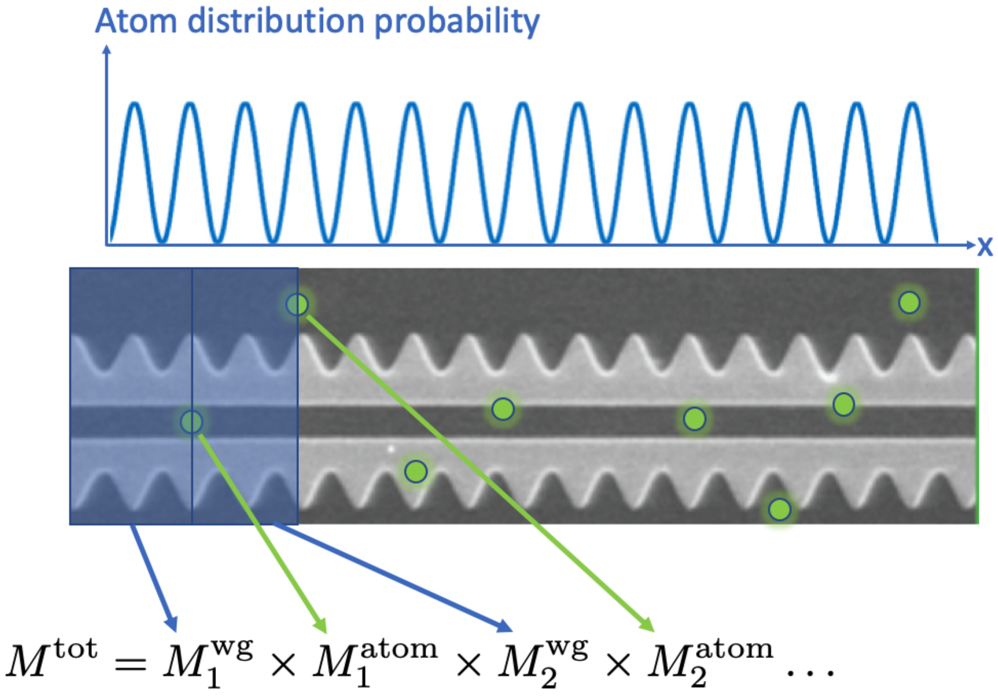

Figure 5.8: Diagrammatic look at the transfer matrix model. For a TE probe simulation, atoms are distributed along the APCW in the $x$ direction weighted by the sinusoidal intensity distribution of a light at the TE dielectric band edge. Light propagation along the APCW is modeled with the transfer matrix model. Each atom and the waveguide segments between adjacent pairs of atoms are represented with a transfer matrices, with the total transfer matrix being the product of all transfer matrices. The transmission of the whole system can be extracted from the total transfer matrix.

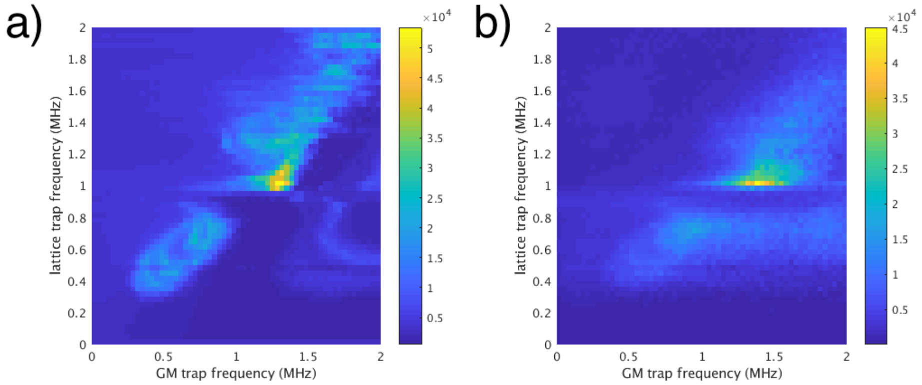

Figure 5.9: Optical lattice trap frequency and guided mode trap frequency both scanned from 0 MHz to 2 MHz. With the optical lattice chrip frequency kept at 1 MHz. Atoms initialized at 50 µK at 70 µm away from the GM trap. a) shows a 1D simulation with a the optical lattice represent by a moving sine wave and GM trap as a gaussian function. b) shows a 2D simulation with optical lattice profile calculated with COMSOL and GM profile calculated with MPB. The colorbar is the integration of the number of atoms in the center gap of the APCW with respect to time in arbitrary unit. The similarities of the two figure show that the “ping pong” atom trapping scheme is a general phenomina regardless of the detail implementation of optical lattice and the GM trap.

## *Chapter 6*

# EXPERIMENTAL RESULTS

After discussing the experiment setup and the simulation method in chapter 4 and chapter 5, I will present various experimental results and comparison to simulations. The clocked spectrum provide deep information of the atomic trajectory around APCW and also the interaction between atoms and photonic modes. When compared with the simulation, useful information such as parameters like $\Gamma_{1D}^{\text{eff}}$, ${}_{1D}^{\text{eff}}$, beam power, and timing can be extracted and feedback to adjust the experiment setup or help design new experiments. In this chapter clock spectra of various combinations of guided modes and probes polarization are examined in detail. The Casimir-Polder potential which originated from the interaction between atom and dielectric can also be measured with the clocked spectrum, and we obtain comparable results in the literature. The experimental results of various attempts for cooling and trapping atoms into the guided mode trap are also documented. Finally, comparing experimental and simulation also provides “actionable” information for trapping and cooling atoms.

## 6.1 Application of Clocked Spectra

As it will be discussed in the following sections, the comparison between the experimental results and the simulation establishes strong correspondence between our measurements and simulations for various features of clocked spectra involving various combination of probe and Stark beams polarization (*e.g.*, (TM probe, TM Stark), (TM probe, TE Stark) and (TE probe, TE Stark)). These results provide further validation of our numerical simulations, which are based upon calculated atomic trajectories as atoms brought by the moving lattice pass around and through nanoscopic regions of the APCW in the presence of forces from the lattice itself, Stark GMs, and surface forces. With a reasonable degree of confidence, we can then attempt to use the measured clocked spectra to provide insight into atomic trajectories that are currently beyond direct observation.

A practical application of clocked spectra is already being used extensively in our laboratory. That is calibrating the intensity of optical fields involved in the experiment, such as optical lattice beams and GMs of the APCW. This calibration provides us information about the actual power delivered to the APCW from a known input power at the optical fiber coupled to the sequence of waveguides that lead to the actual APCW[109]. Both TM and TE GM powers can be calibrated with the clocked spectra.

Another practical application is the validation of trap parameters for GM traps formed from the summation of red and blue GMs [38, 52]. The basic idea is that the blued detuned TM GM can be used to separate atoms interacting with the TE probe into two distinct classes. Because of the AC-Stark shift and the spatial intensity distribution of the TM blue GM, an atom entering the center vacuum gap of the APCW will experience a more substantial AC Stark shift than an atom passing around the side. By validating this effect in our simulations, we can then utilize it to separate the side and gap classes of atoms in a clocked spectrum experimentally. This process provides useful timing and spectral information to implement a recursive loading scheme described in chapter 2. This separation also enables us to measure the dynamics of the atoms inside the center vacuum gap of the APCW.

The Casimir-Polder potential between the atoms and the dielectric can also be probed using the clocked spectra. By comparing the experiment to simulations using a simplified approximated potential, we can measure the $C_3$ coefficient which agrees to within 50 % to 200 % of the experimental value in the literature (cite). A full calculation of the CP potential as in Ref. [40, 52] of the APCW is under development. This ability to measure the Casimir-polder potential is important since the trapping region is close to the dielectric surface (less than 100 nm), where the Casimir-Polder force is significant compared to the optical dipole force from the GMs.

A quite different application of our system of clocked-atoms delivered to a PCW is utilization of this time-dependent, optically dense atomic medium for novel nonlinear optical experiments, such as soliton propagation, as investigated in Ref. [61]. The relevant pulse durations are much smaller than the free space atomic lifetime $\tau \simeq 30$ns for the Cesium D1 line, which is in turn much shorter than the atom transit time through the APCW, so the pulses could be triggered to interact with an optical system with selected values of $\Gamma_{1D}^{\text{eff}}$, $J_{1D}^{\text{eff}}$, $\Delta_{\text{AC}}$, $\Gamma'$ as in Fig. 6.2(c) by varying the offset of the input pulse and lattice clock timing. A theoretical analysis and experiment results will be presented in chapter 7.

Another possibility is opto-mechanics. In our modeling and experiments, the GM probe is kept weak to avoid affecting atomic motion as well as saturation, allowing modeling of optical transmission and reflection by way of matrix transfer techniques. That is, atoms strongly affect the probe response, but the probe only weakly affects atomic motion. On the other hand, the Stark GMs in this work presented are far detuned so that their transmission is only weakly modified by the atoms, but clearly, the atomic motion is strongly influenced by sufficiently intense Stark GMs, as in Fig. 5.7. Consider now that the probe and Stark GMs are one and the same field with intensity sufficient to drive atomic saturation as well as to create optical forces that modify atomic motion. We would then be in a regime requiring a self-consistent description of the internal and external degrees of freedom for atoms and optical fields within the APCW (*i.e.*, a nonlinear regime for opto-mechanics with atoms). Although we have carried out such measurements with our current experiment, the results are beyond our existing simulation capabilities.

## 6.2 Comparing Average Spectra

Before having the ability to observe clocked spectra, a way to compare the experiment results to simulation is to average the spectra over the whole atom cloud. Fig. 6.1(a) shows the experiment results of transmission spectra of a TM probe with various powers of a blue-detuned TM Stark GM which is 58 GHz detuned from the cesium $D2$ $F = 3$ ground state transition. Experimentally, two blue detuned TM Stark GMs counter-propagate and add incoherently in the APCW with 100 MHz frequency difference. As the blue detuned TM Stark GM power increases, the peak optical density reduces and the spectra broadened to the red side. At some power range, the spectra show two distinct peaks. These peaks correspond to different categories of atomic trajectories, and this point will be explored extensively in the following sections. Figure 6.1(b) and (c) show the same experiment condition reproduced in the simulation in 2D and 3D, respectively. In the simulation the spectra is calculated by averaging over 5 pancakes. 2D and 3D simulations show similar spectra, as expected. Since the Cs D1 and D2 line are far from the TM band gap, the APCW behaves like a waveguide for the TM mode. The GM profile remains relatively similar along the APCW, so the 2D simulations should behave similarly to the 3D ones.

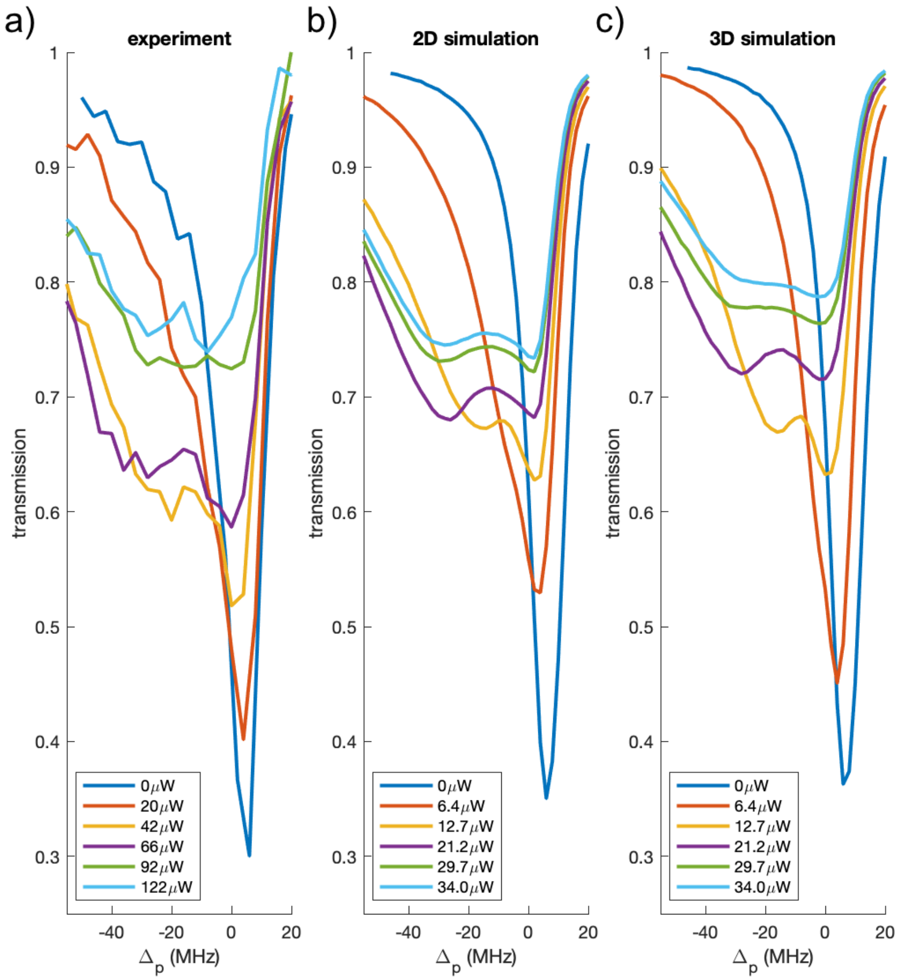

Figure 6.1: a) Measured spectra average over the atom cloud with a blue detuned TM GM with power ranging from 0 μW to 122 μW. b) Spectra averaged over 5 pancakes in 2D simulation with a blue detuned TM GM with power ranging from 0 μW to 34 μW. c) Spectra average over 5 pancakes in 2D simulation with a blue detuned TM GM with power ranging from 0 μW to 34 μW.

## 6.3 Fitting Clocked Spectrum

We can fit the spectrum in a way similiar to section 4.4, but instead of fitting the average spectrum we can fit at different time within a lattice period. We fit the measured ‘clocked’ spectra to a transmission model of the probe field through the PCW that was developed in [3, 50], which is expressed as follows:

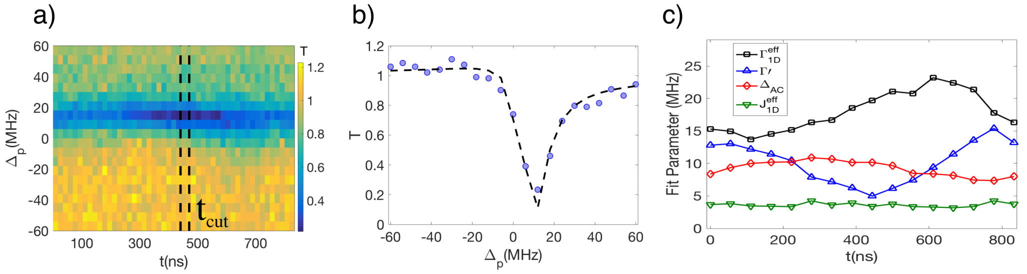

Figure 6.2: a) By scanning the probe detuning we can create this 2D image in lattice time $t$ and probe detuning $\Delta_\text{p}$ to gain more insight into the arrival time of different classes of atoms and extract spectra for various arrival times. This information helps to determine the coupling of the atoms to the waveguide and can reveal time dependent AC-Stark shifts. Cuts at certain times reveal spectra which we fit to extract parameters $\{\Gamma_\text{1D}^\text{eff}(t), \Gamma'(t), \Delta_\text{AC}(t), J_\text{1D}^\text{eff}(t)\}$ for an effective model (eq. 6.1). An example of slices taken over an interval '$t_\text{cut}$' and summed is given in (b). c) The fit parameters extracted for spectra at varying lattice times $t$ in (a). Each spectrum is taken by combining 3 time bins (each of duration $\simeq$ 50 ns) and fitting to a transmission model given in Ref. [50]. Note that $\Gamma_\text{1D}^\text{eff}$ changes the most across time and denotes the coupling strength of the atomic sample to the structure. $J_\text{1D}^\text{eff}$, the coherent coupling term, remains relatively constant and small across time.

$$T(\Delta_p, t) = \left| \frac{\Delta_p + i\Gamma'/2}{(\Delta_p + J_\text{1D}^\text{eff}(t)) + i(\Gamma' + \Gamma_\text{1D}^\text{eff}(t))/2} \right|^2. \tag{6.1}$$

Here $\Delta_p$ is the detuning between the probe frequency and the free-space atomic resonance frequency, $\Gamma'$ is the atomic decay rate into all modes (mostly free-space) other than the GM of interest, and $\Gamma_\text{1D}^\text{eff}(t)$ and $J_\text{1D}^\text{eff}(t)$ are the emission rate into the waveguide and the atom-atom coupling rate for the GM of interest, respectively. The time dependence of $\Gamma_\text{1D}^\text{eff}$ and $J_\text{1D}^\text{eff}$ arises from the periodic arrival and transit of the atoms. For the ideal case of a single lattice 'pancake' with atomic and probe frequencies near the band edges of the APCW, we would find that

$$\Gamma_\text{1D}^\text{eff}(t) = \sum_{i=1}^{N_\text{at}} \Gamma_\text{1D}^{ii}\left(r_i(t)\right), \tag{6.2}$$

where $N_\text{at}$ is the number of atoms within a single pancake and $r_i$ is the position of the $i^\text{th}$ atom.

However, in our experiment, it is difficult to disentangle the number of atoms interacting with the waveguide and the spatial variation of $\Gamma_{\mathrm{1D}}$ for different atoms and trajectories. Hence, we introduce $\Gamma_{\mathrm{1D}}^{\mathrm{eff}}$ as an effective atomic coupling to the waveguide, and likewise for the term $J_{\mathrm{1D}}^{\mathrm{eff}}$, which was found to be quantitatively adequate for the analyses in [50].
In nanoscopic terms, $J_{\mathrm{1D}}^{ij}$ and $\Gamma_{\mathrm{1D}}^{ij}$ relate to the real and imaginary components of the Green's function for radiative interactions between atoms $(i, j)$, mediated by the GM of interest of the APCW.

From the effective model of Eq. 6.1, the coupling strengths $\Gamma_{\mathrm{1D}}^{\mathrm{eff}}(t)$ and $J_{\mathrm{1D}}^{\mathrm{eff}}(t)$ can be extracted as functions of the clocked lattice time by taking detuning cuts of the 2D spectrum at fixed times in Fig. 6.2(a) and fitting each spectrum to the above model. An example of a transmission spectrum at $t_{\mathrm{cut}} = 450$ns is shown in Fig. 6.2b. We fit the measured clocked transmission spectra to an effective model that was developed in [3, 50] for a random number of atoms trapped above a 1D PCW and moving along $x$. The three fit parameters for this effective model are, $\Gamma_{\mathrm{1D}}^{\mathrm{eff}}$ and $J_{\mathrm{1D}}^{\mathrm{eff}}$, which describe effective decay rates and frequency shifts, respectively, for $N$ atom radiative interactions with the measured GM (TE or TM), as well as $\Gamma'$ for single-atom decay into all other modes (principally free-space modes), which is assumed to have no collective effects [4].

The coupling strengths $\{\Gamma_{\mathrm{1D}}^{\mathrm{eff}}(t),\ J_{\mathrm{1D}}^{\mathrm{eff}}(t)\}$ and decay rate $\Gamma'(t)$ are extracted as functions of the clocked lattice time $t$. Fig. 6.2c provides an example of such temporal behavior of $\{\Gamma_{\mathrm{1D}}^{\mathrm{eff}}(t),\ J_{\mathrm{1D}}^{\mathrm{eff}}(t), \Gamma'(t)\}$ over a lattice period. Here $\Gamma_{\mathrm{1D}}^{\mathrm{eff}}(t)$ changes over time reflecting the atom density and coupling to the structure in a lattice period. $J_{\mathrm{1D}}^{\mathrm{eff}}(t)$ remains relatively constant indicating a small contribution from atom-atom interactions, which is unsurprising given that these experiments are taken far from the dielectric bandedge where the coherent coupling term is small. This technique thereby provides otherwise inaccessible information about radiative interactions along the APCW as pancakes of atoms move through the device.

## 6.4 Clocked spectrum with Stark GMs

For the previously described clocked spectra, atoms experience spatial and temporal variations of AC Stark shifts $\Delta_{\mathrm{AC}}^{\mathrm{lattice}}(r, t)$ due to the complex structure of the optical fields of the moving optical lattice and CP forces in the vicinity of the APCW. In this section, we investigate experimentally and numerically clocked transmission spectra in the presence of a far-detuned GM that produces its spatial distribution of AC Stark shifts $\Delta_{\mathrm{AC}}^{\mathrm{GM}}(r,t)$ near the surfaces of the APCW, as illustrated by the TM and TE GM mode profiles shown in Fig. 2.3(b). The GMs here are launched incoherently from each fiber port of the APCW in order to avoid the large vector shifts on the atomic energy levels. We achieve this "incoherent sum" by detuning one of GMs by 100 MHz which is a fast enough beat-note that the atomic motion is unaffected, however, not large enough compared to the overall GM detunings of 58 GHz and 600 GHz to create any appreciable difference from the point of view of the atoms (*i.e.*, an atom interacting with a GM detuned by 58 GHz and 600 GHz behaves similarly to one interacting with a 58.1 GHz and 600.1 GHz detuned GM).

In principle, we can choose any GM polarizations for the probe and Stark fields, as well as detuning and Stark shift depending on the effect desired on the atomic signal. In the following subsections we will examine in detail three combinations of Stark GM and probe polarization and detuning, namely: (blue detuned TM Stark GM; TM probe), (blue detuned TM Stark GM; TE probe) and (red detuned TE Stark GM; TE probe). Additionally, here we focus on lattice speeds of $0.51\,\mathrm{m\,s^{-1}}$; however, we can easily adjust this speed by changing the beat frequency between the two lattice beams, and have experimentally investigated lattice speeds from $0.7\,\mathrm{m\,s^{-1}}$ down to $0.02\,\mathrm{m\,s^{-1}}$.

### TM Stark GM with TM Probe

As shown in the first column of panels in Fig. 6.3(ii)(a-d), the addition of static GM fields leads to clocked spectra with much richer structure than absent these fields. The measured spectra exhibit variations in transmission on time scales $\delta t \simeq 100$ns and associated length scales $\delta z \simeq 50$nm for lattice velocity of $0.51\,\mathrm{m\,s^{-1}}$, under the influence of a TM GM with power range $0 \leqslant P_{Stark} \leqslant 92\mu$W and blue detuning of 58 GHz from the D2 line. The configuration of the involved beams is presented in Fig. 6.3(i). Here, the atoms enter in $F = 3$ and the probe beam is tuned around the $F = 3 \longrightarrow F' = 4$ transition of the D1 line of Cs, with detuning $\Delta_p = \omega_{\mathrm{probe}-\omega_a}$(where $\omega_a$ is the free-space transition frequency), to avoid inhomogeneous broadening associated with the D2 excited-state tensor shifts from the free-space optical lattice.

Fig. 6.3(ii)(a) shows the clocked spectrum without the TM Stark GM, the average detuning of $\Delta_p = 8$ to 10 MHz is the AC Stark shift from the red-detuned optical lattice beams, this detuning is consistent with the calculation and simulation by using the lattice beam detuning, power, and diameter measured experimentally. The optical density at negative detuning around 600 ns is contributed by the Casimir-Polder potential between the atoms and the dielectric, which can be varified by the simulation and will be explained in detail in section 6.7. The AC shift from the Casimir-Polder is negative because although the D1 cesium ground state is shifted to lower frequency, the excited state is shifted to lower frequency by roughly double the magnitude compare to the ground state. So the transition frequency is reduced[63].

In the presence of the TM Stark GM for the measurements in the left column, atoms experience a repulsive dipole force, and the atomic transition frequency is shifted in the negative direction than that of in the optical lattice. Atoms arriving at the side of the APCW facing the incoming moving lattice begin to climb up the repulsive potential created by the blue TM Stark GM and lose kinetic energy. As atoms climb this potential, the AC Stark shift they experience increases due to the spatial intensity of the TM Stark GM. Evident in the data is that atom arrivals at different times exhibit different Stark shifts. As the TM Stark GM power increases, the AC Stark shift becomes more significant. The corresponding peak AC Stark shifts in the vacuum spaces surrounding the APCW are estimated to be $0 \leqslant \Delta_{\mathrm{AC}}^{\mathrm{GM}} \leqslant 60\mathrm{MHz}$, bounded by the kinetic energy of the atoms imposed by the lattice speed. As the TM Stark GM power continues to increase, the atoms are blocked from entering the vicinity of the APCW, and the optical density is reduced.

Moving to higher power for the TM Stark GM in the left column of Fig. 6.3b, we observe an evolution of atomic signatures where atoms arriving at different times within one pancake experience different Stark shifts. Good correspondence between experiment and simulation is displayed in the columns of Fig. 6.3. The second column Fig. 6.3(ii)(e-h) is the clocked spectra calculated with 2D simulation and the third column Fig. 6.3(ii)(i-l) is done with 3D simulation. The results of 2D and 3D simulations are similar, and agrees with the intuition that the TM Stark GM and TM probe mode profiles are similar along the APCW. A temporally varying atomic signature on the scale of ~100 ns, while itself of interest, can be used to determine the arrival time of atoms and their spatial distribution around the surfaces of the

APCW. This information cannot be extracted from the data alone, but when aided by numerical simulations and validations, can enable 'actionable' information to be obtained from the measured clocked spectra.

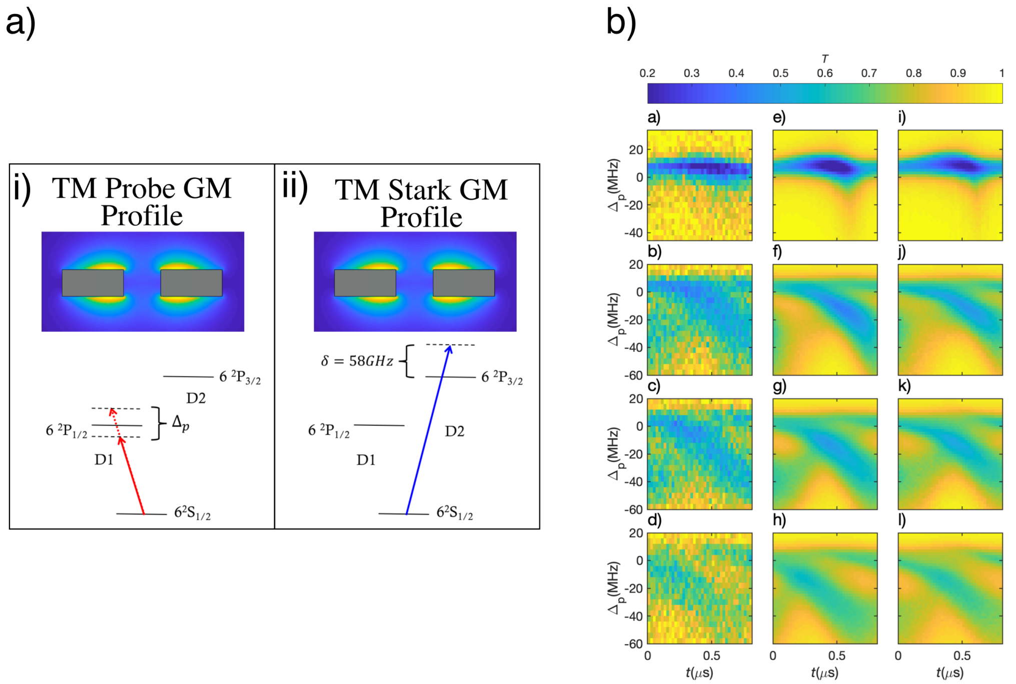

Figure 6.3: a) The beam frequency and polarization parameters. i) The TM probe GM spatial profile. Below shows the frequency detuning of the probe beam which is scanned around the free-space D1 resonance. ii) The TM Stark GM profile with the detuning from the D2 line. The detuning is held fixed for all measurements at 58 GHz b) A comparison of the data (a-d) and simulation (e-h). In both cases, there are two TM GMs of the APCW being excited, namely 1) a weak TM probe beam with variable frequency $\omega_p$ and detuning $\Delta_p = \omega_p - \omega_a$, with $\omega_a$ the free-space frequency of the $F = 3 \longrightarrow F' = 4$ transition in the D1 line of atomic Cs and 2) a TM Stark GM with a sequence of increasing powers from zero in the top panels. For the measurements in the left column of Fig. 6.3b, the sequence of input powers is $P_{Stark}$ = 0, 42, 66 and 92μW from top to bottom, while for the simulations in the right column, from top to bottom, the internal power sequence is $P_{Stark}$ = 0, 12.6, 19.8 and 27.6 μW for the GM detuning of 58 GHz from $F = 3$ on the D2 line. As the simulated TM Stark beam power is increased the atomic sample response alters in both time and detuning in ways similar to increasing the power in the simulation. This allows the intensity of guided modes to be calibrated by comparing the data and simulation.

### TM Stark GM and TE Probe

In this measurement, the Stark GM is still blue detuned from $F = 3$ on the cesium D2 line by 58 GHz and TM polarized. But now the probing is with a TE probe. The APCW TE band edges are designed to be aligned to the cesium $D1$ and $D2$ transitions, so the D1 probe profile has very high-intensity contrast along the $x$ axis of the APCW. Also, the TE probe intensity is concentrated in the gap and the side at the thickest parts of the device. The left column Fig. 6.4(a-d) shows the experimental result, similar to the experimental result of the blue TM Stark GM with a TM probe, the clock spectra also show that atoms experience different AC Stark shifts within an optical lattice period $\tau_{\text{lattice}}$. Since the probe power is very weak ~30 pW, the atom trajectories are minimally affected by the change of the probe polarization. The atoms' trajectories remain the same, and the TE probe is probing different region with different probe profile compare to the TM probe.

One experiment difficulty is to align the probe into pure TE polarization. During the aligning procedure, the scattering from the fiber node tether is minimized, however, sometimes the scattering of the node tether on the other end is not also minimized, indicating that the polarization in the APCW is not purely TE. This inconsistency can result in slightly different TE clocked spectra. For example in Fig. 6.4c, the clocked spectra shows two prominent horizontal strips similar to that in the 3D simulation Fig. 6.4(i-l). Whereas the experiment results in the first column Fig. 6.4b(a-d) have a downward sloping feature indicating there might a mixture of TM component in the probe.

Due to the contrast of the TE probe along the APCW, the 2D and 3D simulations show different results. Fig. 6.4 shows the measured and simulated spectra for a blue-detuned TM Stark GM with TE probe. Evident in this figure is that the agreement between simulation and experiment, while still good, is not quite as good compared to Fig. 6.3. We suspect this is due to the usage of TE GMs for probing, which have a complicated modulation pattern in the $x$ direction that is not addressed in the current 2D simulations [50]. A major difference between the 2D and 3D simulation is that the outer side of the APCW has a much larger surface area in the 3D simulation, leading to a higher contribution from the "sides" atom that experiences small AC Stark shift from the GM, which is evident in the second and third column in Fig. 6.4. The filtered trajectory clocked spectra of the TE probe can provide important information useful for trapping. Since the TE probe is intense in the center gap and the side, coupled that with the AC Stark shift difference created by the TM Stark GM, we can identify the timing and the detuning when the atoms enter the center gap, this will be explained in detail in section 6.8.

#### TE Stark GM and TE Probe

Fig. 6.5 shows the measured and simulated clocked spectra for a red-detuned TE Stark GM with TE probe. A red detuned TE Stark GM is a component of a stable GM trap. So the ability to calibrate the TE GM power is critical for creating a stable trap in the center gap of the APCW. In Fig. 6.5, the experiment and simulation again show good agreement, indicating that the numerical simulation of the atom trajectories can provide valuable information to interpret the experimental results.

### 6.5 “Slingshot” Sequence and Cooling

In the attempt to trap atoms in the center gap in the APCW, we aligned a pair of lin ⊥ lin polarization gradient cooling beams in order to co-propagate with the optical lattice beams. Also, two counterpropagating TM polarized GM are added to Doppler cool atoms in the vicinity of the APCW. In order for the polarization gradient cooling (PGC) to work, the atoms have to move through the polarization gradient which is the size $\lambda/4$. In the usual lattice delivery setup, the atoms are trapped within optical lattice pancake which confined them within $\pm\frac{\lambda}{4}$, which prevents the atoms from cooling with PGC technique. In the “slingshot” experiments, one of the optical lattice beams (south-to-north, which is pointing from the science MOT to the chip) is gradually turned off as the atoms approach the device, leaving the atoms radially confined in the single optical beam (*i.e.* the single north-to-south lattice component). After the one optical lattice beam is turned off, the north-to-south (Chip to MOT) cooling then turns on to slow down the incoming atoms. After the atoms stop, the other cooling beam is turned on to cool the atoms.

Fig. 6.6 summarizes some experimental results of this cooling process. For all experiments a D2 $F = 4 \to F = 4$ auxiliary GM is added to pump the atoms into $F = 3$ near the APCW to increase the lifetime after the atoms have been cooled down. The small signals around ~15 ms are due to the stop and go sequence. In some of the measurements, the signals are separated temporarily; for example in Fig. 6.6a and the second and third panels in Fig. 6.6e, it is not clear whether this is because the atom cloud is separated into two groups and pass the APCW in two groups or that the atoms are being pushed back by the cooling beam, which is more likely. Fig. 6.6a and Fig. 6.6c show the spectra for experiment with only the chip to MOT cooling beam $B_{\text{atom}}$, with Fig. 6.6a using a weaker cooling beam, so the atoms are pushed back and detected again by the APCW in a later time. In Fig. 6.6b and Fig. 6.6d are the spectra with both cooling on, which seems to “squeeze” the temporary, which is not well understood. Fig. 6.6e shows spectra with a single chip to MOT beam scanned from $-30\,\text{MHz}$ to $5\,\text{MHz}$ in steps of $5\,\text{MHz}$. As the cooling beam detuning decreases, the atoms are being squeezed.

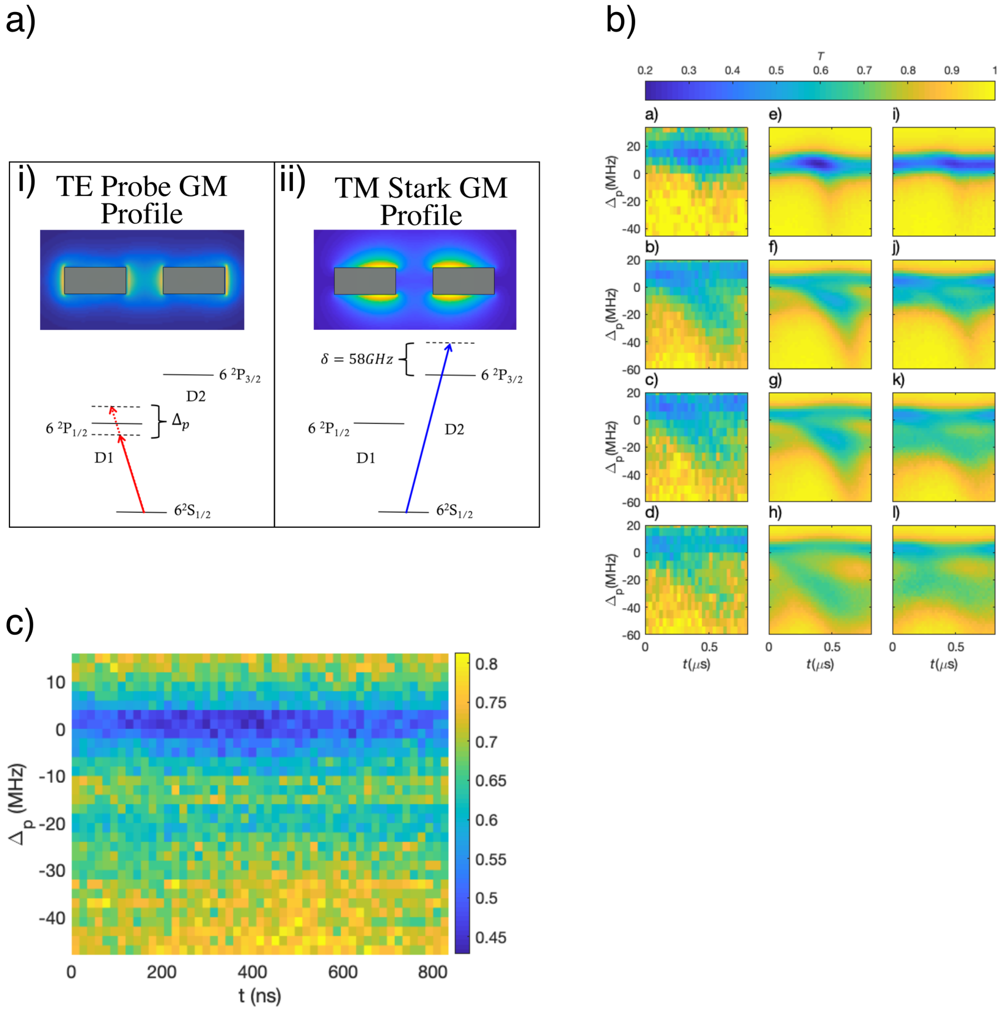

Figure 6.4: i) The beam frequency and polarization parameters. a) The TE probe GM spatial profile. Below shows the frequency detuning of the probe beam which is scanned around the free-space D1 resonance. b) The TM Stark GM profile with the detuning from the D2 line. The detuning is held fixed for all measurements at 58 MHz ii) A comparison of data (a-d), 2D simulation (e-h) and 3D simulation (i-l). A blue detuned TM Stark GM is excited in the APCW, and the atoms are probed with a weak TE probe with detuning $\Delta_p$. For the measurements in the left column of the Figure, the sequence of input powers is $P_{\text{Stark}} = \{0, 20, 30, 52\}\mu$W from top to bottom. For the simulations in the right column, from top to bottom, the internal power sequence is $P_{Stark} = \{0, 3.7, 5.6, 9.7\}\mu$W for the GM detuning of 58 GHz from $F = 3$ on the D2 line. c) Another clocked spectrum with 35 μW blue-detuned TM Stark GM and TE probe, taken with another device. This clocked spectrum shows two horizontal stripe similar to Fig. 6.4b(l).

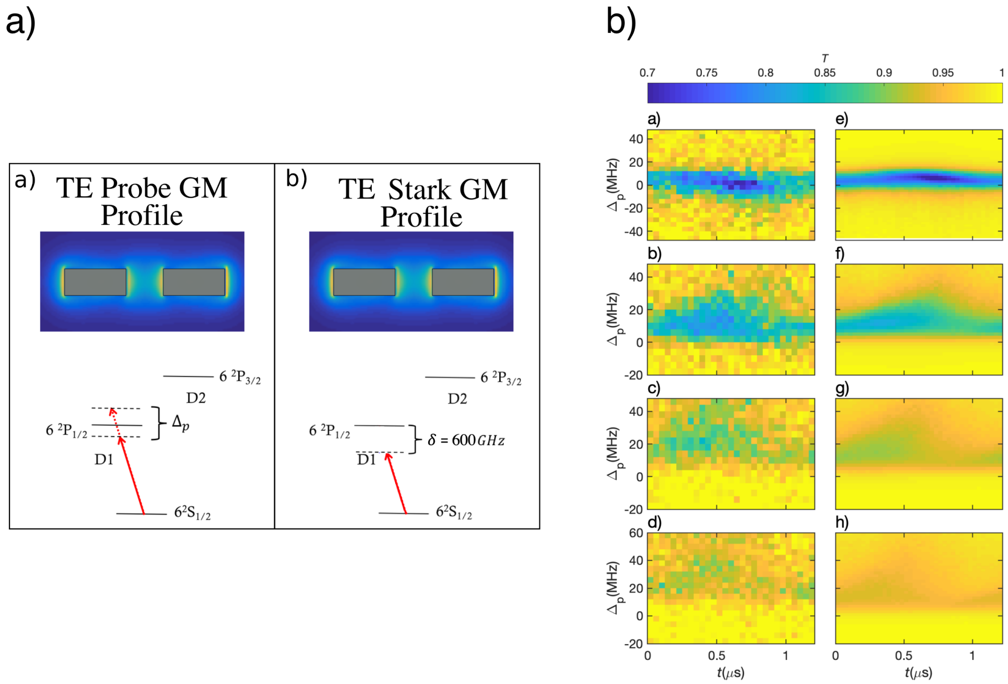

Figure 6.5: i) The beam frequency and polarization parameters. a) The TE probe GM spatial profile. Below shows the frequency detuning of the probe beam which is scanned around the free-space D1 resonance. b) The TE Stark GM profile with the detuning from the D1 line. The detuning is held fixed for all measurements at −600 GHz ii) A comparison of data (a-d) and 2D simulation (e-h). A blue detuned TM Stark GM is excited in the APCW, and the atoms are probed with a weak TE probe with detuning $\Delta_p$. For the measurements in the left column of Fig. 6.5b, the sequence of input powers is $P_{\text{Stark}} = \{0, 40, 104, 140\}\mu$W from top to bottom. For the simulations in the right column, from top to bottom, the internal power sequence is $P_{Stark} = \{0, 45, 135, 195\}\mu$W for the GM detuning of 600 GHz from $F = 3$ on the D2 line.

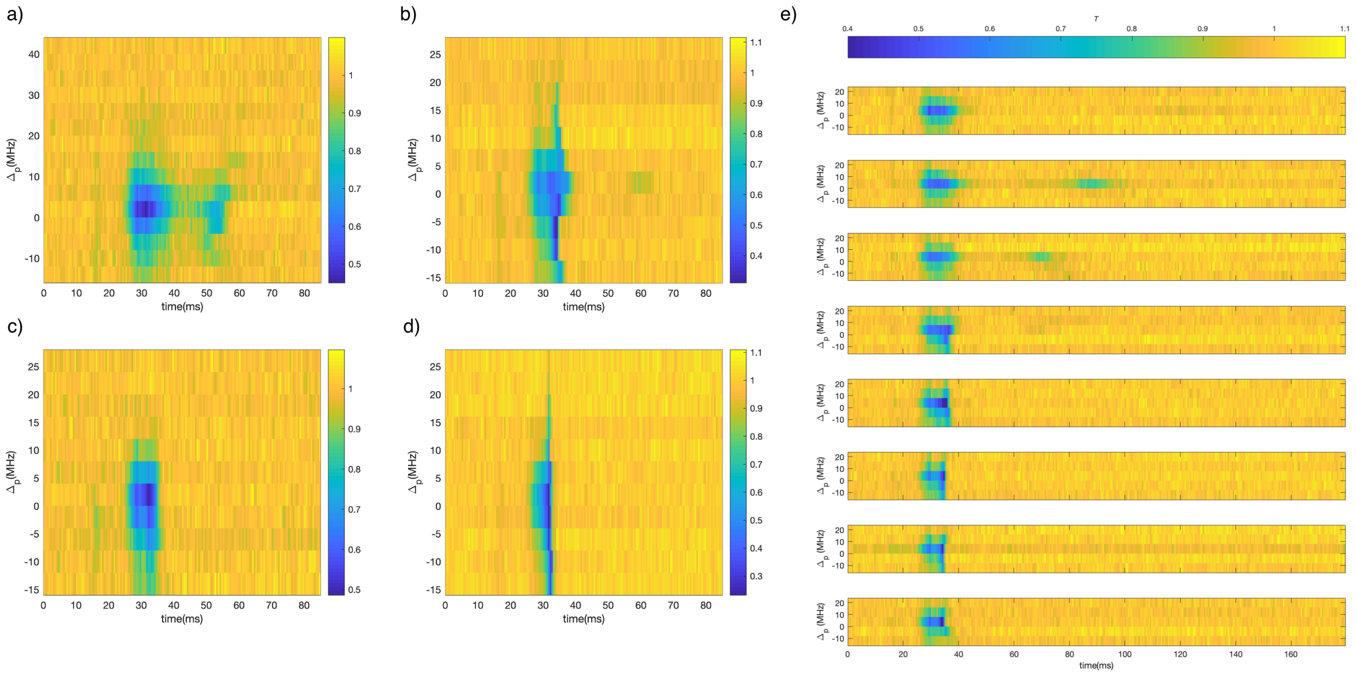

Figure 6.6: a) Spectrum for sling shot experiment with 40 μW blue detuned TE GM and 38 μW red detuned TE GM. With chip to MOT cooling beam $B_{\text{atom}}$ red detuned by 20 MHz. b) Spectrum for sling shot experiment with 40 μW blue detuned TE GM and 38 μW red detuned TE GM. With both free space cooling beam on and detuned by 15 MHz. c) Spectrum for sling shot experiment with 45 μW blue detuned TE GM and 38 μW red detuned TE GM. With $B_{\text{atom}}$ red detuned by 20 MHz, with higher power. d) Spectrum for sling shot experiment with 45 μW blue detuned TE GM and 38 μW red detuned TE GM. With both cooling beam red detuned by 20 MHz, the MOT to chip cooling beam stronger than the other cooling beam to cool the atoms while deaccelerating. e) Spectrum for sling shot experiment with 33 μW blue detuned TE GM and 66 μW red detuned TE GM. The $B_{\text{atom}}$ detuning are scaned, from −30 MHz to 5 MHz in steps of 5 MHz from top to bottom. All experiments are done with a $F = 4 \longrightarrow F' = 4$ optical pumping GM and guided mode doppler TM cooling beam red detuned by 30 MHz. Atoms are probed with a 30 pW TE probe.

## 6.6 Trapping Measurement

### “Differential” Clocked Spectrum

By creating a potential difference between the gap and side of the APCW, the blue-detuned TM Stark GM provides a useful tool to probe the atom dynamics in the center gap region of the APCW. A practical application is measuring the GM intensity or trap depth *in situ*. Fig. 6.7 illustrate the idea of the “differential” measurement. In this example, a red TE Stark GM is measured. Two clocked spectra were taken, one with a blue TM Stark GM (referred as GM1 from now on) with TE probe, the other with the blue TM Stark GM and the red TE Stark GM combined (referred as GM2 from now on) and also probe with a TE probe. In order to remove the effect of device absorbing cesium atoms from the measurements, the two clocked spectrum measurements are interleaved. *E.g.* measure −48 MHz for GM1 and then −48 MHz for GM2, −44 MHz for GM1 and then −44 MHz and so on. The two GMs and a cut of the potential at the thick part of the APCW along the $y$ direction are shown in Fig. 6.7i-iii. Fig. 6.7iv is the clocked spectrum for GM1 and Fig. 6.7v for GM2. The two clocked spectra look similar, but the difference between the two clocked spectra can reveal the effect of the additional red detuned TE Stak GM in GM2. Fig. 6.7vi shows the spectra in Fig. 6.7v subtracted by 6.7iv, the yellow and blue region indicate that the red-detuned TE Stark GM not only modifies the potential but also changes the timing of atom arrival, the blue region occurs earlier than the yellow region indicating that atoms arrive at the center gap earlier due to the attractive force from the red TE Stark GM. The probe frequency difference between the blue and the yellow region shows the potential difference in the center gap of the APCW, ∼20 MHz corresponds to ∼1 mK in this case. The 2D simulated clocked spectrum is shown in Fig. 6.7vii. Fig. 6.7viii shows the different components of Fig. 6.7vii. It is clear that the main contribution is from the “gap” components, showing that the “differential” measurement is most sensitive to the difference in the potential in the central gap of the APCW.

### Trapping measurements

With the cooling setup and the ability to determine the intensity of each component of the GM trap, we performed some experiments aimed to for trapped atoms in the center gap of the APCW. First, atoms are loaded and transport to the APCW with the slingshot experiment sequence, and cooled with polarization cooling around the APCW. The GM trap and a $F = 4 \rightarrow F' = 4$ optical pumping beam are on all this

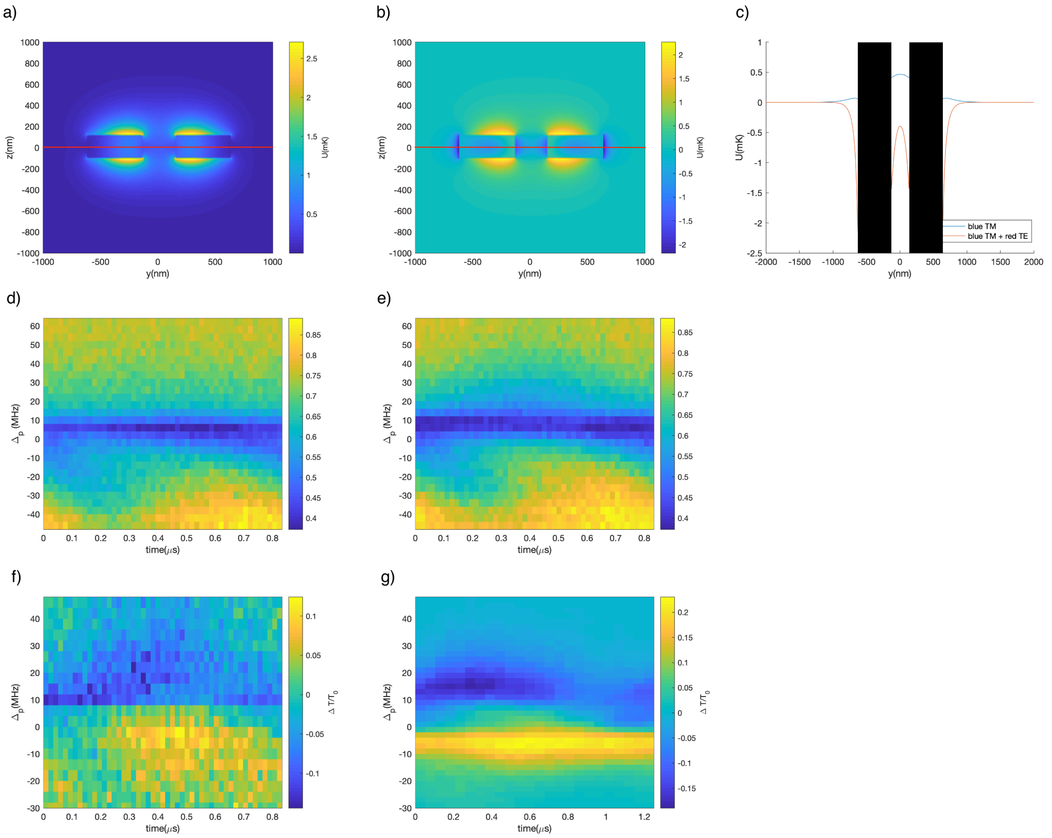

Figure 6.7: a) GM profile for GM1: a blue detuned TM Stark GM. b) GM profile for GM2: a blue detuned TM Stark GM + a red detuned TE Stark GM. c) A cut along the $y$ direction at the thickest part of the APCW, d) A measured clocked spectrum for GM1 with a weak TE probe. e) A measured clocked spectrum for GM2 with a weak TE probe. f) the difference between the clocked spectra showed in d and e. g) Simulated clocked spectrum for f.

time. After the atoms are cooled around the device, the lattice beams turned off and the probe is turned on. The results of these measurement are shown in Fig. 6.8c. Without any guided mode, the probe transmission is reduced by ~5 % in ~5 ms, and with a red-detuned TE Start GM, the probe transmission raised from 0.9 to 1 with the lifetime ~5 ms, with both blue TE Stark GM and red TE Stark GM to form a stable trap, the probe transmission starts with even lower initial value. These results may be interpreted as atom trapping; however, upon further inspection, a large part of these signal is from device cooling after the lattice turned off. Fig. 6.8a shows the change in reflection spectrum when the device is heated with a heater, as the temperature increases the spectrum move to a lower frequency. Before the trapping experiment, the device is tuned by an external heating laser to approximately align the first resonance to the Cesium D1 line, as shown in the red trace Fig. 6.8d. The optical lattice beams further heat the device to a slightly lower frequency, which increases the transmission slightly, and cause the slight dip in transmission after the lattice turns off in Fig. 6.8c, as indicated by the green arrow in Fig. 6.8d (green inset). With the GM on, the device is heated so that the Cesium D1 line is now aligned to the side of the first resonance, when the lattice turns off the transmission increase, as indicated by the red arrow in Fig. 6.8d (red inset).

## 6.7 Measuring Casimir Polder Potential

A full calculation of the CP potential of an atom around the non-trivial geometry of our dielectric structure is extremely involved and requires huge numerical resources. To simplify the calculation, the $C_3$ coefficient of short range van der Walls atom-surface attraction for both Cs ground-state and $6P_{1/2}$ excited state are taken from Ref. [36, 63]. The CP potential for a single nano-beam in the APCW is approximated by only considering the atom-surface attraction force of the atom and its closest dielectric surface. A full calculation of the CP potential as in Ref. [40, 52] of the APCW is under development. However, as seen in Fig. 6.9, our current measurements are already sensitive to the $C_3$ coefficient chosen for the Cs $D1$ transition in our simplified van der Waals model [26, 44]. This simple theory, though not complete, is nonetheless important in generating good correspondence between experiment and simulation. Finally, we note that achieving trapped atoms inside the structure will make our system more sensitive to surface forces. This will enable the ability to investigate CP potentials further and investigate deviations due to additional surface forces such as the deposition of Cs atoms on the waveguide surface [75].(I elaborate on this point in the Chapter. 3)

### Surface Forces

Experiments measuring the influence of surface forces on BECs have shown that alkali atoms adsorbed on the surfaces can produce strong electric fields creating potentials larger than the traditional CP potential [37, 68]. The following is a discussion of how this might affect our system and provide some preliminary indications that such forces are likely not present in our system.

At our current (rather poor) level of accuracy between experiment and simulation, we find no indication that additional surface forces are relevant besides CP. If such

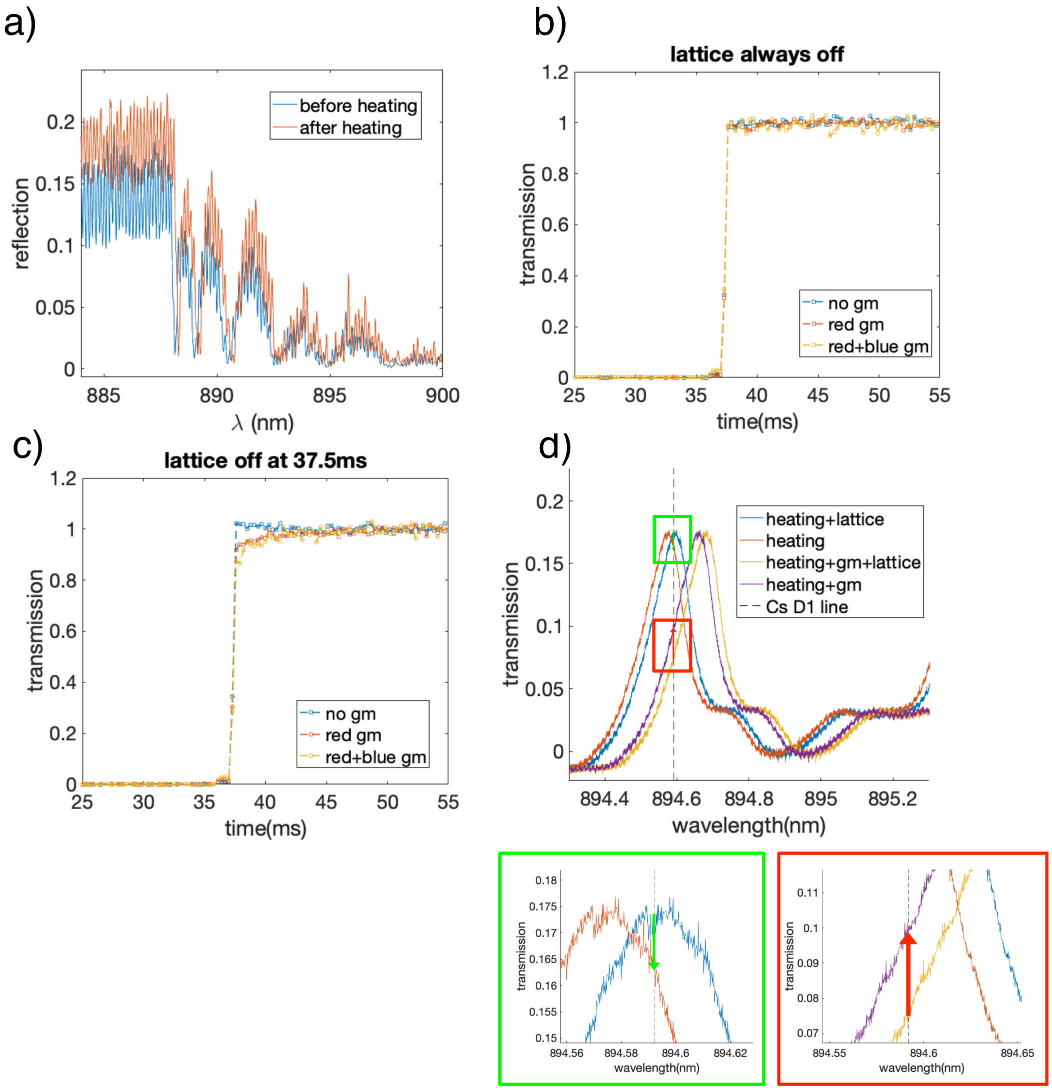

Figure 6.8: a) measured reflection of an APCW around Cesium D1 transision frequency before and after heating, the APCW frequency shifted to lower frequency after heating. b) Trapping experiment without lattice beam for comparison with (c). c) Trapping experiment with lattice beams on, and with various GM settings. d) Illustration of the origin of signals in (c). The green arrow(magnified in the green inset) shows the slight reduction in transmission without the GMs. The red arrow (magnified in the red inset) shows the increase in transmission when the device is heated with GMs.

forces were to exist in our system with strengths similar to CP then atom trapping would still be possible only the guided mode trap potentials would need to be altered to accommodate the extra potential. If, however, these forces were much larger (order of magnitude) than CP then we would no longer be able to deliver a GM Stark potential sufficient to cancel the new potential due to the power handling limitations

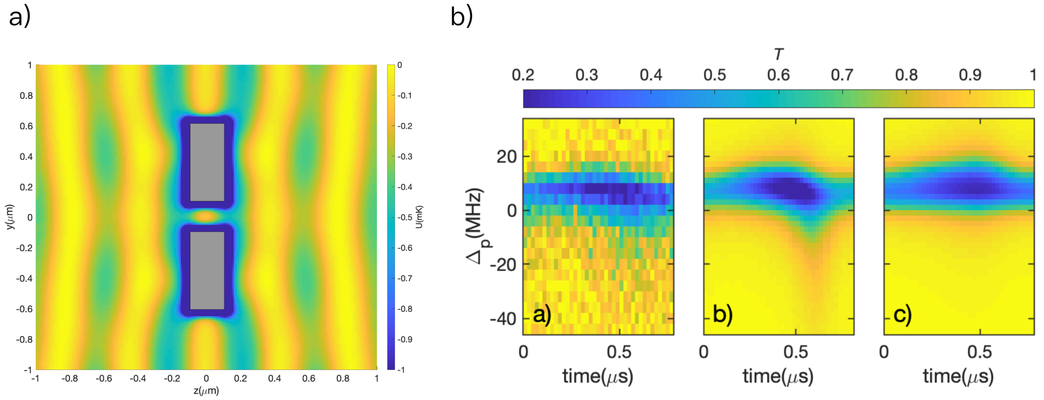

Figure 6.9: a) A potential used in the simulation with optical lattice and the simplified Casimir-Polder potential. b) A comparison of clocked spectra for b(a) experimental data, b(b) simulation with the CP potential and b(c) simulation without the CP potential, for the case of no Stark GM and probing with a weak TM probe. The addition of the CP potential is essential for obtaining good correspondence between experiment and simulation.

of our current devices. A new generation of devices has been fabricated and is being evaluated that should allow 20× higher powers for GM traps.

As for possible mechanisms for additional surface potentials beyond CP, we have devoted considerable effort to understanding the deposition of Cs on our structures. We are able to measure shifts in our bandstructure due to Cs deposition to 1 part in $10^5$, which has allowed us to compare to theoretical models of the index of refraction of the material deposited on the waveguide. For the case of Cs metal deposition with a permittivity $\epsilon_{\mathrm{Cs}} = -3.8 + 1.2i$, our models (that assume a conformal coating) predict that the dielectric bandedge shifts to higher frequency with increasing mass deposited. However, if a dielectric coating is being deposited on the structure (for example $\mathrm{Cs_2O}$ with a permittivity $\epsilon_{\mathrm{Cs_2O}} = 4.8 + 0.8i$), our models predict that the dielectric bandedge would shift to lower frequency with increased deposition. Experimentally, we observe that in measurements such as reported in Chapter 3, the bandedge shifts to lower frequency without exception, which is consistent with a dielectric ($e.g.$ $Cs_xO$) coating on the structure (of thickness ~5-10 nm).

We have further reviewed the literature investigating atom-surface interactions as it relates to patches of deposited alkali atoms. Ref. [75] discusses the interaction of BECs with surface forces and the role of alkali atoms deposited on the surface of metals which could influence these interactions. It appears that this effect is largely due to the comparable work function of the metal and the ionization energy of the atom creating a localized dipole at the surface. The electric field gradient from the dipole creates a spatially dependent force on the BEC to which such experiments are quite sensitive. Again, in our experiment the deposition is on a dielectric surface (Silicon Nitride) and not a metal. Furthermore, our measurements of the bandedge shift is consistent with a conformal deposition of an insulator so no surface dipoles should be present. In fact, Ref. [75] discuss the case where atoms are adsorbed on glass and determine the electric field gradient. The effects are stated to be negligible for atoms on glass (albeit at distance scales much larger than in our work), which is the closest analogue to our Silicon Nitride waveguides. Such experiments with BECs are carried out by observations of changes in trap frequency of the BEC and are as such highly sensitive to changes in the environment. In contrast, we do not yet have trapped atoms so our measurements are currently far from the accuracy regime of those mentioned above. We believe that achieving trapped atoms will help us to make more precise measurements of the surface forces through trap frequency shifts and allow is to definitively answer this important question, unless of course these additional surface forces are so large as to preclude trapping.

Currently, we are developing techniques for measuring the mass loading on our waveguides using the mechanical vibration spectrum. These devices exhibit mechanical Q's of $\sim 2 \times 10^5$ at $\sim$ 2.3MHz so we are optimistic that measurements of the mechanical frequency shift can shed some light on the mechanism of Cs loading onto the waveguide.

### 6.8 Actionable Information

The combination of blue detuned TM GMs and TE probe can provide useful "actionable" information. An example of the general intuition is as follows. As illustrated in Fig. 2.3(b), a TM mode is primarily sensitive to atomic trajectories that intersect the top of the waveguide, while for the TE mode, the regions of highest intensity are on the sides and in the gap between the two beams. Hence, a TE probe can improve our sensitivity to gap and side atoms. In order to distinguish between these two classes of trajectories (side and gap), a TM Stark GM with blue detuning (as in Fig. 6.10(a,b)) can be used to separate atoms interacting with the TE probe into two distinguishable classes. Because of the AC-Stark shift and the spatial intensity distribution of the TM blue GM, an atom entering the vacuum the gap of the APCW will experience a larger AC Stark shift than an atom passing around the side.

One important application is to employ the lattice delivery method to achieve high fractional filling of the trap sites within the APCW by way of a recursive loading scheme (*i.e.*, some small probability to transfer one atom from the moving lattice to a GM trap for the passage of each successive lattice 'pancake'). Such recursive loading requires detailed understanding of the experimental signatures of atoms entering the central vacuum gap of the APCW, including the probability with which atoms actually enter the central gap. With the reliability of the simulations validated, we have some confidence in the result in Fig. 6.10(a) and Fig. 6.10(b), which suggests that a significant fraction of atoms delivered to the APCW do enter the vacuum gap under appropriate conditions of lattice speed and intensity for a TM Stark GM.

This being the case, the next step is to identify the operational signatures for the class of 'gap' atoms in a clocked spectrum, which we have done in Fig. 6.10(c) by way of a TE probe GM. Here, the total clocked spectrum based upon all atom trajectories from the simulation is decomposed into a set of clocked spectra for individual trajectory classes, including the class of trajectories that pass through the central vacuum gap. Figure 6.10(d) zooms into the clocked spectrum by examining spectral cuts at successive time intervals to identify times and detunings for which the gap atoms have distinct spectral signatures. Clearly, the spectrum for all atoms (black curve) has a large peak around probe detuning $\Delta_p \simeq -30$MHz, which predominantly results from atoms entering the central gap at clocked times around $t \simeq 20$ns . For these times and detunings (*i.e.*, $\Delta_p \approx -30\,\text{MHz}$ at $t \approx 20\,\text{ns}$), another GM could be triggered in real time to selectively target gap atoms while they transit the vacuum gap of the APCW in successive lattice 'pancakes'.

## 6.9 Conclusion and Outlook

Trapping and cooling atoms at distance ~100 nm from the internal surfaces of dielectric photonic crystal waveguides (PCWs) requires a new set of advances relative to standard atomic physics techniques. Towards this end, I have described experiments and numerical simulations to understand better the motion of cold atoms under the influence of forces from GM fields within a PCW, external illumination with light transverse to the PCW axis, and CP interactions at the surfaces of the PCW. In particular, a moving optical lattice has been utilized to transport cold atoms to the surfaces and vacuum spaces of a nanoscopic PCW. By way of synchronous detection of the passing optical lattice and EM transmission spectra, we find rich phenomenology related to temporal and spatial variations of AC-Stark shifts, radiative absorption from and emission into GMs, and (vacuum) surface forces, all of which strongly affect atomic motion.

In addition to empirical characterization of the resulting phenomena, my colleagues and I have carried out extensive numerical simulations in an attempt to achieve effective modeling tools with quantitative prediction capabilities, as well as to provide physical insight. Initial validation of the simulations has been made by way of direct comparisons of simulated and measured clocked transmission spectra and reasonable correspondence achieved. By way of our simulations, we can then infer underlying characteristics of atomic motion and internal fields, and to some modest degree, control atomic dynamics within and near the PCW (*e.g.*, maximizing the number of atoms that pass through the central vacuum gap of the PCW and providing operational signatures manifest in the associated clocked spectra).

Understanding the interplay of forces from GM traps, moving optical lattices, and surfaces of the APCW on the motion of atoms constitutes a significant step towards GM trapping of arrays of atoms within unit cells along the PCW. With current experimental condition, we estimate ~2 atoms per pancake delivered to the vacuum gap of the APCW. Since each experiment cycle delivers $\sim$ 1800 pancakes, a modest trap transfer efficiency of 2 % leads to $\sim$ 70 successful trapping events per cycle. Observations of single and collective radiative phenomena would then become possible in this engineered photonic environment, as Refs. [20, 33, 42, 51] described theoretically.

Throughout this thesis, we have treated the atoms as classical point particles without interactions. Surely, at densities of $1 \times 10^{12}$ atoms cm$^{-3}$, encountered around and within the APCW, these assumptions are no longer completely valid and a richer set of atomic interactions are accessible. Future experiments should investigate more carefully density dependent effects, including inelastic hyperfine changing collisions and light-assisted collisions, which are critical for loading free-space optical tweezers [58, 91].

Moreover, we have ignored the wave character of the atoms (*e.g.*, at $v_{\text{lattice}} = 0.51\,\text{m}\,\text{s}^{-1}$ the deBroglie wavelength $\lambda_{\text{dB}} \simeq 6\text{nm}$). However, as the atomic velocity is reduced during cooling and trapping, $\lambda_{\text{dB}}$ can become comparable to the dimensions of the vacuum spaces in the APCW (*e.g.*, at 10μK, $v_{\text{atom}} = 0.03\,\text{m}\,\text{s}^{-1}$, and $\lambda_{\text{dB}} \simeq 100\text{nm}$). In this regime, novel physics might be manifest as we arc back to the beginning of atom interactions with periodic nano-structures [26, 59].

Aside from trapping atoms in these nano-structures one can imagine specifically designed experiments tailored toward more precise measurements of CP forces at dielectrics surfaces. The ubiquity of the lattice delivery method does not require a structure as complicated as the APCW and in fact a more simple structure would ease the transition of our 2D simulations to a full 3-dimensional simulation model.

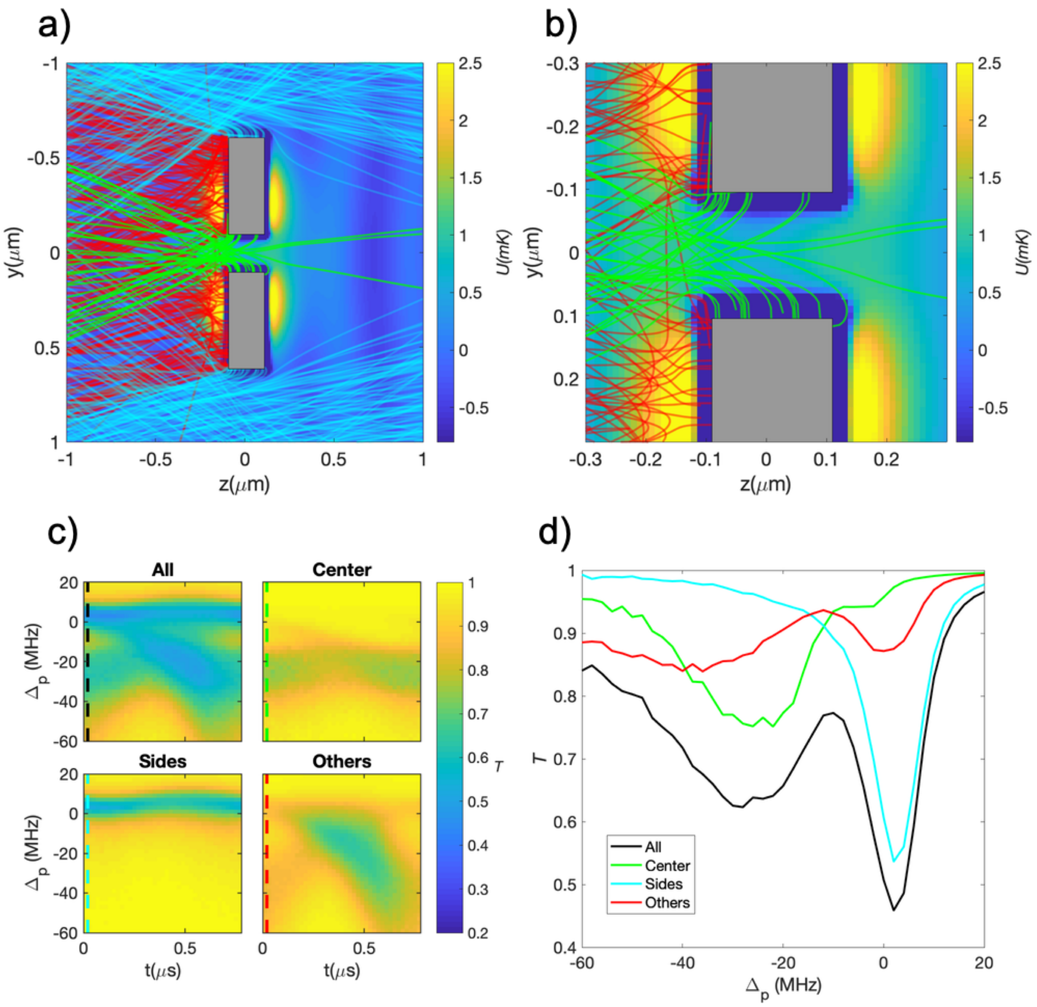

Figure 6.10: a) Different classes of atom trajectories with a TM blue detuned Stark beam. The green trajectories are the ‘center’ trajectories that enter the gap of the APCW. The blue trajectories are the ‘sides’ trajectories that go around the sides of the APCW. And the red trajectories are ‘other’ trajectories that bounce from or crash on the surface facing incoming atoms of the APCW. b) A zoomed view of the center gap showing atom trajectories entering the APCW. A large fraction of atoms penetrate deep into the gap before crashing into the dielectric wall via CP forces. c) The clocked spectra for a TE probe of the different classes of atom trajectories shown in (a) and (b). Notice the separation of different classes in both time and AC stark shift. d) A cut at 20 ns in the clocked spectrum, as shown by the dashed lines in (c). The black line shows the spectrum of all trajectories. The color lines show the spectra of corresponding classes of trajectories in (a,b). The spectrum for all atoms (black curve) has a large peak around probe detuning $\Delta_p \simeq -30$ MHz, which predominantly results from atoms entering the central gap. For these times and detunings, another GM could be triggered in real time to selectively target gap atoms (*e.g.*, for trapping) while they transit the vacuum gap of the APCW in successive lattice ‘pancakes’.

## *Chapter 7*

# PULSE-PROBE MEASUREMENT

As mentioned in Chapter 6, a different application of our system of clocked-atoms delivered to a PCW is the utilization of this time-dependent, optically dense atomic medium for novel nonlinear optical experiments, such as soliton propagation, as investigated in Ref. [61]. In this chapter, I present the experimental results and the theoretical model of the experiments.

### 7.1 Experimental Setup

The experimental apparatus for the pulse-probe measurements are the same as the one described in Chapter 3, with the addition of a pulse modulation setup. The pulse modulation setup consists of two Jenoptik electro-optic modulators (EOM), and two YYLabs modulator bias controllers. The modulator bias controllers feedback to the bias voltages to minimize the transmitted light when the pulse is off. The delay between the two pulses is adjusted to make sure the two EOMs switch on and off simultaneously. With this setup, we can obtain $\sim 1 \times 10^6$ extinction ratio. After the pulse modulation setup, the pulses are sent into the probe GM filtering setup.

The pulse probe measurements can be taken in either the optical lattice clocked delivery configuration or the sling-shot configuration. With the optical lattice clocked delivery configuration, the input pulses are triggered by the optical lattice clock timing signal. The offset time can be changed so the pulses could interact with an optical system with selected values of $\Gamma_{\mathrm{1D}}^{\mathrm{eff}}, J_{\mathrm{1D}}^{\mathrm{eff}}, \Delta_{\mathrm{AC}}, \Gamma'$ as in Fig. 6.2(c). In the sling-shot configuration, the repetition rate of the pulse can be higher, as long as it is slower than the atomic decay rate $\Gamma$. This higher repetition rate allows us to gather more data from one experimental cycle, which reduces the statistical uncertainty.

One critical aspect of the experiment is maintaining the stable APCW spectrum, so the optical properties of the APCW remain the same throughout the experiment. The bin size of the photon count histogram is 200 ps, so for each configuration $\sim 100$ cycles of experiments are required to accumulate enough counts. Considerable effort has been made to make sure the probe frequency is always aligned with the APCW transmission spectrum. The tuning process is described in section 3.3.

## 7.2 Experimental Results

Here I present the experimental results of the pulse-probe measurements. Fig. 7.1 shows the results of pulse-probe measurements for selected average probe powers. The experiment is done with the sling-shot configuration, with atoms delivered to the APCW at the speed of $0.5\,\mathrm{m\,s^{-1}}$. The probe is modulated with the pulse modulation setup, and is on all the time during the experiment with a repetition rate of 5 MHz and duration of 2 ns. The transmitted photon counts collected during the 1 ms while atoms pass through the device are collected to produce the blue traces in Fig. 7.1. Also, after the pulses end, 15 ms of photon counts are collected to generate the reference traces colored red in Fig. 7.1. During this time the optical lattice power is kept at constant to prevent the thermal effect from changing the optical properties of the device. The photon counts $C$ are normalized to one experiment cycle (5000 pulses).

I present two analysis of the experimental data in Fig. 7.2. Fig. 7.2a shows the percentage difference between the area of the output pulse and the reference pulse. $C_{\mathrm{ref}}$ is the integrated counts (*i.e.*, area) of the reference pulse(i,e, no atoms), and $C_p$ is the area of the output pulse with atoms present. $\Delta C = C_{\mathrm{ref}} - C_p$ is the area difference. In fig. 7.2a, $\frac{\Delta C}{C_{\mathrm{ref}}}$ oscillates as $\sqrt{P_{\mathrm{probe}}}$ increase. We believe the phenomenon is similar to the “area law” derived by McCall and Hahn [73]. The area law describes the evolution of the area as the pulse propagates through the atomic medium. Pulses with areas that are even multiples of $\pi$ will propagate through the atomic medium without changing their shape, independent on the inhomogeneous broadening of the atoms. Moreover, the area law describes the evolution of the area of the pulse, for any value of the input area. For input areas that are not even multiples of $\pi$, the atomic medium is not transparent, and after propagating in the medium for enough time, the area will approach the closest even multiple of $\pi$. McCall and Hahn derived the area law for classical dense atomic medium. Ana Asenjo-Garcia and Jenny Sheng have shown that it is also valid for a system consisting of a PCW and a 1D atom array, here in the thin sample regime of McCall and Hahn.

In Fig. 7.2b, $C_{\mathrm{tail}}$ is the integrated counts for 5 ns after the pulse, beginning at $t = 127.5$ ns. As the input pulse area $\sqrt{P_{\mathrm{probe}}}$ increases, $C_{\mathrm{tail}}$ also increases, showing stronger population inversion after the pulse. This observation agrees with theoretical model as described in the next section.

One difficulty of the pulse-probe experiment is that to observe the area law, or the Rabi frequency of the atomic ensemble, the number of atoms and $\Gamma_{\mathrm{1D}}$ have to be the same for each pulse. Due to random atomic position in each cycle of delivery of atoms, this is not the case for our optical lattice delivery experiment, so the oscillations for these experiments smear out after averaging. These difficulties could be overcome by trapping atoms in the vacuum gap, or precise control of atoms number and position around the device with optical tweezers.

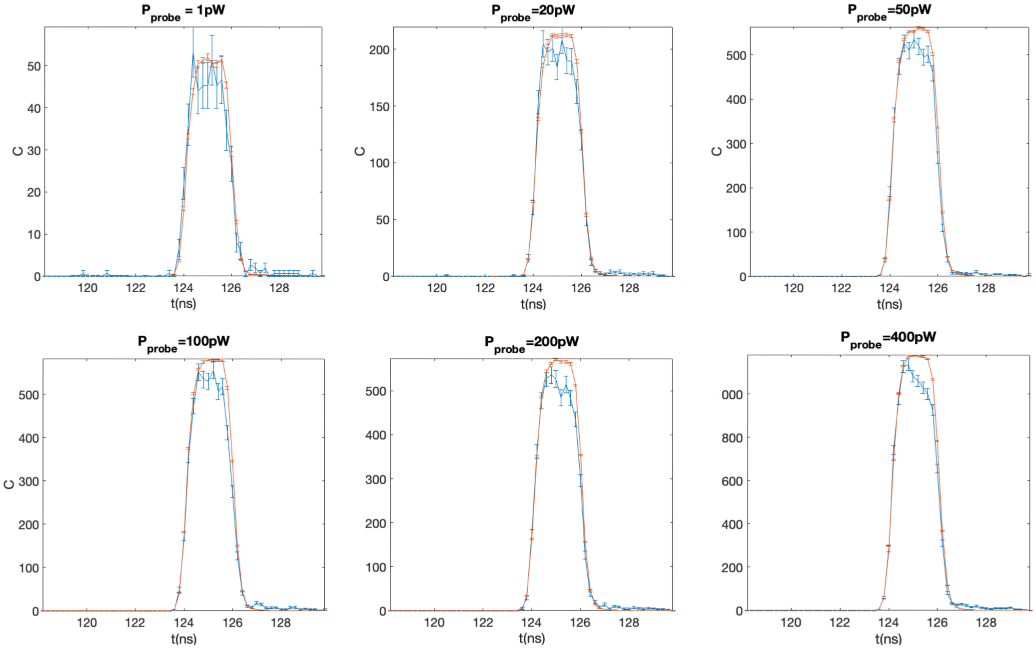

Figure 7.1: Results of pulse-probe measurements for selected probe powers. The red traces are the output pulses without atoms being delivered to the device (*i.e.*, reference pulses), and the blue traces are the output pulses taken as the optical lattice delivers the atom to the APCW in the sling-shot configuration. The input probe pulse is triggered with a repetition rate of 5 MHz with the duration of 2 ns, and the probe power $P_{\text{probe}}$ is the average power delivered to the APCW. The output pulses without atoms (red traces) have smaller error bar since they are averaged over 15 ms, longer than the 1.0 ms averaging time of the output pulses with atoms (blue trace). The photon counts $C$ are normalized to one experiment cycle (5000 pulses).

## 7.3 Theoretical Model

In this section, I present the theoretical model developed by Ana Asenjo-Garcia and Jenny Sheng to calculate the output pulse for our experiment, which Ana Asenjo-Garcia did the numerical calculation. Fig. 7.3 illustrates the setup. A pulse with field magnitude $\mathcal{E}_R^{\text{in}}(t)$ and duration $\tau$ is input from the left side. The pulse propagates along a medium consisting of a 1D array of $N$ atoms with periodicity $d$ coupled to a photonic crystal waveguide. The spontaneous emission rates into the waveguide and free space modes are $\Gamma_{\text{1D}}$ and $\Gamma'$, respectively. In this model, we assume that all

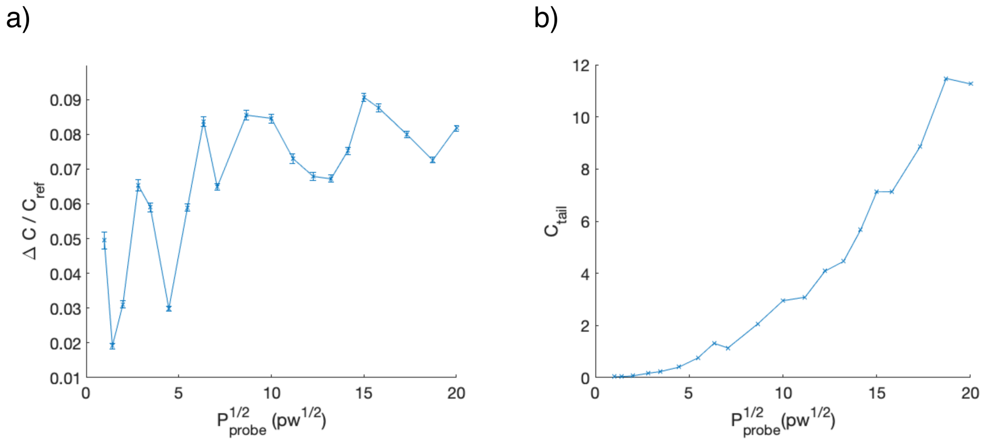

Figure 7.2: These analysis are done on the set of data presented in Fig. 7.1. a) $\Delta C$ is defined as the difference of pulse area with and without atoms. And $C_{\text{ref}}$ is the pulse area of the output pulse without atoms. By plotting $\frac{\Delta C}{C_{\text{ref}}}$ against the square root of the input probe power $\sqrt{P_{\text{probe}}}$, we observe an oscillatory input to output mapping. We suggest that this phenomenom is similar to the "area law" derived by McCall and Hahn [73]. b) $C_{\text{tail}}$ is the integrated counts for 5 ns after the pulse, beginning at $t = 127.5$ ns. The increase of $C_{\text{tail}}$ indicates a larger excited-state population as $\sqrt{P_{\text{probe}}}$ increases.

the atoms couple to the PCW in the same way, so the $\Gamma_{\text{1D}}$ and $\Gamma'$ are the same for all atoms.

To calculate the time dynamics of the fields we need to solve the evolution of the atomic density matrix in the waveguide regime far from a band edge of the PCW. The output field can be recovered using the generalized input-output equation. The master equation is given by

$$\dot{\rho}_A = \frac{i}{\hbar}\left[\mathcal{H}_{\text{tot}}, \rho_A\right] + \mathcal{L}\left[\rho_A\right], \tag{7.1}$$

where $\mathcal{L}$ is the Lindblad operator. The hamiltonian operator $\mathcal{H}_{\text{tot}}$ is the sum of the pump Hamiltonian and atom-atom interaction Hamiltonian, $\mathcal{H}_{\text{tot}} = \mathcal{H}_{\text{p}} + \mathcal{H}_{\text{int}}$. For a pulse with carrier frequency on resonance with the atomic transition frequency, the pump Hamiltonian is

$$\mathcal{H}_p = -\hbar\mathcal{E}_R^{\text{in}}(t)\sqrt{\frac{\Gamma_{\text{1D}}}{2}}\sum_{j=1}^{N}\left(\hat{\sigma}_{eg}^{j}e^{ikz_j} + \hat{\sigma}_{ge}^{j}e^{-ikz_j}\right) \tag{7.2}$$

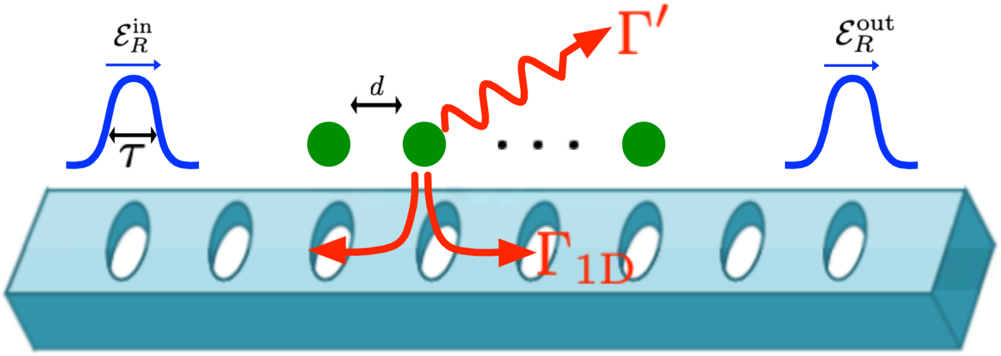

Figure 7.3: A right moving input pulse of magnitude $\mathcal{E}_R^{\mathrm{in}}(t)$ and duration $\tau$ propagates along a waveguide coupled with an 1D array of atoms with periodicity $d$. The spontaneous emission rates into the waveguide and free space are $\Gamma_{1\mathrm{D}}$ and $\Gamma'$, respectively.

where $k$ is the guided mode wave-vector, and $z_j$ is the position of atom $j$. The atom-atom interaction Hamiltonian is given by

$$\mathcal{H}_{\mathrm{int}} = \frac{\hbar\Gamma_{1\mathrm{D}}}{2}\sum_{i,j=1}^{N}\sin\left(k\left|z_i - z_j\right|\right)\hat{\sigma}_{eg}^{i}\hat{\sigma}_{ge}^{j}. \tag{7.3}$$

And the Lindblad operator is

$$\mathcal{L}\left[\rho\right] = \frac{1}{2}\sum_{i,j=1}^{N}\left(\Gamma_{1\mathrm{D}}\cos\left(k\left|z_i - z_j\right|\right) + \Gamma'\delta_{ij}\right)\times\left(2\hat{\sigma}_{ge}^{i}\rho\hat{\sigma}_{eg}^{j} - \hat{\sigma}_{eg}^{i}\hat{\sigma}_{ge}^{j}\rho - \rho\hat{\sigma}_{eg}^{i}\hat{\sigma}_{ge}^{j}\right) \tag{7.4}$$

Finally, with the input-output equation, the output of the right propagating component of the electric field is

$$\hat{E}_R^{+}(z_{\mathrm{end}}) = \mathcal{E}_R^{\mathrm{in}}(t)e^{ikz_{\mathrm{end}}} + i\sqrt{\frac{\Gamma_{1\mathrm{D}}}{2}}\sum_{j=1}^{N}\hat{\sigma}_{ge}^{j}e^{ik(z_{\mathrm{end}}-z_j)} \tag{7.5}$$

where $z_{\mathrm{end}}$ is the position at the end of the 1D atom array.

For the numerical calculate, the input and output pulses are digitized by creating a histogram of photon counts from the SPCM. The master equation eq. 7.1 is then solved with the digitized input pulse. Fig. 7.4 shows the comparison between theory and experiment. For an toy model, the theoretical calculations are performed for a single atom ($N = 1$) coupling to the PCW, with $\frac{\Gamma_{1D}}{\Gamma'} = 2.2$ and Rabi frequency $\frac{\Omega}{\Gamma'} = 1.8$, while the calculations for Fig. 7.5 are done for $N = 4$ , $\frac{\Gamma_{1D}}{\Gamma'} = 0.55$ and $\frac{\Omega}{\Gamma'} = 3.6$. For the two calculations, the product of atom number and $\Gamma_{1D}$, $N\Gamma_{1D}$ , are kept the same, and the Rabi frequency, (*i.e.*, the pulse itensity) is adjusted to fit the experimental result. Both calculations agree well with the experiment, it is thus difficult to extract actual atom number from the experiment, although one can estimate a value for $\frac{N\Gamma_{1D}}{\Gamma'} = 2.2$. From the measurement of atom number in the optical lattice, and by fitting the experimental clocked spectrum with numerical simulation, we estimate on average of 2 atoms enter the center vacuum gap per optical lattice pancake, and at the center vacuum gap $\frac{\Gamma_{1D}}{\Gamma'} \sim 10$, so the estimation of $\frac{N\Gamma_{1D}}{\Gamma'} = 2.2$ is lower than expected.

The shape of the transmitted pulse is affected by two factors. The first factor is the optical depth. As the atoms re-emit the light, there is destructive interference with the incoming pulse and this leads to the tilted profile of the output pulse. The second factor is the Rabi frequency, which causes atomic population inversion. If the Rabi frequency is large enough by the end of the pulse duration, the atom will be inverted and the light will be transmitted again, causing oscillation within the pulse. In the experiment the pulse intensity is not strong enough for this to happen, however, it is still significant enough to "flatten" the later part (after $\Gamma' t = 0.3$) of the output pulse.

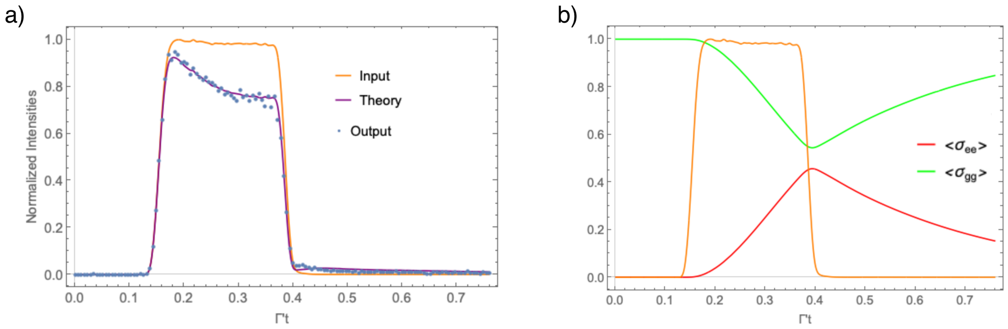

Figure 7.4: a) Intensity of the input (orange) pulse and experimental output (blue dots) pulse. The theoretical calculated transmission pulse is in purple, which is calculated for $N = 1$, $\frac{\Gamma_{1D}}{\Gamma'} = 2.2$ and $\frac{\Omega}{\Gamma'} = 1.8$. b) Excited and ground state populations are calculated with the experimental pulse, for the same parameters.

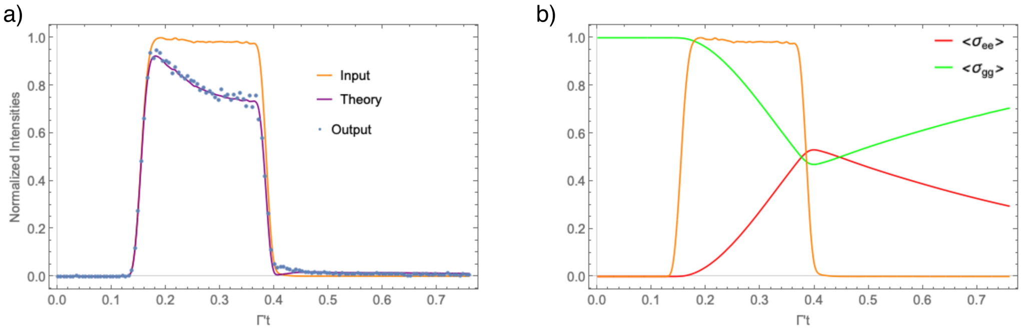

Figure 7.5: a) Intensity of the input (orange) pulse and experimental output (blue dots) pulse. The theoretical calculated transmission pulse is in purple, which is calculated for $N = 4$, $\frac{\Gamma_{1D}}{\Gamma'} = 0.55$ and $\frac{\Omega}{\Gamma'} = 3.6$. b) Excited and ground state populations are calculated with the experimental pulse, for the same parameters.

# BIBLIOGRAPHY

[1] DJ Alton, NP Stern, Takao Aoki, Hansuek Lee, E Ostby, KJ Vahala, and HJ Kimble. Strong interactions of single atoms and photons near a dielectric boundary. *Nat. Phys.*, 7(2):159, 2011. doi: 10.1038/nphys1837.

[2] Takao Aoki, Barak Dayan, E. Wilcut, W. P. Bowen, A. S. Parkins, T. J. Kippenberg, K. J. Vahala, and H. J. Kimble. Observation of strong coupling between one atom and a monolithic microresonator. 443(7112):671. ISSN 1476-4687. doi: 10.1038/nature05147. URL `https://www.nature.com/articles/nature05147`.

[3] A Asenjo-Garcia, J D Hood, D E Chang, and H J Kimble. Atom-light interactions in quasi-one-dimensional nanostructures: A Green's-function perspective. *Phys. Rev. A*, 95(3):033818–16, March 2017. doi: 10.1103/PhysRevA.95.033818.

[4] A Asenjo-Garcia, M Moreno-Cardoner, A Albrecht, H J Kimble, and D E Chang. Exponential improvement in photon storage fidelities using subradiance and "selective radiance" in atomic arrays. *Phys. Rev. X*, 7:031024, Aug 2017. doi: 10.1103/PhysRevX.7.031024. URL `https://link.aps.org/doi/10.1103/PhysRevX.7.031024`.

[5] A. Ashkin. Acceleration and trapping of particles by radiation pressure. 24(4):156–159. doi: 10.1103/PhysRevLett.24.156. URL `https://link.aps.org/doi/10.1103/PhysRevLett.24.156`.

[6] S Travis Bannerman, Gabriel N Price, Kirsten Viering, and Mark G Raizen. Single-photon cooling at the limit of trap dynamics: Maxwell's demon near maximum efficiency. *New J. Phys.*, 11(6):063044, 2009. doi: 10.1088/1367-2630/11/6/063044.

[7] Daniel Barredo, Vincent Lienhard, Sylvain de Léséleuc, Thierry Lahaye, and Antoine Browaeys. Synthetic three-dimensional atomic structures assembled atom by atom. 561(7721):79. ISSN 1476-4687. doi: 10.1038/s41586-018-0450-2. URL `https://www.nature.com/articles/s41586-018-0450-2`.

[8] Kristian Baumann, Christine Guerlin, Ferdinand Brennecke, and Tilman Esslinger. Dicke quantum phase transition with a superfluid gas in an optical cavity. 464(7293):1301–1306. ISSN 1476-4687. doi: 10.1038/nature09009. URL `https://www.nature.com/articles/nature09009`.

[9] J-B Béguin, EM Bookjans, SL Christensen, HL Sørensen, JH Müller, ES Polzik, and J Appel. Generation and detection of a sub-poissonian atom

number distribution in a one-dimensional optical lattice. *Phys. Rev. Lett.*, 113 (26):263603, 2014. doi: 10.1103/PhysRevLett.113.263603.

[10] Helmar Bender, Christian Stehle, Claus Zimmermann, Sebastian Slama, Johannes Fiedler, Stefan Scheel, Stefan Yoshi Buhmann, and Valery N Marachevsky. Probing atom-surface interactions by diffraction of bose-einstein condensates. *Phys. Rev. X*, 4(1):011029, 2014. doi: 10.1103/PhysRevX.4.011029.

[11] Jeff Bezanson, Alan Edelman, Stefan Karpinski, and Viral B. Shah. Julia: A fresh approach to numerical computing. *CoRR*, abs/1411.1607, 2014. URL `http://arxiv.org/abs/1411.1607`.

[12] P. Bienias, S. Choi, O. Firstenberg, M. F. Maghrebi, M. Gullans, M. D. Lukin, A. V. Gorshkov, and H. P. Büchler. Scattering resonances and bound states for strongly interacting rydberg polaritons. 90(5):053804. doi: 10.1103/PhysRevA.90.053804. URL `https://link.aps.org/doi/10.1103/PhysRevA.90.053804`.

[13] Daniel Bloch and Martial Ducloy. Atom-wall interaction. In *Advances in atomic, molecular, and optical physics*, volume 50, pages 91–154. Elsevier, 2005. doi: 10.1016/S1049-250X(05)80008-4.

[14] Immanuel Bloch, Jean Dalibard, and Wilhelm Zwerger. Many-body physics with ultracold gases. 80(3):885–964. ISSN 0034-6861. doi: 10.1103/RevModPhys.80.885. URL `http://link.aps.org/doi/10.1103/RevModPhys.80.885`.

[15] M. Brune, F. Schmidt-Kaler, A. Maali, J. Dreyer, E. Hagley, J. M. Raimond, and S. Haroche. Quantum rabi oscillation: A direct test of field quantization in a cavity. 76(11):1800–1803. doi: 10.1103/PhysRevLett.76.1800. URL `https://link.aps.org/doi/10.1103/PhysRevLett.76.1800`.

[16] A. P. Burgers, L. S. Peng, J. A. Muniz, A. C. McClung, M. J. Martin, and H. J. Kimble. Clocked atom delivery to a photonic crystal waveguide. *Proceedings of the National Academy of Sciences*, 116(2):456–465, 2019. ISSN 0027-8424. doi: 10.1073/pnas.1817249115. URL `https://www.pnas.org/content/116/2/456`.

[17] Hilton W. Chan, Adam T. Black, and Vladan Vuletić. Observation of collective-emission-induced cooling of atoms in an optical cavity. 90(6):063003. doi: 10.1103/PhysRevLett.90.063003. URL `https://link.aps.org/doi/10.1103/PhysRevLett.90.063003`.

[18] D E Chang, L Jiang, AV Gorshkov, and HJ Kimble. Cavity qed with atomic mirrors. *New J. Phys.*, 14(6):063003, 2012. doi: 10.1088/1367-2630/14/6/063003.

[19] Darrick E. Chang, Vladan Vuletić, and Mikhail D. Lukin. Quantum nonlinear optics — photon by photon. 8(9):685–694. ISSN 1749-4893. doi: 10.1038/nphoton.2014.192. URL `https://www.nature.com/articles/nphoton.2014.192`.

[20] DE Chang, JS Douglas, A González-Tudela, C-L Hung, and HJ Kimble. Colloquium: Quantum matter built from nanoscopic lattices of atoms and photons. *Rev. Mod. Phys.*, 90(3):031002, 2018. doi: 10.1103/RevModPhys.90.031002.

[21] M Chevrollier, Daniel Bloch, G Rahmat, and Martial Ducloy. Van der waals-induced spectral distortions in selective-reflection spectroscopy of cs vapor: the strong atom–surface interaction regime. *Opt. Lett.*, 16(23):1879–1881, 1991. doi: 10.1364/OL.16.001879.

[22] K S Choi, H J Kimble, J D Hood, D E Chang, C L Hung, A Goban, S P Yu, M J Martin, J A Muniz, J H Lee, A C McClung, and O Painter. Atom-light interactions in photonic crystals. page 11. URL `http://arxiv.org/abs/1312.3446`.

[23] Steven Chu. The manipulation of neutral particles. *Rev. Mod. Phys*, pages 685–706, 1998.

[24] J. Ignacio Cirac and Peter Zoller. Goals and opportunities in quantum simulation. 8:264–266. ISSN 1745-2481. doi: 10.1038/nphys2275. URL `https://www.nature.com/articles/nphys2275`.

[25] J D Cohen, S M Meenehan, and Oskar Painter. Optical coupling to nanoscale optomechanical cavities for near quantum-limited motion transduction. 555 (2011):550–555. URL `http://www.opticsinfobase.org/abstract.cfm?uri=oe-21-9-11227`.

[26] Alexander D Cronin, Jörg Schmiedmayer, and David E Pritchard. Optics and interferometry with atoms and molecules. *Rev. Mod. Phys.*, 81(3):1051, 2009. doi: 10.1103/RevModPhys.81.1051.

[27] Andrew J. Daley, Martin M. Boyd, Jun Ye, and Peter Zoller. Quantum computing with alkaline-earth-metal atoms. 101(17):170504. doi: 10.1103/PhysRevLett.101.170504. URL `https://link.aps.org/doi/10.1103/PhysRevLett.101.170504`.

[28] J. Dalibard and C. Cohen-Tannoudji. Laser cooling below the doppler limit by polarization gradients: simple theoretical models. 6(11):2023–2045. ISSN 1520-8540. doi: 10.1364/JOSAB.6.002023. URL `https://www.osapublishing.org/josab/abstract.cfm?uri=josab-6-11-2023`.

[29] Jean Dalibard and Claude Cohen-Tannoudji. Laser cooling below the doppler limit by polarization gradients: simple theoretical models. *JOSA B*, 6(11): 2023–2045, 1989. doi: 10.1364/JOSAB.6.002023.

[30] Ivan H. Deutsch and Poul S. Jessen. Quantum-state control in optical lattices. 57(3):1972–1986. doi: 10.1103/PhysRevA.57.1972. URL `https://link.aps.org/doi/10.1103/PhysRevA.57.1972`.

[31] E. Dimova, O. Morizot, G. Stern, C. L. Garrido Alzar, A. Fioretti, V. Lorent, D. Comparat, H. Perrin, and P. Pillet. Continuous transfer and laser guiding between two cold atom traps. 42(2):299–308. ISSN 1434-6079. doi: 10.1140/epjd/e2007-00022-0. URL `https://doi.org/10.1140/epjd/e2007-00022-0`.

[32] Peter Domokos and Helmut Ritsch. Collective cooling and self-organization of atoms in a cavity. 89(25):253003. doi: 10.1103/PhysRevLett.89.253003. URL `https://link.aps.org/doi/10.1103/PhysRevLett.89.253003`.

[33] J S Douglas, H Habibian, C-L Hung, AV Gorshkov, H J Kimble, and D E Chang. Quantum many-body models with cold atoms coupled to photonic crystals. *Nat. Photonics*, 9(5):326–331, 2015. doi: 10.1038/nphoton.2015.57.

[34] R. W. P. Drever, J. L. Hall, F. V. Kowalski, J. Hough, G. M. Ford, A. J. Munley, and H. Ward. Laser phase and frequency stabilization using an optical resonator. 31(2):97–105. ISSN 1432-0649. doi: 10.1007/BF00702605. URL `https://doi.org/10.1007/BF00702605`.

[35] Manuel Endres, Hannes Bernien, Alexander Keesling, Harry Levine, Eric R. Anschuetz, Alexandre Krajenbrink, Crystal Senko, Vladan Vuletic, Markus Greiner, and Mikhail D. Lukin. Atom-by-atom assembly of defect-free one-dimensional cold atom arrays. 354(6315):1024–1027. ISSN 0036-8075, 1095-9203. doi: 10.1126/science.aah3752. URL `https://science.sciencemag.org/content/354/6315/1024`.

[36] H. Failache, S. Saltiel, M. Fichet, D. Bloch, and M. Ducloy. Resonant coupling in the van der waals interaction between an excited alkali atom and a dielectric surface: an experimental study via stepwise selective reflection spectroscopy. *The European Physical Journal D - Atomic, Molecular, Optical and Plasma Physics*, 23(2):237–255, May 2003. ISSN 1434-6079. doi: 10.1140/epjd/e2003-00098-4. URL `https://doi.org/10.1140/epjd/e2003-00098-4`.

[37] Sebastian Fuchs, Robert Bennett, Roman V. Krems, and Stefan Yoshi Buhmann. Nonadditivity of optical and casimir-polder potentials. *Phys. Rev. Lett.*, 121:083603, Aug 2018. doi: 10.1103/PhysRevLett.121.083603. URL `https://link.aps.org/doi/10.1103/PhysRevLett.121.083603`.

[38] A. Goban, K. S. Choi, D. J. Alton, D. Ding, C. Lacroûte, M. Pototschnig, T. Thiele, N. P. Stern, and H. J. Kimble. Demonstration of a state-insensitive, compensated nanofiber trap. *Phys. Rev. Lett.*, 109:033603, Jul 2012. doi: 10.

1103/PhysRevLett.109.033603. URL `https://link.aps.org/doi/10.1103/PhysRevLett.109.033603`.

[39] A Goban, C-L Hung, S-P Yu, J D Hood, J A Muniz, J H Lee, M J Martin, AC McClung, KS Choi, D E Chang, and H J Kimble. Atom–light interactions in photonic crystals. *Nat. Commun.*, 5:3808, 2014. doi: 10.1038/ncomms4808.

[40] A Goban, C-L Hung, J D Hood, S-P Yu, J A Muniz, O Painter, and H J Kimble. Superradiance for atoms trapped along a photonic crystal waveguide. *Phys. Rev. Lett.*, 115:063601, Aug 2015. doi: 10.1103/PhysRevLett.115.063601. URL `https://link.aps.org/doi/10.1103/PhysRevLett.115.063601`.

[41] Alejandro González-Tudela and J Ignacio Cirac. Quantum emitters in two-dimensional structured reservoirs in the nonperturbative regime. *Phys. Rev. Lett.*, 119(14):143602, 2017. doi: 10.1103/PhysRevLett.119.143602.

[42] Alejandro González-Tudela, C-L Hung, Darrick E Chang, J Ignacio Cirac, and HJ Kimble. Subwavelength vacuum lattices and atom–atom interactions in two-dimensional photonic crystals. *Nat. Photonics*, 9(5):320, 2015. doi: 10.1038/nphoton.2015.54.

[43] B Gouraud, D Maxein, A Nicolas, O Morin, and J Laurat. Demonstration of a memory for tightly guided light in an optical nanofiber. *Phys. Rev. Lett.*, 114(18):180503, 2015. doi: 10.1103/PhysRevLett.114.180503.

[44] Maxwell D Gregoire, Nathan Brooks, Raisa Trubko, and Alexander D Cronin. Analysis of polarizability measurements made with atom interferometry. *Atoms*, 4(3):21, 2016. doi: 10.3390/atoms4030021.

[45] Rudolf Grimm, Matthias Weidemüller, and Yurii B Ovchinnikov. Optical dipole traps for neutral atoms. *Advances In Atomic*, 42:95–170. doi: 10.1016/S1049-250X(08)60186-X. URL `http://adsabs.harvard.edu/cgi-bin/nph-data_query?bibcode=2000AAMOP..42...95G&link_type=EJOURNAL`.

[46] Rudolf Grimm, Matthias Weidemüller, and Yurii B Ovchinnikov. Optical dipole traps for neutral atoms. In *Advances in atomic, molecular, and optical physics*, volume 42, pages 95–170. Elsevier, 2000. doi: 10.1016/S1049-250X(08)60186-X.

[47] Serge Haroche and Daniel Kleppner. Cavity quantum electrodynamics. *Phys. Today*, 42:24, 1989. doi: 10.1063/1.881201.

[48] Atsushi Hatakeyama, Markus Wilde, and Katsuyuki Fukutani. Classification of light-induced desorption of alkali atoms in glass cells used in atomic physics experiments. *e-Journal of Surface Science and Nanotechnology*, 4:63–68, 2006. doi: 10.1380/ejssnt.2006.63.

[49] Alan C. Hindmarsh, Peter N. Brown, Keith E. Grant, Steven L. Lee, Radu Serban, Dan E. Shumaker, and Carol S. Woodward. Sundials: Suite of nonlinear and differential/algebraic equation solvers. *ACM Trans. Math. Softw.*, 31(3):363–396, September 2005. ISSN 0098-3500. doi: 10.1145/1089014.1089020. URL `http://doi.acm.org/10.1145/1089014.1089020`.

[50] J D Hood, A Goban, A Asenjo-Garcia, M Lu, S-P Yu, D E Chang, and H J Kimble. Atom–atom interactions around the band edge of a photonic crystal waveguide. *Proc. Natl. Acad. Sci. U.S.A.*, 113(38):10507–10512, 2016. doi: 10.1073/pnas.1603788113.

[51] C-L Hung, Alejandro González-Tudela, J Ignacio Cirac, and H J Kimble. Quantum spin dynamics with pairwise-tunable, long-range interactions. *Proc. Natl. Acad. Sci. U.S.A.*, page 201603777, 2016. doi: 10.1073/pnas.1603777113.

[52] CL Hung, SM Meenehan, DE Chang, O Painter, and HJ Kimble. Trapped atoms in one-dimensional photonic crystals. *New J. Phys.*, 15(8):083026, 2013. doi: 10.1088/1367-2630/15/8/083026.

[53] Francesco Intravaia, Carsten Henkel, and Mauro Antezza. Fluctuation-induced forces between atoms and surfaces: The casimir–polder interaction. In *Casimir Physics*, pages 345–391. Springer, 2011. doi: 10.1007/978-3-642-20288-9_11.

[54] John D. Joannopoulos, Steven G. Johnson, Joshua N. Winn, and Robert D. Meade. *Photonic Crystals: Molding the Flow of Light (Second Edition)*. Princeton University Press, 2 edition, 2008. ISBN 0691124566. URL `http://www.amazon.com/Photonic-Crystals-Molding-Light-Second/dp/0691124566%3FSubscriptionId%3D13CT5CVB80YFWJEPWS02%26tag%3Dws%26linkCode%3Dxm2%26camp%3D2025%26creative%3D165953%26creativeASIN%3D0691124566`.

[55] Sajeev John. Strong localization of photons in certain disordered dielectric superlattices. 58(23):2486–2489. doi: 10.1103/PhysRevLett.58.2486. URL `https://link.aps.org/doi/10.1103/PhysRevLett.58.2486`.

[56] A. M. Kaufman, B. J. Lester, and C. A. Regal. Cooling a single atom in an optical tweezer to its quantum ground state. 2(4):041014, . doi: 10.1103/PhysRevX.2.041014. URL `https://link.aps.org/doi/10.1103/PhysRevX.2.041014`.

[57] A. M. Kaufman, B. J. Lester, C. M. Reynolds, M. L. Wall, M. Foss-Feig, K. R. A. Hazzard, A. M. Rey, and C. A. Regal. Two-particle quantum interference in tunnel-coupled optical tweezers. 345(6194):306–309, . ISSN 0036-8075, 1095-9203. doi: 10.1126/science.1250057. URL `https://science.sciencemag.org/content/345/6194/306`.

[58] A M Kaufman, B J Lester, and C A Regal. Cooling a single atom in an optical tweezer to its quantum ground state. *Phys. Rev. X*, 2:041014, Nov 2012. doi: 10.1103/PhysRevX.2.041014. URL `https://link.aps.org/doi/10.1103/PhysRevX.2.041014`.

[59] DW Keith, ML Schattenburg, Henry I Smith, and DE Pritchard. Diffraction of atoms by a transmission grating. *Phys. Rev. Lett.*, 61(14):1580, 1988. doi: 10.1103/PhysRevLett.61.1580.

[60] H. J. Kimble, M. Dagenais, and L. Mandel. Photon antibunching in resonance fluorescence. 39(11):691–695. doi: 10.1103/PhysRevLett.39.691. URL `https://link.aps.org/doi/10.1103/PhysRevLett.39.691`.

[61] Alexander Kozhekin and Gershon Kurizki. Self-induced transparency in bragg reflectors: gap solitons near absorption resonances. *Phys. Rev. Lett.*, 74(25):5020, 1995. doi: 10.1103/PhysRevLett.74.5020.

[62] SJM Kuppens, KL Corwin, KW Miller, TE Chupp, and CE Wieman. Loading an optical dipole trap. *Phys. Rev. A*, 62(1):013406, 2000. doi: 10.1103/PhysRevA.62.013406.

[63] A. Laliotis, I. Maurin, M. Fichet, D. Bloch, M. Ducloy, N. Balasanyan, A. Sarkisyan, and D. Sarkisyan. Selective reflection spectroscopy at the interface between a calcium fluoride window and cs vapour. *Applied Physics B*, 90(3):415–420, Mar 2008. ISSN 1432-0649. doi: 10.1007/s00340-007-2927-9. URL `https://doi.org/10.1007/s00340-007-2927-9`.

[64] A Landragin, J-Y Courtois, G Labeyrie, N Vansteenkiste, CI Westbrook, and A Aspect. Measurement of the van der waals force in an atomic mirror. *Phys. Rev. Lett.*, 77(8):1464, 1996. doi: 10.1103/PhysRevLett.77.1464.

[65] Fam Le Kien, Philipp Schneeweiss, and Arno Rauschenbeutel. Dynamical polarizability of atoms in arbitrary light fields: general theory and application to cesium. 67(5):92. ISSN 1434-6079. doi: 10.1140/epjd/e2013-30729-x. URL `https://doi.org/10.1140/epjd/e2013-30729-x`.

[66] P. D. Lett, P. S. Julienne, and W. D. Phillips. Photoassociative spectroscopy of laser-cooled atoms. *Annual Review of Physical Chemistry*, 46(1):423–452, 1995. doi: 10.1146/annurev.pc.46.100195.002231. URL `https://doi.org/10.1146/annurev.pc.46.100195.002231`. PMID: 24329894.

[67] Paul D. Lett, Richard N. Watts, Christoph I. Westbrook, William D. Phillips, Phillip L. Gould, and Harold J. Metcalf. Observation of atoms laser cooled below the doppler limit. 61(2):169–172. doi: 10.1103/PhysRevLett.61.169. URL `https://link.aps.org/doi/10.1103/PhysRevLett.61.169`.

[68] Yu-ju Lin, Igor Teper, Cheng Chin, and Vladan Vuletić. Impact of the casimir-polder potential and johnson noise on bose-einstein condensate stability near

surfaces. *Phys. Rev. Lett.*, 92:050404, Feb 2004. doi: 10.1103/PhysRevLett.92.050404. URL `https://link.aps.org/doi/10.1103/PhysRevLett.92.050404`.

[69] Victor Liu and Shanhui Fan. $S^4$ : A free electromagnetic solver for layered periodic structures. *Computer Physics Communications*, 183(10):2233 – 2244, 2012. ISSN 0010-4655. doi: 10.1016/j.cpc.2012.04.026. URL `http://www.sciencedirect.com/science/article/pii/S0010465512001658`.

[70] Peter Lodahl, Sahand Mahmoodian, and Søren Stobbe. Interfacing single photons and single quantum dots with photonic nanostructures. 87(2):347–400. ISSN 0034-6861, 1539-0756. doi: 10.1103/RevModPhys.87.347. URL `https://link.aps.org/doi/10.1103/RevModPhys.87.347`.

[71] Peter Lodahl, Sahand Mahmoodian, Søren Stobbe, Arno Rauschenbeutel, Philipp Schneeweiss, Jürgen Volz, Hannes Pichler, and Peter Zoller. Chiral quantum optics. *Nature*, 541(7638):473, 2017. doi: 10.1038/nature21037.

[72] Andrew D. Ludlow, Martin M. Boyd, Jun Ye, E. Peik, and P.O. Schmidt. Optical atomic clocks. 87(2):637–701. ISSN 0034-6861, 1539-0756. doi: 10.1103/RevModPhys.87.637. URL `https://link.aps.org/doi/10.1103/RevModPhys.87.637`.

[73] S L McCall and E L Hahn. Self-induced transparency. 183(2):457–485. doi: 10.1103/PhysRev.183.457. URL `http://link.aps.org/doi/10.1103/PhysRev.183.457`.

[74] Andrew Corby McClung. *Photonic Crystal Waveguides for Integration into an Atomic Physics Experiment*. PhD thesis, California Institute of Technology, 2017.

[75] J. M. McGuirk, D. M. Harber, J. M. Obrecht, and E. A. Cornell. Alkali-metal adsorbate polarization on conducting and insulating surfaces probed with bose-einstein condensates. *Phys. Rev. A*, 69:062905, Jun 2004. doi: 10.1103/PhysRevA.69.062905. URL `https://link.aps.org/doi/10.1103/PhysRevA.69.062905`.

[76] Harold J. Metcalf and Peter van der Straten. *Laser Cooling and Trapping*. Springer-Verlag, New York, 1999.

[77] Harold J Metcalf and Peter Van der Straten. *Laser cooling and trapping*. Springer Science & Business Media, 2012.

[78] John Michael Obrecht, RJ Wild, M Antezza, LP Pitaevskii, S Stringari, and Eric A Cornell. Measurement of the temperature dependence of the casimir-polder force. *Phys. Rev. Lett.*, 98(6):063201, 2007. doi: 10.1103/PhysRevLett.98.063201.

[79] M Oria, M Chevrollier, D Bloch, M Fichet, and M Ducloy. Spectral observation of surface-induced van der waals attraction on atomic vapour. *EPL (Europhysics Letters)*, 14(6):527, 1991. doi: 10.1209/0295-5075/14/6/005.

[80] Thibault Peyronel, Ofer Firstenberg, Qi-Yu Liang, Sebastian Hofferberth, Alexey V. Gorshkov, Thomas Pohl, Mikhail D. Lukin, and Vladan Vuletić. Quantum nonlinear optics with single photons enabled by strongly interacting atoms. 488(7409):57–60. ISSN 1476-4687. doi: 10.1038/nature11361. URL `https://www.nature.com/articles/nature11361`.

[81] William D. Phillips. Nobel lecture: Laser cooling and trapping of neutral atoms. *Rev. Mod. Phys.*, 70:721–741, Jul 1998. doi: 10.1103/RevModPhys.70.721. URL `https://link.aps.org/doi/10.1103/RevModPhys.70.721`.

[82] William D Phillips. Nobel lecture: Laser cooling and trapping of neutral atoms. *Rev. Mod. Phys.*, 70(3):721, 1998. doi: 10.1103/RevModPhys.70.721.

[83] Hannes Pichler, Soonwon Choi, Peter Zoller, and Mikhail D Lukin. Universal photonic quantum computation via time-delayed feedback. *Proc. Natl. Acad. Sci. U.S.A.*, page 201711003, 2017. doi: 10.1073/pnas.1711003114.

[84] E. M. Purcell. *Spontaneous Emission Probabilities at Radio Frequencies*, pages 839–839. Springer US, Boston, MA, 1995. ISBN 978-1-4615-1963-8. doi: 10.1007/978-1-4615-1963-8_40. URL `https://doi.org/10.1007/978-1-4615-1963-8_40`.

[85] E. L. Raab, M. Prentiss, Alex Cable, Steven Chu, and D. E. Pritchard. Trapping of neutral sodium atoms with radiation pressure. 59(23):2631–2634. doi: 10.1103/PhysRevLett.59.2631. URL `https://link.aps.org/doi/10.1103/PhysRevLett.59.2631`.

[86] Gerhard Rempe, Herbert Walther, and Norbert Klein. Observation of quantum collapse and revival in a one-atom maser. 58(4):353–356. doi: 10.1103/PhysRevLett.58.353. URL `https://link.aps.org/doi/10.1103/PhysRevLett.58.353`.

[87] Ralf Ritter, Nico Gruhler, Helge Dobbertin, Harald Kübler, Stefan Scheel, Wolfram Pernice, Tilman Pfau, and Robert Löw. Coupling thermal atomic vapor to slot waveguides. *Phys. Rev. X*, 8(2):021032, 2018. doi: 10.1103/PhysRevX.8.021032.

[88] M. S. Safronova, U. I. Safronova, and Charles W. Clark. Magic wavelengths, matrix elements, polarizabilities, and lifetimes of cs. 94(1). ISSN 2469-9926, 2469-9934. doi: 10.1103/PhysRevA.94.012505. URL `http://arxiv.org/abs/1605.05210`.

[89] G Sagué, E Vetsch, W Alt, D Meschede, and A Rauschenbeutel. Cold-atom physics using ultrathin optical fibers: Light-induced dipole forces and surface interactions. *Phys. Rev. Lett.*, 99(16):163602, 2007. doi: 10.1103/PhysRevLett.99.163602.

[90] T. A. Savard, K. M. O'Hara, and J. E. Thomas. Laser-noise-induced heating in far-off resonance optical traps. *Physical Review A*, 56(2):R1095–R1098. ISSN 1050-2947, 1094-1622. doi: 10.1103/PhysRevA.56.R1095. URL `https://link.aps.org/doi/10.1103/PhysRevA.56.R1095`.

[91] Nicolas Schlosser, Georges Reymond, Igor Protsenko, and Philippe Grangier. Sub-poissonian loading of single atoms in a microscopic dipole trap. *Nature*, 411(6841):1024, 2001. doi: 10.1038/35082512.

[92] Pablo Solano, Jeffrey A Grover, Jonathan E Hoffman, Sylvain Ravets, Fredrik K Fatemi, Luis A Orozco, and Steven L Rolston. Optical nanofibers: a new platform for quantum optics. In *Advances In Atomic, Molecular, and Optical Physics*, volume 66, pages 439–505. Elsevier, 2017. doi: 10.1016/bs.aamop.2017.02.003.

[93] D A Steck. Cesium d line data. . URL `http://george.ph.utexas.edu/~dsteck/alkalidata/cesiumnumbers.pdf`.

[94] D A Steck. *Quantum and Atom optics*. . URL `http://atomoptics-nas.uoregon.edu/~dsteck/teaching/quantum-optics/`.

[95] NP Stern, DJ Alton, and HJ Kimble. Simulations of atomic trajectories near a dielectric surface. *New J. Phys.*, 13(8):085004, 2011. doi: 10.1088/1367-2630/13/8/085004.

[96] CI Sukenik, MG Boshier, D Cho, V Sandoghdar, and EA Hinds. Measurement of the casimir-polder force. *Phys. Rev. Lett.*, 70(5):560, 1993. doi: 10.1103/PhysRevLett.70.560.

[97] Endre Süli and David F. Mayers. *An Introduction to Numerical Analysis*. Cambridge University Press, 2003. doi: 10.1017/CBO9780511801181.

[98] J D Thompson, TG Tiecke, N P de Leon, J Feist, AV Akimov, M Gullans, A S Zibrov, V Vuletić, and M D Lukin. Coupling a single trapped atom to a nanoscale optical cavity. *Science*, 340(6137):1202–1205, 2013. doi: 10.1126/science.1237125.

[99] R. J. Thompson, G. Rempe, and H. J. Kimble. Observation of normal-mode splitting for an atom in an optical cavity. 68(8):1132–1135. doi: 10.1103/PhysRevLett.68.1132. URL `https://link.aps.org/doi/10.1103/PhysRevLett.68.1132`.

[100] TG Tiecke, Jeffrey Douglas Thompson, Nathalie Pulmones de Leon, LR Liu, Vladan Vuletić, and Mikhail D Lukin. Nanophotonic quantum phase switch with a single atom. *Nature*, 508(7495):241, 2014. doi: 10.1038/nature13188.

[101] P. J. Ungar, D. S. Weiss, E. Riis, and Steven Chu. Optical molasses and multilevel atoms: theory. 6(11):2058–2071. ISSN 1520-8540. doi: 10.1364/JOSAB.6.002058. URL `https://www.osapublishing.org/josab/abstract.cfm?uri=josab-6-11-2058`.

[102] S. J. van Enk and H. J. Kimble. Strongly focused light beams interacting with single atoms in free space. 63(2):023809. doi: 10.1103/PhysRevA.63.023809. URL `https://link.aps.org/doi/10.1103/PhysRevA.63.023809`.

[103] E Vetsch, D Reitz, G Sagué, R Schmidt, ST Dawkins, and A Rauschenbeutel. Optical interface created by laser-cooled atoms trapped in the evanescent field surrounding an optical nanofiber. *Phys. Rev. Lett.*, 104(20):203603, 2010. doi: 10.1103/PhysRevLett.104.203603.

[104] Vladan Vuletić, Cheng Chin, Andrew J. Kerman, and Steven Chu. Degenerate raman sideband cooling of trapped cesium atoms at very high atomic densities. *Phys. Rev. Lett.*, 81:5768–5771, Dec 1998. doi: 10.1103/PhysRevLett.81.5768. URL `https://link.aps.org/doi/10.1103/PhysRevLett.81.5768`.

[105] Vladan Vuletić, Cheng Chin, Andrew J. Kerman, and Steven Chu. Degenerate raman sideband cooling of trapped cesium atoms at very high atomic densities. 81(26):5768–5771. doi: 10.1103/PhysRevLett.81.5768. URL `https://link.aps.org/doi/10.1103/PhysRevLett.81.5768`.

[106] Carl E Wieman, David E Pritchard, and David J Wineland. Atom cooling, trapping, and quantum manipulation. *Rev. Mod. Phys.*, 71(2):S253, 1999. doi: 10.1103/RevModPhys.71.S253.

[107] W. Wohlleben, F. Chevy, K. Madison, and J. Dalibard. An atom faucet. 15(2):237–244. ISSN 1434-6060, 1434-6079. doi: 10.1007/s100530170171. URL `https://epjd.epj.org/articles/epjd/abs/2001/08/d01004/d01004.html`.

[108] Eli Yablonovitch. Inhibited spontaneous emission in solid-state physics and electronics. 58(20):2059–2062. doi: 10.1103/PhysRevLett.58.2059. URL `https://link.aps.org/doi/10.1103/PhysRevLett.58.2059`.

[109] S-P Yu, JD Hood, JA Muniz, MJ Martin, R Norte, C-L Hung, S M Meenehan, J D Cohen, O Painter, and HJ Kimble. Nanowire photonic crystal waveguides for single-atom trapping and strong light-matter interactions. *Appl. Phys. Lett.*, 104(11):111103, 2014. doi: 10.1063/1.4868975.

[110] Su-Peng Yu. *Nano-Photonic Platform for Atom-Light Interaction*. PhD thesis, California Institute of Technology, 2017.

[111] Emil Zeuthen, Michael J. Gullans, Mohammad F. Maghrebi, and Alexey V. Gorshkov. Correlated photon dynamics in dissipative rydberg media. 119 (4):043602. doi: 10.1103/PhysRevLett.119.043602. URL `https://link.aps.org/doi/10.1103/PhysRevLett.119.043602`.

[112] Philip Zupancic. Dynamic holography and beamshaping using digital micromirror devices. URL `http://greiner.physics.harvard.edu/assets/theses/zupancic_thesis.pdf`.

# *Appendix A*

# CONFIGURATION FILE FOR 2D SIMULATION

Source Code A.1: 2D simulation configuration YAML file.

```yaml
#All time unit in us.
#All length unit in nm.
#
#2D simulation
#210kHz lattice trap frequency
#with blue TM stark beam guided mode
#with Casimir Polder Potential
#
#initial atom position read from previous simulation output
simulation-type: 2D
fields-config:
    field:
        field-type: ScalarFieldNode
        dim: 2
        fields:
            casimir-polder-ground-state:
                field-type: ScalarFieldNode
                dim: 2
                fields:
                    casmir-polder1:
                        field-type: ScalarField
                        D-type: Float
                        dim: 2
                        init-type: file
                        filename:
                        ↪   /home/lucaspeng/data/potential/6s1_2cp_500.h5
                        variable: cp
                        pos: [9400.0,23890.0]
                        size: [1200, 1510]
                        scaling: "t->1.0"
                    casmir-polder2:
                        field-type: ScalarField
                        D-type: Float
                        dim: 2
                        init-type: file
```

```yaml
                        filename:
                        ↪   /home/lucaspeng/data/potential/6s1_2cp_500.h5
                        variable: cp
                        pos: [9400.0,24600.0]
                        size: [1200, 1510]
                        scaling: "t->1.0"
                scaling: "t->1.0"
            casimir-polder-excited-state:
                field-type: ScalarFieldNode
                dim: 2
                fields:
                    casmir-polder1:
                        field-type: ScalarField
                        D-type: Float
                        dim: 2
                        init-type: file
                        filename:
                        ↪   /home/lucaspeng/data/potential/6p1_2cp_500.h5
                        variable: cp
                        pos: [9400.0,23890.0]
                        size: [1200, 1510]
                        scaling: "t->1.0"
                    casmir-polder2:
                        field-type: ScalarField
                        D-type: Float
                        dim: 2
                        init-type: file
                        filename:
                        ↪   /home/lucaspeng/data/potential/6p1_2cp_500.h5
                        variable: cp
                        pos: [9400.0,24600.0]
                        size: [1200, 1510]
                        scaling: "t->1.0"
                scaling: "t->-0.0"
            lattice-beams:
                field-type: VectorFieldNode
                dim: 2
                fields:
                    right-beam:
                        field-type: VectorField
                        D-type: Complex
                        dim: 2
                        init-type: file
```

```
                        filename:
                        ↪  /home/lucaspeng/data/potential/Exy_60u_0_right_thick_small.h5
                        variable: field
                        pos: [0.0,15000.0]
                        size: [20000, 20000]
                        scaling: "t->1.0+0.0im"
                    left-beam:
                        field-type: VectorField
                        D-type: Complex
                        dim: 2
                        init-type: file
                        filename:
                        ↪  /home/lucaspeng/data/potential/Exy_60u_0_left_thick_small.h5
                        variable: field
                        pos: [0.0,15000.0]
                        size: [20000, 20000]
                        #scaling: "t->1.0+0.0im"
                        scaling: "t->exp(im*(2*pi*1.2*t))"
                scaling: "t->-0.0001008184" #210k
            guided-mode:
                field-type: ScalarFieldNode
                dim: 2
                fields:
                    tmd2:
                        field-type: ScalarField
                        D-type: Float
                        dim: 2
                        init-type: file
                        filename: /home/lucaspeng/data/potential/tmd2.h5
                        variable: tmd2
                        pos: [8140.4, 23147.5]
                        size: [3690.75,3690.75]
                        scaling: "t->2.0"
                scaling: "t->1.0"
        scaling: "t->1.0"
trajsolver-config:
    simulation-config:
        traj_num: 100000
        tstart: 100.0
        tend: 125.0
        tdiv: 0.01
    solver-config:
        solver: ADAMS
```

```
        reltol: 1e-10
        abstol: 1e-7
    atom-config:
        init-type: from-file
        filename: /home/lucaspeng/data/lucas/result/init.h5
        time: 100.0 #read the atoms position at time 100us
        radial-temperature: 450e-6 #irrelavent when reading initial
        ↪   condition from a file
        axial-temperature: 450e-6 #irrelavent when reading initial
        ↪   condition from a file
        init-speed: -340.8 #irrelavent when reading initial condition from
        ↪   a file
        init-range:  #initialize atoms in pancake [x1 x2 y1 y2], irrelavent
        ↪   when reading initial condition from a file
            pancake1: [68776.0, 69226.0, 100.0, 49900.0]
            pancake2: [68350.0, 68810.0, 100.0, 49900.0]
            pancake3: [67924.0, 68384.0, 100.0, 49900.0]
            pancake4: [67495.0, 67958.0, 100.0, 49900.0]
            pancake5: [67069.0, 67532.0, 100.0, 49900.0]
    in-boundary: #atoms in these areas are removed from the simulation
        beam1: [9890.0, 10110.0, 10110.0, 9890.0,
                24380.0, 24380.0, 24910.0, 24910.0]
        beam2: [9890.0, 10110.0, 10110.0, 9890.0,
                25090.0, 25090.0, 25620.0, 25620.0]
    out-boundary: #atoms out of these areas are removed from the simulation
        edge: [100.0, 69900.0, 69900.0, 100.0,
               100.0, 100.0,   49900.0, 49900.0]
    save-range: #save atom trajectories in this time range
        tstart: 101.0
        tend: 124.0
job-config:
    #scan guided-mode scaling from 1 to 16 in step of 1
    type: single-scan-scaling
    range_i_start: 1
    range_i_step: 1
    range_i_end: 16
    plot-range: [25,1250]
    jobs:
        job1:
            field: guided-mode
            scaling: "t->(@i-1)*1.0"
    filter: #filter trajectories, options: none, gap, sides, other.
        type: none
```

```
        tstart: 101.0
        tend: 124.0
        roi: [9000.0, 11000.0, 11000.0, 9000.0, 26000.0, 26000.0, 24000.0,
        ↪  24000.0]
        gap: [9900.0, 10100.0, 10100.0, 9900.0, 24900.0, 24900.0, 25100.0,
        ↪  25100.0]
        side1: [9900.0, 10100.0, 10100.0, 9900.0, 25610.0, 25610.0,
        ↪  40000.0, 40000.0]
        side2: [9900.0, 10100.0, 10100.0, 9900.0, 10000.0, 10000.0,
        ↪  24390.0, 24390.0]
    movie-output:
        tstart: 110.0
        tend: 117.0
        tdiv: 0.02
        range: [9000.0, 11000.0, 24000.0, 26000.0]
        res: [10.0,10.0]
    probe:
        field:
            field-type: ScalarFieldNode
            dim: 2
            fields:
                 ted1:
                     field-type: ScalarFieldNode
                     dim: 2
                     fields:
                         ted1:
                             field-type: ScalarField
                             D-type: Float
                             dim: 2
                             init-type: file
                             filename:
                             ↪  /home/lucaspeng/data/potential/ted1.h5
                             variable: ted1
                             pos: [8140.4, 23147.5]
                             size: [3690.75,3690.75]
                             scaling: "t->2000.0"
                     scaling: "t->1.0"
                 tmd2:
                     field-type: ScalarFieldNode
                     dim: 2
                     fields:
                         tmd2:
                             field-type: ScalarField
```

```
                         D-type: Float
                         dim: 2
                         init-type: file
                         filename:
                         ↪  /home/lucaspeng/data/potential/tmd2.h5
                         variable: tmd2
                         pos: [8140.4, 23147.5]
                         size: [3690.75,3690.75]
                         scaling: "t->2500.0"
                 scaling: "t->1.0"
        scaling: "t->1.0"
spectrum:
    name: ["ted1","tmd2"]
    mode: 2
    # mode: option for 2D only
    # 1 to distributed atom with cos^2 distribution along x, for TE
    ↪  probe.
    # 2 to distributed uniformly for TM probe
    vector-shift: 1 # 1 to enable vector shift
    gamma-1d: 1.0
    gamma-prime: 5
    probe-contrast: 1.0
    lattice-width: 32000 #in nm
    lattice-unit: 370 #nm
    atom-beam-waist: 30000 #in nm
    pos-variance: 0.05 #in lattice unit
    k-ratio: 0.98 #k = Xpoint_k * k-ratio
    use-all-atom: true #overwrite total-atom-number when true
    total-atom-number: 100000
    avg-atom-number: 2000
    iteration: 20
    frequency: #in MHz
        start: -60
        end: 20
        step: 2.0
    time: #in us
        start: 110.36
        end: 117.0275
        step: 0.020825
```